# The crustal structure of the eastern Walvis Ridge
A classical hotspot example?
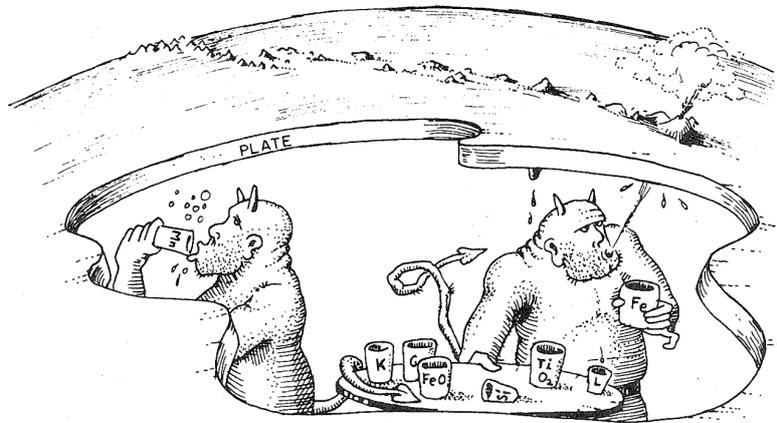
Dissertation zur Erlangung des Doktorgrades
der Naturwissenschaften

vorgelegt dem Fachbereich Geowissenschaften an der
Universität Bremen

von

Tanja Fromm

Alfred-Wegener-Institut für Polar- und Meeresforschung
Bremerhaven, Mai 2015

Universität Bremen   AWI   HELMHOLTZ GEMEINSCHAFT

EIDESSTATTLICHE ERKLÄRUNG

Tanja Fromm
Deichsmoor 15
27624 Geestland

Hiermit versichere ich, dass ich

1. die Arbeit ohne unerlaubte fremde Hilfe angefertigt habe,

2. keine anderen als die von mir angegebenen Quellen und Hilfsmittel benutzt habe und

3. die den benutzten Werken wörtlich oder inhaltlich entnommenen Stellen als solche kenntlich gemacht habe.

Bremerhaven, den 21. Mai 2015

_____
Tanja Fromm

Die vorliegende Dissertation wurde am 24.07.2015 an der Universität Bremen verteidigt. Der Prüfungsausschuss bestand aus Prof. Dr. Wilfried Jokat (erster Gutachter), Prof. Dr. Cornelia Spiegel (zweite Gutachterin), Prof. Dr. Dr. h.c. Gerold Wefer, Prof. Dr. Heinrich Villinger, PD Dr. Christian Scheibner und Rebecca Schlegel.

Title picture by Holden and Vogt, 1977

Zusammenfassung

Der Walfischrücken ist ein über 3000 km langes submarines Gebirge im Südatlantik, das aus einzelnen Vulkanen und zahlreichen kleineren und größeren Rücken besteht. Er erstreckt sich von Namibia am afrikanischen Kontinentalrand bis nach Tristan da Cunha, einer Vulkaninsel in der Nähe des Mittelatlantischen Rückens. An manchen Stellen erhebt sich diese gewaltige Struktur vom 5000 m tiefen Meeresbecken bis an die Meeresoberfläche und sogar darüber hinaus.

Die Hypothesen über den Ursprung des Walfischrückens sind eng mit der Debatte über Manteldiapire verknüpft: Entweder ist der Walfischrücken die Spur des Tristan Hotspots ('heisser Fleck') oder das Ergebnis von Spannungsabbau durch normale Plattentektonik. Die Hotspot-Hypothese bringt den Rücken ferner mit kontinentalen Flutbasalten in Verbindung, von denen angenommen wird, dass sie von einem ankommenden Manteldiapir verursacht wurden. Eine enge zeitliche und räumliche Beziehung zwischen der Ablagerung von Flutbasalten und Kontinentalaufbrüchen führte zu der Idee, dass Manteldiapire einen großen Einfluß auf Kontinentalaufbrüche haben.

Im Jahre 2011 wurde eine große geophysikalische Messungkampagne am Walfischrücken in der Nähe des Kontinentalrandes durchgeführt, um die Fragen nach dem Ursprung des Rückens und den Einfluß eines möglichen Manteldiapirs auf die Öffnung des Südatlantik zu untersuchen. Hier stelle ich die Krustenstruktur des Rückens und des angrenzenden Kontinents vor, die ich anhand zweier seismischer Refraktionprofile und deren Schwere-Modellierung abgeleitet habe. Eines der Profile liegt etwa 600 km von der Küste entfernt, und erstreckt sich 480 km quer über den Kamm des Rückens. Das andere Profil deckt den Kontinentalrand ab. Es erstreckt sich 430 km entlang der Rückenachse und wird 290 km an Land fortgeführt.

Meine Ergebnisse zeigen, dass der Walfischrücken aus verdickter ozeanischer Kruste mit einer Mächtigkeit von 18-22 km besteht. Die Krustenmächtigkeit nimmt mit zunehmender Entfernung vom Kontinentalrand ab. Magmatische Gesteine überlagern eine Bruchzone sowie ozeanische Kruste und müssen daher nach der Entstehung der Bruchzone gebildet worden sein. Darüber hinaus ist die Bruchzone etwa 100 km von der Hauptrückenachse entfernt. Dies deutet darauf hin, dass der Walfischrücken unabhängig von dieser Bruchzone entstand. Ich schließe daraus, dass der Walfischrücken nicht durch Spannungsabbau entlang einer Bruchzone entstanden ist, sondern unterstützen einen Hotspot-bedingten Ursprung.

Anormal hohe seismische Krusten-Geschwindigkeiten über 7,3 km/s treten in der unteren Kruste im Kontinent-Ozean Übergang auf. Dieser Hochgeschwindigkeitsunterkrustenkörper (HVLCB) setzt sich in der unteren kontinentalen Kruste fort und endet am Kaokogürtel. Ähnliche HVLCB wurden entlang des Kontinentalrandes südlich des Walfischrückens entdeckt. Vergleicht man Lage und Ausdehnung der HVLCBs, liegt das seewärte Ende des HVLCB am Walfischrücken in vergleichbarer Entfernung von der Küste. Unter dem Kontinent dagegen kann der HVLCB 100 km weiter als bei den südlichen Profilen nachgewiesen werden, was

auf die Anwesenheit einer Mantelanomalie während des anfänglichen Riftstadiums hindeutet. Zusätzliche seismische Untersuchungen mit orthogonaler Profilorientierung zeigen, dass die Ausdehnung dieses HVLCB lokal begrenzt ist und er unter der kontinentalen Kruste schmaler ist als unter der ozeanischen Kruste. Der Einfluss des Hotspots scheint daher lokal begrenzt gewesen zu sein und die Verteilung des intrudierten Materials ähnelt eher einem schmalen Kanal, anstatt eines breiten Diapirkopfes.

Deshalb bezweifel ich, dass ein massiver Diapirkopf während der Öffnung des Südatlantiks existierte. Daraus folgt, dass der Kontinentalaufbruch vermutlich nicht von einem Manteldiapir initiiert wurde.

Summary

The Walvis Ridge is a more than 3000 km long submarine ridge in the South Atlantic, which consists of single volcanoes and numerous smaller and larger ridges. It stretches from Namibia at the African continental margin to the volcanic island of Tristan da Cunha near the Mid-Atlantic Ridge. At some places this remarkable structure raises from the 5000 m deep sea basins to the sea surface or even above.

The hypotheses about its origin are strongly related to the great debate about the existence of deep mantle plumes: The ridge is thought to be either the hotspot trail of the Tristan hotspot or the result of stress release caused by normal plate tectonics. The hotspot hypothesis further links the ridge to continental flood basalts, which are thought to be emplaced by an arriving plume. A temporal and spatial relation between the eruption of flood basalts and continental breakup gave rise to the idea that plumes are an important parameter for controlling continental breakups.

In 2011 a large geophysical experiment was carried out at the landfall of Walvis Ridge in order to constrain its origin and the influence of the proposed plume head on the opening of the South Atlantic. Here, I present the crustal structure of the Walvis Ridge and the adjacent continental crust derived from two seismic refraction lines and gravity modelling. One line extends 480 km across the ridge in approximately 600 km distance to the coastline. The other profile covers the continental margin. It extends 430 km along the ridge axis and continues 290 km onshore.

My results show that the Walvis Ridge consists of thickened oceanic crust with a thickness of 18-22 km. The crustal thickness decreases with increasing distance from the continental margin. Magmatic rocks cover a major fracture zone and pre-existing oceanic crust. Therefore, they must have been emplaced after the transform fault became inactive. Furthermore, the fracture zone is in about 100 km distance from the main ridge axis indicating that the ridge formed independent of the fracture zone. I conclude that normal stress release along a transform fault cannot account for the formation of the Walvis Ridge and support a hotspot origin.

Abnormally high seismic velocities above 7.3 km/s are observed in the lower crust at the continent-ocean transition. This high velocity lower crustal body (HVLCB) intrudes into the continental crust and terminates at the Kaoko fold belt. Similar HVLCB have been observed along the continental margin south of Walvis Ridge. The seaward termination of the HVLCB at Walvis Ridge is comparable to those. In contrast, the landward termination occurs 100 km further in land and is attributed to the presence of a mantle anomaly during the initial rift stage. Complementary seismic studies with a perpendicular line orientation show that this HVLCB is very limited in its width, even narrower than offshore. The influence of the hotspot was therefore very localized and the distribution of intrusive material resembles a narrow conduit rather than a broad plume head. I therefore question the presence of massive plume head during the the opening of the South Atlantic. From this it follows that the continental breakup has unlikely

been initiated an arriving plume head.

Contents

List of Figures

List of Tables

Abbreviations

COB	Continent-ocean boundary
COT	Continent-ocean transition
HVLCB	High velocity lower crustal body
LAB	Lithosphere-asthenosphere boundary
LIP	Large igneous province
Moho	Mohorovičić discontinuity, crust-mantle boundary
OBH	Ocean bottom hydrophone
OBS	Ocean bottom seismometer or more general ocean bottom station
Pg	Seismic phase refracted within the crust
PmP	Reflection from the crust-mantle boundary
Pn	Seismic phase refracted in the mantle
RGR	Rio Grande Rise
SDR	Seaward dipping reflector
SPP	Sao Paolo Plateau
WR	Walvis Ridge

1   Introduction and Motivation

1.1   Hotspot volcanism and continental breakup

Worldwide we observe volcanism that is not related to plate boundaries at subduction zones or mid ocean ridges where magma sources are easy to identify. There are numerous so called hotspots of volcanism 'in the centre' of tectonic plates without an obvious reason and an available melt source. Volcanoes form linear chains showing age progression along the line. The most prominent example is the Hawaii-Emperor chain in the Pacific-Ocean.

The source of such intraplate volcanism is highly controversial and two fundamentally different hypotheses exist regarding its origin (e.g. Storey, 1995; Foulger, 2011). One widely used model is a hot mantle plume rising from the core-mantle boundary (Wilson, 1965; Morgan, 1971). The other hypothesis proposes solely tectonic controlled volcanism as alternative (e.g. Anderson, 2005).

The plume model is based on a thermal mantle anomaly, which transports hot material from the deep mantle to the outer lithosphere, where it melts through the crust and creates a volcano at the surface (Fig. 1.1.1, e.g. Wilson, 1965; Morgan, 1971). Plate movement above the hotspot cuts off the melt supply to the volcano and a new volcano forms next to the old one. In this way a the hotspot creates an age progressive volcanic chain with the most recent activity located near the hotspot position.

Volcanic chains can be thousands of kilometre long and often link to flood
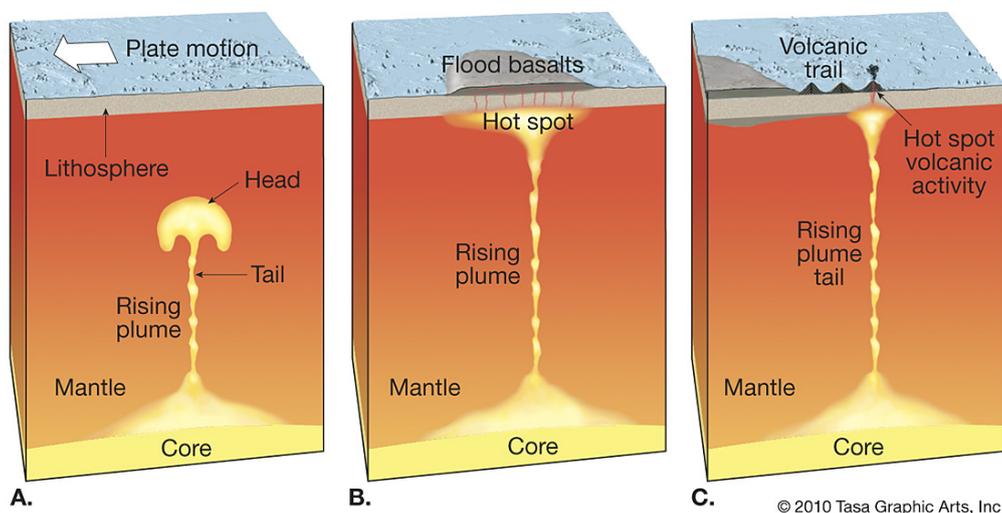
Figure 1.1.1:   Illustration of the mantle plume model. A) A rising plume develops a large mushroom shaped head, which consists of deep mantle material with increased temperature. B) Upon arrival at the crust the melt transported by the plume head erupts at the surface and forms a flood basalt province. C) The plume tails produces a volcanic trail as the plate overrides the plume position. Figure printed with kind permission of Tasa Graphic Arts, Inc.

basalts (or large igneous provinces, LIP), which mark the beginning of magmatic activity. LIPs are huge areas ($> 0.1 \cdot 10^6 \, \mathrm{km}^2$) covered with flood basalts, which erupted within relatively short igneous pulses ($1 - 5 \, \mathrm{Ma}$) and a maximum lifespan of $50 \, \mathrm{Ma}$ (Bryan and Ferrari, 2013). LIPs have been identified in various geological settings: continental flood basalt provinces, submerged oceanic plateaus and passive volcanic continental margins have been recognized as LIPs. An overview can be found in Bryan and Ferrari, 2013. The origin of LIPs is closely related to the mantle plume hypothesis. The formation of flood basalts requires large amounts of melt, which is attributed to newly arriving mantle plumes. During their rise through the mantle, they develop a large mushroom shaped head containing substantial volumes of abnormally hot mantle material that provides the large amounts of melt for the formation of flood basalt provinces.

Another remarkable observation is that LIPs are often found at continental margins and have erupted close to the time of continental breakup (e.g. Courtillot et al., 1999). This close spatial and temporal proximity led to the hypothesis that arriving mantle plumes might play an important role in the breakup process. Upon arrival at the lithosphere the plume material spreads out to a large disk and the hot and buoyant material raises the overlying lithosphere inducing increased stress at the surface (Richards et al., 1991). Additionally, it thermally and chemically erodes the overlying crust (Sobolev et al., 2011). Once the lithosphere is disintegrated, mantle material intrudes and erupts at the surface forming the flood basalts. Such processes weaken the lithosphere and thus might finally crack the plate and push continents apart. This purely plume driven breakup theory of continental plates by Wilson, 1965 and Morgan, 1971 unites the origin of hotspot volcanism, eruption of flood basalts and continental breakup in one theory.

However, this is only one possible hypothesis and recent findings point to a more passive role for mantle plumes highlighting the importance of pre-existing weak structures and old suture zones for continental breakup (Buiter and Torsvik, 2014). Furthermore the existence of plumes in general is questioned as unresolved inconsistencies between plume model predictions and observations persist. The main weaknesses of this theory are: (1) No anomalous heat flow or temperature has been detected for most 'hotspots' (Anderson and Natland, 2007); (2) some ocean island chains conflict with the strict age-progression of volcanic chains, (mainly the Pacific hotspots, McNutt et al., 1997; Davis et al., 2002); (3) not all volcanic chains connect to flood basalts and not all flood basalts have a trailing volcanic chain (Courtillot et al., 2003); (4) surface uplift before the emplacement of flood basalts is hardly recognizable (Buiter and Torsvik, 2014).

An alternative to the plume model is the plate model (Fig. 1.1.2, Anderson, 2005). This model explains all volcanism with tectonic related processes controlled by local stress conditions, the plates fabric and mantle fertility. Normal mechanisms of non-rigid plate tectonics, including recycling of crust, cause a chemically inhomogeneous shallow mantle, which might naturally contain a small amount of partial melt (Sheth, 1999). If local stress conditions lead to regions of lithospheric extension and therefore thinning, decompression melting enhances magmatism. Age progressing volcanic chains are explained with propagating cracks associated
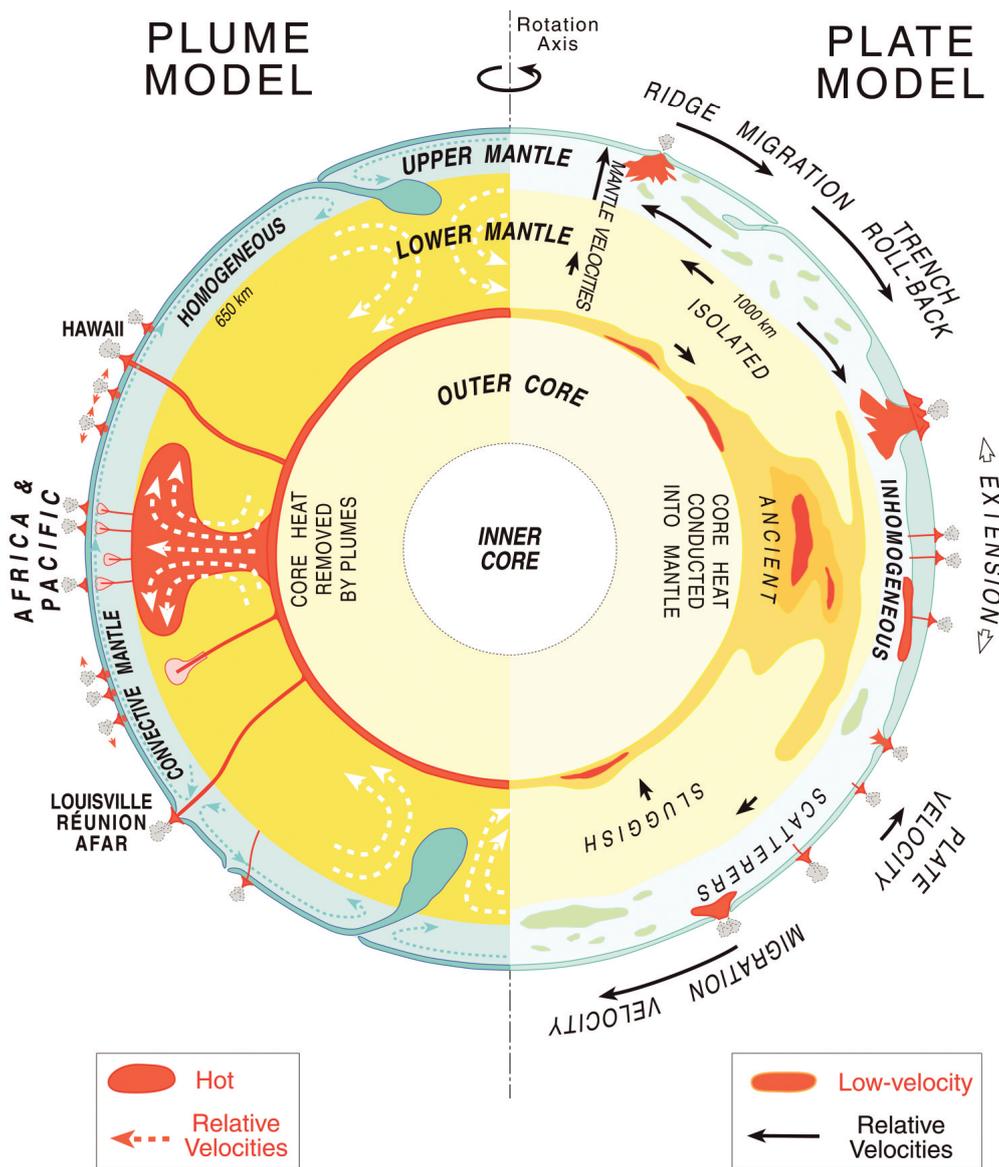
Figure 1.1.2: Illustration of the plume and the alternative plate model (Anderson, 2005). The plume model assumes a homogeneous mantle and the core as a heat source. Consequently, plumes rise to the outer crust and transport heat and deep mantle material. In contrast, the plate model assumes an inhomogeneous upper mantle as heat and melt source. Melting anomalies like hotspots and volcanic margins are localized by stress distribution and pre-existing fabric of the plates.

with long lasting strain fields (Sheth, 1999). For example, Hirano et al., 2006 explained a small age-progressing island chain in the Pacific Ocean by advancing lithospheric fractures caused by plate flexure in response to a subduction zone. The formation of LIPs is attributed to small scale convection in the shallow mantle induced at the boundary between thin and thick lithosphere. This edge likewise focus strain and increases the probability of ruptures (King and Anderson, 1995).

The plate model confines mantle processes to the upper sublithospheric mantle rejecting many unfounded assumptions made within the plume model development.

The controversy between adherents of the two different models is deep and fierce debates bluster at conferences, in publications and corresponding replies and comments (e.g. McNutt, 2006; Hofmann and Hart, 2007; Anderson and Hamilton, 2008). The data basis for observations is scarce, has been even scarcer at the beginning of the plume model development, and many presumptions have to be made. Within this thesis I present new observations, which help to assess the assumptions and predictions of both models. For this purpose I have analysed data from one of the classical examples for the plume model: The Walvis Ridge in the South Atlantic.

1.2   The Walvis Ridge

The Walvis Ridge is a remarkable bathymetric feature in the South Atlanic stretching over 3000 km from the African continental margin to the islands of Tristan Da Cunha near the Mid-Atlantic Ridge (Fig. 1.2.1) It is a classical example for the plume model: an age progressing volcanic ridge connects continental flood basalts to the current hotspot location, resembling the plume head and tail of the Tristan hotspot. The Etendeka continental flood basalts in Namibia erupted 132 Ma, contemporaneous to the opening of the South Atlantic (Renne et al., 1996). The volcanic margin of the South Atlantic is equally part of the large igneous province emplaced by the Tristan plume head. Passive volcanic continental margins are rifted margins with abundant traces of volcanism. The continent-ocean transition is covered by thick lava wedges visible as seaward dipping reflector sequences (SDR) in seismic reflection data and magmatic underplating characterized by abnormally high seismic velocities in the lower crust (> 7.2 km/s), which is interpreted as intruded mantle material at increased temperature (White et al., 2008). Previous studies revealed SDRs and magmatic underplating south of Walvis Ridge (Bauer et al., 2000; Schinkel, 2006; Hirsch et al., 2009). The volume of the magmatic underplating increases towards the north (Becker et al., 2014), which can be accounted to approaching the melt source. Interestingly, the continental margin north of the Walvis Ridge is non-volcanic (Contrucci et al., 2004; Coffin et al., 2006).

Corresponding volcanic features can be identified at the South American side: the large Paraná flood basalts in Brazil and the Rio Grande Rise offshore. Although the Paraná flood basalts are more than ten times larger than the Etendeka flood basalts (Peate, 1997), the offshore volcanism is focused on the Walvis Ridge. Unlike the African side, the South American side does not reveal a clear continuous connection between the hotspot and the flood basalts. The continental margin and the Rio Grande Rise are connected by the Torres Arch, a bathymetric high, which is much less distinct than the Walvis Ridge (Fig. 1.2.1). All this volcanic features of the South Atlantic have been attributed to the Tristan hotspot (e.g. Wilson, 1965).

Although the Walvis Ridge is an often invoked example for the plume hypothesis, there are contradicting observations and different models exist for its origin.
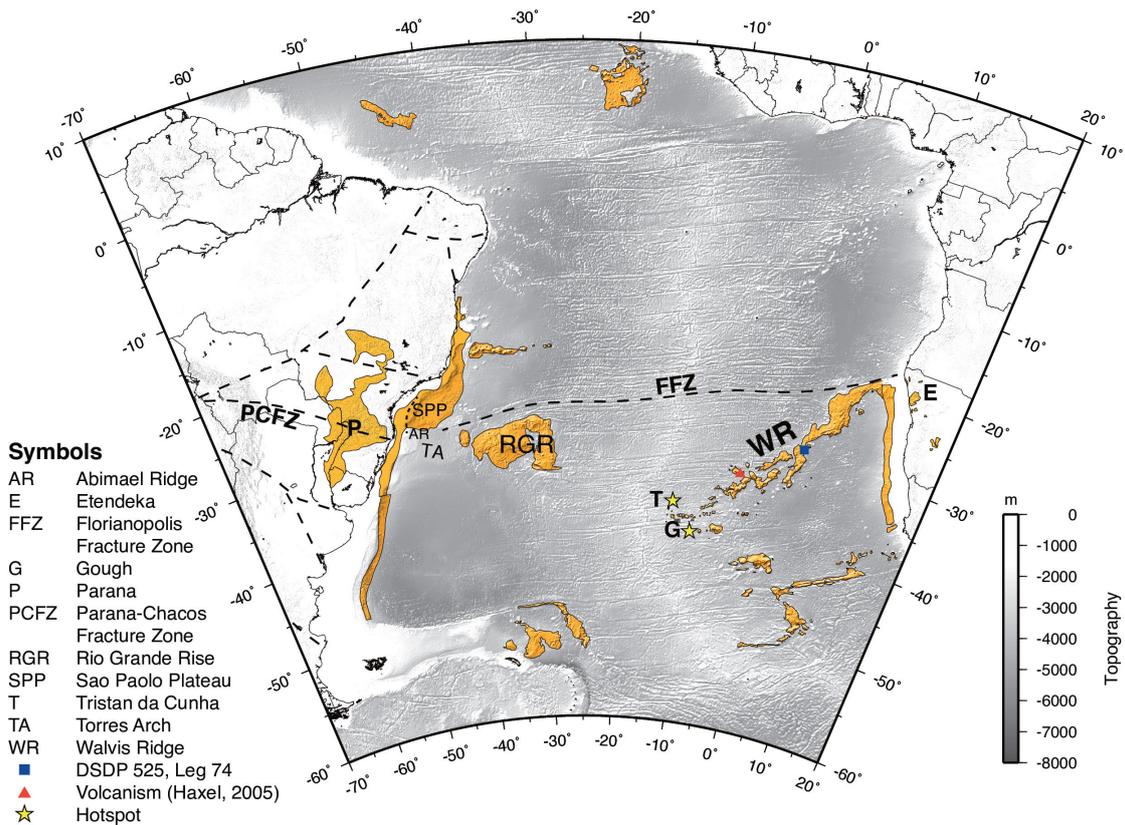
Figure 1.2.1:   General map of the South Atlantic with main structures and igneous features (orange, after Coffin et al., 2006). Transform faults, fracture and shear zones are indicated by dashed lines.

Some geochemical studies have revealed differences in the isotopic composition of present day Tristan alkaline rocks and basalts from the 90-80 Ma Walvis Ridge (DSDP Site 525, Leg 74, Ussami et al., 2012). This has been interpreted as evidence against the Tristan hotspot as common source, and instead as traces of detached continental lithosphere (Comin-Chiaramonti et al., 2011). Another contradicting observation was recent seismic activity at a 40 Ma old part of the ridge, which has been interpreted as volcanic eruptions (Haxel and Dziak, 2005). Volcanic activity at a large distance (nearly 800 km) from the hotspot contradicts the strict age progression proposed by an underlying mantle plume and indicates a tectonic source.

An alternative for the origin of Walvis Ridge is intraplate stress release and a pure plate tectonic origin (Fairhead and Wilson, 2005). The alignment of ridge segments to fracture zones connected via perpendicular segments has been interpreted as evidence for a stress release origin. The easternmost part of the ridge (east of 5° E) is a massive feature and bounded by the Florianopolis Fracture Zone (FFZ, also called Rio Grande Fracture Zone) in the north. Here, dipping reflector sequences shaped like the SDRs along volcanic margins were found dipping towards the ridge. Elliott et al., 2009 interpreted these dipping reflectors as in-

dication for an extensional component of the fracture zone and proposed a short lived spreading center at the FFZ that created the eastern Walvis Ridge.

1.3   Main objectives

The aim of this thesis is to determine the crustal architecture of the eastern Walvis Ridge with a special focus on the junction of the Walvis Ridge with the continental margin and the evolution of the early Tristan hotspot trail.
The main objectives are:

1. What is the extent and volume of magmatic underplating? Can the north-ward increase of underplating be confirmed?
2. How did the presumed plume interact with the continental lithosphere? Did it significantly modify/intrude the continental crust?
3. Which inherited (continental) structures might have been involved and how were they utilized in the breakup process?
4. Did a plume head drive the continental breakup?
5. Can we further constrain the origin of the Walvis Ridge? Is it hotspot derived or caused by stress release? How did the presumed hotspot interact with fracture zones?
6. How did the Walvis Ridge evolve? Do we find changes in the crustal structure along the Walvis Ridge?

In order to answer these research questions new geophysical data was acquired in a large multidisciplinary experiment. The dataset and its processing is introduced in the following chapter 2. Chapter 3 contains the results I obtained during my thesis formatted for publishing in scientific journals. Chapter 4 summarizes the conclusions and finally, chapter 5 gives an outlook to further research.

2   Datasets, Methods and Processing

2.1   New geophysical datasets

The data analysed in this study was acquired as part of a large scale research program using several different methods to image the junction of Walvis Ridge with the continental margin and investigate the influence of a proposed plume head on the African continental crust. The whole experiment was part of the priority programme SPP1375 of the Deutsche Forschungsgemeinschaft (DFG), which is called 'South Atlantic Margin Processes and Links with onshore Evolution' (SAMPLE). Publications with results from all disciplines are listed online at `http://www.sample-spp.de/publications`. The field work for this experiment was carried out 2010 and 2011 on- and offshore Namibia as a cooperative effort of Geomar Kiel, GFZ Potsdam and the Alfred-Wegener-Institute, Bremerhaven (AWI). Seismic, seismological, bathymetric and magnetotelluric data was acquired in active source experiments and long term passive observations. The marine seismic data was collected with RV Maria S. Merian during cruise MSM 17-1/2 in December 2010 and January 2011 (Fig. 2.1.1, Behrmann et al., 2012). At the same time active seismic data was recorded onshore allowing long profiles that image the continent-ocean transition (Ryberg et al., 2014).

For this dissertation I modelled the crustal structure of the Walvis Ridge using refraction seismic data and satellite derived gravity data along two profiles. Profile 150 was collected perpendicular to the ridge axis 600 km from the coast, whereas profile 100 extends 430 km along the ridge axis, crosses the coastline and continues onshore to a total length of 720 km (Fig. 2.1.1).

2.2   Data acquisition and processing

The basic principle of seismic surveys is the measurement of travel times. A source emits seismic waves, which travel through the Earth's interior, are reflected and refracted at impedance contrasts within the ground and finally recorded at receivers. The larger the offset between source and receiver the deeper can rays penetrate the subsurface and image deeper geological structures.

For marine surveys the seismic source is built of airguns, which are towed behind a ship and release highly pressurized air to create a short seismic pulse. The signal is then recorded by a streamer or an ocean bottom seismometer or hydrophone (OBS/H, Fig. 2.2.1). A streamer is a long cable containing hydrophones and is towed behind the vessel. The data is recorded onboard and can be viewed in real time. OBS/H rest on the seafloor and are battery powered devices, which record the data in an internal storage. They are equipped with an anchor weight that is hooked to the device and can be released via an acoustic command send from the ship or at a programmed release time. Once the anchor is detached the station floats up, can be picked up by the vessel and the data is read from the internal storage. The sensor used in this experiment was an E-2PD hydrophone from OAS Inc. or the HTI-01-PCA hydrophone from HIGH TECH INC. For this sur-
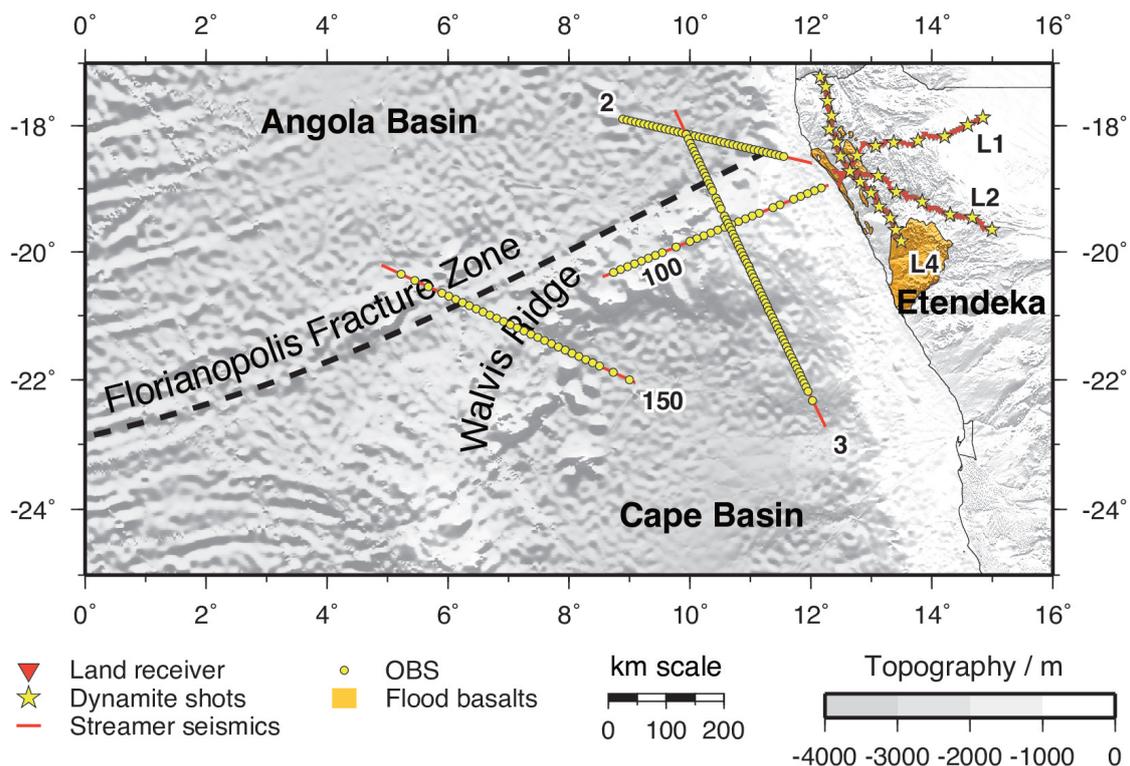
Figure 2.1.1: Overview map of the seismic data acquired during cruise MSM 17-1/2 and an onshore field campaign (Ryberg et al., 2014). I analysed the data for profiles 100 and 150, T. Ryberg analysed profile L4 (Ryberg et al., 2015), L. Planert analysed profiles 2 and 3 (Planert et al., 2013).

vey most stations were equipped with hydrophones (OBH). The data was recorded with an MBS, MLS or MTS recorder of SEND GmbH at 100 or 200 Hz sample frequency. Further technical details can be found in Behrmann et al., 2012.

Onshore surveys use dynamite shots or vibrating plates (vibroseis) as signal source and seismometers or geophones as receivers. For this study dynamite shots with charges between 250 and 400 kg were used. The data was recorded continuously at 100 samples per second with DSS CUBEs (Fig. 2.2.2). The sensor was a vertical component geophone with an eigenfrequency of 4.5 Hz. Further details are listed in the field report (Ryberg et al., 2014).

The recorded seismic data is cut into traces starting with zero at the time of the signal release. These traces are merged with navigational data and arranged as a seismogram in gathers either per station or per shot depending on the survey geometry (Fig. 2.2.3). The x-axis is the distance between the source and receiver, the y-axis displays the time since the signal has been released. Thus, a seismogram plots the signals' travel time as a function of the travelled distance. The strongest recorded signal is the direct arrival from the source to the receiver. Arrivals travelling through the ground are much weaker but they contain the desired information about the structure and characteristics of the subsurface. Seismic reflection data is usually further processed, but because of the small number of channels (four
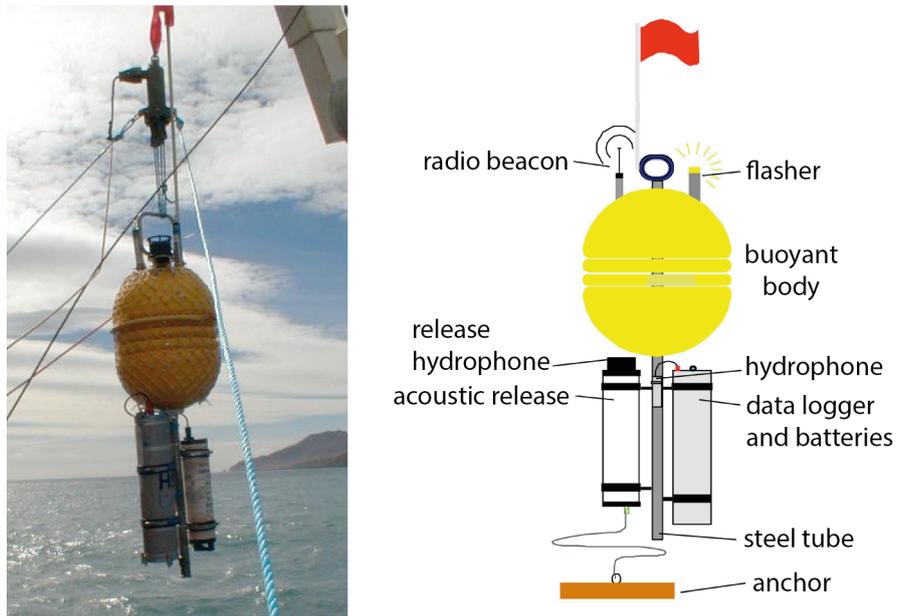
Figure 2.2.1:   Principle design of a marine seismic recorder (Ocean Bottom Hydrophone, OBH) used during MSM 17-1/2 (Flueh and Bialas, 1996)

Figure 2.2.2:   Seismic recorder (DSS Cube, right) and geophone (left) used for the land receiver
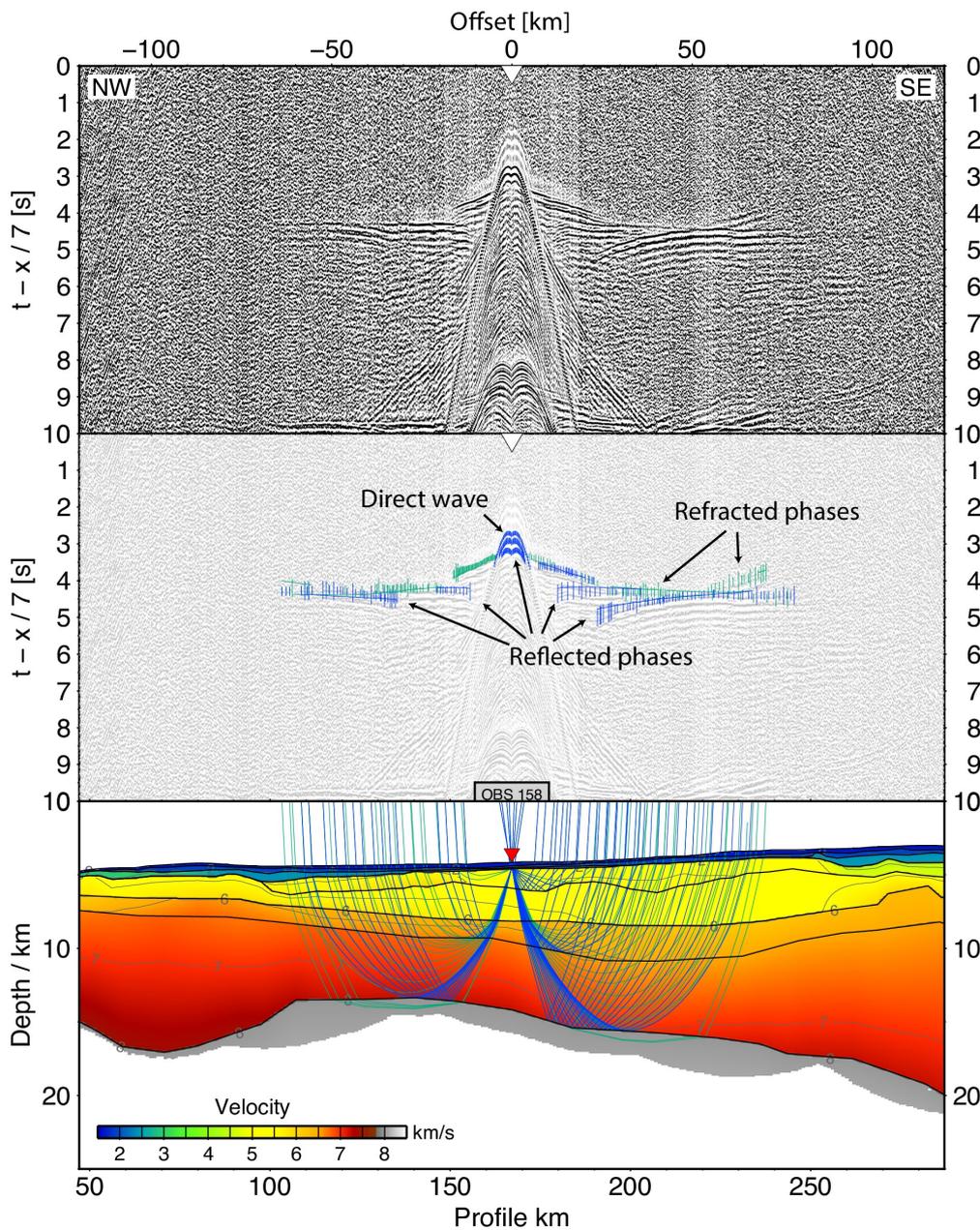
Figure 2.2.3: Principle of refraction seismic data arranged in a seismogram (top panel) with the travel time as a function of the distance between the source and receiver. Signal arrivals can be correlated across the traces and identified as different seismic phases - green refracted - blue reflected (middle panel). Refracted and reflected phases follow different ray paths and contain information about the velocity structure and reflectors within the ground (bottom panel).

channels along a 100 m streamer) available in this experiment, the reflection data was not analysed any further and the interpretation was limited to a single channel plot.

Once the data has been arranged in seismogram, the marine stations have to be relocalized. This is necessary because the exact station position at the seafloor is unknown. Only the position of its deployment is known. While it sinks to the seafloor, the device may slightly drift away due to oceanic currents. I calculated this offset from the direct arrival. The direct arrival has a hyperbolic shape and is symmetric around zero if the station is correctly located. I fitted a hyperbola to the direct arrivals and obtained the amount of shift from the fitting coefficients. The movement from the deployment coordinates was in the range of a couple of tenth meters up to maximum 500-600 m. The offsets were then corrected with the obtained shift and the station location and its water depth was updated.

2.3   Modelling

I modelled the crustal structure along two profiles with seismic refraction and reflection data and then verified the result by modelling satellite derived gravity data. The ray tracing was carried out using the rayinvr software package (Zelt and Smith, 1992), the gravity was modelled using the software IGMAS (Götze and Lahmeyer, 1988). I followed standard procedures and will briefly outline them in the following two sections.

2.3.1   P-wave velocity model

Before setting up the velocity model, I picked travel time arrivals in the OBH seismograms with the software ZP (Zelt, 2004b). For this, I filtered the data with a 3-14 Hz bandpass filter and applied an automatic gain control (AGC, 1 s time window) for amplification. For sedimentary phases and the direct arrival I filtered with higher frequencies or used the unfiltered raw data to avoid filter effects. The different filters have to be used carefully as the selected corner frequencies influence the onset of arrivals.

For the 2D model setup I projected the sources and receivers on a straight profile line and at the same time kept the source-receiver distance unchanged. This leads to lateral smearing of the model in case stations have a large distance to the projected profile line and may prevent exact fitting of the arrivals due to 3D effects.

The starting model incorporated the bathymetry, sedimentary layers and basement topography obtained from the simultaneously recorded streamer data. The seismic reflection data did not yield any velocity information about the sedimentary layers since the short streamer length prevented a detailed velocity analysis. Nevertheless, the reflection data constrained the main sediment layers and the basement topography. I used 1D velocity profiles obtained from the seismograms to set up the initial starting model for the crustal structure. The refracted phases directly contain information on the layer velocity, whereas the layer thickness is constrained by reflected phases. Refracted phases resemble straight lines (if not affected by topography effects) or slighly bend lines in case of strong velocity gradients. Reflected phases resemble a hyperbolic shape. Velocity information can

be calculated from the reflection hyperbolas using a normal move out analysis but the results are less accurate than velocities derived from refracted phases.

I used the software rayinvr for the ray tracing and forward modelling following a top to bottom approach (Zelt and Smith, 1992; Zelt, 1999). The final model has been inverted with a least square algorithm to derive error statistics and uncertainty estimations. Within this modelling process I developed a graphical user interface for the ray tracing software, which greatly facilitates modelling. The software is available to the public and has been presented at a conference. A paper is currently under review (chapter 3.1)

2.3.2   Gravity modelling

After the seismic modelling I developed density models using the software IGMAS (Götze and Lahmeyer, 1988) to verify that the derived crustal structure is consistent with observed gravity anomalies obtained from satellite data (Sandwell et al., 2014; Pavlis et al., 2008). I converted the P-wave velocity model to an initial density model using the empirical velocity-density relation by Ludwig et al., 1970. The seismic layer geometry remained unchanged, but layers were merged and the number of nodes reduced to simplify the model as far as possible. To improve the fit between observed and calculated gravity anomalies I divided the seismic layers into several polygons that account for lateral density variations. The basic geometry was then left unchanged as far as possible and the densities were inverted to fit the calculated gravity with the measured data. In case the residual remained larger than ~30% without unreasonable changes in density or geometry I revised the seismic model and data for ambiguous interpretations. Because I modelled satellite derived gravity data I focused on the long wavelength variation and accepted larger miss fits (~20%) in the small wavelength variations. Additionally, the Walvis Ridge is a highly three dimensional structure and 2D models are therefore strongly influenced by 3D effects. That means structures located beside the profile line influence the anomalies along the profile, but are not imaged by the seismic data.

3   Contributions to scientific journals

Within the context of this dissertation I wrote four publications. One is a methodical paper and presents a software I wrote for facilitating the modelling process of deep seismic data ('PRay - A graphical user interface for interactive visualization and modification of rayinvr models', in review at *Journal of Applied Geophysics*). The second paper is a short summary of four deep seismic profiles at the landfall of Walvis Ridge, extracting the most important results of the project for a high ranked journal ('South Atlantic opening - A plume induced breakup?', in review at *Geology*). The third and fourth paper are more detailed data paper about the two profiles I analysed ('The onset of Walvis Ridge: plume influence at the continental margin' and 'Interaction between hotspot and fracture zone: The crustal structure of Walvis Ridge at 6°E'). The publication strategy did not allow the submission of the longer data paper before the publication of the short summarizing paper had been secured. Therefore, both data paper are still to be submitted. I consider *Tectonophysics* for publication of these data papers.

PRay - A graphical user interface for interactive visualization and modification of rayinvr models

Tanja Fromm
in review at *Journal of Applied Geophysics*

In this paper I present the software *PRay*, which implements graphical editing of seismic refraction data mainly utilizing the software rayinvr by Zelt and Smith, 1992. Even though this software is 13 years old, it is still widely used for modelling deep seismic data. The interface has been developed in course of my own modelling to optimize the work flow. The code is written in the scripting language Perl and uses the graphical extension Tk.

I wrote the whole program code myself and made it available for others. Bug reports and testing was provided by users within the Geophysics section of AWI and later by external users.

South Atlantic opening - A plume induced breakup?

Tanja Fromm, Lars Planert, Wilfried Jokat, Trond Ryberg, Michael Weber, and Jan Hinrich Behrmann
in review at *Geology*

We present four P-wave velocity models located at the junction of the Walvis Ridge with the continental margin. Two profiles have a landward prolongation and cover the continent-ocean transition, the other two profiles are located offshore and cross the ridge axis. The results show that a high velocity lower crustal body is confined to the continental margin and intrudes 100 km into the continental crust. The presence of this body is confirmed and determined to 100 km width by an independent profile crossing the prolongation of the ridge axis onshore. This is a

remarkably small affected area compared to the proposed large impact of a plume head. We therefore question that a plume head initiated the breakup of South America and Africa.

I calculated the two P-wave velocity models of profiles 100 and 150 and wrote the paper. L. Planert modelled profiles 2 and 3. W. Jokat supervised the work and was Chief Scientist during cruise MSM17/2. T. Ryberg acquired the onshore data. J. Behrmann was Chief Scientist during cruise MSM17/1. J. Behrmann, W. Jokat, T. Ryberg and M. Weber proposed the project. All authors discussed the results and revised the manuscript.

The onset of Walvis Ridge: plume influence at the continental margin
Tanja Fromm, Wilfried Jokat, Jan Hinrich Behrmann, Trond Ryberg, and Michael Weber
to be submitted to Tectonophysics

We present a P-wave velocity model along the axis of Walvis Ridge with an onshore prolongation. The profile is 720 km long and extends from a clearly oceanic to a continental domain. We report high velocities in the lower crust within the transition of thickened oceanic crust to continental crust. The continental crust is affected a further 100 km inland than the volcanic continental margin south of Walvis Ridge. Because the width of this body is constrained to 100 km by independent seismic measurements, we interpret this extended area as a part of the Tristan hotspot trail and not as the signature of a large plume head.

I calculated the P-wave velocity model and wrote the manuscript. W. Jokat supervised the work and was Chief Scientist during cruise MSM17/2. T. Ryberg acquired the onshore data. J. Behrmann, W. Jokat, T. Ryberg and M. Weber proposed the project. All authors discussed the results and revised the manuscript.

Interaction between hotspot and fracture zone: The crustal structure of Walvis Ridge at 6°E
Tanja Fromm, Wilfried Jokat, and Jan Hinrich Behrmann
to be submitted to Tectonophysics

We present a P-wave velocity model crossing the Walvis Ridge approx. 600 km west of the coastline. The model shows volcanic structures north of the Florianopolis Fracture Zone, one of the main fracture zones of the South Atlantic and the northern boundary of the Walvis Ridge closer to the shore. Basalt layers covering older oceanic crust indicate magmatic activity after the fracture became inactive, which was likely well after the plate has passed the hotspot and is therefore interpreted as late stage volcanism. The fracture zone extends in about 100 km distance to the crustal root of the Walvis Ridge indicating that both structures evolved without interference. Therefore, I support a hotspot related origin of the Walvis Ridge and reject a formation as 'leaky' transform fault.

I calculated the P-wave velocity model and wrote the manuscript. W. Jokat

supervised the work and was Chief Scientist during MSM17/2. J. Behrmann and W. Jokat proposed the project. All authors discussed the results and revised the manuscript.

3.1   PRay - A graphical user interface for interactive visualization and modification of rayinvr models

PRay is a graphical user interface for interactive displaying and editing of velocity models for seismic refraction data. It is optimized for editing rayinvr models but can also be used as a dynamic viewer for ray tracing results from other software. The main features are the graphical editing of nodes and fast adjusting of the display (stations and phases). It can be extended by user defined shell scripts and links to phase picking software. PRay is open source software written in the scripting language Perl, runs on Unix like operating systems including Mac OS X and provides a version controlled source code repository for community development (`http://aforge.awi.de/gf/project/pray/`).

3.1.1   Introduction

The ray tracing software rayinvr by Zelt and Smith (1992) is still widely used to model wide angle seismic data. According to Google Scholar 40 to 50 new publications per year use the program for analysing seismic refraction data.

Rayinvr models are set up as layers with a variable number of depth and velocity nodes. The nodes are defined in a specifically formatted ASCII file, which is difficult to read and handle especially for people starting to use the software. For graphical editing of model files Zelt (2004a) published the tool vmed. However, this program does not display traced rays and arrivals. Rayinvr provides a static display for X-windows or postscript as graphical output for the ray tracing results and theoretical arrivals. If a specific part of the model has to be studied in detail, with different stations or phases the code has to be rerun. For larger datasets this is particularly time consuming and would benefit from being optimized.

RayGUI, provided by Song and Brink (2004), combines editing of models and displaying of ray tracing results. Unfortunately it cannot import rayinvr formatted models and additional configuration is needed. Furthermore, all files required by rayinvr are newly created by the program before invoking it. Hence manual changes are overwritten.

PRay combines the capabilities of vmed and RayGUI: graphical model editing and display of ray tracing results while retaining the original formats of rayinvr. Existing programs are used whenever possible; stand-alone tools and scripts (user may add their own) are connected in one interface. It is easy for new users to try PRay because it runs in directories containing rayinvr models without any extra configuration.

Thus, PRay provides a fast and flexible control interface for modelling wide angle seismic data. Though it is mainly intended for rayinvr formatted models, it can also be used as a viewer for other formats created e.g. by Tomo2D (Korenaga et al., 2000), although functionality is limited. PRay is written in the scripting language Perl/Tk, hence no compilation is necessary. Perl is usually available by
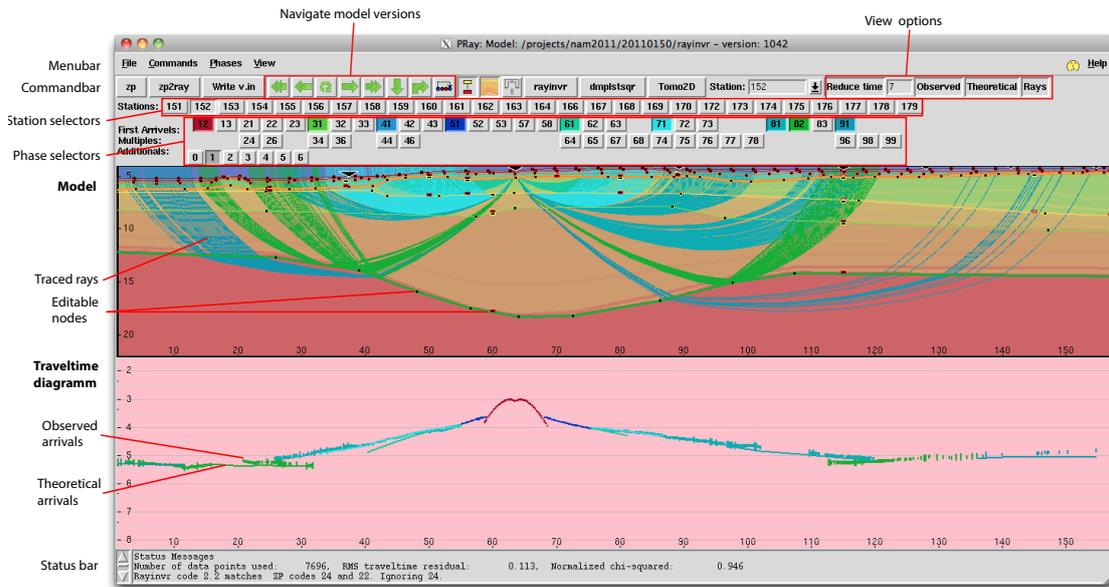
Figure 3.1.1: The main window of PRay shows the model with traced rays above the traveltime diagram. Displayed stations and phases can be quickly switched with buttons above the model diagram. The model can be edited by dragging nodes to a new position. Having the ray paths and arrivals close together in one window makes it easy to find the nodes to change in your model.
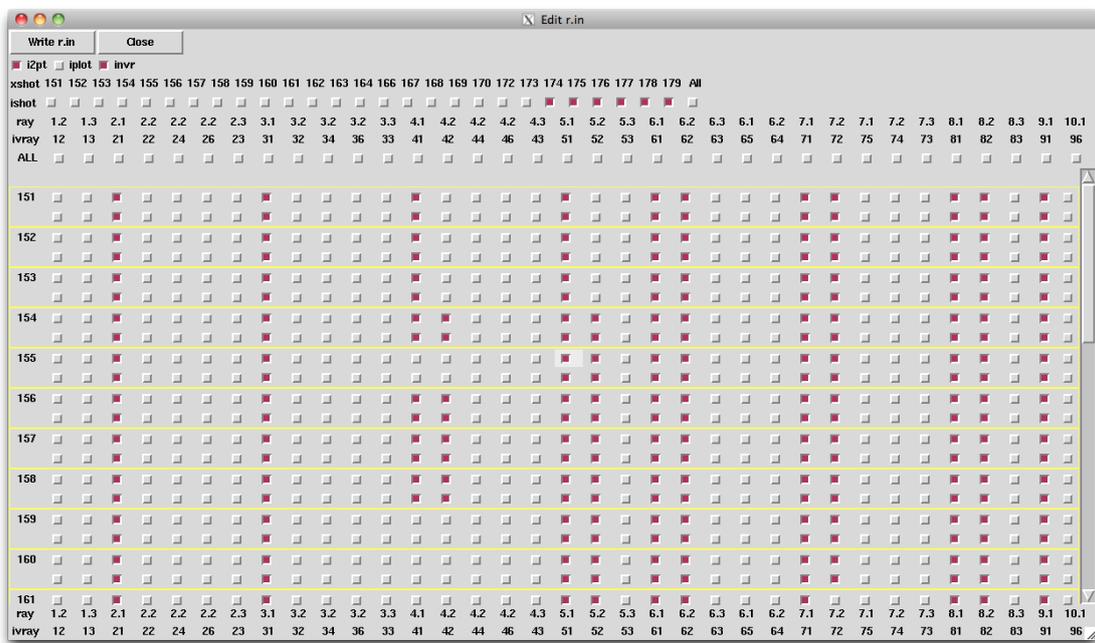
Figure 3.1.2: The graphical editing of rayinvr configuration file simplifies selection of stations and phases for the ray tracing process.

Figure 3.1.3: Having all velocity nodes arranged by layer in one window makes it easy to change several nodes with regard to velocities in upper and lower layers.

default for Unix-like systems and Mac OS X, only the Tk graphic modules have to be added. They are freely available by CPAN (The Comprehensive Perl Archive Network - www.cpan.org) and Perl offers an easy installation routine.

3.1.2   Program features

It is PRay's philosophy to make the modellers life easier. Therefore all information is read from original rayinvr files and no extra configuration is required (although possible).

The main PRay window displays the velocity model and travel times (Figure 1). Functions are available via a menu- and toolbar or mouse context menu. Stations and phases can quickly be selected/deselected using buttons in the toolbar. This enables the user to investigate different parts of the model in detail without having to rerun rayinvr or recreate plots. Traced rays as well as observed and theoretical arrivals can be switched on and off. Reduction time for the record section can be changed, whilst contours and gradients are drawn into the model space.

PRay allows the user to add, modify or delete velocity and depth nodes using the mouse. Depth nodes can be dragged to their new position, velocity nodes can be displayed and modified individually, or in an extra window together with all nodes (Figure 2). Nodes can be graphically selected to toggle partial derivatives or pinch out layers.

During the modelling process picked arrivals often have to be reviewed in the original data files. PRay offers a link to directly start a user defined program for a selected station. PRay is preconfigured for this task using the program ZP by Zelt (2004b) and can also change phase codes for selected travel time picks in the original ZP pick files.

PRay provides a simple control of the different model versions by saving the model files with a version number and an optional user comment. Quick navigation between different versions is offered and models can be compared. This is especially useful after inverting the model a couple of times.

When changing only a small portion of the model not all phases and stations are involved. They can be simply removed from the display with previously described buttons. But considering that the ray tracing process is greatly accelerated if fewer rays are traced, they should be excluded from calculations. A graphical editor for the rayinvr configuration file supports selecting labelled stations and phases for computing as well as some other important tracing parameters (Figure 3).

To further facilitate forward modelling model velocities, distances and time differences can be measured in the travel time plot. In addition 1D velocity depth profiles can be exported.

PRay does not provide publication-ready graphics but can write traced rays and traveltimes in a GMT-readable format. Therefore, users who have worked with rayinvr before and already have sets of scripts meeting their needs can continue working with them. User defined scripts can even be included in PRay and run directly from the menu.

3.1.3   Summary

PRay provides a user-friendly interactive interface to make modelling of seismic refraction data with rayinvr easier. It is freely available, requires no compilation, reduces editing of rayinvr files to a minimum and allows users to add their own scripts. It can also be used for tomography models, although functions are limited to dynamic viewing without editing abilities. Users are invited to further develop this program in a community. The source code, a version controlled code repository, user editable documentation (wiki) and a tracking system for updates/bug reports are available at `http://aforge.awi.de/gf/project/pray`.

3.2 South Atlantic opening - A plume induced breakup?

Upwelling hot mantle plumes are thought to disintegrate continental lithosphere and are considered as a driver of active continental breakup. We investigated the crustal structure of the classical plume and breakup related Walvis Ridge at its intersection with the continental margin and searched for anomalous modifications caused by the proposed plume head. The overall structure we observed suggests that no broad plume head existed during opening of the South Atlantic and anomalous mantle melting occurred only locally. We therefore question the importance of a plume head as a driver of continental breakup and further speculate that the hotspot was present before the rifting, leaving a track of kimberlites in the African craton.

The processes of lithospheric weakening that finally allow continents to break are still poorly understood and geophysical data constraints are sparse. Various ideas exist about the underlying mechanisms that cause continental breakups, ranging from changing plate boundary forces to mantle dynamics. A much debated model involves the arrival of a deep mantle plume (Wilson, 1965; Storey, 1995). Mantle plumes are deep seated thermal anomalies carrying hot and buoyant material from the core mantle boundary to the lithosphere-asthenosphere boundary (LAB). The LAB forms a rheological barrier to the plume's further ascent, and so the mantle material spreads out as a large disk (Griffiths and Campbell, 1991). In the original model, Morgan (1971) postulated that regional uplift and stress induced by thermal doming cracked the continents and pushed them apart. More recent simulations showed that plumes have the potential to thermally and chemically erode the base of the lithosphere (Sobolev et al., 2011) and promote the accumulation of melt that further exacerbates lithospheric weakening. The upwelling plume material intrudes the crust, partly accumulates at the crust-mantle boundary (Moho), which can be mapped by seismic methods and partly erupts at the surface as large flood basalt provinces (Ridley and Richards, 2010). The formation of flood basalt provinces is often in close spatial and temporal proximity to continental breakups, which has led to the controversial concept that the impact of plume heads arriving at the base of the lithosphere initializes continental breakup (Morgan, 1971; Richards et al., 1991; Cande and Stegman, 2011). However, this model is only one possible end member and global observations from continental margins with and without flood basalt provinces suggest a very different explanation: pre-existing weak zones and a prior history of rifting in combination with general plate movements might be more important driving factors for breakups (Buiter and Torsvik, 2014; Armitage et al., 2010).

Here we use seismic refraction data to image the crustal structure of a hotspot track and the proposed site of plume head impact: the easternmost Walvis Ridge including the junction with the Namibian coast (Duncan, 1984, Fig. 3.2.1). The area is well covered by four, mostly amphibious, deep seismic sounding profiles (we used in total 166 ocean bottom stations, 99 land receivers, 12864 airgun shots and 13 dynamite shots). The data image 2490 km of crust and upper mantle along
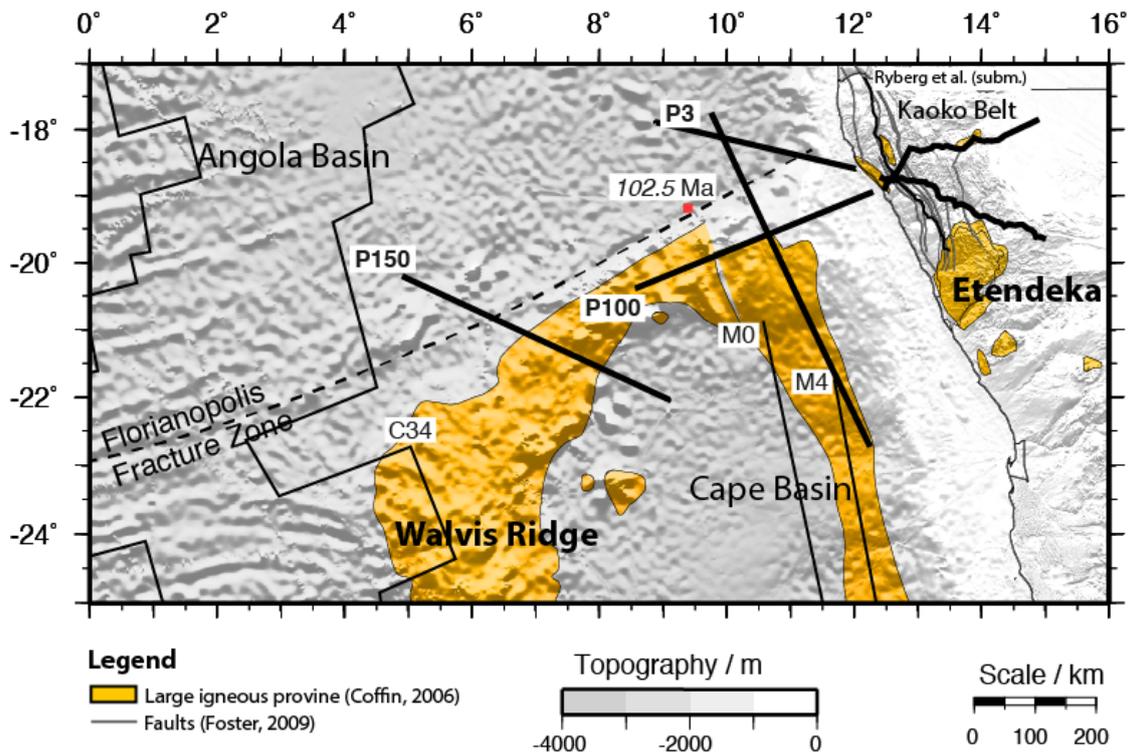
Figure 3.2.1:   Location of the deep crustal seismic profiles at Walvis Ridge. Magnetic anomalies with the ages (Gee and Kent, 2007): C34 - 83.5 Ma, M0 - 120.6 Ma, M4 - 125.7 Ma. The red square marks the dated ODP Site 530 Leg 75 (Hay and Sibuet, 1984).

profiles varying in length from 480 to 720 km. One profile is located along the ridge axis and continues onshore, while the other three cross the Walvis Ridge at different angles and locations. The travel times of refracted and reflected P-phases were used to derive 2D velocity models using standard modelling procedures (Zelt and Smith, 1992; Zelt, 1999; Korenaga et al., 2000). Further details and data examples are available as supplementary materials.

3.2.1   Results

Our P-wave velocity models (Fig. 3.2.2) show that the edifice of the Walvis Ridge most likely consists of closely spaced seamounts and thickened oceanic crust (up to 35 km) beneath a cover of extrusive rocks such as hyaloclastites and basalt lava flows. The transition from the Walvis Ridge to the adjacent basins reveals drastic differences between the northern and the southern flanks as well as along the axis of the ridge. While the southern flank gradually converts into the transitional crust of the volcanic margin (Fig. 3.2.2b), the northern flank is characterized by a sharp transition from 35 km thick crust below the ridge to 5-6 km thick oceanic crust in the Angola Basin (Figs. 3.2.2b,c). This strong lateral variation is limited to the area close to the continental margin. Further offshore (Fig. 3.2.2a), both
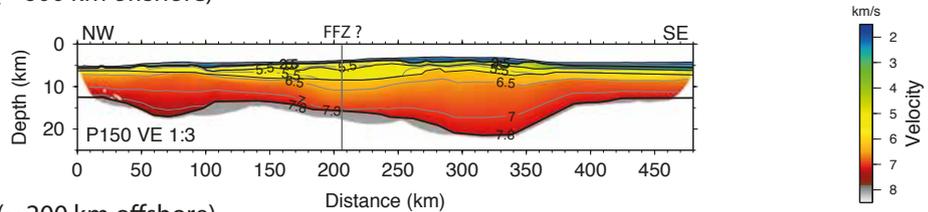
Figure 3.2.2: P-wave velocity models from top to bottom: a) P150 across Walvis Ridge (WR) 600 km offshore, b) P3 across WR 200 km offshore, c) P2 across Angola Basin and WR with an angle of 45°, d) P100 along axis. All models are plotted with the same scaling and a vertical exaggeration of 3. Reflectors are marked with thick black lines. White model areas have no ray coverage and are not resolved.

flanks transfer smoothly into oceanic crust, but with some additional volcanism and thickened crust at the northern flank.

This surprisingly precipitous jump in crustal thickness on the Angola Basin side can be explained by the kinematic evolution of the South Atlantic (Fig. 3.2.4). The Angola Basin is considerably younger than the Cape Basin (up to 20 Ma, Gee and Kent, 2007; Hay and Sibuet, 1984) and the northern flank of Walvis Ridge is affected by the Florianopolis Fracture Zone (FFZ). The crust formed initially to the north of Walvis Ridge has likely been sheared along the FFZ and transferred to the South American margin as the Sao Paolo Plateau (Fig. 3.2.4b). The younger/thinner crust found today in the Angola Basin was formed after the magmatic activity associated with the hotspot was located further westwards (Fig. 3.2.4c). This implies that the plume tail did not supply sufficient additional melt to thicken the oceanic crust 200–600 km away in the Angola Basin.

In W-E direction along the axis of Walvis Ridge the crustal thickness increases from 18 to 30 km towards the coast. The thickness of the continental crust reaches 40 km below the Kaoko Fold Belt. Further inland we observe a slight decrease to 36 km and indications for an intrusive body at the edge of the model. This observed crustal root beneath the fold belt is consistent with findings of onshore seismological experiments (Heit et al., 2013) and gravity models (Maystrenko et al., 2013). Close to the coast, the models show high seismic velocities (up to 7.5km/s) in the lower crust of the Walvis Ridge. This high velocity lower crustal body (HVLCB) tapers out about 300 km offshore, much like other HVLCBs found along the SW African coast (Bauer et al., 2000; Schinkel, 2006; Hirsch et al., 2009). Compared to these models, where the HVLCBs do not reach closer than 50 km offshore from the coast, the Walvis HVLCB continues until a few tens of kilometers beneath the continental interior (Fig. 3.2.1) Independent onshore seismic profiles indicate that this eastern promontory of the Walvis HVLCB is only 100 km wide (Ryberg et al., 2015), which is considerably narrower than further offshore at P3 (Fig. 3.2.2b), where its width is almost equivalent to the bathymetric expression of Walvis Ridge (160 km). Hence, compared to the southern volcanic margin, the additional area of intrusive lower crust at the landfall of Walvis Ridge is at most 100×100 km^2 (Fig. 3.2.3, inset). According to our data, the remaining continental crust including the root of the Kaoko Fold Belt has not been significantly influenced by the proposed plume head.

3.2.2 Discussion

The intruded area is surprisingly small in comparison to the often-cited diameter of plume heads, which is between 800 and 2000 km based on the regional extent of flood basalt volcanism (White and McKenzie, 1989; Griffiths and Campbell, 1990) and theoretical calculations (Tan et al., 2011). However, the exact location of the hotspot during breakup is crucial for the interpretation of our results: a distant location could account for the relatively limited intruded area. Unfortunately, the location of the plume impact is not well constrained. Some authors place it at the South American plate near the larger Paraná flood basalts (O'Connor and Duncan,
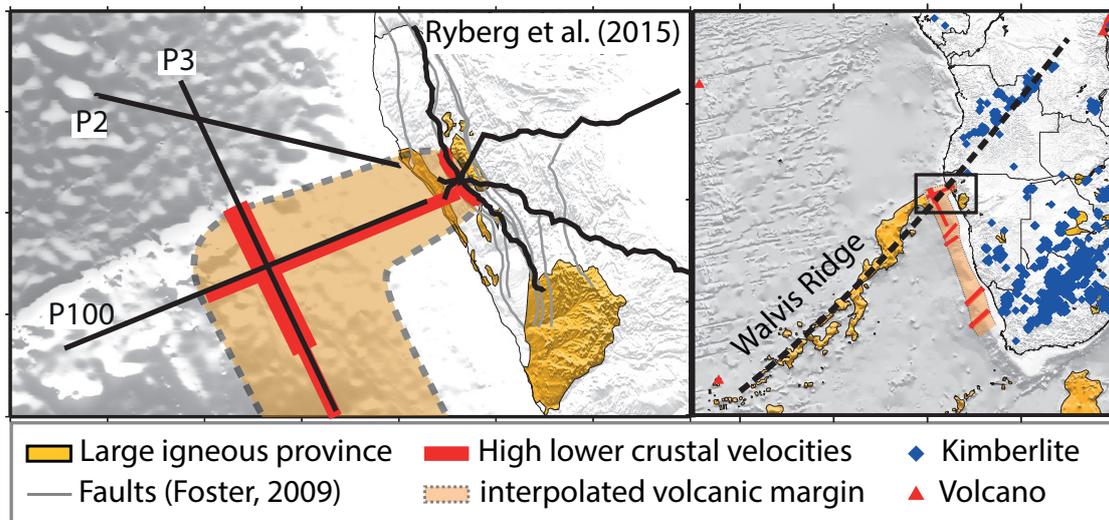
Figure 3.2.3: Distribution of HVLC observed in the presented models (left) and their relation to onshore faults and flood basalts. Track of the Tristan hotspot extended on the African continent (right). The dashed line follows the axis of Walvis Ridge and coincides with kimberlites intrusions onshore. Together with the narrow track-like promontory of the HVLC in prolongation of the Walvis Ridge it indicates that both volcanic features might be related.
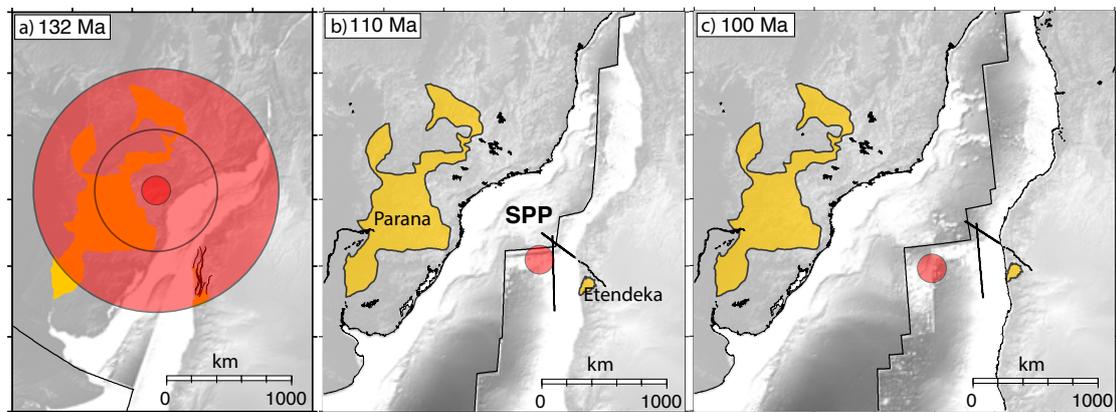
Figure 3.2.4: Reconstruction of the South Atlantic opening (Pérez-Díaz and Eagles, 2014). The large red circles in a) mark the location of the plume head with 1000 and 2000 km diameter, respectively (O'Connor and Duncan, 1990). The small red circles denote the location of the plume stem with a diameter of 200 km. The reconstructed positions of profiles 2 and 3 are indicated by a black line. Thin black lines in a) show faults (Foster et al., 2009). Other black lines mark plate boundaries. Yellow areas indicate continental flood basalts (Coffin et al., 2006).

1990; VanDecar et al., 1995) while others locate it at the African plate (Duncan, 1984; White and McKenzie, 1989). The more recent findings indicate a position near Paraná, although this requires a mobile hotspot and cannot be achieved with a fixed hotspot position (Ernesto et al., 2002). In this case the Namibian margin would have only been influenced by the outer ambit of the plume head and we would expect a different geometry of the affected area. The limited encroachment into African continental crust might be explained by greater distance from the centre, but then it should be much wider than the observed 100 km resembling a large diameter circle (Fig. 3.2.4a). Furthermore, the area of the intruded lower crust onshore, formed during impact of the proposed plume head, should be greater than offshore, because the latter was formed after the plume head had dissipated. It is thought provoking that we find the contrary: attenuated magmatism during continental breakup and increased magmatism during the formation of the easternmost portions of Walvis Ridge. Instead, the confinement of intruded continental crust to a narrow strip in the landward prolongation of the Walvis Ridge seamount chain suggests a hotspot track origin and is not the signature of a plume head.

Our observations are inconsistent with a significant impact of the Tristan plume as a driving force in the opening of the South Atlantic. The absence of a large plume head signature can be interpreted in terms of (i) the non-development of a head during plume ascent, or (ii) the pre-existence of a hotspot before the time of breakup. The development of 'headless' plumes is at odds with current models of mantle dynamics and an additional melt source for the flood basalt provinces would be needed, which cannot be produced by normal rifting alone (White and McKenzie, 1989). Small scale convection is an alternative for the production of excess melt without a plume head involved. In such a case only the plume tail would leave a hotspot track but is otherwise not needed for the breakup process. Another mechanism that might resemble a 'headless' plume is the arrival of several smaller plumes (O'Connor et al., 2012). While this would significantly decrease the affected area, it does not explain the small volume of crustal intrusions into the continental crust.

In the alternative scenario, a hotspot was already established a long time prior to the breakup, but its volcanic manifestation was attenuated due to the thickness and strength of the African lithosphere. An indication for such a pre-existing hotspot is the geometry of the continental HVLCB and its relation to continental fault systems. In Namibia the northern Etendeka basalts are associated with deep-reaching coast-parallel faults (Foster et al., 2009), which extend well beyond the area of basalt outcrops and intruded lower crust. Even if the surface basalts were eroded, the geometry of the intra-crustal intrusions should be original and unaltered. In the plume head scenario it is difficult to explain why only this localized crustal portion was affected even though the faults are much longer and would have been completely underlain by the plume head (Fig 3.2.4a). Despite the fact that the continental crust had pre-existing weak zones and was weakened by rifting, volcanism was attenuated. In other words, the hotspot itself had limited abilities to actively impinge the continental crust unless given an easy conduit to the surface, such as a major basement penetrating continental fault, an oceanic

a) pre-rift phase

Continental crust

Depleted lithospheric mantle

Refertilized mantle
Asthenosphere

Low-degree melting

Hotspot

b) rifting phase

South America   Parana   Etendeka   Africa

High-degree melting

oceanic

c) normal seafloor spreading   crust Walvis Ridge

SDR

HVLC

not to scale   modified after Griffin, 2013
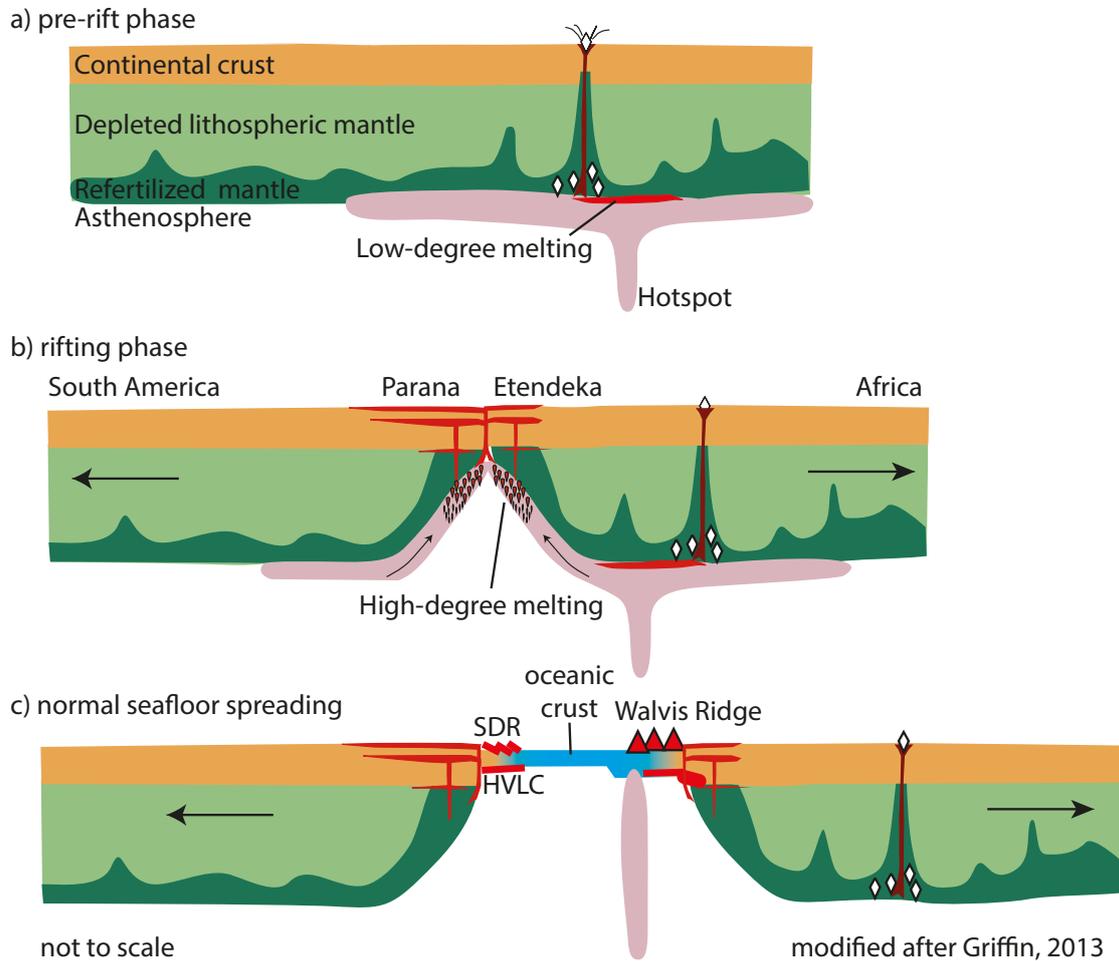
Figure 3.2.5: Sketch of the proposed breakup model.
a) The hotspot existed prior to the rifting and formed low degree melts at the
hotspot location. Lithospheric structure focused intrusions venting to the surface
and marking the hotspot trail by Kimberlites (Griffin et al., 2013).
b) Changing plate boundary forces (Jokat et al., 2003) stretched the lithosphere
and initiated rifting. Decompression melting at the thinned areas generated large
volumes of melt, which formed the large flood basalt provinces. The following
onset of seafloor spreading was characterized by excessive melt extraction building
the volcanic margins
c) Further plate movement over the hotspot formed the Walvis Ridge.

spreading center or a fracture zone.

The presence of a well-established hotspot prior to continental breakup implies that the Walvis Ridge hotspot track might extend onto the African continent. Volcanic features in the prolongation of Walvis Ridge include a lineament of kimberlites, scattered along the eastwards extrapolated ridge axis (Fig. 3.2.3) Such rocks have long been associated with hotspots underneath thick continental lithosphere and indicate the presence of a thermal anomaly beneath the craton (Crough et al., 1980; Griffin et al., 2013). Some of them show an age progression as proposed by the hotspot model (Crough et al., 1980; Moore et al., 2008) although it is not as clear as for oceanic island chains or even contradicting (Bailey and Foulger, 2003). If these features were formed in coincidence with the Tristan hotspot, the onset of the Walvis Ridge cannot mark the beginning of the Tristan hotspot chain (Fig. 3.2.5). Furthermore, the hotspot could not actively erode the thick lithosphere beneath the craton and impinged lithosphere only at pre-existing weak zones. This implies that the source for the large volumes of melt required for the flood basalt volcanism was ponded hotspot material at the base of the lithosphere as previously suggested (Sleep, 2006). With the onset of rifting in response to changing plate boundary forces driven by spreading systems in the young ocean basins around Antarctica (Jokat et al., 2003), new melt pathways became available for the ponded melt to migrate to the surface and form the large flood basalt provinces and the volcanic margins. The asymmetric distribution of the continental flood basalts might be explained with regional geology and rift history. The Paraná flood basalts are located at a major deformation zone, the Paraná-Chacos shear zone, which has also been interpreted as a failed rift arm of a triple junction. Here, extension of up 70 km and/or 150 km of shear movement occurred (Moulin et al., 2010) and might have focused magmatism at that location.

To sum up, we do not find traces of large scale intrusions within the continental crust at the junction with the Walvis Ridge, which would indicate eminent plume head-lithosphere interaction during breakup. Thus, it seems unlikely that the arrival of a plume head initiated the opening of the South Atlantic Ocean.

Author contributions W.J., J.B., M.W. and T.R. conceived the project and secured financial support. W.J., J.B.. L.P. carried out the geophysical experiments during the RV M.S.Merian cruise MSM17. T.R. collected the onshore data. L.P. analysed profiles 2 and 3. T.F. modelled profiles 100, 150 and wrote the paper with contributions from all of the co-authors. All authors discussed the results and commented on the manuscript.

Competing Interests The authors declare no competing financial interests.

Correspondence   Correspondence and requests for materials should be addressed to W.J. (email: Wilfried.Jokat@awi.de).

Additional information   Supplementary information about the methodology, more detailed data examples and uncertainty estimations is available in the online version of the paper.

3.2.3 Supplementary information - South Atlantic Opening: a plume induced breakup?

T. Fromm[1] , L. Planert, W. Jokat, J. H. Behrmann, T. Ryberg and M. Weber

Here we provide a short description of the methods used and present error statistics for the velocity models, data examples of recorded seismic sections, picked and traced travel times as well as the corresponding ray paths. Resolution and DWS (derivated weight sum) plots demonstrate the model uncertainty. The different types of plots are due to different modelling approaches described in the methods section.

Methods

Data acquisition and processing   The marine seismic source consisted of a $8 \times 8\,l$ G-gun array ($64\,l$ or 3905 cu. in. in total) operated at 200 bar (2900 psi) in 8 m water depth. Profiles 100 and 150 were shot with an interval of 90 s resulting in approx. 230 m shot distance and 13 km separation between the OBH (Ocean Bottom Hydrophones), while profiles 2 and 3 had a denser shot and receiver distribution (60 s shooting interval, 125 m shot distance and 7.6 km OBH separation). The dynamite shots onshore were loaded with charges of 250 to 400 kg with approx. 22–52 km separation. The distance between the land receivers was approx. 6 km. The number of OBH, land receivers and dynamite shots varied between the profiles. Profile 100 (720 km long) extends along the ridge axis and consists of 27 OBH, 48 land receivers and 8 dynamite shots. Profile 150 (480 km long) crosses Walvis Ridge 600 km offshore and consists of 27 stations. Profile 3 (600 km long) crosses Walvis Ridge 200 km offshore and consists of 74 stations. And finally profile 2 (670 km long) crosses the Angola Basin and the landfall of Walvis Ridge. It consists of 39 OBH, 52 landstations and 7 dynamite shots. Data examples for all profiles are shown in supplementary figures 3.2.6 – 3.2.9. The data was processed using a standard procedure including relocation of OBH and projection on straight lines. Travel times were picked on the processed seismic section after applying a deconvolution and time and offset variant bandpass filtering.

---

[1]Tanja.Fromm@awi.de

Modelling and uncertainties We followed a top to bottom approach, first fitting the upper layers before modelling the lower ones. The upper sedimentary strata and basement topography was constrained by single channel streamer records of the airgun shots.

The crustal velocity structure was modelled with two different methods. For profiles 100 and 150 we used a layer based method (the rayinvr software package, Zelt and Smith, 1992) and for profiles 2 and 3 a tomographic approach (tomo2D software package, Korenaga et al., 2000). In the layer based method the model is represented by crude layers with velocity nodes distributed with variable spacings along the upper and lower boundaries. The velocity field between the nodes is linearly interpolated and boundaries can be reflective but might also only be used to change the velocity gradient. The layer boundaries do not necessarily reflect geological boundaries.

The velocity structure for the tomographic models is defined on a dense irregular grid of velocity nodes. We used a horizontal node spacing of 250 m and 500 m in the marine part and 1 km in the less-well resolved land part of the models. Vertical node spacing increases linearly from 100 m at the seafloor to 250 m at depths equal and greater than 40 km below seafloor. Model regularization in the inversion is accomplished by the use of correlation lengths, which control the size of those model areas affected by a velocity update of a grid cell. We used a horizontal correlation length of 1.5 km at the seafloor, which linearly increases to 10 km at the model bottom, and a vertical correlation length with corresponding values of 0.3 km and 2 km, respectively. Reflectors are implemented as floating reflectors, which are independent from the underlying velocity grid. For the reflector nodes, the appropriate regularization length scales are taken from the horizontal 2D velocity correlation lengths at the corresponding depths. For the modelling of the crustal portions we utilized spatially variable velocity damping for the overlying sedimentary portions and incorporated velocity jumps into the input models at primary features such as the basement and the crust-mantle boundary (Moho).

The uncertainties for the travel time picks were manually assigned varying between 60 ms and 250 ms. Altogether 188.949 picks were traced and all models reached consistency with the picked arrivals within an RMS deviation of 118 ms or less. More details on the modelling errors are listed in supplementary tables 3.2.1–3.2.4. The model uncertainty was estimated by changing velocities and depth nodes until the resulting travel time residuals became larger than the pick uncertainties (for profile 100 and 150). This results in $\Delta v = 0.2$ km/s and $\Delta d = 1$ km for reflector depths.

Unit	n	t_{rms}/s	χ^2
Sediments (incl. refl.)	1945	0.061	0.753
Crust (airgun shots)	7133	0.097	0.615
Crust (dynamite shots)	198	0.222	1.427
Mantle	396	0.311	2.128
Boundary			
Moho (airgun shots)	755	0.203	1.022
Moho (dynamite shots)	47	0.374	2.290
Basement	141	0.084	1.464
Total	10550	0.115	0.726

Table 3.2.1: Summarized error statistics for model P100 showing the number of traveltime picks (n), the RMS error (t_{rms}) and the normalized χ^2 value for different model units and corresponding boundaries. Results for the model units combine refractions (respective turning rays); results for the boundaries combine respective reflections. Note that the result for 'Sediments' includes some additional intra-sedimentary reflections. The basement is further constrained by single-channel streamer data. Note that the uncertainty for the sparse land data is usually larger than for the marine data.

Unit	n	t_{rms}/s	χ^2
Sediments	942	0.070	0.855
Crust	5729	0.074	0.475
Mantle	244	0.094	0.494
Boundary			
Moho	2369	0.097	0.558
Basement	517	0.101	1.803
LVZ (top)	65	0.045	0.208
LVZ (bottom)	254	0.092	0.921
Total	10120	0.082	0.607

Table 3.2.2: Summarized error statistics for model P150 (c.f. caption of Table 3.3.1). The low velocity zone (LVZ) north of the ridge is bound by reflections from the top and bottom but remains relatively poor resolved due to missing refracted phases (see Fig. 3.2.11)

Unit	n	t_{rms}/s	χ^2
Sediment (incl. Refl.)	8223	0.030	0.77
Crust (airgun shots)	20784	0.053	1.09
Crust (dynamite shots)	239	0.102	2.87
Mantle (airgun shots)	16911	0.087	2.12
Mantle (dynamite shots)	34	0.079	1.72
Boundary			
Basement	1175	0.063	1.11
Intra-crustal	2156	0.063	1.12
Moho (airgun shots)	8536	0.056	0.97
Moho (dynamite shots)	123	0.075	1.56
Total	58181	0.061	1.34

Table 3.2.3: Summarized error statistics for model P2 (c.f. caption of Table 3.2.1). Note that the uncertainty for the sparse land data is usually larger than for the marine data.

Unit	n	t_{rms}/s	χ^2
Sediment (incl. Refl.)	6542	0.029	1.06
Flows	10869	0.049	1.3
Crust	54989	0.054	1.82
Mantle	15483	0.082	1.88
Boundary			
Basement	3090	0.023	0.62
Intra-crustal 1	3867	0.034	0.72
Intra-crustal 2	8719	0.090	5.01
Moho (Angola Basin)	1437	0.075	3.51
Moho (WR and Walvis Basin)	5094	0.097	4.97
Total	110090	0.059	2.08

Table 3.2.4: Summarized error statistics for model P3 (c.f. caption of Table 3.3.1). The 'Flows' unit represents the uppermost crustal layer beneath Walvis Ridge and further south in the Walvis Basin. 'Intra-crustal 1' is the base of the 'Flows' unit; 'Intra-crustal 2' combines top HVLCB and top underplating.
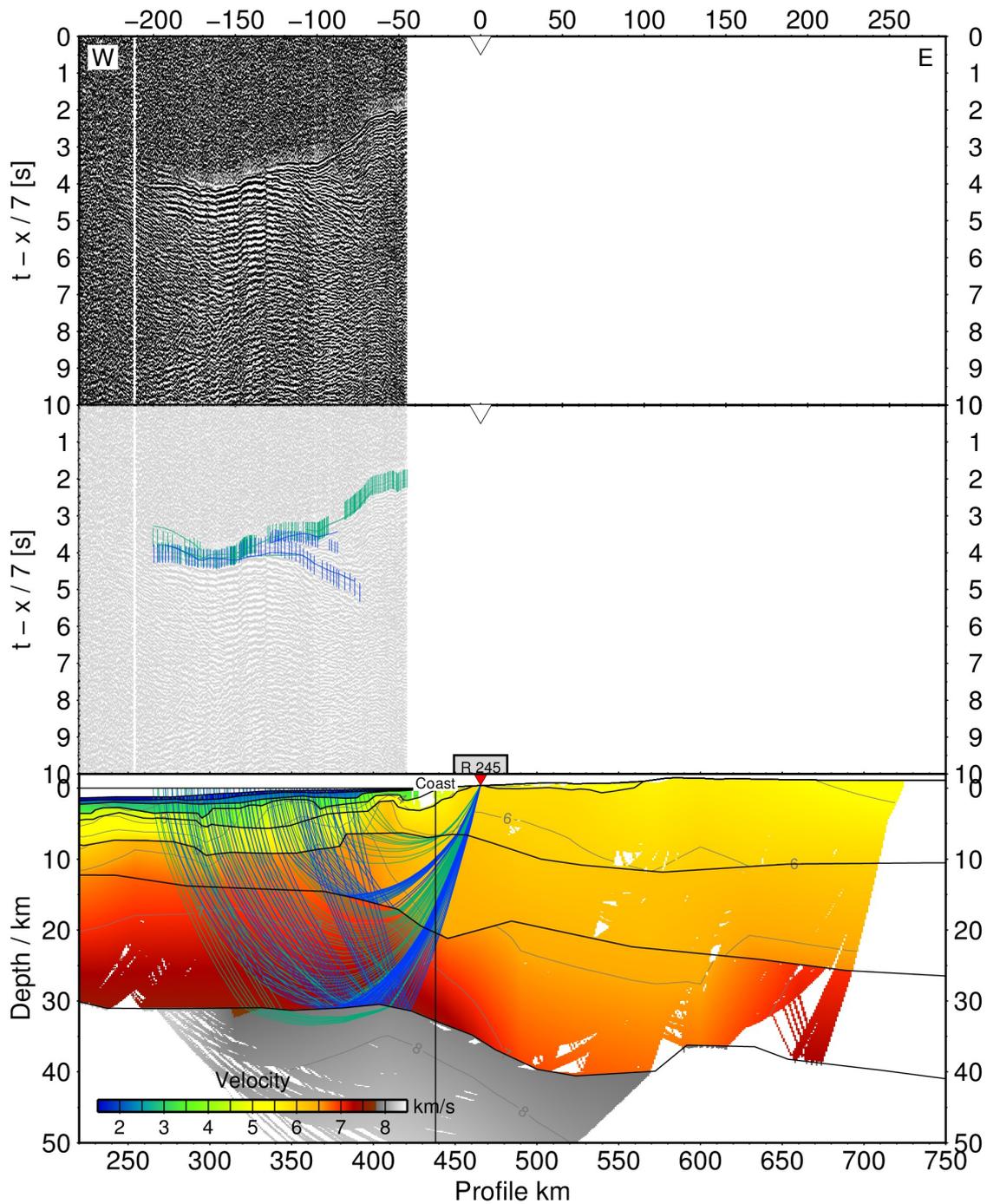
Figure 3.2.6: Data example for P100 showing recorded seismic data (top), traced arrivals (center) and ray coverage (bottom). The data are bandpass filtered with 3.5-13 Hz corner frequencies and amplified with an automated gain control (AGC) of 1 s. Picks are vertical bars with variable length representing the pick uncertainty. The number of drawn rays is reduced for clarity. This section shows airgun shots recorded by a receiver onshore. The data quality is excellent with long offsets and clear PmP and Pn phases.
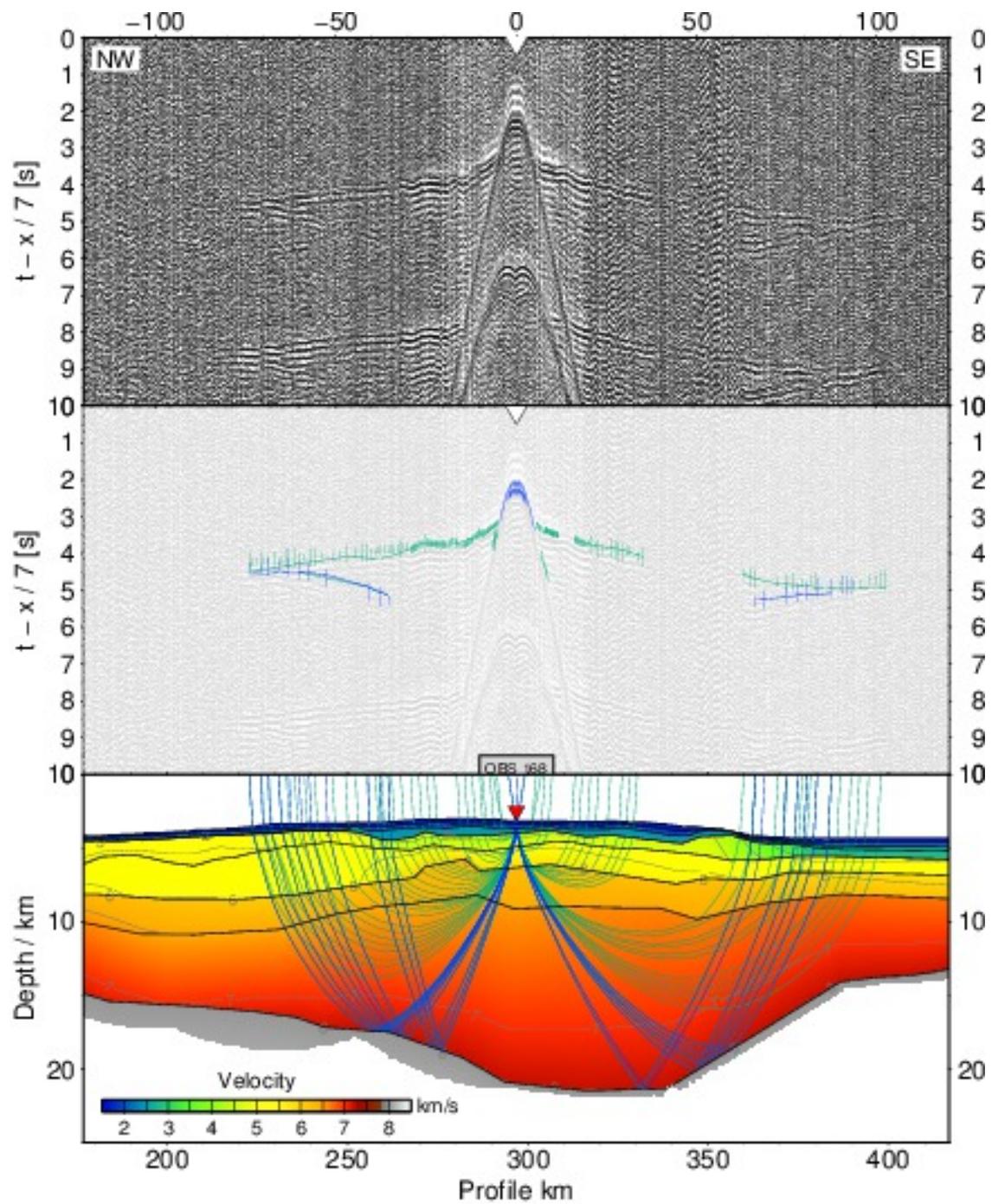
Figure 3.2.7: Data example for P150 with the same plotting parameter as used for Fig. 3.2.6. This station shows clear crustal arrivals and Moho reflection.
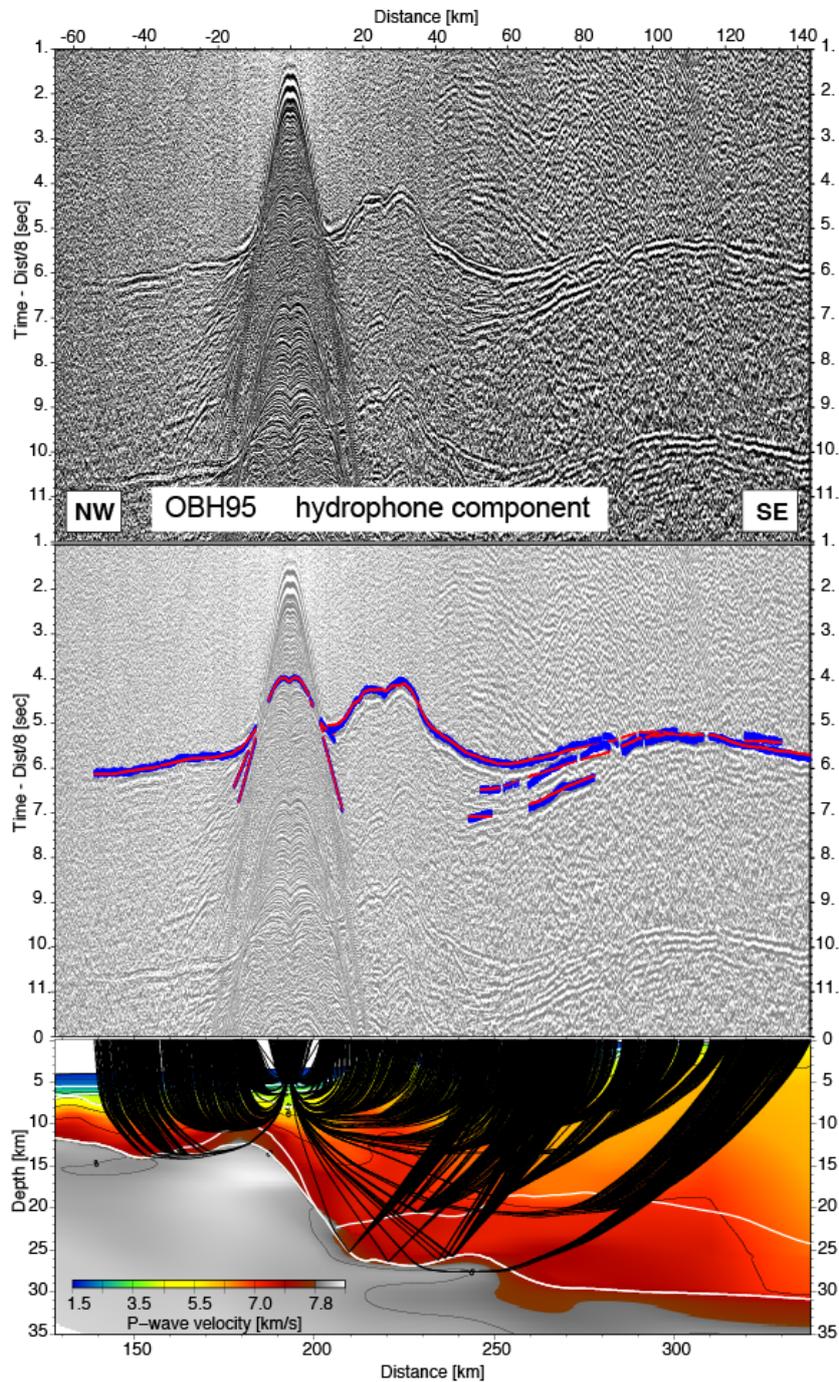
Figure 3.2.8: (Top): Seismic record section (reduced to 8 km/s) of OBH95 on profile 2. (Center): Computed traveltimes (red dots) and associated pick-uncertainties (blue bars). (Bottom): Corresponding ray paths through the final tomographic solution of profile 2.
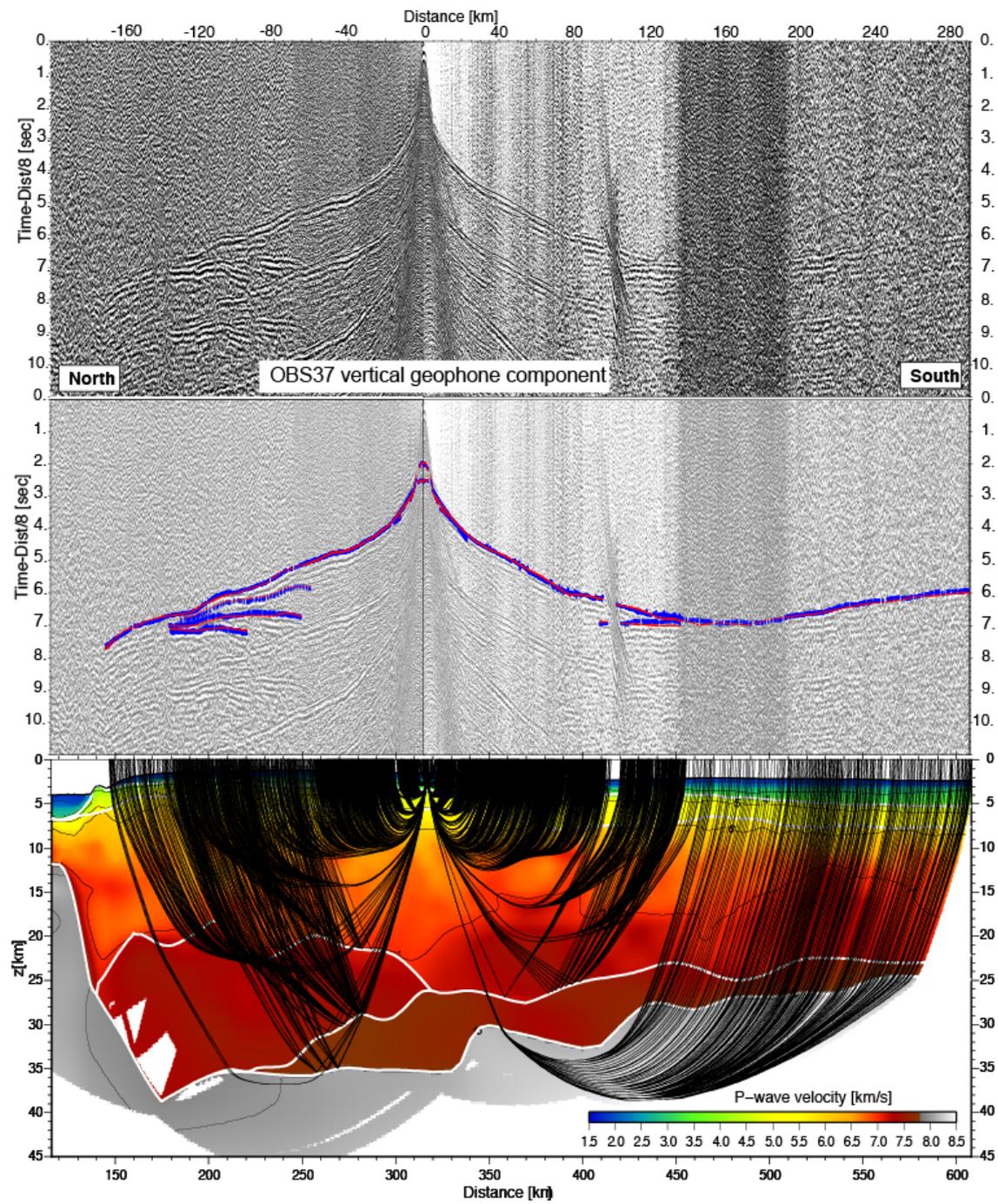
Figure 3.2.9: Data example for an OBS station of profile 3.
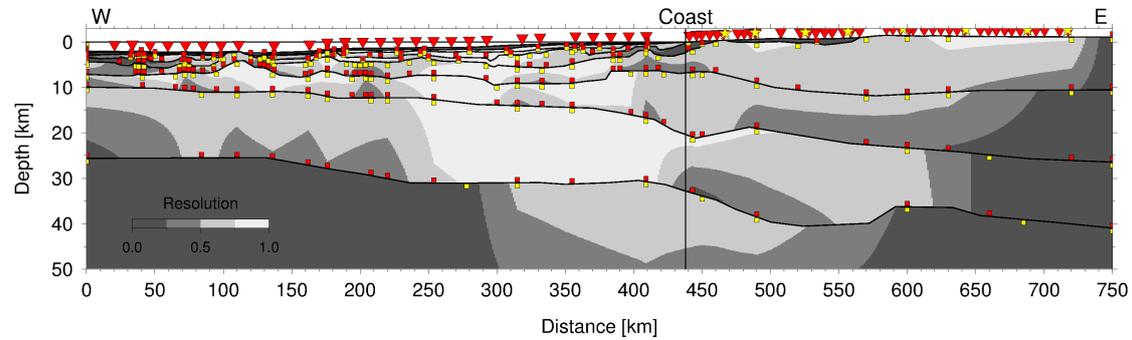
Figure 3.2.10: Resolution for profile 100. The diagonal elements of the resolution matrix indicate the linear dependence of the true model and the relative number of rays sampling each model parameter. Values greater than 0.5 are considered reasonably well resolved within the given uncertainty (here $\Delta v = 0.2$ km/s, $\Delta d = 1$km.).
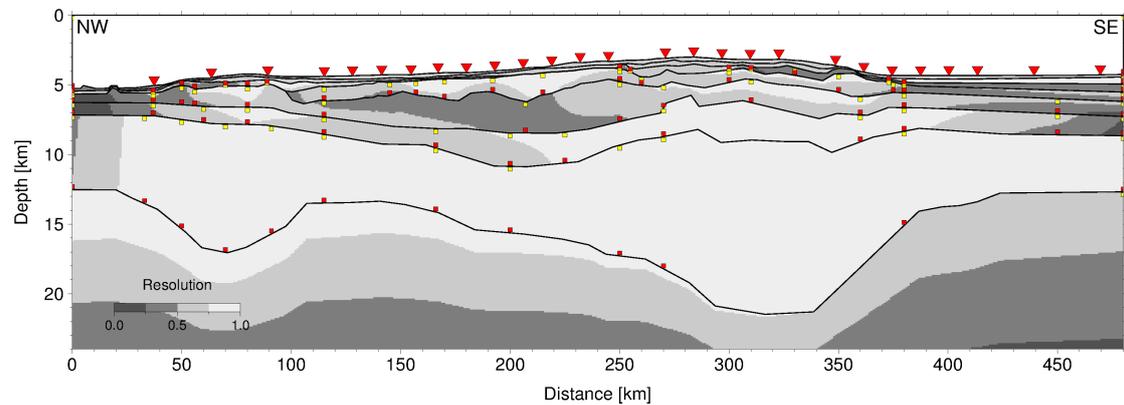
Figure 3.2.11: Resolution for profile 150. The model is well resolved in the lower crust. The lower resolution north of the ridge (LVZ) is due to a velocity inversion, which does not produce refracted waves and is therefore only constrained by reflections.
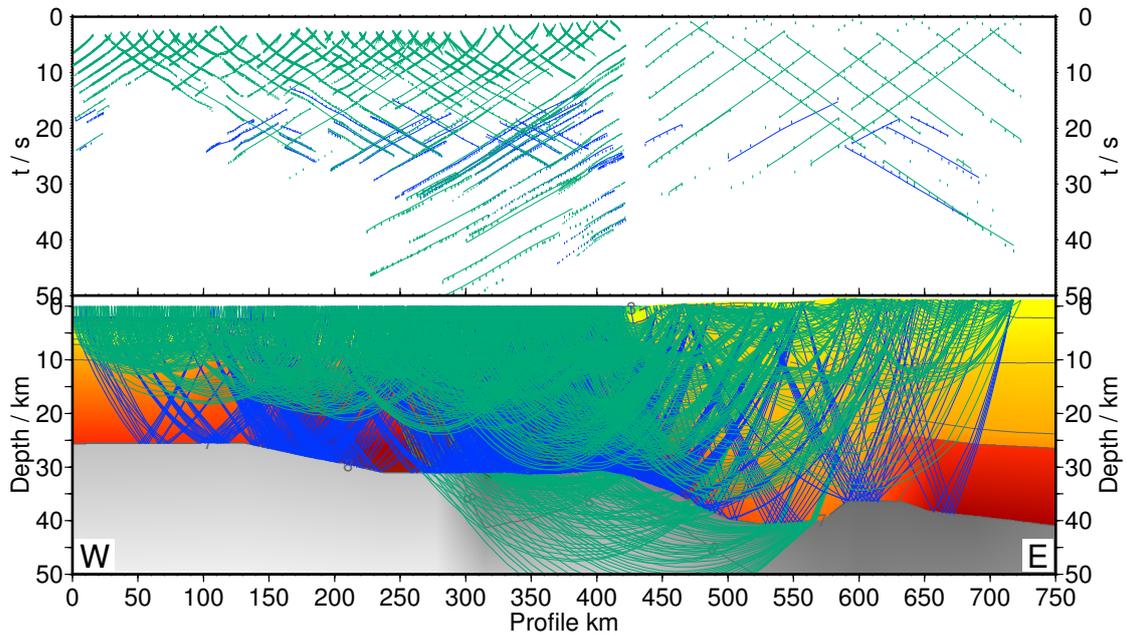
Figure 3.2.12: Ray tracing results (top) and ray coverage (bottom) for all stations of profile 100.
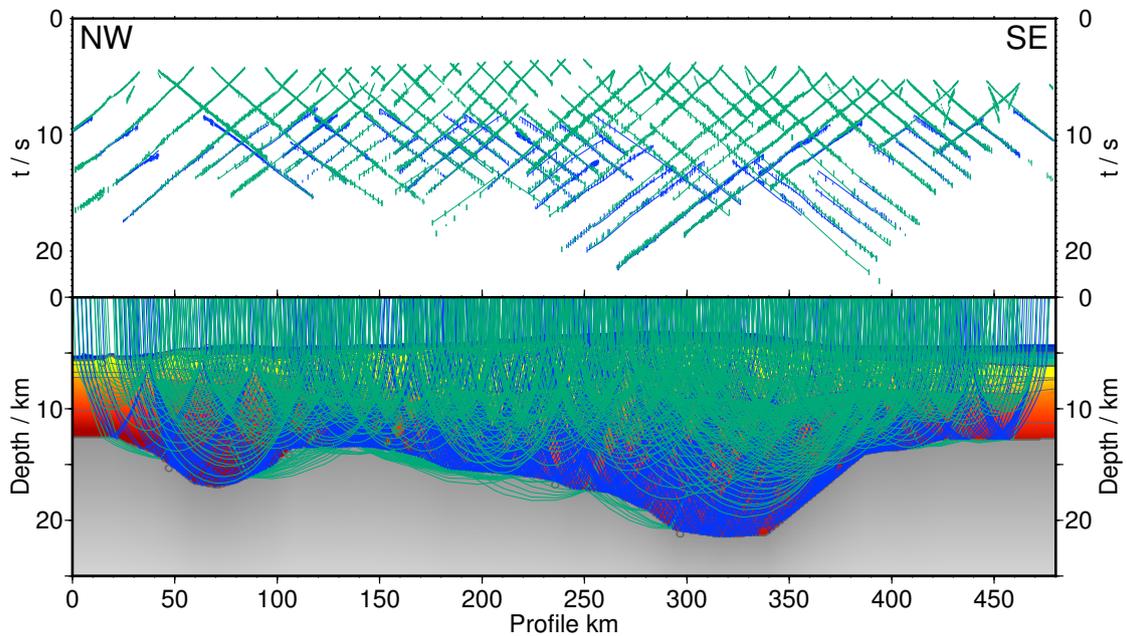
Figure 3.2.13: Ray tracing results (top) and ray coverage (bottom) for all stations of profile 150.
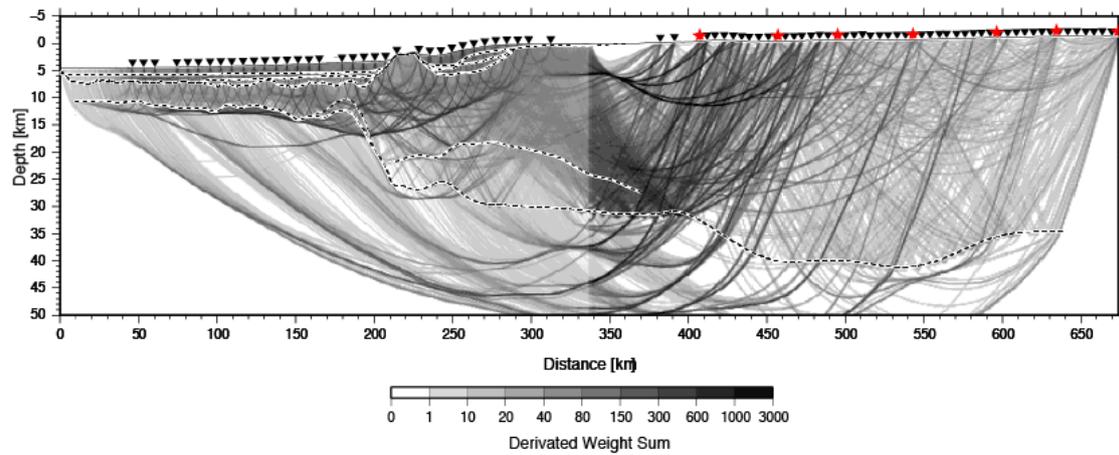
Figure 3.2.14: Derivative weight sum (DWS) of profile 2. The DWS is the column-sum vector of the normalized derivative matrix. It represents a weighted sum of the ray path length influenced by a model parameter and, due to the matrix normalization it also depends on the pick-uncertainty of each ray. Altogether, this results in a rough assessment of solution sensibility on the basis of data quantity and quality. Hence, a high DWS value can be ascribed either to a denser sampling of rays or to an accumulation of higher quality rays with smaller pick-uncertainties.
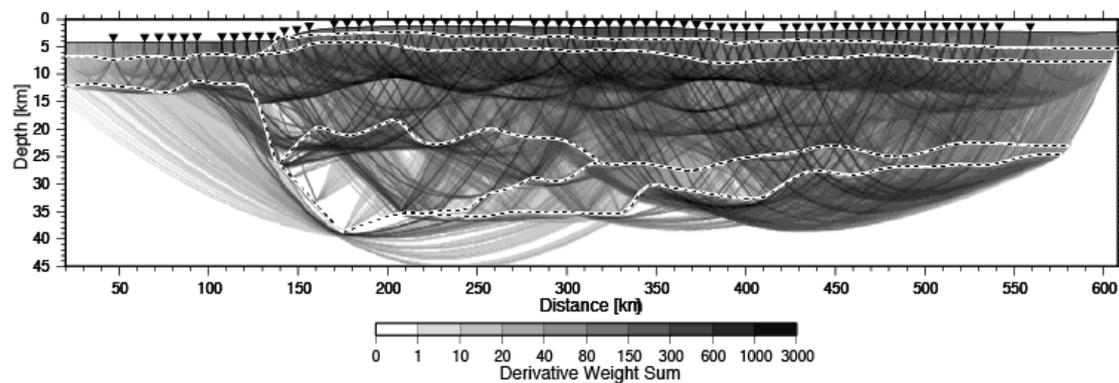
Figure 3.2.15: Derivative weight sum (DWS) of profile 3 (c.f. caption 3.2.14).

3.3   The onset of Walvis Ridge: plume influence at the continental margin

Large igneous provinces are often found in close spatial and temporal proximity with continental breakups. The large volumes of melt are thought to be provided by an arriving deep mantle plume, which is widely considered to trigger the breakup itself. The opening of the South Atlantic is a classical example for this model. Flood basalts are present on both conjugate margins as well as aseismic ridges connecting them with the current hotspot location at Tristan da Cunha. To determine the effect of the plume head on the continental crust, a deep seismic profile was acquired in 2011 at the junction of Walvis Ridge with the African continent. We present a P-wave velocity model extending 430 km along the crest of the ridge and continuing onshore to a total length of 720 km. Crustal velocities beneath Walvis Ridge vary between 5.5 km/s and 7.0 km/s, a typical range for oceanic crust. The crustal thickness of 22 km, however, is approximately three times larger than of normal oceanic crust. The continent-ocean transition is characterized by 30 km thick crust with strong lateral variation in the upper crust and a high velocity lower crustal body (HVLCB), where velocities reach up to 7.5 km/s. The HVLCB is 100 km longer than HVLCBs observed south of Walvis Ridge and reaches into the continental crust before it ceases at the 40 km thick crust of the Kaoko fold belt. Such high seismic velocities indicate that hot material intruded the continental crust during the initial rifting stage. However, the remaining continental crust seems unaffected by intrusions and the root of the Kaoko belt is not eroded. We conclude, that the plume head did not modify the continental crust on a large scale, but was a rather local anomaly. Thus, it seems unlikely that the plume drove or initiated the breakup process. We further propose that the hotspot already existed underneath the craton prior to the breakup and ponded melt erupted at accruing rift structures providing magma for the flood basalts.

3.3.1   Introduction

A problem in modern plate tectonics is to understand the driving forces controlling the plate movements. Several mechanisms are discussed: plate boundary forces such as ridge push and slab pull, mantle convection induced basal drag, gravitational potential and deep mantle plumes. Although all potentially influence plate movements, their relationship and relative significance are still unclear. It is not understood, how and why continents break and which parameters control the line of breakup. Large forces are required to break continents by pure extension, although several processes can reduce the required forces and facilitate breakup, e.g. the stress distribution and geometry of rifting (Brune et al., 2012). Regarding the line of breakup, an increasing number of evidences indicate that large plates
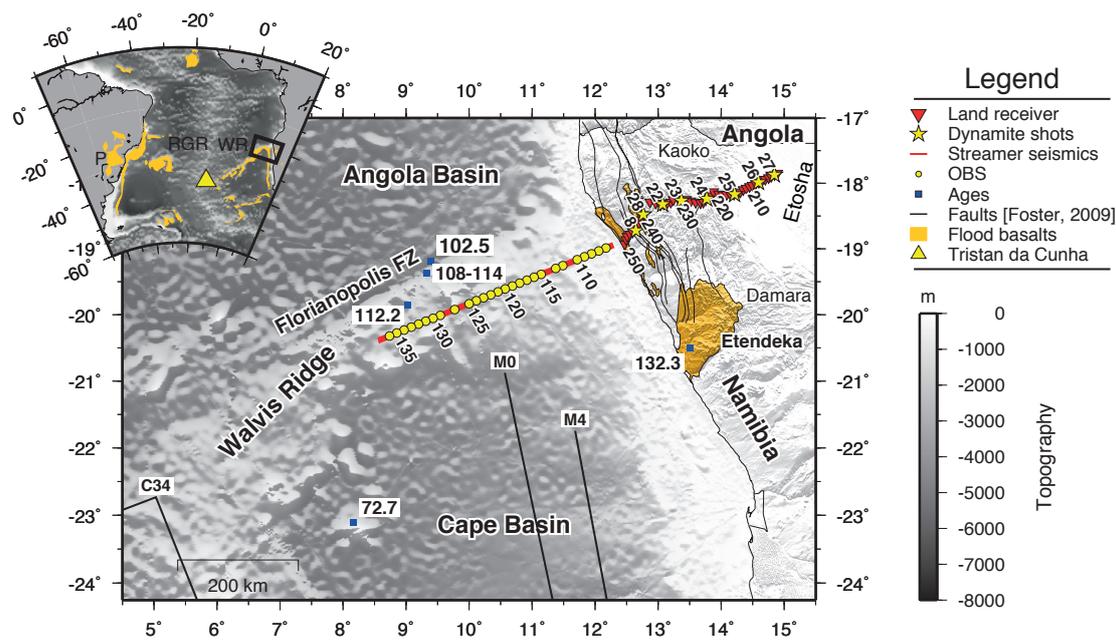
Figure 3.3.1:   Overview map of the South Atlantic and close up of the working area (boxed region). P Paraná, RGR Rio Grande Rise, WR Walvis Ridge. The presented profile 100 extends along the axis of Walvis Ridge and crosses the Kaoko Fold Belt onshore. The total length of the profile is 720 km. Magnetic anomalies modified after Seton et al., 2012. The presence of M0 and M4 immediately north of WR is not well constrained and disputed (Rabinowitz and LaBrecque, 1979; Eagles, 2007; Moulin et al., 2010). Ages for magnetic anomalies after Gee and Kent, 2007: C34 - 83.5 Ma, M0 - 120.6 Ma, M4 - 125.7 Ma. Age for the oceanic crust north of WR is derived from sedimentation rates (ODP Leg 75, Site 530, Hay and Sibuet, 1984). Other ages after Rohde et al., 2012.

preferentially separate along lines of weaknesses, which are reactivated by underlying mantle processes (Ziegler and Cloetingh, 2004; Lundin and Doré, 2005; Buiter and Torsvik, 2014). Lines of weakness could be old fracture zones, former plate boundaries or areas of repeated extension and compression (Lundin and Doré, 2011). In addition to utilizing old weak zones, some processes generate new ones. A hot lithosphere is weaker than a cool one, thus processes increasing temperatures generally weaken the crust. For example, large mantle convection cells might accumulate hot upwelling mantle material beneath continental plates, increasing their temperature and therefore weaken the crust until it finally gives way (Gurnis, 1988). Another popular explanation for these increased temperatures are deep mantle plumes transporting hot material from the core mantle boundary to the upper mantle. When they arrive at the lithosphere with a voluminous mushroom-shaped head, the hot material heats and erodes the lithosphere allowing large amounts of melt to intrude the crust and erupt at the surface, where they form large igneous provinces (LIP, Morgan, 1971; Courtillot et al., 1999; Sobolev et al., 2011). After the initial eruptions the plume head is no longer relevant for the on-

going volcanism, however its thin remaining tail can produce linear age-progressive volcanic ridges or seamounts as the plate moves over the plume position. For a mid-ocean ridge-centered plume a pair of aseismic ridges is created on the diverging plates. Because LIPs are often found in combination with rift systems and their main eruptions prior or during the initial rift stages (Courtillot et al., 1999), plumes are thought to be one of the driving forces for continental breakup (Morgan, 1971; Richards et al., 1989) or at least enhance existing early stage rifting and significantly increase the chances for a breakup (Ziegler and Cloetingh, 2004; Brune et al., 2013). Examples for LIPs in close connection with breakups and hotspot trails are found in India, in the Indian Ocean and in the North Atlantic. The Deccan traps in India connect to the Reunion hotspot via the Mascarene-Chagos-Laccadive Ridge (Collier et al., 2009), the Ninetyeast Ridge in the Indian Ocean marks the Kerguelen hotspot trail (Grevemeyer and Flueh, 2000) and in the North Atlantic the Iceland-Faroer Ridge (Richardson et al., 1998) and the Iceland-Greenland Ridge connect Iceland to the North Atlantic Volcanic Province. However, some ridges cannot unanimously be associated with a LIP or rifting processes, but are also candidates for plume-lithosphere interactions, like Cocos- and Carnegie Ridge. They might be the surface expression of the Galapagos hotspot and are in spatial correlation with the Caribbean large igneous province (Sallarès et al., 2003; Sallarès et al., 2005).

The opening of the South Atlantic is another classical example for plume related continental breakup. Continental flood basalts are present on both conjugate margins and a pair of aseismic ridges marks the plume trail to the current hotspot position (Fig. 3.3.1). The larger Paraná flood basalt province in South America was emplaced prior and during the initial rift stage 137 to 127 Ma ago (Turner et al., 1994). The conjugate, and eminent smaller, Etendeka flood basalts erupted simultaneously in Namibia with peak volcanism at 132-129 Ma (Renne et al., 1996). Subsequently, the Walvis Ridge formed on the African plate overriding the plume tail. The continued volcanism formed the remarkable submarine ridge stretching 3100 km from the African continent almost to the present-day Mid-Atlantic Ridge. As proposed for hotspot derived seamount chains, its ages progressively decrease towards the source: from 114 Ma at the north-eastern end close the Namibian continental margin, to 27-49 Ma in the south-western guyot province and recent at the current hotspot position Tristan da Cunha. Since those rock samples are not evenly distributed along Walvis Ridge, the age of the older part of the ridge up to C34 is poorly constrained. Only two closely spaced dredges provide age constrains and ODP drillings in this area did not reach the basement (Leg 40, Sites 362, 363 Bolli et al., 1978; Leg 75, Site 503-532 Hay and Sibuet, 1984). Magnetic anomalies M0 and M4 can be identified south of Walvis Ridge close to the Namibian margin, but not on the ridge itself or north of it (Cande et al., 1989; Nürnberg and Müller, 1991; Eagles, 2007).

The conjugate Rio Grande Rise on the South American plate lacks the elongated shape and volcanic lineaments of Walvis Ridge and was likely formed with the hotspot located at the Mid-Atlantic Ridge, similar to present day Iceland (O'Connor and Duncan, 1990). After 80 Ma the volcanism changed from on-axis

to intraplate resulting in the guyot province of Walvis Ridge without corresponding features on the South American plate. During the hotspot evolution, magma production was not constant but varied with periods of 10-20 and 5 Ma overlaying a general decline of volcanism (Adam et al., 2007; Gallagher and Hawkesworth, 1994).

Even though the evolution of Walvis Ridge seems to be well understood the existence of mantle plumes is still controversial and different origins are discussed. The Walvis Ridge might be the result of fracture zone with an extensional component (a failed rift arm of a triple junction) producing the volcanism (Le Pichon and Fox, 1971; Fairhead and Wilson, 2005; Elliott et al., 2009) or a combination of hotspot and fracture zone (Haxel and Dziak, 2005). Those models are based on the proximity of Walvis Ridge to the Florianopolis Fracture Zone (FFZ), a major fracture in the South Atlantic marking the northern boundary of Walvis Ridge. The FFZ can be traced across the Mid-Atlantic Ridge and has been an active deformation zone in South America (Torsvik et al., 2009, and references within).

Thus, Walvis Ridge is an excellent location to study breakup mechanism with hotspot influence and thus, test the previously described model. Here, we like to present the results of a combined on-/offshore deep seismic profile at the junction of Walvis Ridge with the Namibian continental margin (Fig. 3.3.1). The seismic line aims to investigate the crustal fabric at the transition zone between flood volcanism and ridge formation. We were especially interested in information on how far the continental crust was modified landwards by this thermal event. The profile presented here extends 430 km along the axis of Walvis Ridge. Onshore Namibia it was prolonged by 290 km to investigate the velocity structure at the transition of the Walvis Ridge to the Namibian mainland by recording the offshore airgun shots and acquiring a deep seismic sounding profile with explosives onshore.

3.3.2 Data aquisition, Processing and Modelling

Here we present one of five deep seismic profiles, which were acquired as part of a large geophysical on- and offshore experiment, consisting of deep seismic sounding, seismology and magnetotelluric experiments. Our profile extends 430 km along the axis of Walvis Ridge and continues 290 km onshore Namibia (Fig. 3.3.1). The transect has a total length of 720 km.

Acquisition and processing Marine wide angle seismic data were acquired with the research vessel Maria S. Merian during the cruise MSM17/2 in January 2011. The seismic source signal was generated by an $8 \times 8\,l$ G-gun array ($64\,l$ or 3905 cu. in. in total) operated at 200 bar (2900 psi) and 8 m water depth. In total 27 ocean bottom stations (OBS) and 50 land stations recorded the airgun shots along our line. The OBS had a spacing of approximately 13 km. A shooting interval of 90 s resulted in a mean shot point distance of 230 m. The seismic signals were recorded by the OBS at a sampling rate of 200 or 250 Hz mainly from a hydrophone component and simultaneously by a 100 m long, four channel streamer (Fig. 3.3.2).
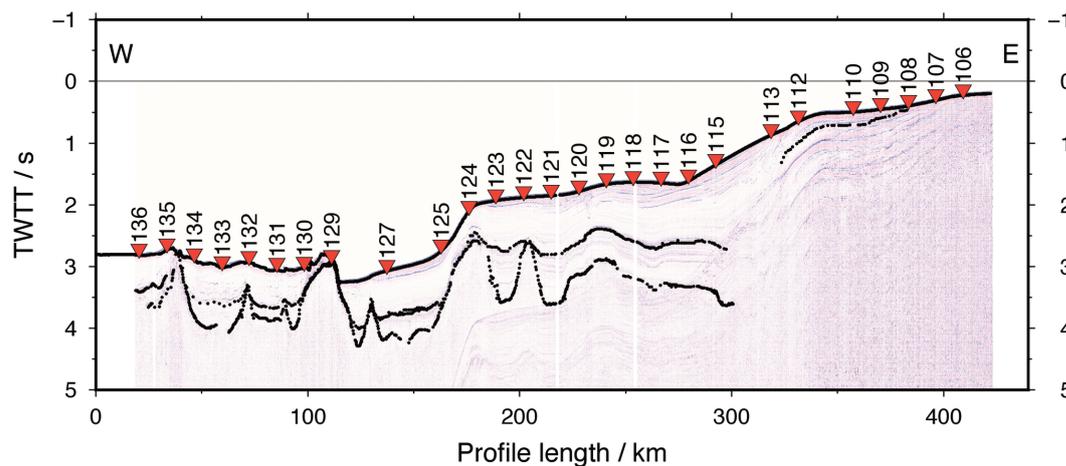
Figure 3.3.2:   One channel raw seismic reflection profile with interpretation and OBS positions (red triangles). The first multiple affects data at profile km 170–430. Multiple seamounts with variable size are revealed along the profile. Note the change in their shape and sediment cover beyond profile km 220.

In addition to the marine source, explosives were used onshore to determine the crustal structure of the continental part of the transect. Eight shots with charges between 250 and 400 kg were fired at distances between 22 and 45 km. The receiver stations onshore had a mean distance of 6 km. For logistical reasons the locations of onshore shots and receivers had to follow roads and valleys, which led to an uneven spacing and occasionally large distances from the projected profile.

The data processing included offset calculation and relocation of the OBS stations. Offsets between shots and receivers were calculated as the shortest distance between their positions. OBS and landstations were arranged in receiver gathers for the airgun shots, while shot gathers were used for the onshore shots. Since currents may shift the OBS while it sinks to the bottom, its exact position at the seafloor is unknown and might slightly differ from the deployment site. This shift can be calculated using the direct arrivals. The first arrival of the source signal resembles a hyperbola with its apex at zero offset if the station location is correct. A hyperbola was fitted and the calculated inline shift was used to correct the offsets. The maximum shift was 130 m.

The data quality was highly variable and strongly dependent on the station position and type of source. The OBS show refracted crustal phases (Pg) with offsets varying from 30 to 180 km (average offset of 60 km). Reflections from the crust-mantle boundary (PmP phases) are rare and have mostly low signal to noise ratios. Phases refracted in the mantle (Pn) could not be observed on the OBS. In contrast, almost all land stations recorded excellent airgun signals with clear Pg and PmP. Additional Pn phases were observed on most onshore stations with offsets up to 380 km. The dynamite shots recorded on the land stations had an excellent signal to noise ration for the first arrivals at offsets up to 100 km, but at larger offsets and first and second arrivals (like PmP) were rarely unequivocal.

No seismic signals from the dynamite shots could be identified on the OBS. Only the OBS closest to the coast recorded a sufficiently strong signal from the nearest onshore shot. Figures 3.3.3–3.3.7 show several data examples along the line from all different recorder and source types used.

For picking arrivals we used the software ZP (Zelt, 2004b). Since the main signal energy was around 6 Hz, we filtered the data with a 3.5-13 Hz bandpass and applied an automatic gain control (AGC) if necessary. Pick uncertainties were manually assigned and ranged 30 and 250 ms depending on the signal to noise ratio and offsets of phases. Later arrivals generally have larger uncertainties.

Modelling   For creating a 2D velocity model, stations were projected on a straight line, while leaving the source-receiver distances unchanged (Zelt, 1999). The projection was calculated with minimized perpendicular distances for the OBS positions and then extended onshore to cover the landstations. Distances between OBS and the projected profile are small (only up to 600 m). In contrast, recording stations onshore had to be placed along roads and valleys, which caused large distances of up to 40 km perpendicular to the calculated transect. Hence, the 2D modelling in these areas assume a homogeneous crust up to 40 km perpendicular to the profile. This is, of course, not the case and larger errors for the crustal model are the consequence. For the marine part of the transect, we used the acquired seismic reflection data (Fig. 3.3.2) to determine the sediment thickness and variations of the acoustic basement. Since the streamer was too short for a standard velocity analysis, sedimentary velocities were solely calculated from OBS recordings. Phase identification and correlation for stations was difficult due to highly variable basement topography with large buried seamounts (diameters up to 40 km) approx. every 30 km.

Forward modelling was done with the software rayinvr (Zelt and Smith, 1992) following a top to bottom approach by changing velocities and layer depths to fit the observed phase onset and slope. Layer boundaries within the igneous crust were modelled to account for different velocity gradients (large gradient for the upper crust, small gradient for the lower crust). Thus, they are mostly not constrained by reflections. The model was finally inverted with a least square method to optimize the data fit and calculate error statistics (Tab. 3.3.1). The final velocity model is shown in Figure 3.3.9 and described in detail in section 3.3.3.

Resolution and Model uncertainties   In total 10550 picks were traced with an overall travel time residual of 0.115 ms, which is in the range of the assumed pick uncertainties. The total fit of a model can be judged by the χ^2 value, which ideally should be 1 or smaller. We obtain $\chi^2 \approx 0.73$. For further details, Table 3.3.1 summarizes the error estimations for the final model. The resolution plot illustrates the negative effect of seamounts, which often generate diffractions rather than refracted phases and prevent ray propagation across the structure (Fig. 3.3.4). Thus, those areas generally have a lower resolution. The resolution matrix as well as χ^2 are a mathematical estimation for the error and uncertainty and strongly
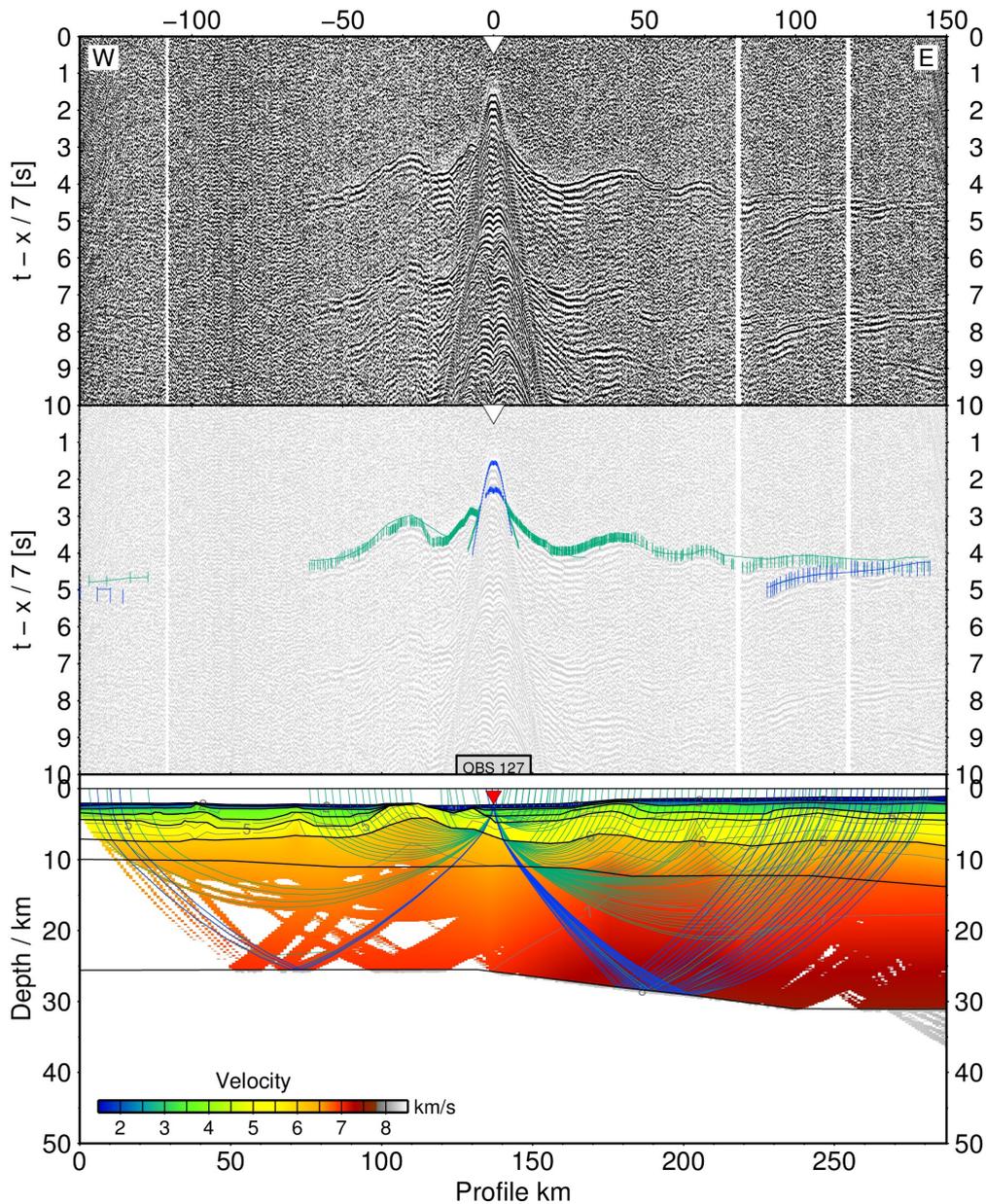
Figure 3.3.3: Data example for recorded seismic data (top), traced arrivals (centre) and ray coverage (bottom). This and the following record sections are reduced with 7 km/s. The data are bandpass filtered with 3.5-13 Hz corner frequencies and amplified with an automated gain control (AGC) in a 1 s time window. Picks are vertical bars with variable length representing the pick uncertainty. The number of drawn rays is reduced for clarity.

The variable basement topography highly influences the travel times and causes discontinuous refractions (Pg - green picks and rays). This station is one of the few stations with continuous refracted crustal phases and a clear moho reflection (PmP - blue picks and rays) at least to one side of the station.
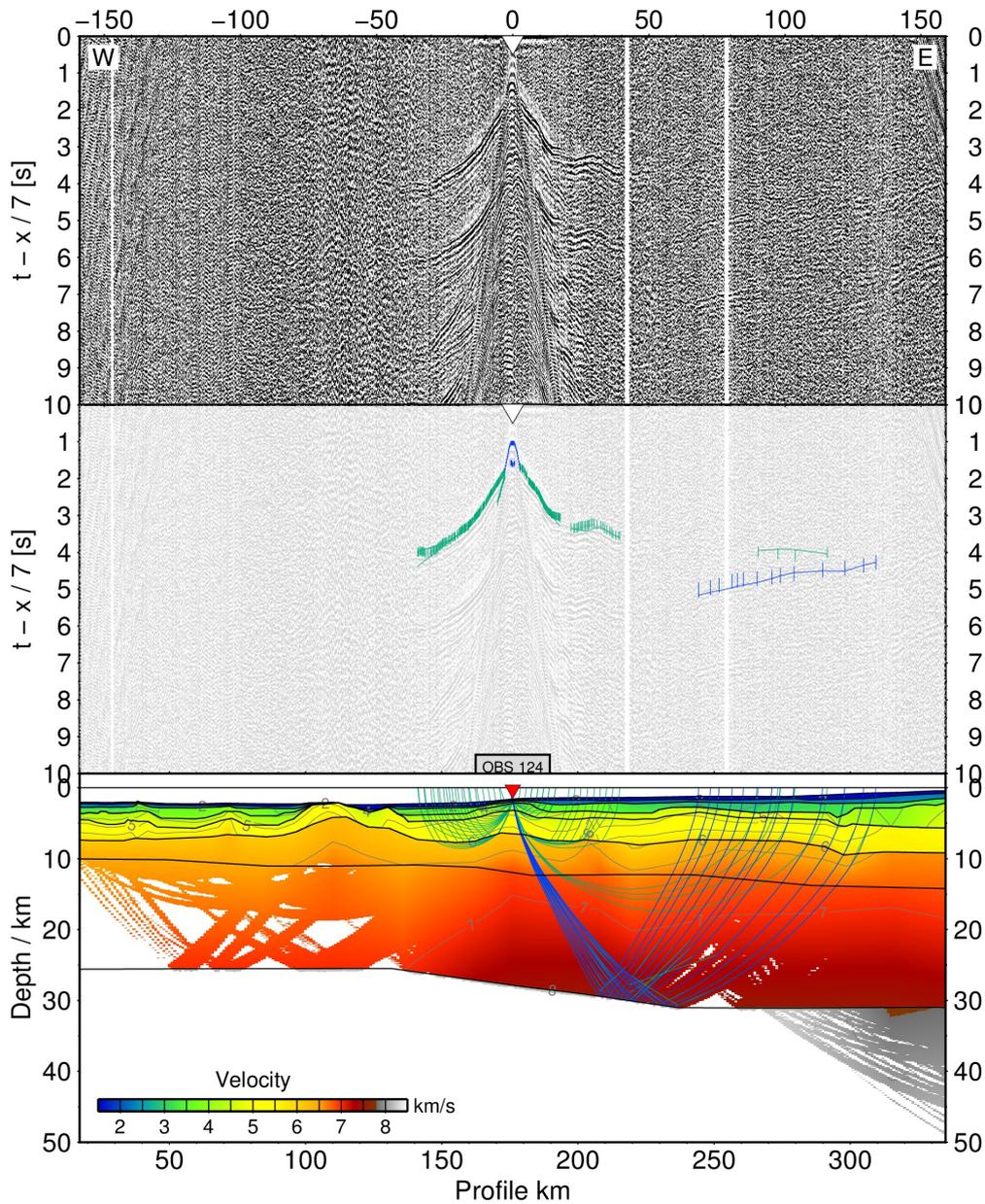
Figure 3.3.4: Data example for recorded seismic data, traced arrivals and ray-coverage. Refer to Fig. 3.3.3 for a detailed description of the graph.
The strong masking effect of the basement topography prevents continuous crustal refractions, velocities of the lower crust have therefore been mostly constrained by PmP moveouts.
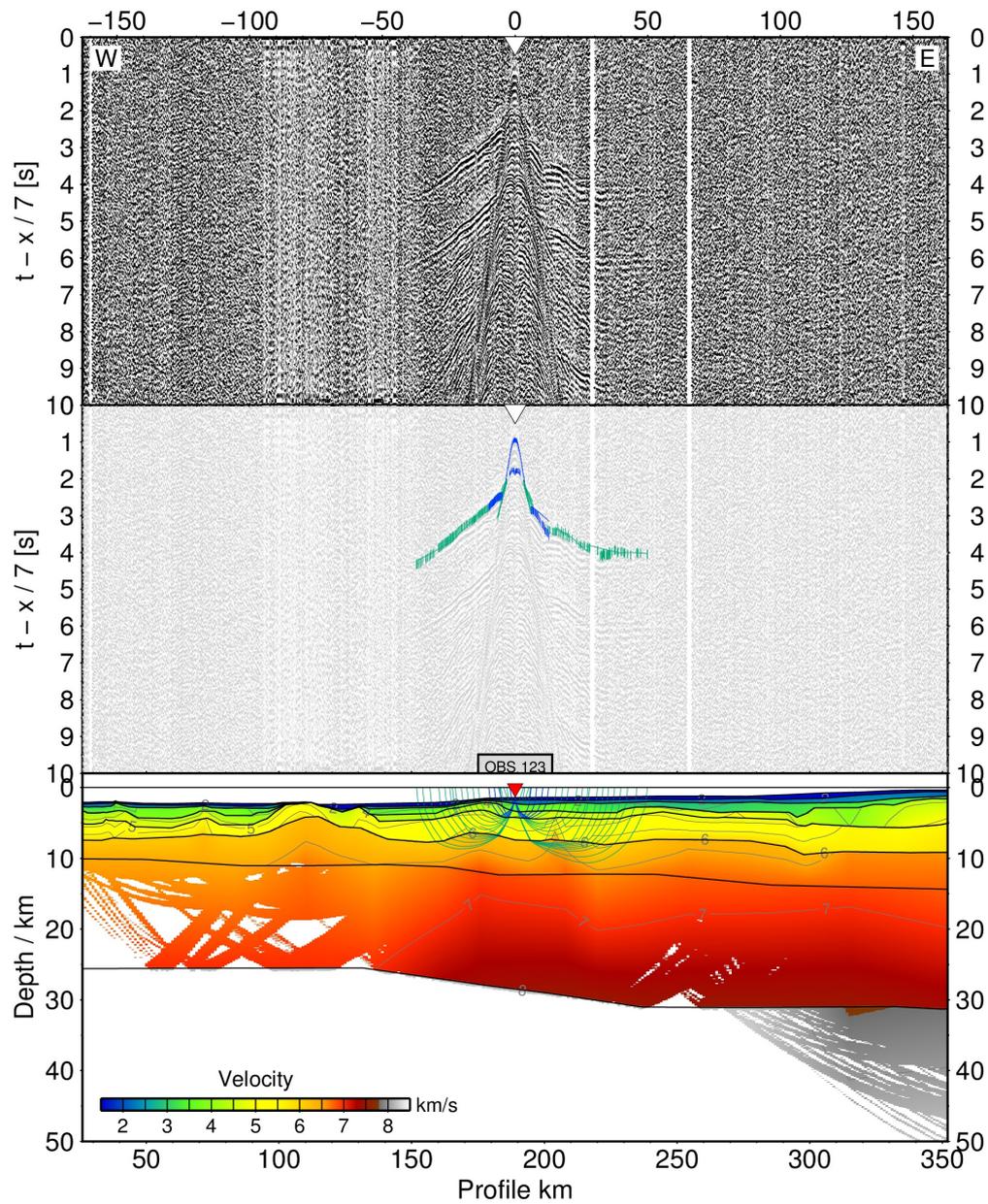
Figure 3.3.5: Data example for recorded seismic data, traced arrivals and ray-coverage. Refer to Fig. 3.3.3 for a detailed description of the graph.
The upper crustal phases in the transitional part of the profile occasionally indicate velocity inversions and strong lateral heterogeneities preventing long offset refractions. Arrivals on the right side do not represent gradients typically seen in oceanic crust.
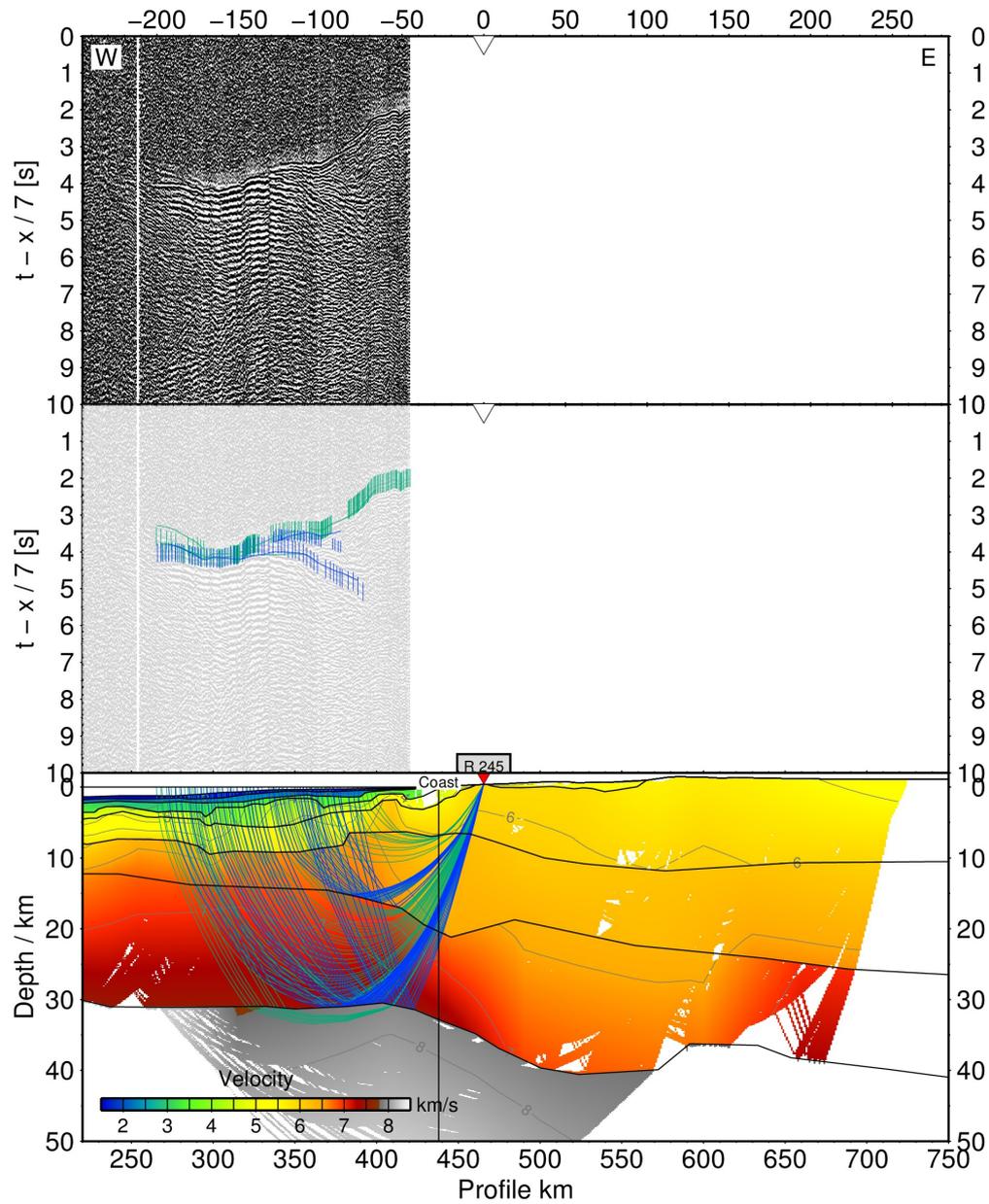
Figure 3.3.6: Data example for recorded seismic data, traced arrivals and ray-coverage. Refer to Fig. 3.3.3 for a detailed description of the graph.

Airgun shots recorded by a receiver onshore. The data quality is excellent with long offsets and clear PmP and Pn phases.
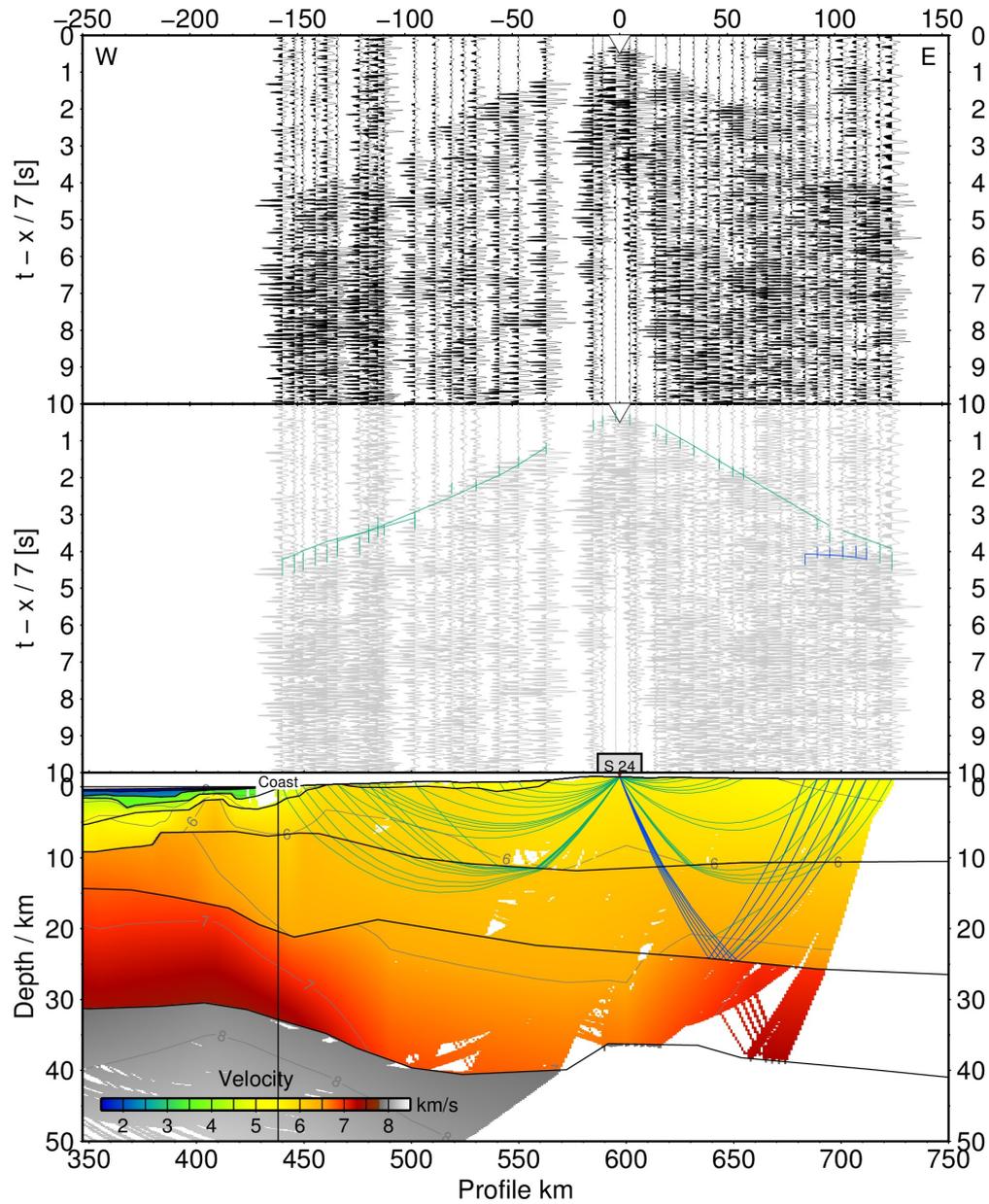
Figure 3.3.7: Data example for recorded seismic data, traced arrivals and ray-coverage. Refer to Fig. 3.3.3 for a detailed description of the graph.

Dynamite shot with a charge of 300 kg recorded by 48 land receivers. A clear reflection on the right side has been interpreted as a reflection from the top of an intrusive body. An alternative interpretation as PmP results in a dramatic decrease in crustal thickness, which is inconsistent with gravity data (Fig. 3.3.14).
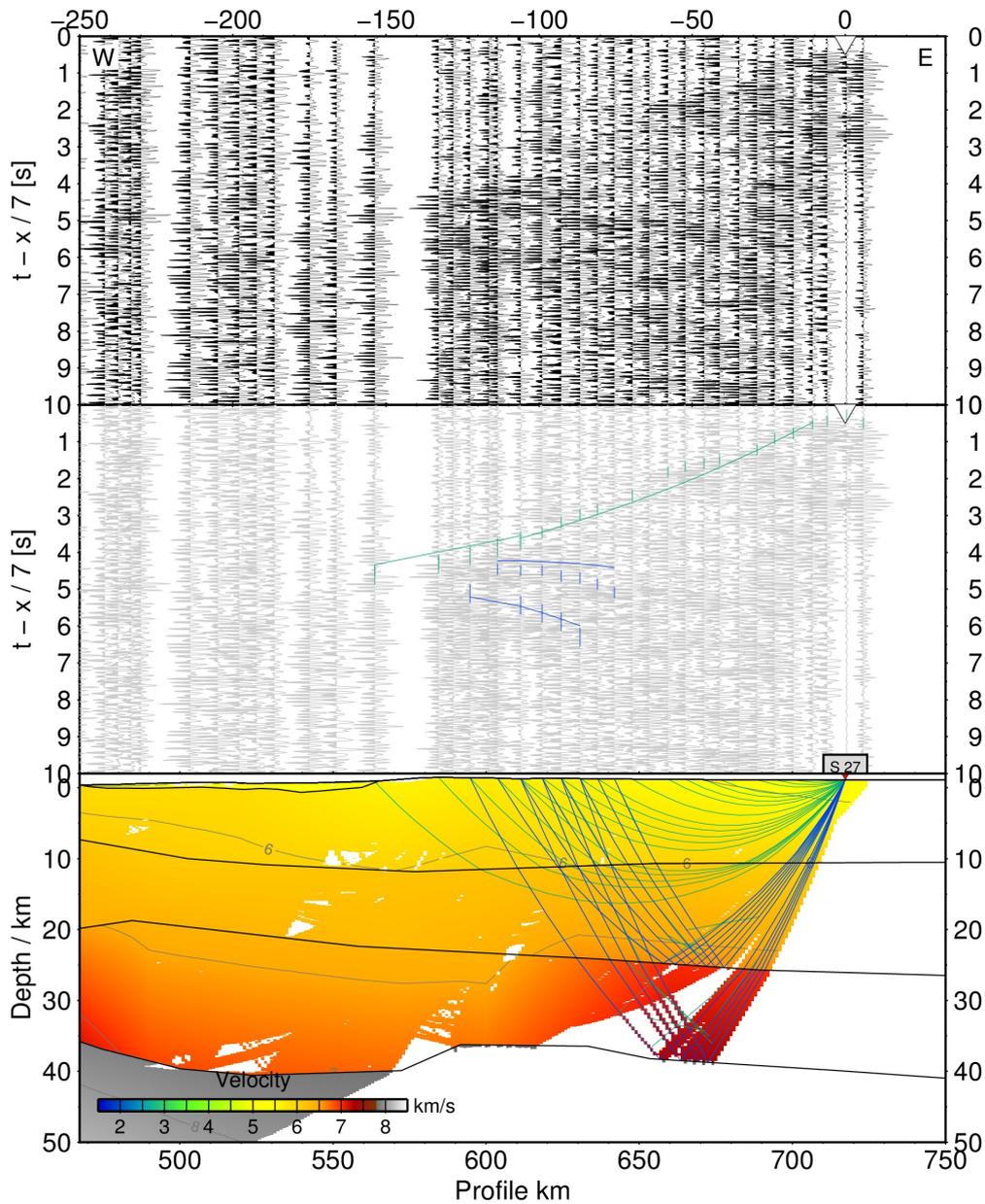
Figure 3.3.8: Data example for recorded seismic data, traced arrivals and ray-coverage. Refer to Fig. 3.3.3 for a detailed description of the graph.

Dynamite shot with a charge of 300 kg recorded by 48 land receivers. The east-ernmost shot displays two reflection on the left side, which are interpreted as reflections from the top of an intrusive body and the crust-mantle boundary.

depend on the distribution and number of model parameter. A better judgement can be made by taking the ray coverage into account, which reveals missing refracted waves for the lower crust (Fig. 3.3.11). This is commonly seen in crustal models and caused by the low velocity gradient in this layer. Velocities in the lower crust are therefore calculated from the move-out of PmP reflections. Consequently, models have a velocity-depth ambiguity with uncertainties of $\pm 0.2\,\mathrm{km/s}$ and $\pm 3\,\mathrm{km}$ for the lower crust.

Unit	n	t_{rms}/s	χ^2
Sediments (incl. refl.)	1945	0.061	0.753
Crust (airgun shots)	7133	0.097	0.615
Crust (dynamite shots)	198	0.222	1.427
Mantle	396	0.311	2.128
Boundary			
Moho (airgun shots)	755	0.203	1.022
Moho (dynamite shots)	47	0.374	2.290
Basement	141	0.084	1.464
Total	10550	0.115	0.726

Table 3.3.1: Summarized error statistics for model P100 showing the number of traveltime picks (n), the RMS error (t_{rms}) and the normalized χ^2 value for different model units and corresponding boundaries. Results for the model units combine refractions (respective turning rays); results for the boundaries combine respective reflections. Note that the result for 'Sediments' includes some additional intra-sedimentary reflections. The basement is further constrained by single-channel streamer data. Note that the uncertainty for the sparse land data is usually larger than for the marine data.
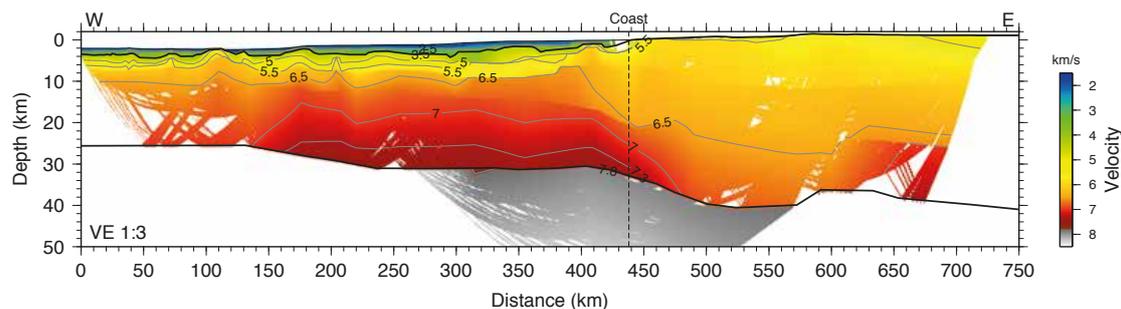

Figure 3.3.9: Final seismic velocity model obtained from rayinvr. Contour lines are drawn and annotated for selected velocities. White areas are not covered by ray paths.

3.3.3   Results and Interpretation

Here, we describe and interpret the velocity model of the transect (Figs. 3.3.9 and 3.3.12). Based on the model structures and velocity depth profiles (Fig. 3.3.13),
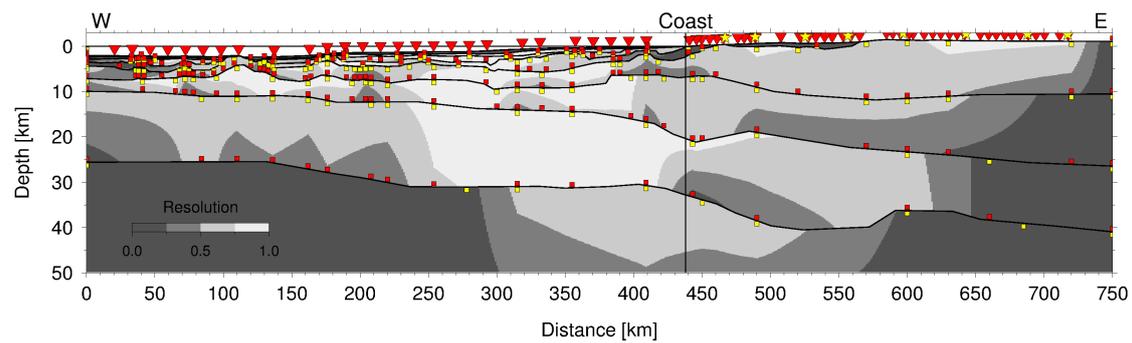
Figure 3.3.10: Resolution plot for the final velocity model. Plotted values are the diagonals of resolution matrix and range between 0 and 1. Nodes with values larger than 0.5 are considered as well resolved (Zelt and Smith, 1992; Lutter et al., 1990).

we divide the profile into three sections: (1) thickened oceanic crust in the west (km 0 to 180), (2) a transitional zone which is characterized by intrusions and a high velocity lower crustal body (km 180 to 420) and (3) a partly underplated, but otherwise unaltered continental crust below the Namibian mainland (km 420 to 720).

Thickened oceanic crust (km 0 to 180)   Between km 0 and 170, the profile has a relative constant water depth of 2000 m abruptly decreasing to 1400 m at km 180. The sediment cover is up to 2 km thick, but its thickness is highly variable, due to a number of buried seamounts as revealed in the seismic reflection data (Fig. 3.3.2).

Three layers represent the sediments in our model. The uppermost layer consisting of soft, non-compressed sediments cannot be seen in seismic refraction data, but is deducted from ODP sites (Leg. 40, Site 362, 363, Bolli et al., 1978) and modelled with a velocity of 1.5-1.6 km/s. The next layer is ∼300 m thick with a velocitiy of 2.4 km/s, followed by a layer with velocities ranging from 3.5 to 3.9 km/s (in moats up to 1.4 km thickness). Those velocities can be associated with the deepest drilled sediment layer: limestones deposited in the Lower Aptian (Site 362, Bolli et al., 1978). The underlying basement is heavily distorted by numerous seamounts without a clear reflection in the moats, where a mixture of volcanic rocks and clastic material is likely deposited. This reduces the impedance contrast between sediments and igneous crust (Grevemeyer et al., 2001) and hence, the exact thickness of the sediment layers and the upper oceanic layer 2 is difficult to determine.

The next three layers have velocities (4.2–4.8, 4.8–5.8 and 6.1–6.5 km/s) and gradients characteristic for oceanic layer 2, which consists of pillow basalts and sheeted dikes. The usual thickness is 1.5–2 km, however, along our profile we find an anomalous thickness of 6 km. The lower crust in the west is characterized by velocities and gradients typical for the gabbroic oceanic layer 3 (6.5–7.2 km/s), but is likewise unusually thick (15 instead of 5 km). The crust-mantle boundary
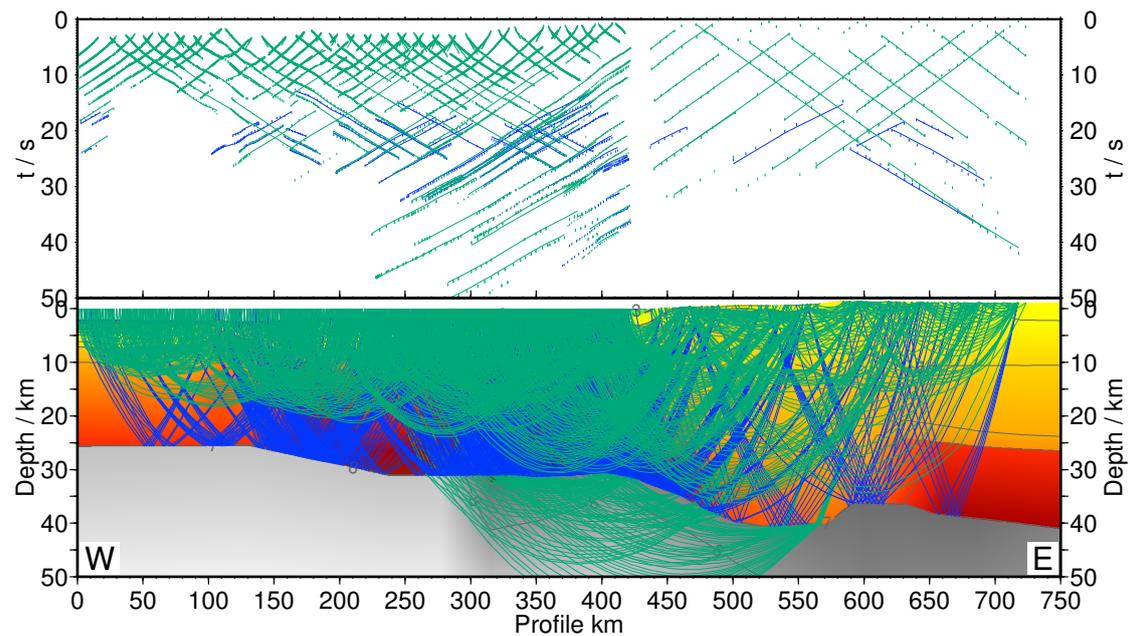
Figure 3.3.11:   Travel time fit (top) and ray coverage (bottom) for the final model. Refracted phases are shown in green, reflections in blue. The ray coverage is a good estimate for the quality of a model and reveals poorly sampled areas, e.g. the lower crust at the western end of the profile (km 0-150), which is solely sampled by crust-mantle reflections.

(Mohorovičić discontinuity or Moho) at 22 km depth below the basement is only sparsely constrained by reflections (PmP-phases). Refracted phases in the upper mantle (Pn-phases) are not observed in this part of the profile. A data example illustrating the typical characteristics of this western profile section is shown in Fig. 3.3.3.

Even though the igneous crust is three times thicker than normal oceanic crust, the thickness ratio between layer 2 and 3 has not changed (6 km/15 km = 2 km/5 km) and we interpret this section of the profile as thickened oceanic crust.

Transitional zone (km 180 to 420)   This part of the transect shows distinct differences from the western section. The most remarkable is the high velocity body in the lower crust (HVLCB), but also the upper crust and sediments have different characteristics. Figures 3.3.4 to 3.3.6 show data examples for this area.

The topography changes and water depth decreases in steps from 2000 m to 140 m with two relatively level areas at water depths of 1400 m and 400 m, respectively. The three sediment layers thicken to 3.0 km towards the coast. Seismic reflection data show more continuous horizons with distinct internal layering and multiple bands of reflectors. The sediment cover on top of the seamounts is generally increasing towards the coast. While the western seamounts cut through the sediment layers and occasionally crop out at the seafloor (km 40, 110), the
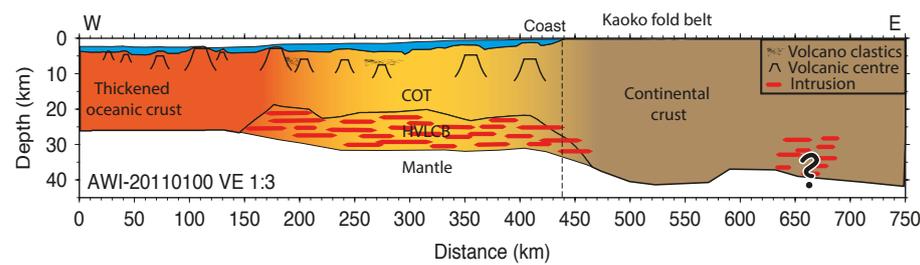
Figure 3.3.12: Geological interpretation of the presented profile. Drawn volcanic centres are based on seismic reflection data and the final velocity model. The blue layer summarizes sedimentary layers.

seamounts east of km 220 are completely covered by up to 1.5 km thick, undisturbed sediments following the contours of the underlying basement topography. Their shape also changes and becomes flat topped appearing like guyots (at km 240 and 280). Other studies (Gladczenko et al., 1998; Elliott et al., 2009) propose that this part of Walvis Ridge erupted subaerial or in shallow water (Bolli et al., 1978). Our data confirms this by showing that the seamounts were heavily eroded by waves during their subsidence below sea level.

The seismic velocities of the uppermost part of the igneous crust are in the same range as in the westernmost part of the transect, but show much stronger lateral velocity variations (3.8 – 5.0 km/s). In addition, some stations indicate a velocity inversion, expressed in a discrete time gap of the first arrivals. Those areas are laterally confined to narrow zones and no reflections constrain velocities or the layer thickness for this areas. They might be caused by lava flows (with high velocities 5.3 km/s) covering older sediment layers or hyaloclastic material with lower seismic velocities.

Velocities of the lower crust are higher than in the western part of the profile (up to 7.5 km). Those high velocities are not directly constrained by refracted phases, as refractions usually do not reach the lowest part of the lower crust, due to the low gradient. But the apparent velocities in this area are higher than in the westernmost part of the profile (7.2 instead of 7.0 km/s) as well as PmP move outs (6.8 km/s instead of 6.4 km/s). The Moho topography is flat and does not mirror the rough basement topography with its numerous seamounts. Upper mantle velocities of 7.9 km are mainly based on Pn phases observed on the land receivers, which recorded the airgun shots at offsets well beyond 200 km.

The high velocity lower crustal body (HVLCB) is 250 km long, 12 km thick and the crystalline crust thickens to 28 km. Other studies also observed such HVLCBs south of Walvis Ridge (Bauer et al., 2000; Hirsch et al., 2009). Their velocities range between 7.6 and 7.4 km/s, respectively. The nature, petrology and evolution of these HVLCBs, in general, is still debated. They appear along volcanic passive margins in the continent-ocean transition zone (COT) and haven been interpreted as accreted mafic material underplating stretched, rifted and heavily intruded continental crust (White et al., 1987) or as intrusions of igneous
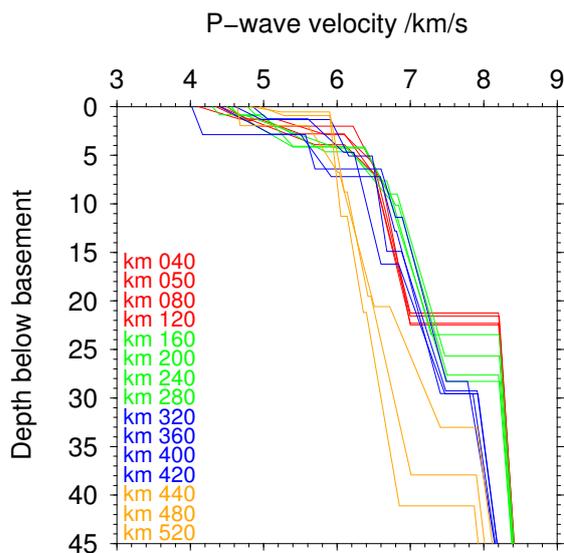
Figure 3.3.13:   Velocity depth plots for selected profile locations. There is no clear transition between continental and oceanic crust visible. Profiles at positions larger than km 440 show decreased velocities in the upper part indicating continental crust. The lower crust however is characterized by high velocities of the HVLCB. Profiles at kilometres less than km 160 have typical gradients for oceanic crust, but with unusual thickness. The crust between km 160 and 420 is affected by the high velocities in the lower crust and km 320–480 reveal large lateral velocity variations in the upper crust without obvious trends.

sills in continental crust without an accreted underplating (White et al., 2008). Opposing those interpretations, which require continental crust, Bauer et al., 2000 suggested that the transitional zone and the HVLCB are entirely composed of igneous material. HVLCB have also been observed independent from continental margins at oceanic plateaus and hot spot tracks. There, they might be explained with fractionated cumulates from picritic mantle melts (Farnetani et al., 1996).

In our model, the abundant seamounts, the strong lateral variations in velocities and gradients in the upper and middle crust, in addition to the high velocities in the lower crust prevent a clear interpretation about the origin of the crust and an exact location of the continent-ocean boundary (COB). We interpret this section as the transition between continental and thickened oceanic crust. It is highly affected by volcanism, but intruded continental blocks might still be present and mixed with entirely igneous parts of crust.

Continental crust (km 420 to 720)   At km 420 the seismic velocities abruptly slow down to 5.3 - 5.9 km/s in the upper crust and to 6.3 - 6.7 km/s in the middle crust, which are typical velocities and gradients for continental crust (Christensen and Mooney, 1995). The HVLCB stretches eastwards approx. 30 km into the continental crust before it abruptly terminates and velocities decrease to normal values for lower continental crust (6.9 km/s). The eastern termination of this

HVLCB roughly coincides with the seaward edge of the Kaoko fold belt, a 590–550 Ma old coast parallel orogen that formed during the amalgamation of Gondwana (Foster et al., 2009). The crust-mantle boundary at 40 km is at a similar depth as further south (Bauer et al., 2000), decreases to 36 km at km 610, where the mountain range of the Kaoko belt meet the plains of the Etosha pan. Further east, at km 650, we added an high velocity body in the lower crust. This area of the profile is not well constrained and and the interpretation of travel time arrivals is ambiguous. We observe reflections from a shallow reflector at two stations (st 24, 27), which are in conflict with reflections from other stations (st 22, 23) covering the same area. Gravity modelling indicates thats there is an intrusive high density body within the crust and we interpret the shallow reflections to originate from the top of this intrusion and not from the Moho. The slight decrease in crustal thickness landwards of the Kaoko fold belt is confirmed by another seismic profile (Planert et al., 2013) and seismological data (Heit et al., 2015). We interpret the thicker crust under the Kaoko belt as the crustal root of this fold belt.

In this part of the transect, we observe only a small section with unusually high velocities in the lower crust. Large scale intrusions or rifted and thinned continental crust are absent, instead, the crust remains mainly undisturbed and the crustal root of the Kaoko fold belt is left intact.

3.3.4 Gravity modelling and results

After the seismic modelling we conducted a 2D gravity modelling to verify that the crustal structure is consistent with observed gravity anomalies.

We used satellite derived free air data for the offshore part of the profile (Sandwell and Smith, 2009) and Bouguer data for the onshore section (Pavlis et al., 2008). The free air anomalies range between -10 and +70 mGal with various short wavelength undulations. The Bouguer anomalies drop from +20 mGal at the coast to -110 mGal beneath the Kaoko fold belt before rising to -90 mGal at the eastern termination of the profile. The initial gravity model was derived from the geometry of the final seismic model and densities, which we calculated from the velocities with the empirical Nafe-Drake curve (Ludwig et al., 1970). We kept the model as simple as possible and merged the sediments into one layer. For areas with large lateral variations we divided the seismic layer into smaller polygons. If seismic layers were not constrained by reflection, we changed the geometry to match the converted density distribution. For example, we modified the upper boundary of the high velocity/density body in the lower crust. Interestingly, we cannot determine the extend of the high density body from the free air anomalies. There is no significant drop in the anomaly level at its sea- or landward termination.

The free air anomalies are dominated by short frequency variations which are well matched and originate in the buried basement topography. Larger deviations of the modelled and observed gravity data are in the region of continent-ocean transition from km 320 to 470, which could not be matched in the short wavelength. The large drop in the Bouguer data within km 430 and 600 is well matched and
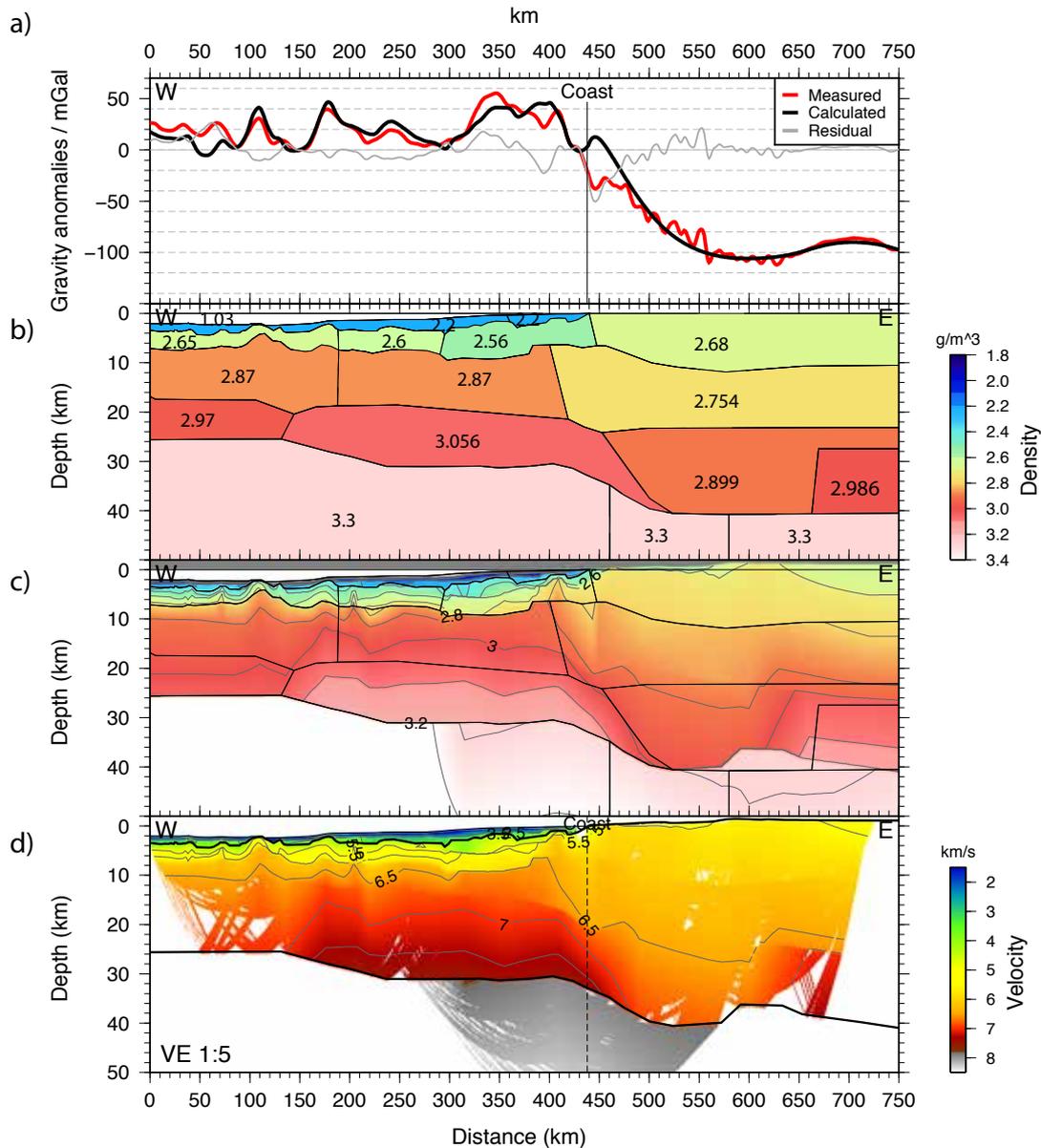
Figure 3.3.14:   Gravity model for profile 100. a) The observed free air satellite and Bouguer data (Sandwell et al., 2014; Pavlis et al., 2008), the modelled gravity data and their deviation. b) The final density model. c) Comparison between the density distribution directly converted from the P-wave velocity model and the geometry of the density model. d) The seismic P-wave velocity model.

caused by the generally lower density of continental crust.

A major miss match between the seismic and the gravity model occurred at the eastward end of the profile at km 600-650. Here, the initial velocity model showed a dramatic decrease in crustal thickness, which was inconsistent with reasonable densities. We therefore reviewed the seismic model and introduced an intrusive crustal body instead of a strong decrease in crustal thickness. The reflected phases, which originally gave rise to this crustal thinning, might be interpreted as reflections from the top of the intrusive body. Nevertheless, we could not completely keep the structural geometry of the seismic model and ascribe that to the large offsets of the station geometry from the 2D profile line and 3D effects. This offsets already caused inconsistencies in the seismic model within the problematic area. Additionally, the ray coverage is sparse.

3.3.5 Discussion

Our study provides a first insight into the deep crustal structure along the axis of Walvis Ridge, revealing the composition of the crust and its variations towards the Namibian coastline. Walvis Ridge has long been interpreted as a hotspot track (Morgan, 1971). In detail, though, while the bathymetry of its western part can easily be interpreted in terms of a volcanic lineament or seamount province, the origin of the massive eastern Walvis Ridge close to the Namibian coast and the nature/position of the continent-ocean transition and boundary are still debated. The position of the COB is important for paleogeographic and plate kinematic reconstructions of the South Atlantic. A better understanding of the eastern Walvis Ridge will also constrain processes driving continental breakup, e.g. how severe the proposed plume impact/thermal anomaly modified the continental crust.

The crustal composition of the eastern Walvis Ridge   Our data and model show that the eastern Walvis Ridge, even though it is a massive bathymetric feature, consists of thickened oceanic crust with a prolongation of the western seamount chain buried under thick sediments. Seamounts can be identified up the coast and their width is inversely proportional to the distance from shore (Fig. 3.3.15). We can interpret the width of the seamounts as an indicator for its total size and volume and, therefore, for the hotspot activity. Thus, the hotspot activity weakens and the melt supply wanes in the oldest part of Walvis Ridge. This is in line with previous observations of a decreasing melt production in the western guyot province (Gallagher and Hawkesworth, 1994).

Comparing the crustal structure of our profile with other hotspot derived ridges is difficult because of the profile orientation. Our profile extends along the ridge axis, but commonly deep seismic profiles cross ridges and, thus, do not reveal variations along the ridge axes. The only analogous region to Walvis Ridge at which deep seismic profiles have been acquired along the ridge axis is the junction of the Iceland-Faroer Ridge with the continental Faroer Islands (Richardson et al., 1998). Unlike in our profile, there is no evidence of individual volcanic centres and the whole ridge has a more pancake-like structure. This difference might be
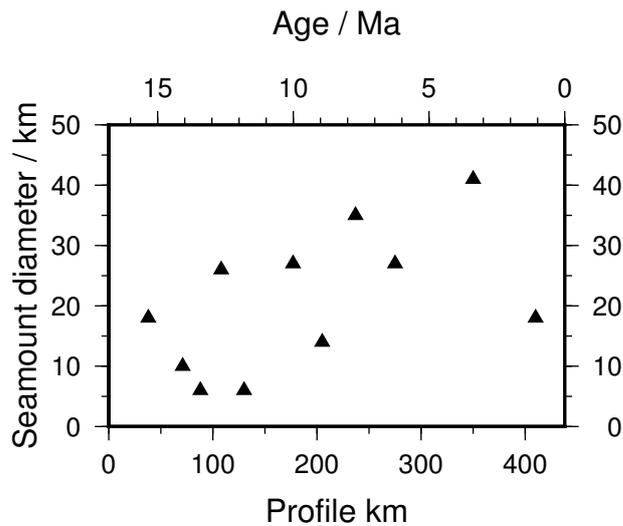
Figure 3.3.15: Seamount size as a function of profile kilometre. We can observe a general decrease in volcanism increasing distance from shore. Taking the age progression of 26 km/Ma (O'Connor and Jokat, in prep) into account, a rough calculation yields a decrease of 2 km/Ma in seamount width.

explained with the different levels of magmatic activity. High melt supply causes fissure eruptions while low melt supply causes point source eruptions (Behn et al., 2004). The Tristan hotspot is less productive than the Iceland hotspot (Gallagher and Hawkesworth, 1994; Ito et al., 1996) and, therefore, might have produced distinct volcanic centers instead of a massive single body.

The crustal composition of the eastern Walvis Ridge and the location of a COB was not yet clearly determined. A location of the COB, defined as the onset of magnetic spreading anomalies and an anomalous gravity high (Rabinowitz and LaBrecque, 1979), is not possible because of the absence of sufficient data to show such magnetic lineations (if existent) and a clear gravity high on the ridge. Previous interpretations of seismic reflection data do not reveal a consistent location of a COB (Sibuet et al., 1984; Gladczenko et al., 1998) and a considerable amount of continental crust was suspected at the eastern Walvis Ridge (Sibuet et al., 1984). Our data do not show a clear COB based on changes in the crustal velocities, due to massive volcanism affecting the crust of the eastern Walvis Ridge. However, they do reveal a 200 km wide COT with increased thickness, surface volcanism and high velocities in the lower crust. The suggested COB locations (Sibuet et al., 1984; Gladczenko et al., 1998) fall within this range. Here, continental crust might be partially present but based on the amount of volcanic features and velocities typical for basaltic material we interpret this transitional zone to consist mainly of igneous material. Similar results with thickened igneous crust forming the COT were found south of Walvis Ridge along the continental margin (Bauer et al., 2000; Schinkel, 2006; Hirsch et al., 2009). The onset of oceanic, or thickened oceanic crust in case of the Walvis Ridge, is at approximately the same distance from shore for all profiles.

In comparison to the ~ 60 km wide COT in the North Atlantic (Richardson et al., 1998), the observed ~ 200 km COT along the southern South Atlantic margin is much wider suggesting differences in the rifting mechanism.

Indications for a plume head? The most prominent feature of our velocity model is the high velocity lower crustal body with velocities up to 7.5 km/s, 12 km thickness and 290 km width. In this section we will discuss the origin of this HVLCB as part of a large igneous province, its implication for the classic plume theory and the continental breakup process.

High seismic velocities in the lower crust and SDRs are typical of volcanic margins and have been observed along both South Atlantic conjugate margins south of Walvis Ridge. Together with the continental flood basalts of Paraná and Etendeka they form a large igneous province, which is characterized by the emplacement of a large volume of magma within a short period of time ($> 0.1 \cdot 10^6$ km^2 within $1 - 5$ Ma, Bryan and Ferrari, 2013). According to the classic plume theory, LIPs are the products of melt that is supplied from a deep thermal mantle plume. During the ascent from the core mantle boundary, it develops a large mushroom-shaped head, which flattens upon reaching the lithosphere-asthenosphere boundary. Melts generated within start to intrude the lithospheric mantle. Parts of this melt reach the crust-mantle boundary and crystallizes there forming areas with high seismic velocities (HVLCB). Other parts reach the surface and form flood basalt provinces and SDRs (Farnetani et al., 1996; Ridley and Richards, 2010; Richards et al., 2013). Seismic data support this model for oceanic LIPs, but the presence of high velocities under continental flood basalts is indistinct. While the Columbia River, Deccan and Siberian flood basalts all appear to be underlain by high velocity (6.9–7.5 km/s) bodies, the Emeishan flood basalts seems to lack fast lower crust at its rims (Ridley and Richards, 2010). The spatial extend of plume-derived magmatism is proposed to be related to the flattening of the plume head at the base of the lithosphere across a large area. Based on the distribution of surface volcanism, White et al., 1987 estimated a diameter of 1000–2000 km for the plume head, Griffiths and Campbell, 1990 suggested 2000–2500 km. Theoretical analysis of mantle heat fluxes and viscosities led Tan et al., 2011 to estimate that the flattened plume might affect the lithosphere over a distance of 1173–1842 km centred on the plume conduit. However, such large structures have never been detected in seismic tomography of the lithosphere-asthenosphere boundary. This is just one of the reasons why the deep plume model is controversial. Alternative models associate some or all hotspot volcanism with decompression melting (Raddick et al., 2002), stress release (Fairhead and Wilson, 2005; Elliott et al., 2009) or small-scale mantle convection (King and Ritsema, 2000) meaning that the magmatism is fed by shallow sources.

The eastern Walvis Ridge is at a key position, linking the first appearance of the plume tail derived seamount chain to the plume head related continental flood basalts. This special location right above the proposed conduit discriminates Walvis Ridge from the rest of the continental margin and makes it ideal to
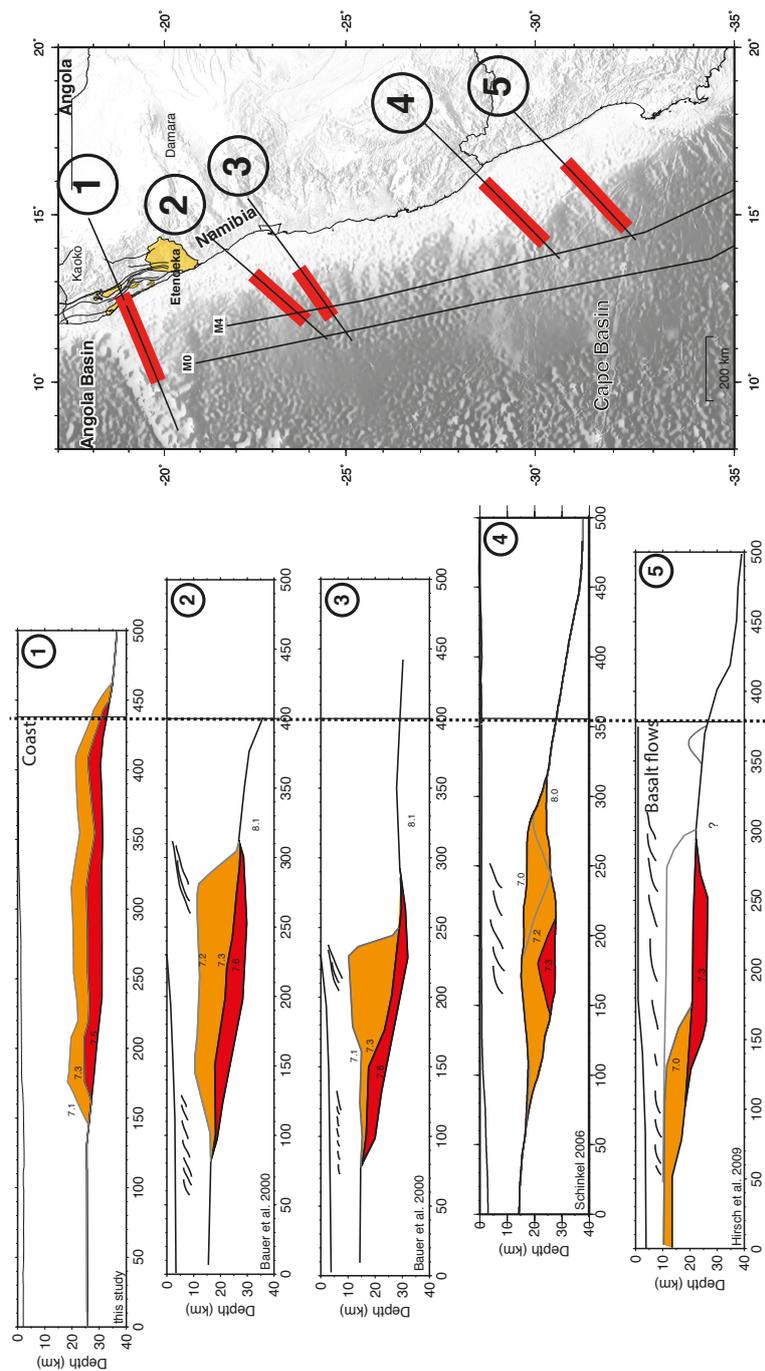
Figure 3.3.16:   Comparison of velocity models along the southern African continental margin arranged from north to south. Areas with velocities > 7.3 are coloured red and orange marks the boundary of the authors interpretation of the high velocity bodies (HVLCB) and varies between 7.0 and 7.2. Dipping lines denote SDR sequences. The map on the right hand side shows the profile locations and positions of HVLCB. Note that the western termination of the HVLCB along our profile (1) is at a similar distance from shore than south of the ridge. But it intrudes around 100 km further into the continental crust. Additional, it terminates at a long N-S trending fault, which Foster et al., 2009 identified as extensional.

investigate the effect of the proposed plume head. The most remarkable difference between our profile and profiles south of Walvis Ridge (Fig. 3.3.16, Bauer et al., 2000; Schinkel, 2006; Hirsch et al., 2009) is the extent of the HVLCB. The seaward extent of the HVLCB along our line does not differ from the southern profiles and is approx. 300 km west of the coastline on all profiles, whereas the landward boundary of our profile lies further east. As a result, the HVLCB along our profile clearly underlies continental crust. Also, the HVLCB is between 100-130 km wider than the southern HVLCB, which means that the intruded and therefore plume affected area at the Walvis Ridge is only 100-130 km wider (Fig. 3.3.16). An independent deep seismic experiment confirms the presence of the observed HVLCB within the continental crust and furthermore reveals a surprisingly narrow width of ∼100 km (Ryberg et al., 2015). While the size of a plume head is estimated to be rather large, the size of the observed HVLCB below Walvis Ridge is unexpected small and indicates only a local influence of the plume head. Moreover, the thermal anomaly seems to be too weak to have significantly modified the old African continental crust leaving the mountain root of the Kaoko fold belt intact. By combining the geometry of the intruded crust with our findings of a sediment covered seamount chain buried at the eastern Walvis Ridge, we suggest that the HVLCB within the continent crust is part of the hotspot trail and not the signature of a large plume head. We conclude that no large plume head was present during the initial rifting phase. Therefore, it is unlikely that the Tristan plume was the main driving force for the South Atlantic opening.

A new breakup scheme   The emplacement of many LIPs in close temporal proximity to episodes of continental breakups (Morgan, 1981) implies a causal relationship (Burke and Dewey, 1973; White and McKenzie, 1989; Hill, 1991; Courtillot et al., 1999). Several weakening processes are ascribed to plumes: the mechanical effects of plume head impingement, erosion of the thermal boundary and lithosphere as well as heating of the overlaying mechanical boundary (Courtillot et al., 1999). The arrival of a plume head has been interpreted as trigger and an active driving force for continental breakup (Morgan, 1971; Richards et al., 1989; Courtillot et al., 1999). However, taking our results into account, the limited size of the modified continental crustal area makes it unlikely that such weakening processes might have affected a large enough area to drive continental breakup in the South Atlantic.

An alternative to the 'active' plume model is the 'passive' plume model. Here, the plume produced melt ponds at the lithosphere-asthenosphere boundary without eroding the overlaying lithosphere and merely utilizes pre-existing weak zones for migrating to the surface (White and McKenzie, 1989). The distribution of surface volcanism and intruded lower crust onshore in Namibia partly supports this model: The northern Etendeka flood basalts overlie the intruded lower continental crust and crop out as N-S oriented elongated structures parallel to or coincident with major regional fault systems (Fig. 3.3.1, faults after Foster et al., 2009). Thus, these faults likely provided the main pathways for melt migration to
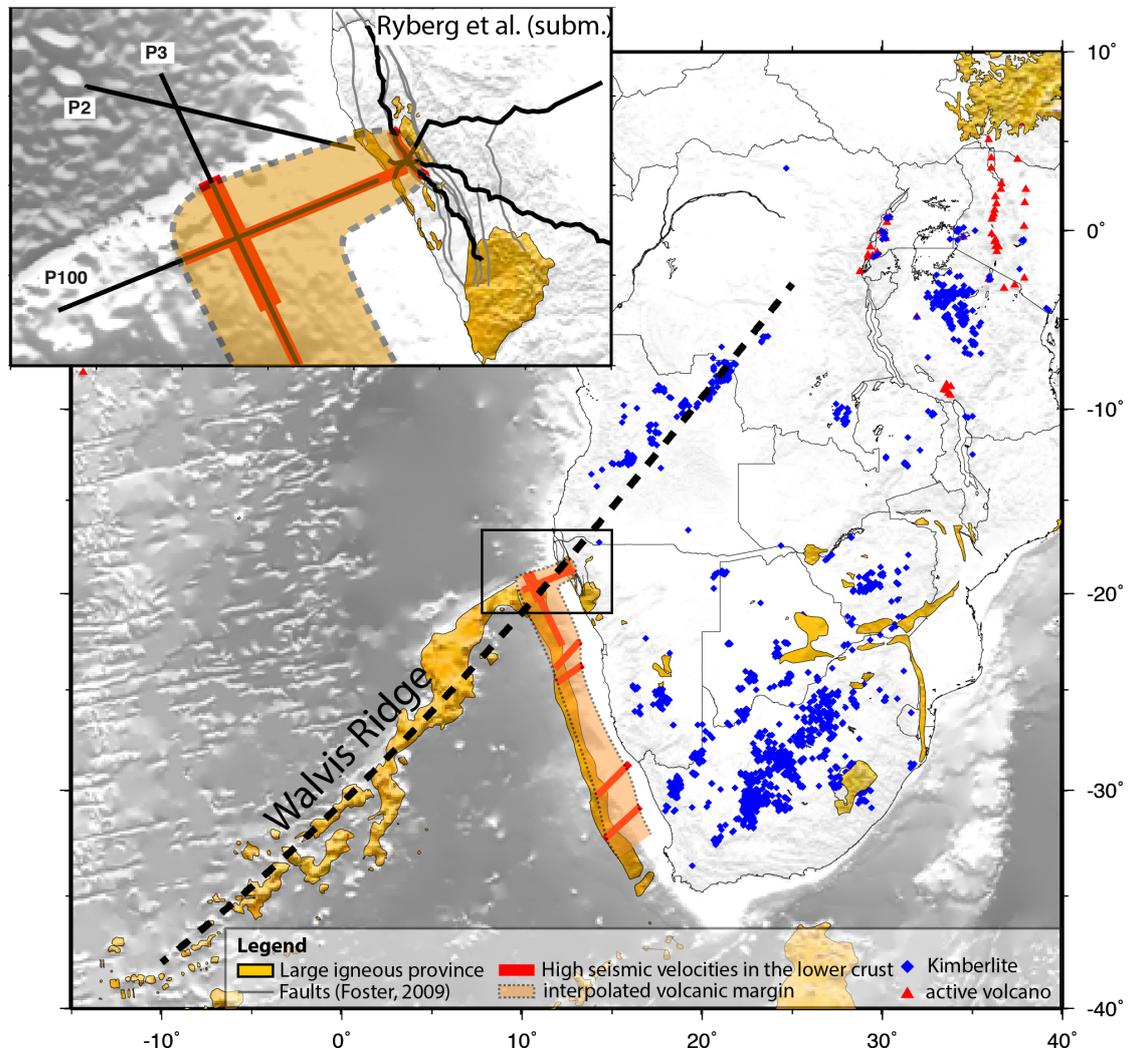
Figure 3.3.17: Distribution of magmatic rocks in Africa. Kimberlites in onshore prolongation of the axis of Walvis Ridge indicate the presence of an anomalous melt source prior to the emplacement of Walvis Ridge. The inset shows the distribution of high velocity lower crustal body at the intersection of the Walvis Ridge with the continent. Crustal structures of the other profiles are published in Ryberg et al., 2015 and Fromm et al., in review.

the surface after the plume arrival. But interestingly, the faults are much longer than the observed volcanic structures. The flood basalts at the surface might have been eroded, but the lower crustal structure represents the original distribution of anomalous mantle material. If the melt utilizes existing crustal faults, those weak structures control the amount and location of volcanism. Thus, if we assume that the plume head material had ponded at the LAB and erupted along weak zones we would expect the intruded area to cover the total length of the fault zones. The 'passive' model fails to explain why the intrusions are confined to a small area at the landfall of Walvis Ridge in the presence of a large plume head and existing weak zones.

So far, our observations of the mainly unaltered continental crust do not support the existence of a huge plume head in the South Atlantic. O'Connor et al., 2012 suggested an alternative to a single large plume and explained the parallel age progression of South Atlantic Hotspot chains (Tristan, Discovery, Shona, Bouvet) with sheet-like upwellings of deep mantle material, which splits into several smaller plumes at higher levels. Consequently, no huge single plume head is formed and the area of expected plume influence is significantly reduced. But also in this case, the initial onshore volcanism (marking the plume head) should be larger than the later (tail-derived) offshore volcanism which is not in agreement with our observations.

We propose a breakup model, where the Tristan hotspot was already present beneath the African craton before the time of Walvis Ridge inception and marked its trace by kimberlite pipes in Angola (Fig. 3.3.18). The prolongation of the seamount chain up to the African coast in conjunction with the absence of a similar continuous feature between the South American continental margin and the Rio Grande Rise indicate a hotspot location on the African plate during the early opening of the South Atlantic. Further support comes from recent seismological data. Heit et al., 2015 located unusual high Vp/Vs ratios in prolongation of the Walvis Ridge and interpreted them as mafic underplatings, which might be related to the Tristan plume track. The intruded continental crust we found at the landfall of Walvis Ridge and in prolongation of the seamount chain supports the existence of the hotspot underneath Namibia during the initial rifting. Furthermore, active hotspots have long been associated with kimberlite occurrences in continental crust e.g. Crough et al., 1980; Torsvik et al., 2010; Griffin et al., 2013. Such kimberlites cluster along lines across the African craton and a clear lineament extends the axes of the Walvis Ridge indicating an existing anomaly prior to the emplacement of Walvis Ridge (Fig. 3.3.17). The hot material might have ponded at the lithospheric base and produced low volumes of melts beneath local zones of thinner lithosphere (Sleep, 2006; Griffin et al., 2013). Existing faults and weak zones in the crust and lithosphere near the thermal anomaly might then have provided vents, creating kimberlite pipes along the hotspot path, but the strong continental crust/lithosphere of the African continent suppressed massive volcanism. Once the rifting started, new deep reaching crustal faults formed at the line of breakup allowing increased ascend of ponded melt (forming the volcanic margins) and massive outpourings of magma, which formed the large igneous provinces of
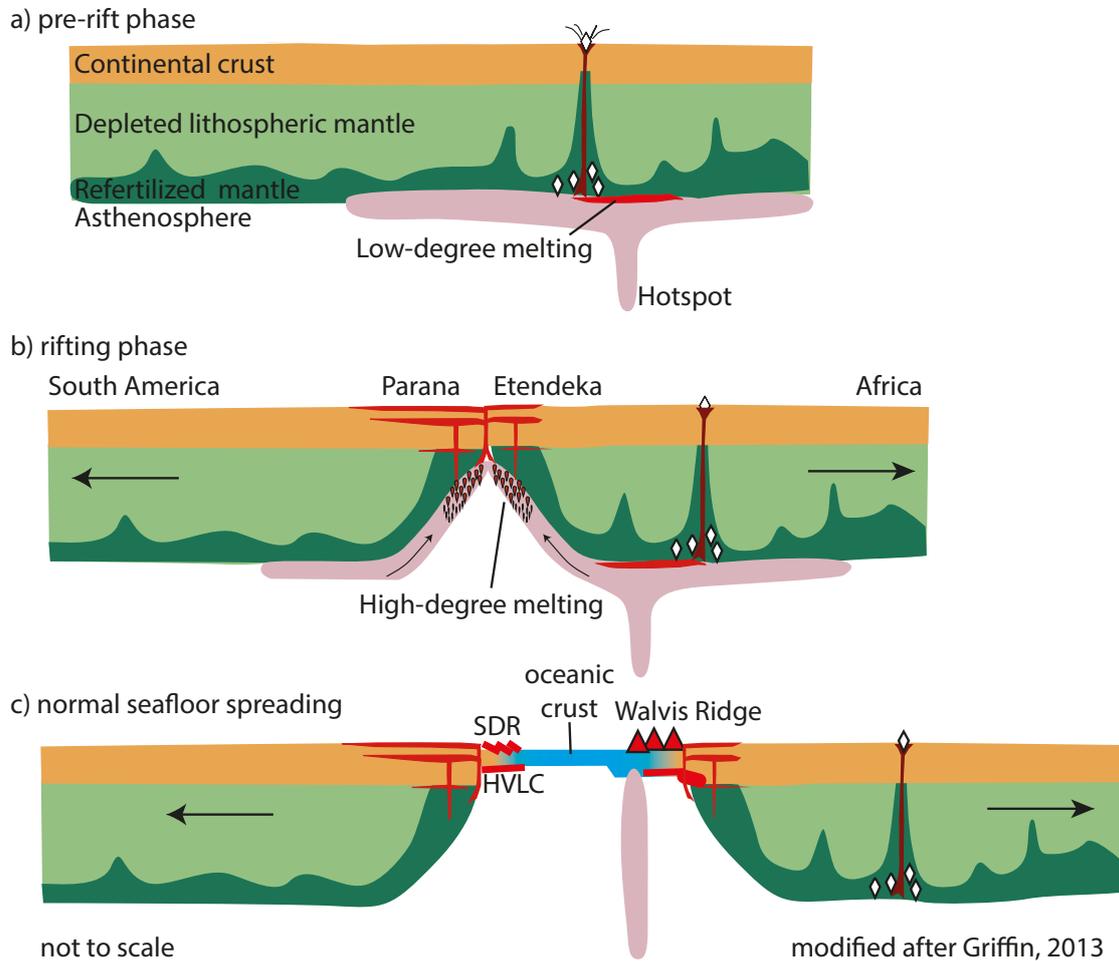
Figure 3.3.18: Sketch of the proposed breakup model.
a) The thermal anomaly existed prior to the rifting and formed low degree melts at the hotspot location. Lithospheric structure focused intrusions at thinner areas and large faults allowed venting to the surface, thus marking the hotspot trail by Kimberlite intrusions.
b) Plate boundary forces stretched the lithosphere and initiated rifting. Large volumes of melt formed by decompression melting at the thinned areas, erupted at the surface emplacing the large flood basalt provinces of Paraná and Etendeka and formed the volcanic margins with their high seismic velocities in the lower crust (HVLC) and seaward dipping reflector sequences (SDR).
c) Further plate movement over the hotspot formed the thickened oceanic crust with its single volcanic centres along the Walvis Ridge.

Paraná and Etendeka. After the beginning of seafloor spreading, young and weak oceanic crust moved over the hotspot location and allowed the formation of the massive volcanics of Walvis Ridge. In such a setting, a plume head is entirely unnecessary.

3.3.6 Conclusions

We presented a P-wave velocity model along the axis of Walvis Ridge with prolongation on the African continent. We found thickened oceanic crust of 22 to 28 km at the ridge and a 130 km wide continent-ocean transition zone underlain by high velocities up to 7.5 km/s in the lower crust. These high seismic velocities are interpreted as basaltic intrusions and associated with hotspot magmatism at the onset of rifting. It reaches approx. 100 km further into the continental crust than HVLCBs detected south of Walvis Ridge and terminates at the crustal root of the Kaoko Fold belt. We interpret the excess size as the direct result of the profile location being right above the hotspot. However, we find the remaining continental crust unaffected by intrusions and, surprisingly, the Kaoko root is not eroded. Regarding the model of plume triggered continental breakup we estimate the affected area to be too small to drive the breakup of the South Atlantic and cannot observe the large amount of magmatism expected from a plume head arrival. We rather propose that existing weak zones were utilized for magma migration to the surface. Furthermore, we suggest that the hotspot was already active before the initial rifting stage, therefore, no plume head arrived during the breakup. The large amounts of melt accumulated beneath the thick cratonic lithosphere until rifting opened new migration pathways and massive volcanism formed the large igneous provinces.

3.4 Interaction between hotspot and fracture zone: The crustal structure of Walvis Ridge at 6°E

The Walvis Ridge is a prominent bathymetric feature and one of the major hotspot trails in the South Atlantic. In this study we present a P-wave velocity model of the deep crustal structure of the eastern Walvis Ridge derived by forward modelling. A 480 km long profile consisting of 27 ocean bottom stations crosses the ridge at 6°E. Surprisingly the Walvis Ridge is not northerly bound by the Florianopolis Fracture Zone but continues into the Angola Basin, where a basement high is present and thick basaltic layers cover older oceanic crust and the fracture zone. Crustal velocities range from 4.4–5.6 km/s in the upper crust, the slower velocities are located at the ridge crest. We observe two crustal roots along the profile: one is located beneath the ridge crest, the other one beneath the northern basement high. The crustal thickness reaches 18 km at the crest and 12 km beneath the basement high. The corresponding lower crustal velocities are 7.2 km/s and 7.4 km/s, respectively. The bathymetric expression of the ridge along the profile is less pronounced than closer to shore. This is mainly attributable to the absence of a thick layer of volcanic debris, rather than to reduced crustal thickness below the basement surface. Therefore, this part of the ridge was never or only briefly subaerially exposed. The basalt layer on top of the fracture zone and the large distance of 100 km between the fracture zone and the centre of the ridge suggest that the ridge and the fracture zone formed independently of each other. This contradicts the alternative origin hypothesis of the Walvis Ridge having formed as a leaky transform fault. The oceanic crust north of the fracture zone, which is buried underneath the basalt layer, is younger than the reconstructed age of hotspot volcanism of the Walvis Ridge. We therefore interpret this structures north of the fracture zone as a product of late stage volcanism and propose that it is part of Walvis Ridge.

3.4.1 Introduction

The Walvis Ridge is one of the most striking bathymetric features of the South Atlantic, rising more than 2000 m above the surrounding seafloor (Fig. 3.4.1). This volcanic ridge stretches SW away from the African continent for over 3000 km to the islands of Tristan da Cunha and Gough near the Mid-Atlantic Ridge. The eastern part of the ridge (east of 3°E) is a continuous, massive structure, whereas the western part is a widely distributed guyot province with loosely connected ridges and scattered seamounts forming a frayed lineament. The entire ridge shows a linear age-progression (O'Connor and Duncan, 1990; Rohde et al., 2012) starting with Cretaceous volcanism at its junction with the African continental margin. The onset of this volcanism is interpreted in close connection with the opening of the South Atlantic and the emplacement of continental flood basalts at approx.
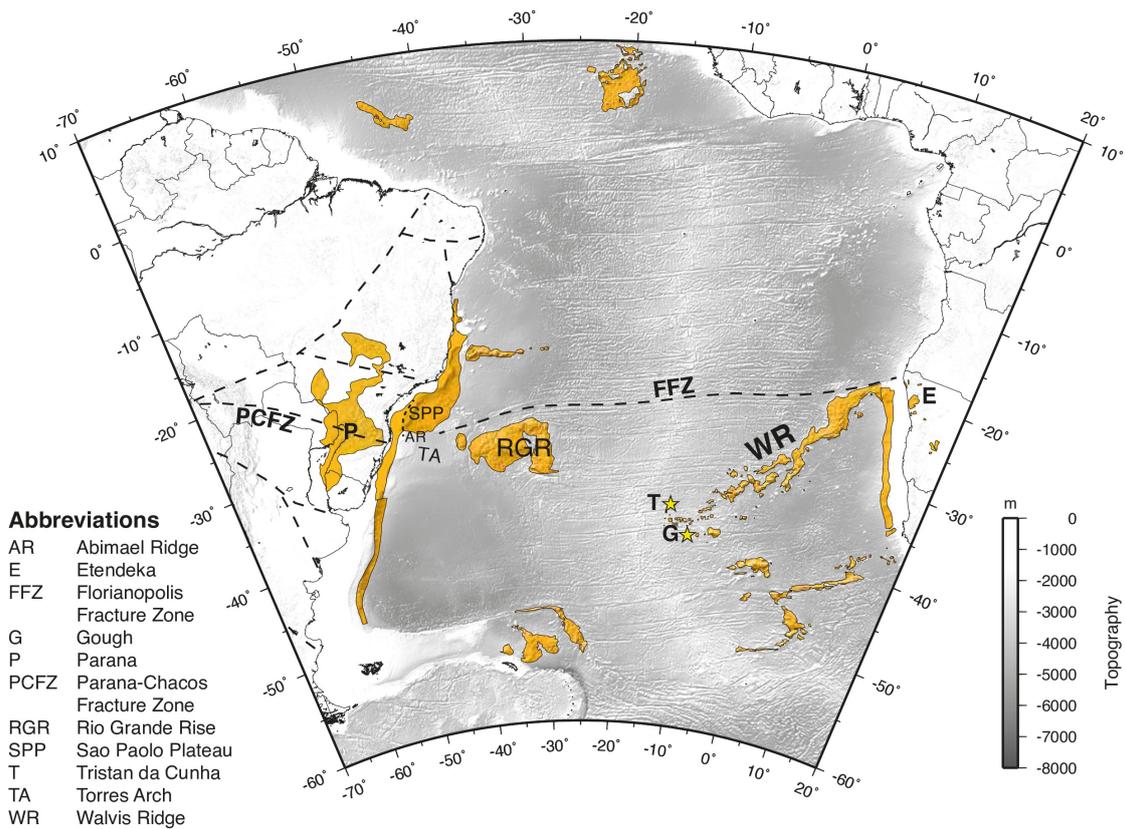
Figure 3.4.1: General map of the South Atlantic with main structures and igneous features (orange, after Coffin et al., 2006). Transformation zones are indicated by dashed lines.

132 Ma (Renne et al., 1996).

The conjugate South American plate shows corresponding volcanic features, although a massive, elongated ridge like the Walvis Ridge is missing and the volcanic structures have a different shape. The Torres Arch is the conjugate structure to the eastern Walvis Ridge and connected to the large Rio Grande Rise via an indistinct bathymetric high. Both structures (Walvis Ridge and Rio Grande Rise) form the conjugate trails of the present day Tristan hotspot (Morgan, 1971). The variable sizes and shapes of the volcanic provinces are explained with reference to the changing relative positions of the hotspot and the Mid-Atlantic Ridge (O'Connor and Duncan, 1990). The Torres Arch, Rio Grande Rise and the eastern Walvis Ridge were formed when the hotspot was close to or at the Mid-Atlantic Ridge. Between 80 and 60 Ma, the Rio Grande Rise and its conjugate, the N-S oriented part of Walvis Ridge at 5°E, might have been emplaced as large igneous province similar to Iceland today. This section of Walvis Ridge lacks the age progression, implying that it developed as a product of large scale eruptions covering a broad region (O'Connor and Duncan, 1990). In contrast, the western seamount province of Walvis Ridge formed within the interior of the African plate, when the Tristan hotspot was well separated from the Mid-Atlantic Ridge. Therefore, no corre-

sponding volcanism occurred on the South American plate. The Walvis Ridge and the Rio Grande Rise are a classical example for hotspot related volcanism (Morgan, 1971).

However, some observations are not consistent with predictions of the hotspot model and alternative tectonic models for the origin of Walvis Ridge exist. Hotspots should form age progressive volcanic chains with active volcanism occurring only at or near the hotspot location. In contrast to this prediction, earthquake swarms in the western seamount province of Walvis Ridge have recently been interpreted as volcanogenic explosions. The large distance to the hotspot location ($\sim$780 km) requires either a much larger reach of the hotspot as anticipated or a different origin for this volcanism (Haxel and Dziak, 2005).

As an alternative, Fairhead and Wilson, 2005 proposed that changes in intra-plate stress triggered the excess magmatism of the Walvis Ridge. In this model, fracture zones play an important role as they separate regions of contrasting stress fields and are locations of intra-plate stress release. The eastern Walvis Ridge is located directly south of the Florianopolis fracture zone (Fig. 3.4.1, FFZ; also referred to elsewhere as Rio Grande fracture zone, e.g. Cappelletti et al., 2013; Heine et al., 2013). The FFZ merges towards the west with the continental Paraná-Chacos shear zone, a line of major deformation prior and during the breakup (Moulin et al., 2010, and references therein). The FFZ might have had an extensional component during the initial opening forming a short lived spreading ridge with increased magmatism building the Walvis Ridge (Elliott et al., 2009). The FFZ and the Walvis Ridge mark a major boundary between the volcanic and non-volcanic passive margins along the African continent.

Numerous studies have focused on the nature of the volcanic margins of South America and Africa, and yet data revealing the structure of Walvis Ridge and Rio Grande Rise do not exist. Here, we present a deep seismic profile acquired 600 km west of the Namibian coast providing information on the crustal fabric underlying a topographically subdued part of Walvis Ridge. This profile offers the opportunity to gain new insights into the origin of Walvis Ridge (with regard to the competing origin hypothesis), the evolution of the Tristan hotspot and the interplay of hotspots with fracture zones. These results will be compared with a more easterly N-S line acquired across a topographically more pronounced part of the Walvis Ridge (P3, Fig. 3.4.2).

3.4.2 Seismic data

The acquired seismic refraction data are part of a larger geophysical experiment conducted by the Alfred Wegener Institute, Helmholtz Zentrum für Polar and Meeresforschung, Bremerhaven (AWI) in January 2011 with the research vessel Maria S. Merian (MSM 17/2) in close cooperation with Geomar, Kiel and the Geoforschungszentrum, Potsdam (GFZ). Multidisciplinary studies in this experiment, including seismological and magnetotelluric experiments, investigated the junction of Walvis Ridge and the African continent both with ocean bottom seismometers and recording stations onshore Namibia.
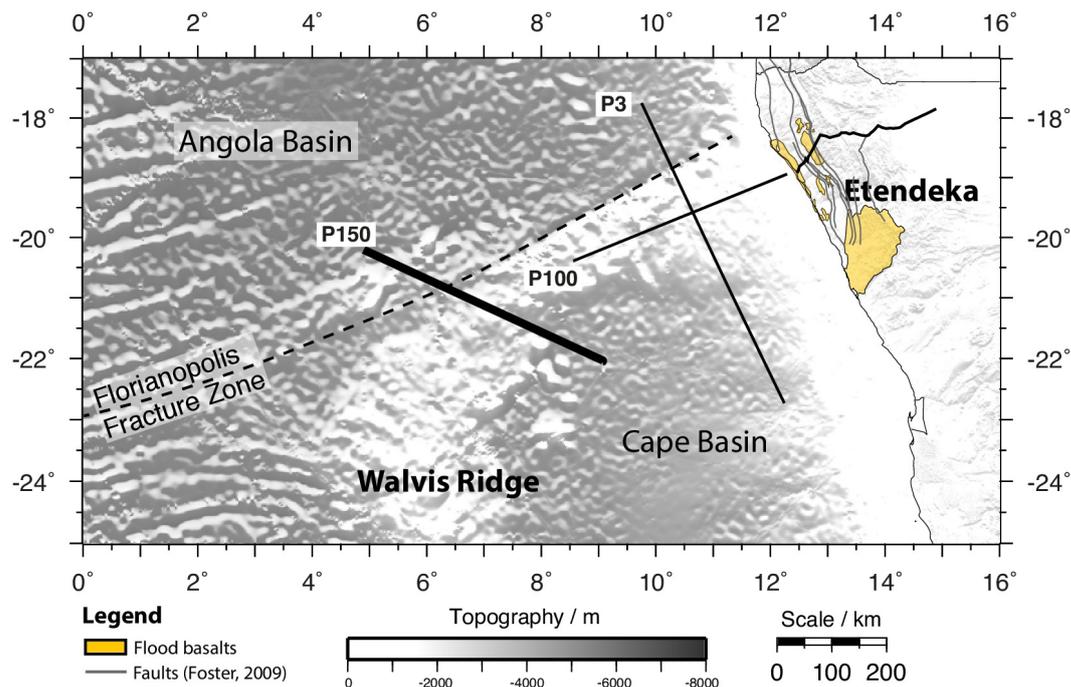
Figure 3.4.2: Location of the presented profile 150 crossing the Walvis Ridge approx. 600 km from the African coastline and other profiles from the same campaign (Fromm et al., in review). Note that the bathymetric expression at the intersection of the profile with the ridge less prominent compared to the East. The Florianopolis Fracture zone is interrupted.

In this study, we present a deep seismic profile that crosses Walvis Ridge in the NW-SE direction at 6°E, approx. 600 km off the Namibian coast (Fig. 3.4.2). Here, the topography of the ridge forms a bathymetric saddle. The saddle is 1000 m deeper than at the western end of P100, 200 km closer to the coast (Fig. 3.4.2). Along the seismic profile the ridge is wider and the flanks are gentler than at P3. Furthermore, the FFZ marking the northern escarpment of the ridge east of 7°E is not visible along the line. The profile extends 480 km across the ridge and into the interiors of the adjacent ocean basins. In total, 29 ocean bottom stations equipped with hydrophones (OBH) were deployed at a spacing of approximately 13 km. Two OBH did not record any data. The data were sampled at either 200 or 250 Hz. The seismic source consisted of $8 \times 8\,l$ ($64\,l$ or 3905 cu in in total) G-gun clusters operated at 200 bar (2900 psi) in 8 m depth. A shooting interval of 90 s resulted in 230 m mean shot spacing. Simultaneously, we acquired reflection data with a short, four channel streamer at 1000 Hz sample rate.

We filtered the data with a bandpass of 3.5-13 Hz and applied an automatic gain control (AGC, 1 s window). Occasionally, we used higher frequencies, especially for sedimentary reflections, which were clearer at frequencies of up to 100 Hz. Arrival times were picked with the software ZP (Zelt, 2004b). In general the data quality is excellent. Almost all stations show continuous crustal refractions, crust-mantle

reflections (PmP-phases) and a few mantle refractions (Pn-phases) at offsets up to 100 km. A strong basement reflector is clearly visible in both the OBHs and the streamer data. For stations located on the ridge crest, however, the basement is diffuse and its rough topography scatters the seismic energy. The seismic reflection data are displayed in Figure 3.4.3 and selected OBH data examples in Figures 3.4.4–3.4.8.

3.4.3 Modelling

Before the initial model set up, the OBH stations need to be relocated. Currents may displace the station while it sinks to the bottom with the result that its real position on the seafloor is slightly different from the deployment position. The shift along the profile line can be calculated from the direct arrivals. For a correctly located instrument they resemble a reflection hyperbola with its apex at zero. But if the station is misplaced along the profile line, the apex is shifted to the left or right. We picked the direct arrivals, computed a hyperbolic curve fit, and determined the in-line shift. The mean shift for all instruments was 160 m (maximum 600 m). Once relocation was complete, we projected the relocated stations onto a straight profile line without modifying the original shot-receiver offsets (Zelt and Smith, 1992).

The starting model was constrained by the bathymetry, sedimentary layers and the basement topography derived from the seismic reflection data. Because the short streamer did not provide enough data for a velocity analysis, we calculated velocities for the sediments using OBH data. Clear sediment reflections at the northern flank of the ridge were observed on both the streamer and OBH recordings and a standard velocity analysis using normal move outs (NMO) was carried out with the OBH data. The crustal structure was modelled with the ray-tracing software rayinvr (Zelt and Smith, 1992) mainly by forward modelling following a top to bottom approach. Velocities and boundaries were adjusted to match the observed slopes and onsets. Finally, we inverted the whole model to obtain error statistics and uncertainty estimates. The final model is shown in Figure 3.4.9.

3.4.4 Error Analysis

The model quality and uncertainty can be estimated from the normalized χ^2-value and the travel time residuals. The normalized χ^2 value depends on the assumed uncertainties for travel time picks, the residuals of calculated arrivals and the node distribution. Our final model has a χ^2 of 0.6 and is therefore well constrained within the given uncertainties (ideally, it should be 1). The travel time residuals of 82 ms are within the estimated pick uncertainties of 60 and 150 ms (depending on the signal to noise ratio). Table 3.4.1 summarizes the mathematical error analysis for the modelled phases and stations. Additionally, we estimate the spatial uncertainty of the model with the resolution plot and the ray coverage (Fig. 3.4.10, 3.4.11). The resolution plot displays the diagonal values of the resolution matrix (values greater than 0.5 are considered well resolved) and reflects the number
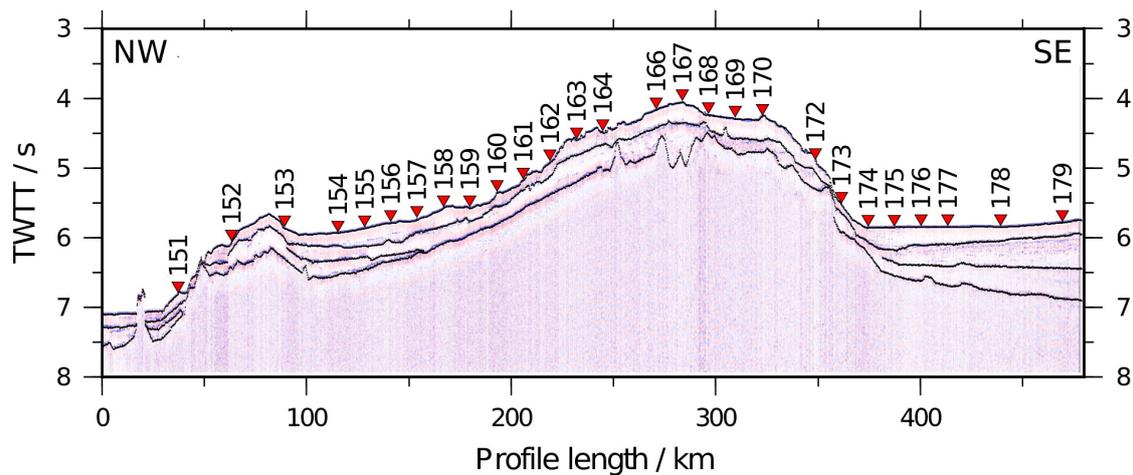
Figure 3.4.3:   Seismic reflection data with interpretation and station locations. Three sediment layers can be identified. The basement varies in amplitude and roughness along the profile. Amplitudes are strong at the northwestern flank of the ridge. The rough basement under the top of the ridge scatters seismic energy, therefore the basement location is more uncertain in this area.

of data constraining a parameter. Therefore, the number and spacing of nodes strongly influence the results of this analysis. As shown in Figure 3.4.11, our model is well resolved, except for the low velocity zone (LVZ) at the northern flank of the ridge. Here, refracted phases needed to constrain velocities are missing. If possible velocities were calculated from move-outs of reflected phases from the base of the low velocity zone. In general, seismic velocities derived from NMO analyses are less accurate than from refracted arrivals, which directly allow the calculation of velocities from the first arrivals.

Although the Moho topography is well constrained with a good coverage of PmP and deep refracted phases, we consider the area below the LVZ at a depth of 14 km to be more uncertain. In particular, the transition around the intersection with the FFZ (Fig. 3.4.9, around km 190) seems to be complex, displaying several intracrustal reflections, which we could not fit at all stations.

Finally, we tested the reliability of our model by perturbing velocity and depth nodes and found, that changes of $\pm 0.2\,\text{km/s}$ and $\pm 2\,\text{km}$ in the lower crust result in model variability within error bounds and so have to be considered as equally possible.
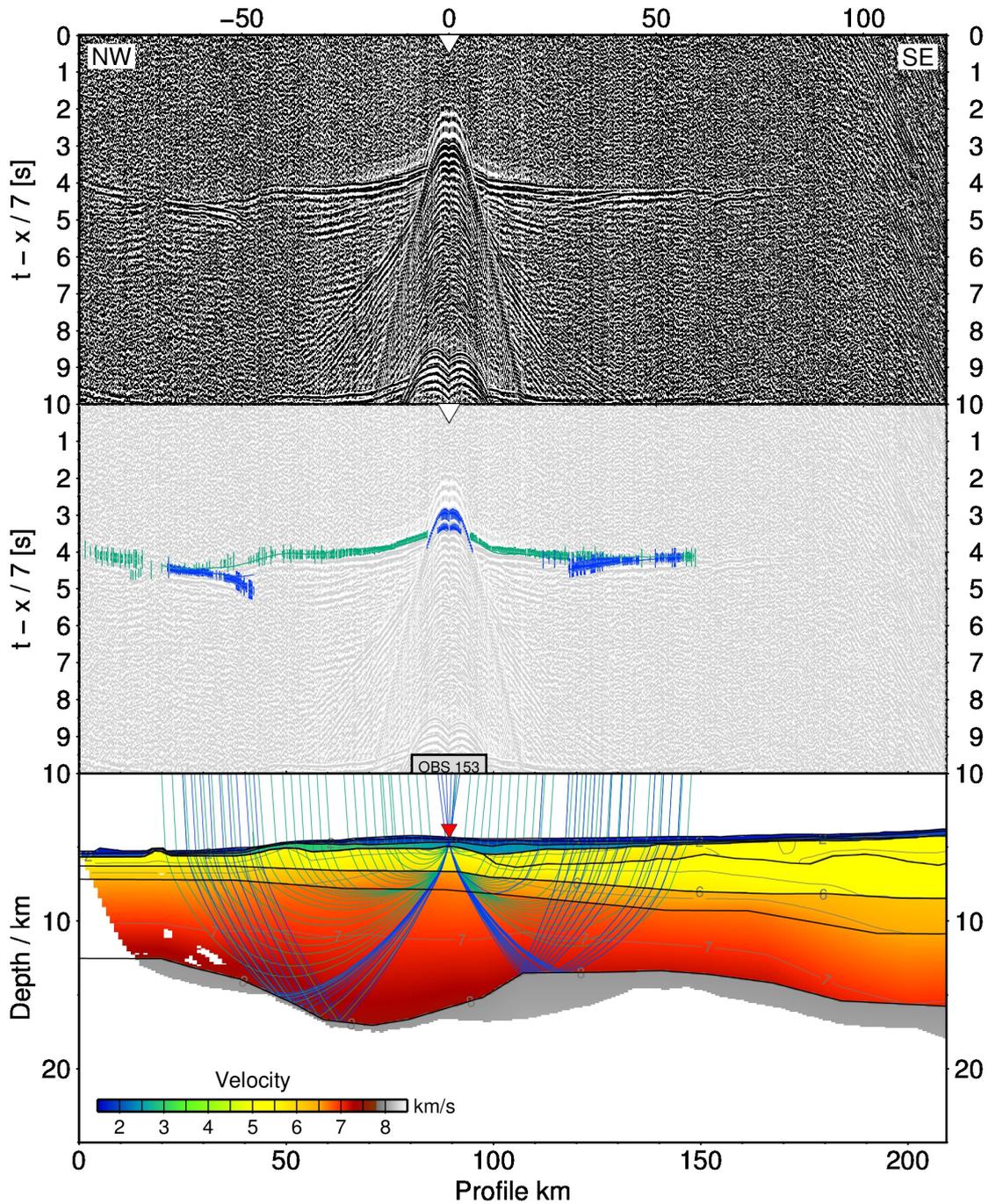
Figure 3.4.4: Data example showing recorded seismic data (top), traced arrivals (center) and ray coverage (bottom). The data are bandpass filtered with 3.5-13 Hz corner frequencies and amplified with an automated gain control (AGC) within a 1 s time window. The travel time picks are indicated by vertical bars with variable length representing the pick uncertainty. The number of drawn rays is reduced for clarity.
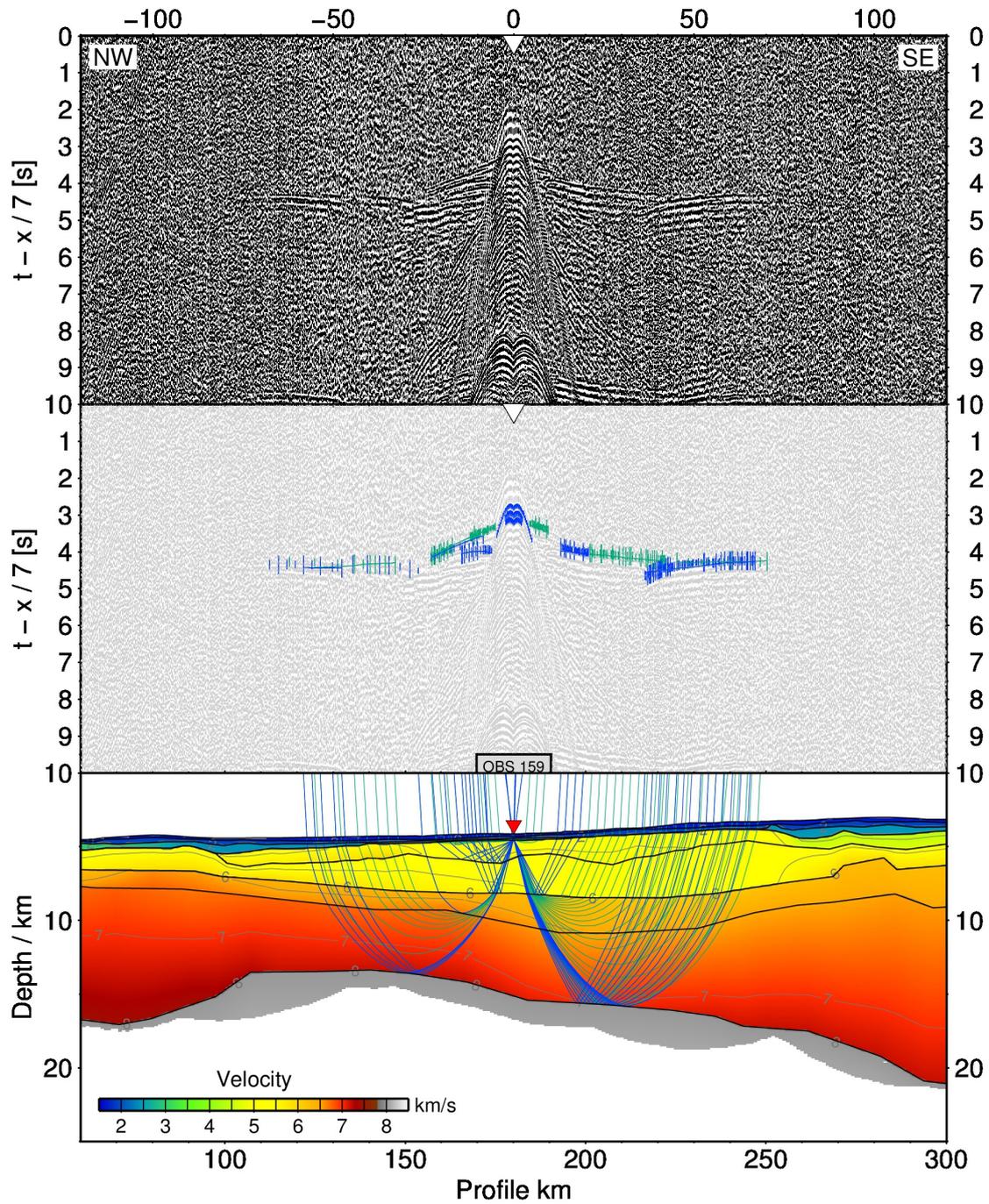
Figure 3.4.5: Data example with the same plotting parameter as used for Fig.
3.4.4
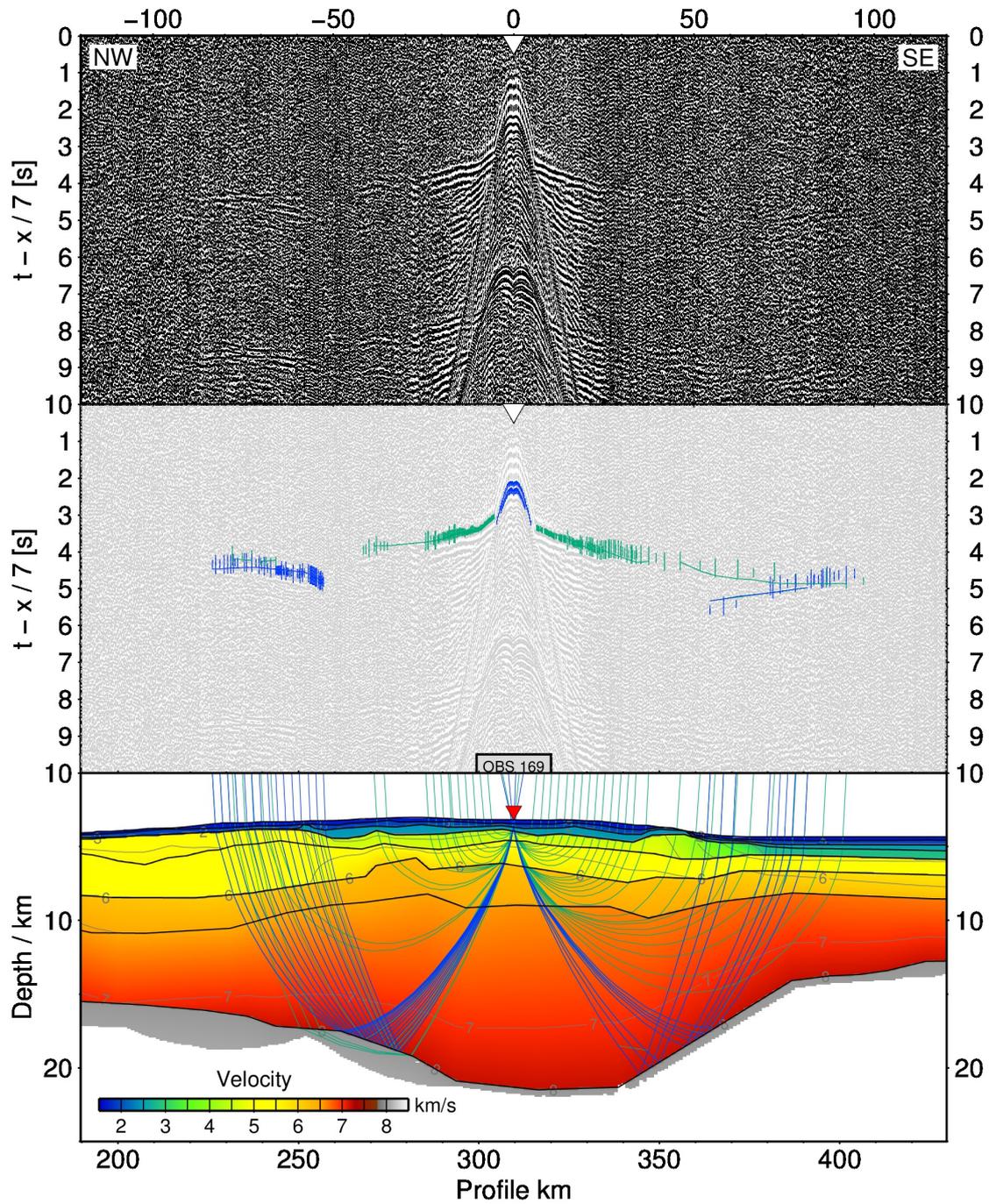
Figure 3.4.6: Data example with the same plotting parameter as used for Fig. 3.4.4
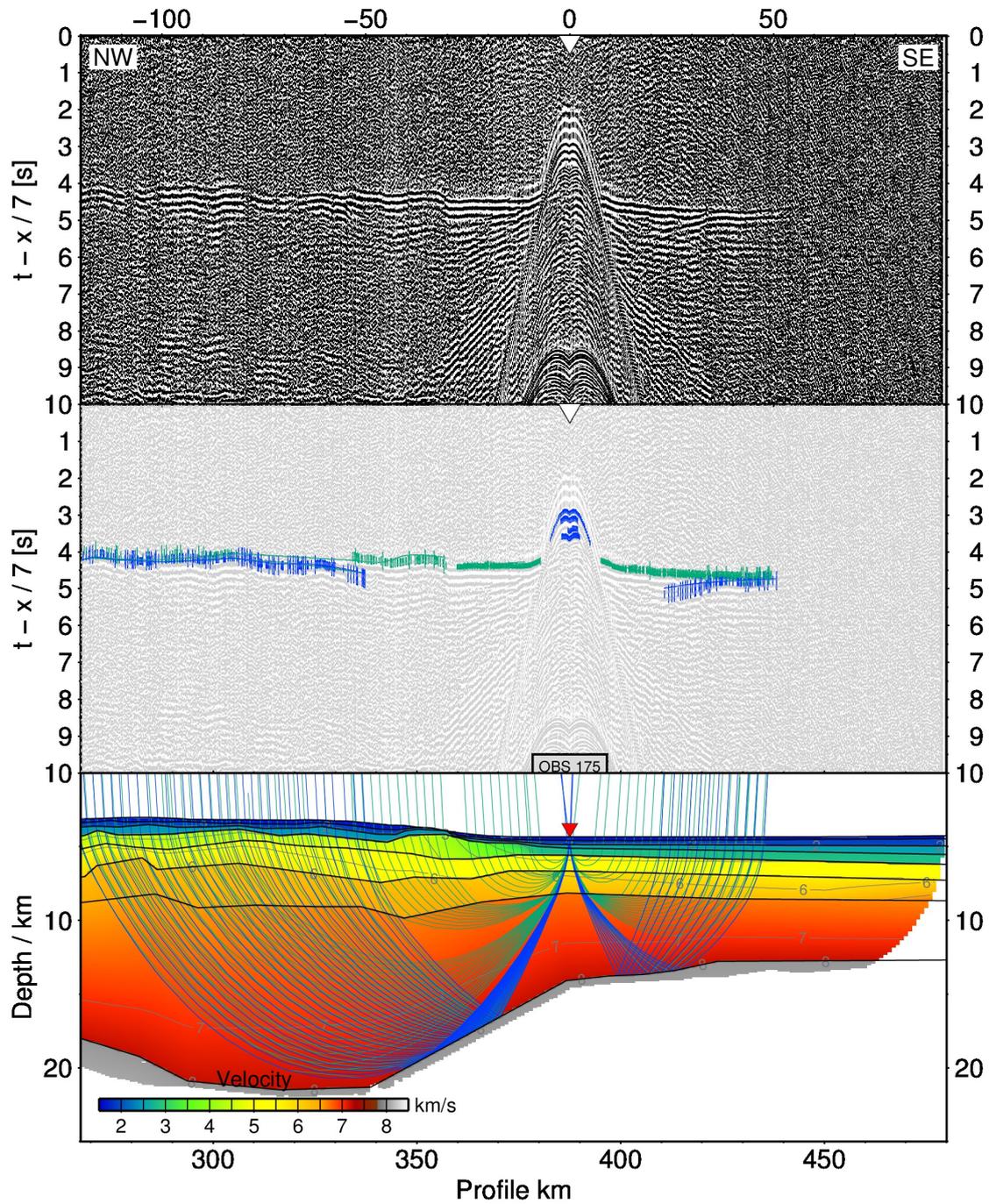
Figure 3.4.7: Data example with the same plotting parameter as used for Fig. 3.4.4
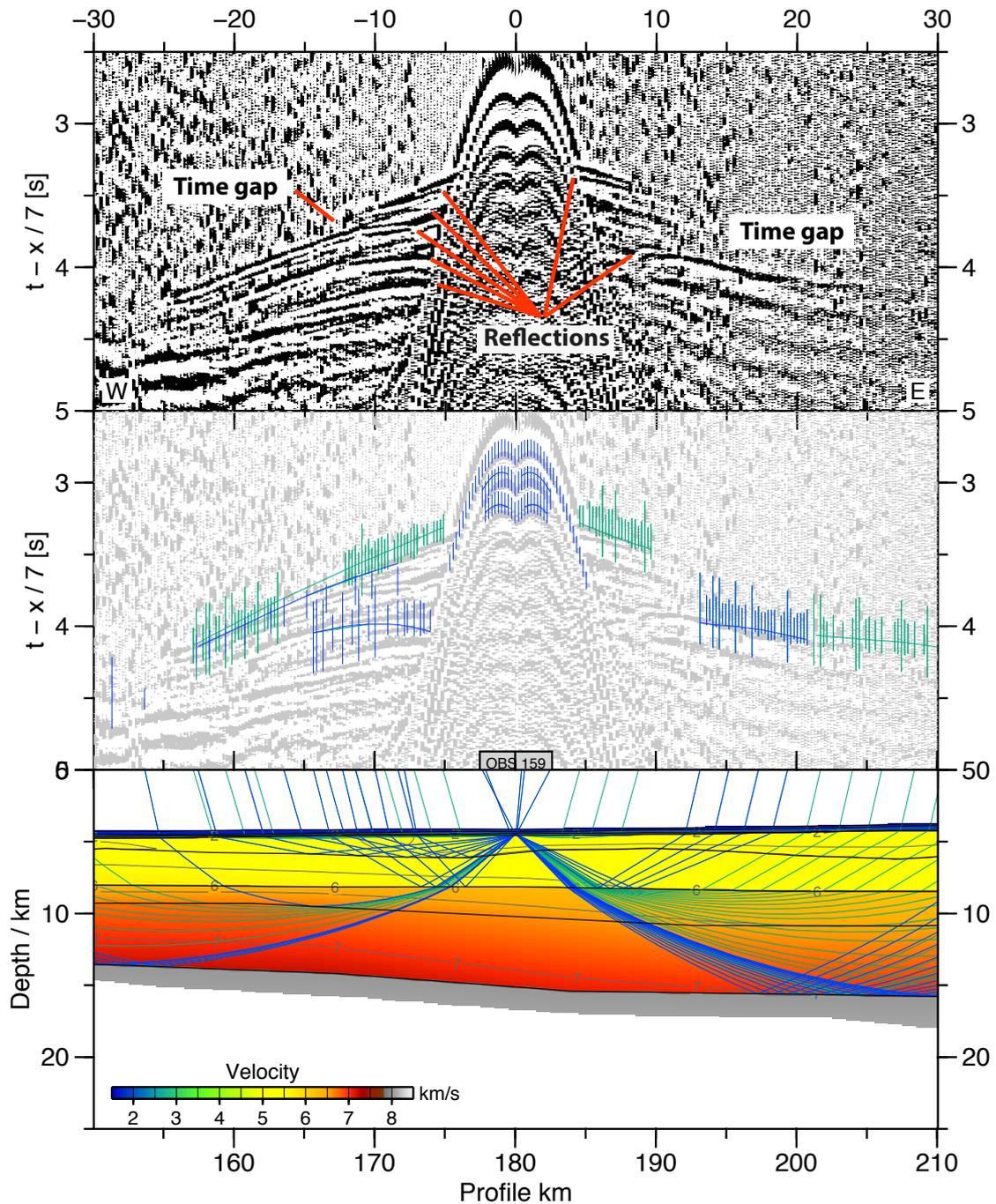
Figure 3.4.8: OBH data for station 159, filtered with 3.5-65 Hz bandpass, true amplitude scaling. This station is located at the northwestern flank of Walvis Ridge and shows features typical of all station along the flank (stations 153-164). The first refracted phase within the basement has asymmetric offsets and displays a time gap between the refracted phases. Reflections from the top and bottom of the low velocity zone can be seen, together with a sequence of closely spaced phases, which indicate reverberating reflections.
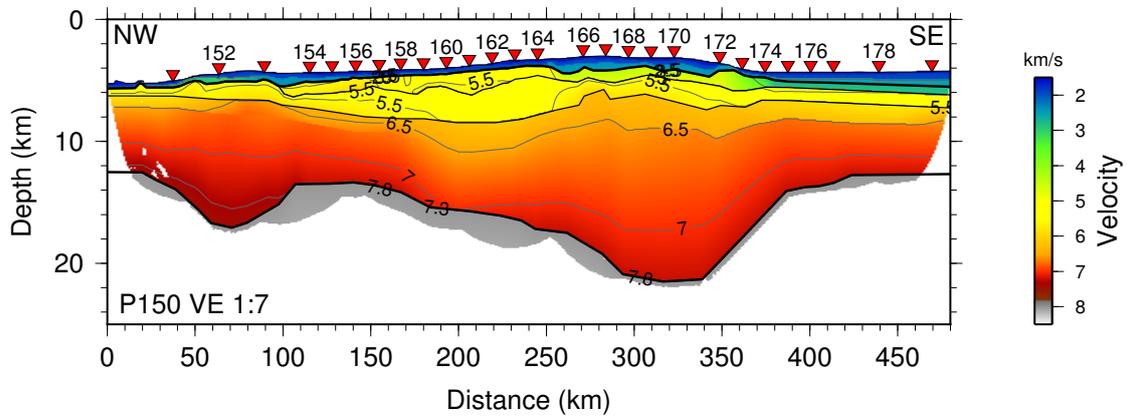
Figure 3.4.9:   Final P-wave velocity model. There is no data coverage for the white areas.
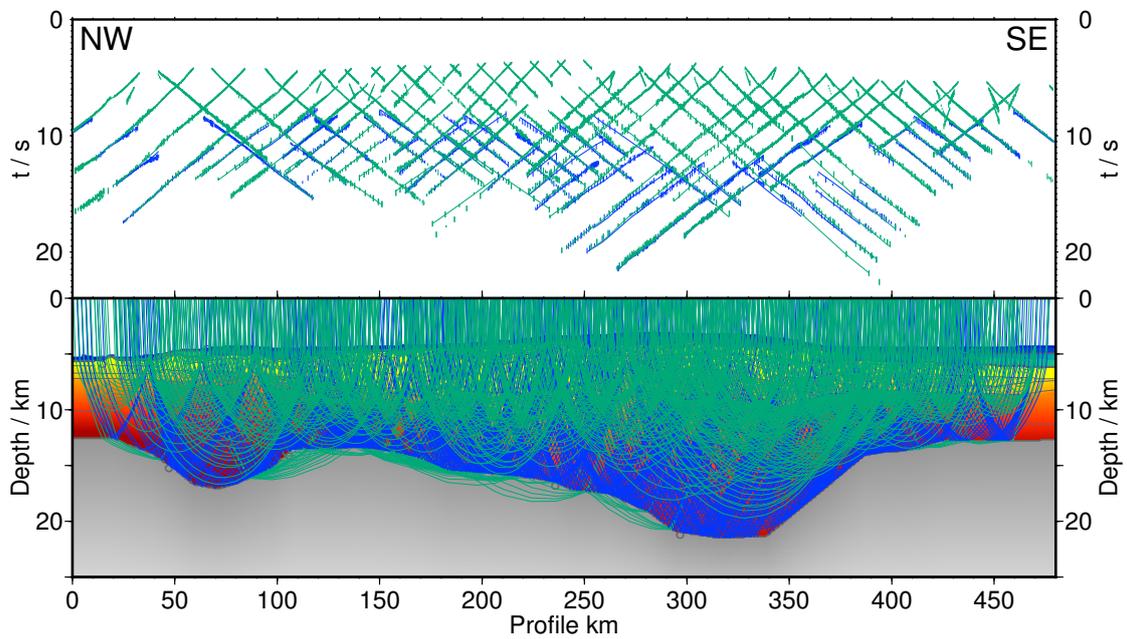
Figure 3.4.10: Ray tracing results (top) and ray coverage (bottom) for all stations of profile 150.
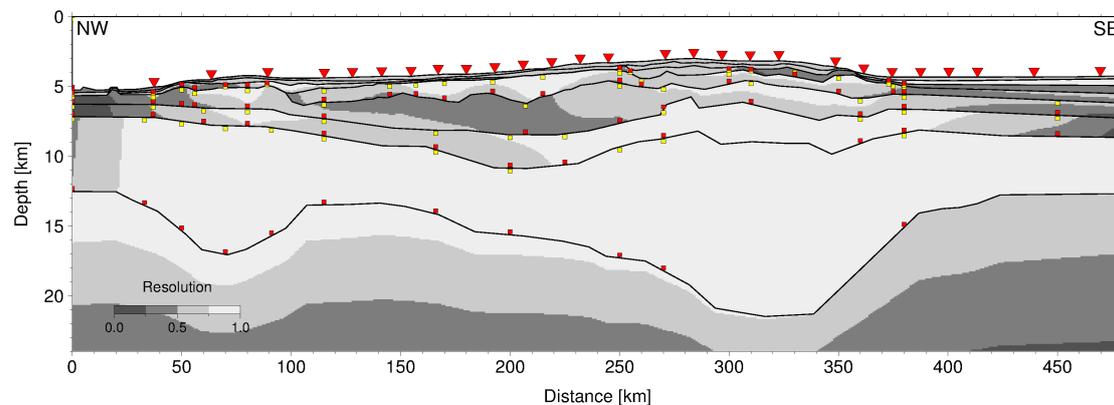
Figure 3.4.11: Resolution for profile 150. The model is well resolved in the lower crust. The lower resolution north of the ridge (LVZ) is due to a velocity inversion, which does not produce refracted waves and is therefore only constrained by reflections.

Unit	n	t_{rms}/s	χ^2
Sediments	942	0.070	0.855
Crust	5729	0.074	0.475
Mantle	244	0.094	0.494
Boundary			
Moho	2369	0.097	0.558
Basement	517	0.101	1.803
LVZ (top)	65	0.045	0.208
LVZ (bottom)	254	0.092	0.921
Total	10120	0.082	0.607

Table 3.4.1: Summarized error statistics for the P-wave modelling. Columns show the number of picks (n), their mean deviation t_{rms} and the normalized χ^2 value for different geological units and boundaries. The boundaries summarize reflected phases and the units main refracted phases (except for the sedimentary layers, which also include some reflections). The low velocity zone (LVZ) north of the ridge is constrained solely by reflections from the top and bottom and is therefore relatively poor resolved (see Fig. 3.4.11)

3.4.5   Results and Interpretation

In this section we describe the final velocity model shown in Figure 3.4.9 and interpret the observed velocities and structures (Fig. 3.4.12). Selected data examples with picked arrivals and ray-tracing results are displayed in Figures 3.4.4–3.4.8.

The seismic reflection data and the velocity model reveal the asymmetric morphology of the Walvis Ridge: the northern flank of the edifice differs significantly from the southern flank. The oceanic crust of the Angola Basin is reached as far as 280 km north of the ridge peak, whereas the Cape Basin lies only 70 km south of it. The wide, northern flank is characterized by a gentle dip towards a basement high at km 25 marking the transition to the Angolan Basin. The bathymetry is mirrored by the crust-mantle topography (Moho) with thickened crust underneath the ridge crest (∼18 km) and the northern seamount (∼12 km).

Therefore, we divide the profile into the main ridge section around the peak from km 250 to 360, which resembles the continuation of the Walvis Ridge and the northern edifice (km 20-250) that has an atypical crustal structure, but is commonly not recognized as a part of Walvis Ridge (Fig. 3.4.1). Both ends of the profile, in the Angola and Cape Basins (km 0–20 and 400–480), show typical properties for oceanic crust.

Sedimentary layers   Based on the seismic reflection data, we modelled three sedimentary layers. They reach a maximum thickness of 1.2 km in the Cape Basin and velocities varying between 1.6 and 3.1 km/s. The two upper layers have been modelled with constant velocities of 1.6 and 1.9 km/s and represent unconsolidated deep-sea sediments. The third sediment layer is laterally variable and represents different types of sedimentary infills. It disappears completely at basement highs and velocities ranging between 2.4 and 3.1 km/s. Within this layer, sediments with the highest velocities of 3.1 km/s fill a basement depression at the northern edifice of the ridge (km 100-150, Fig. 3.4.3), while sediments with the lower velocities of 2.4 km/s overlay the oceanic crust in the Cape Basin.

The crustal architecture   Crustal velocities in the Cape Basin resemble those typical of oceanic crust: The upper 0.5 km thick layer with velocities of 2.8 km/s is therefore likely to consist of pillow basalts, followed by a layer of sheeted dikes with velocities of 5.0–6.2 km/s and gabbro in the lower crust (velocities of 6.6 to 7.2 km/s). The total thickness of the igneous crust is 7.4 km, which is normal for oceanic crust (White et al., 1992).

The oceanic crust north of the ridge in the Angola Basin is not as well constrained. Since the ridge was not expected to extend that far, no station is placed on normal oceanic crust. Only the far offsets of the northernmost station cover this region. However, reflections from the crust mantle boundary (Mohorovic discontinuity or abbreviated Moho) constrain the crustal thickness of 7.2 km. Here, crustal velocities range from 5.2 km/s in the upper crust to 7.4 km/s at the Moho. The lower crustal velocity is higher than for normal oceanic crust but this should
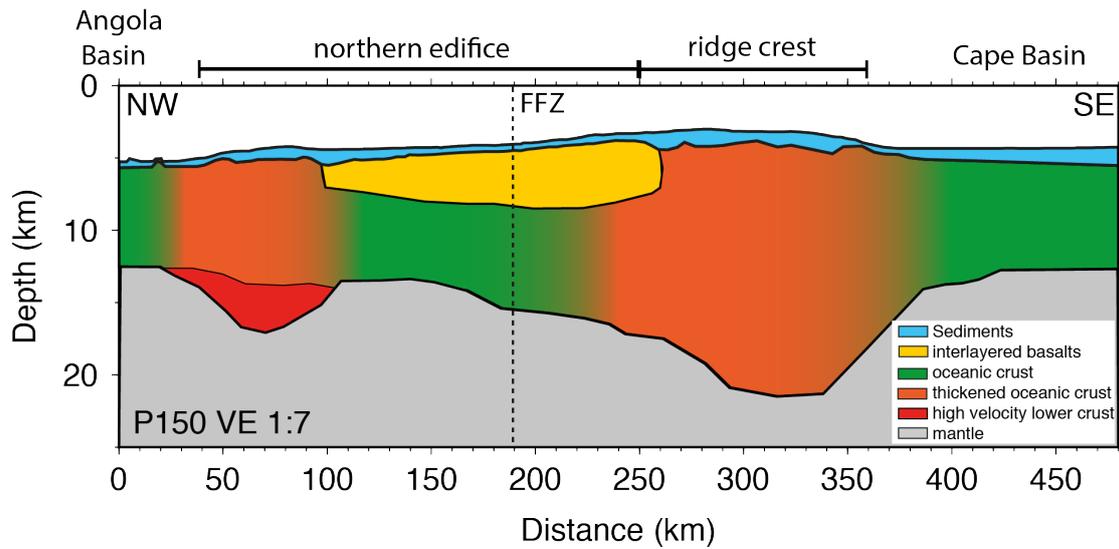
Figure 3.4.12: Geological interpretation of the veloctiy and density model

not be over interpreted due to the sparse data coverage, missing counter shots and
the Moho topography.

The ridge crest   The rough basement at the ridge crest (km 250 to 300) is
only defined by a weak, discontinuous reflector indicating a small velocity contrast
between the basement rocks and the overlying material (Fig. 3.4.3). Additionally,
a few seamounts disturb the basement topography at km 250, 270 and 300. Upper
crustal velocities at the ridge range between 4.4 and 5.6 km/s and display mod-
erate lateral heterogeneities. Seismic velocities can be an indicator for the water
depth of volcanic eruptions. The observed velocities indicate basaltic rocks with a
low degree of fractionation meaning that they have likely erupted well below sea
level (Christensen, 1982). This is consistent with the absence of large amounts of
volcaniclastic material (velocities less than 4.0 km/s, Hill and Zucca, 1987), which
originates in explosive eruptions near the water surface as observed around other
seamounts and volcanic islands e.g. Louisville, the Marquesas or Canary Islands
(Contreras-Reyes et al., 2010; Wolfe et al., 1994; Watts et al., 2006). Thus, we
speculate that this part of Walvis Ridge was never or only briefly located in shal-
low water or a subaerial setting during its active volcanic phase. The mid- and
lower crustal velocities range between 6.2 and 7.2 km/s. Such velocities are typical
of the gabbroic layer of igneous crust. The main ridge is not characterized by the
exceptionally high velocities (> 7.2 km/s) occasionally observed at other hot spot
trails e.g. the Ninetyeast Ridge, Grevemeyer et al., 2001

The northern edifice   The northern flank of the ridge (km 20–250) in be-
tween the crest and the basement high is characterized by a strong and smooth
basement reflector and faster seismic velocities (5.1–5.6 km/s) in the upper crust.
Such basement velocities are typical for basalts, although too high for the pillow

basalts seen in normal oceanic crust. The underlying layer is characterized by slightly lower velocities of 5.4 km/s. Low velocity zones (LVZ) generate no refracted waves and cause a time gap in the travel time curve, which is observed at all 11 OBHs along the northern flank. The thickness of this LVZ increases towards the ridge crest, where we observe a maximum time gap of 600 ms corresponding to 3.8 km thick crust (km 240). Within this layer, we observe a sequence of strong reflections with the same or slightly higher velocities (Fig. 3.4.8). This reflection pattern might be caused by an alternating layering of basaltic rocks and slower sediments, volcaniclastic material or pillow lavas (Inoue et al., 2008), which can amplify amplitudes for certain frequencies due to constructive wave interference (Braile and Smith, 1975). We therefore interpret the upper crust as an inter-layered basalt-sediment sequence. Velocities of 6.2-7.2 km/s characterize the 5.6 km thick middle and lower crust beneath the northern ridge flank. The thickness and shallow velocity gradient indicate gabbroic material of oceanic crust. We therefore interpret the crust beneath the LVZ as oceanic crust that pre-dates the action of the hotspot in the region. Within this pre-hotspot crust we observe slightly lower velocities (6.1-7.0 km/s) at km 200 and a modest decrease in Moho depth (~ 2 km). Here, the interpolated Florianopolis Fracture Zone (FFZ) intersects the profile and we interpret this structural change as indicating the remnants of the fracture zone in the pre-existing oceanic crust. To sum up, we interpret the northern flank to consist of a thick lava sediment layer (possibly lava flows) covering older oceanic crust and the FFZ.

Mantle The mantle seems to be homogeneous with a constant velocity of 8.0 km/s, which is common for oceanic lithosphere (White et al., 1992). Although, the Walvis Ridge is derived from a thermal anomaly within the mantle, we do not observe any velocity variations or anisotropy beneath the ridge.

3.4.6 Gravity modelling

After the seismic modelling we derived a gravity model to confirm that the modelled crustal structure is consistent with observed gravity data. We used free air satellite data (Sandwell et al., 2014) and modelled the density structure with the software IGMAS (Götze and Lahmeyer, 1988). Figure 3.4.13 displays the gravity anomalies, model and a comparison with the seismic model.

First, we converted the P-wave velocity model to a density model using the empirical velocity-density correlation of Ludwig et al., 1970, Fig. 3.4.13 c. We kept the model as simple as possible and merged layers with similar densities, which were not constrained by reflections. Seismically-constrained boundaries were not changed. To improve the fit between calculated and measured data, we divided the layers into polygons to account for possible lateral density variations. The initial density values for the polygons were determined by manual estimation. Finally, we inverted the densities of selected polygons without changing their geometries. We accepted only reasonable values within the boundaries of the velocity-density correlation.

Figure 3.4.13: Gravity model for profile 150. a) The observed free air satellite data (Sandwell et al., 2014), the modelled gravity data and their deviation. b) The final density model. c) Comparison between the density distribution directly converted from the P-wave velocity model and the geometry of the density model. d) The seismic P-wave velocity model.
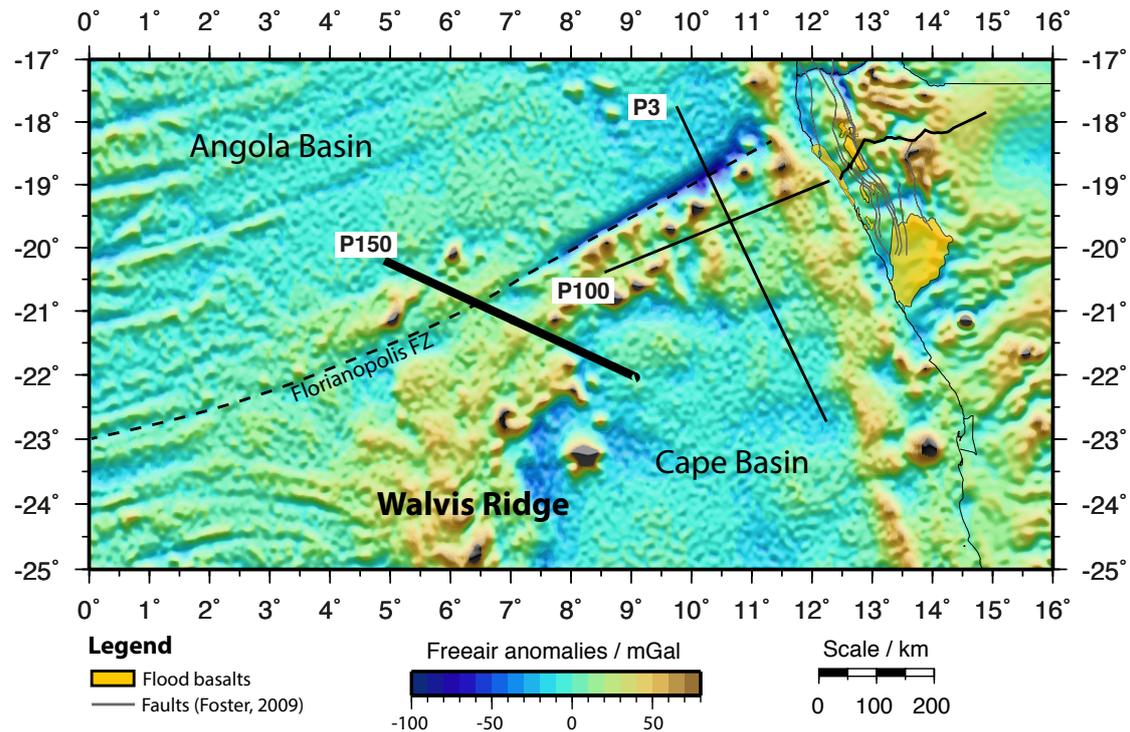
Figure 3.4.14:   Free air gravity anomaly map (Sandwell and Smith, 2009). The expression of the Florianopolis Fracture Zone is suppressed at the intersection with profile 150.

The free air anomaly varies from -18 mGal to +25 mGal along the profile. The minimum is located south east of the crustal root of the Walvis Ridge. The northern basement high, the northern flank and the ridge crest (km 40-340) are characterized by positive anomalies of 10, 23, and 25 mGal with a local minimum at km 190, where the free air anomaly drops from 23 to 6 mGal. Here, the FFZ intersects the profile (Fig. 3.4.14).

Overall, we obtain a good long wavelength fit, with deviations of 5 mGal. Misfits reach ±5 mGal at the northern flank of the ridge (km 50 to 190), where we observed the low velocity zone. This is the region with the poorest resolution in the seismic model; the gravity model misfits may be related to unresolved topography within the basalt sediment layer. The shorter wavelength misfits reach up to 10 mGal, especially at the ridge crest (km 220 to 290). Here, the basement topography has a large influence on the model and yet is poorly constrained by the reflection seismic data. Elsewhere, seamounts are mapped in the basement but not included in the model because a lack of clear reflectors to trace. The ridge itself is a 3D structure with strong variations in all directions, therefore 3D effects are to be expected in the 2D model. We therefore judge the deviations along the model gravity profile to be acceptable.

The decreased seismic velocities at the intersection with the FFZ (km 190) are consistent with a local minimum in the free air data and reduced densities in the

upper and lower crust. Seismic velocities in the lower crust beneath the ridge (km 270-370, 7.2 km/s) are slightly decreased compared to beneath the basement high (km 50 to 100, 7.5 km/s). This is consistent with the modelled densities of 3.005 cm^3 beneath the ridge and 3.033 cm^3 beneath the basement high.

The difference in water depths of the Cape and Angola basins (1000 m) initially caused a large difference of the gravity anomaly level between the two ends of the profile. We added an additional upper crustal layer with a density of 2.17 cm^3 in the Cape Basin, which resembles the upper oceanic crust with velocities of 2.8-2.9 km/s. This layer is absent in the Angola Basin, both in the seismic and gravity model. But one have to keep in mind that the seismic profile does not cover normal oceanic crust in the Angola Basin.

3.4.7   Discussion

In this section we compare the crustal structure modelled in our profile with seismic data along the Walvis Ridge and other hotspot trails. Afterwards, special emphasis is set on the lower crustal velocities. The first two parts of the discussion are limited to the crustal structure beneath the main ridge. The structures north of the FFZ are discussed in the geodynamic framework and, last, the FFZ and its interplay with the hotspot is analysed.

Comparison   The morphology of Walvis Ridge at the profile location is less prominent than closer to shore. The water depth at the ridge crest is 3200 m, about 1000 m deeper than at the western end of P100 (Fig. 3.4.2). However, a comparison of the basement depth at the ridge crest (km 300) with the western end of P100, 200 km away, does not reveal a significant change in depth (Fromm et al., in review). The basement of P100 is in 4.4 km depth, while the basement of P150 lies at 4.0 km. The difference in water depth is therefore not caused by basement topography, but variations in the sedimentary cover. Drilling at the eastern Walvis Ridge (DSDP Leg 40, Site 363) reveals shallow water components in the lowermost layer indicating that this part of the ridge was emplaced subaerially or in shallow water (Bolli et al., 1978). Phreatic eruptions under such conditions would have produced voluminous volcaniclastic material, which likely accumulated in moats between the buried seamounts along P100. As such materials are absent along our profile, the different bathymetric appearance of the ridge might be explained by a contrasting eruption setting: submarine eruptions along P150 would have generated a less pronounced bathymetric feature. Beneath the sedimentary cover, the crustal thickness only differs slightly outside the model uncertainty: 21 km at 9°E (P100) and 18 km at 6°E (this study). Kessling, 2008 observed a more meaningful decrease in crustal thickness, to 13 km, in the western guyot province at 3°W, approx. 1800 km further SW. This crustal thinning is consistent with a general decline in the hotspot activity (Gallagher and Hawkesworth, 1994).

A comparison of the crustal structure with other hotspot trails reveals strong variations in crustal thickness and seismic velocities, although all have a common architecture: a steep velocity gradient in the upper crust and a shallow gradient in
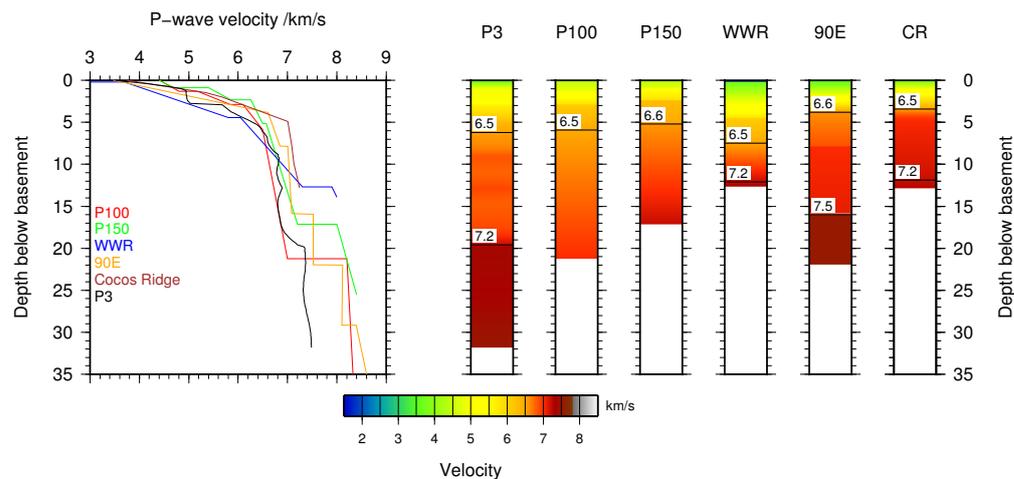
Figure 3.4.15:   Comparison between the crustal structure of profile 150 with other profiles from the Walvis Ridge and other hotspot trails. P3 Fromm et al., in review, WWR western Walvis Ridge Kessling, 2008, 90E Ninetyeast Ridge Grevemeyer et al., 2001, CR Cocos Ridge Sallarès et al., 2003. The annotated contours at 6.5-6.7 km/s mark the transition between oceanic layer 2 and 3 (dikes and gabbro). The contour at 7.2 km/s indicates anomalous high seismic velocities in the lower crust.

the lower crust (Fig. 3.4.15). This architecture is related to the crustal structure of normal oceanic crust. The steep upper crustal gradient relates to its pillow basalt composition, where compaction with depth causes increasing velocities, and the shallow lower crustal gradient reflects the presence of more uniform gabbros (White et al., 1992). The increased crustal thickness of the Walvis Ridge is achieved by thickening in both the upper and lower crust. In contrast, other hotspot trails (namely the Ninetyeast Ridge and the Cocos Ridge Grevemeyer et al., 2001; Sallarès et al., 2003) only reveal a thickened lower crust beneath an upper crust of normal thickness.

Lower crustal structure   Another significant difference between the individual hotspot trails is the presence of high seismic velocities in the lower crust. High seismic velocities in the lower crust have been interpreted as signals of olivine and pyroxene cumulates that form by fractionation of mantle melts (Farnetani et al., 1996). Lower crustal velocities and the crustal thickness therefore allow conclusions to be drawn about mantle potential temperature and mantle composition (Holbrook et al., 2001). Unusually thick crust, formed by fractionation of melts extracted from abnormally hot mantle, should display higher velocities than those expected for normal oceanic crust. However, such velocities are not ubiquitous at hotspot trails. High lower crust is absent from the Galapagos trail (Cocos and Carnegie Ridge) and the Iceland-Faroe Ridge, whereas the Ninetyeast Ridge and Hawaii are both underlain by high velocity lower crustal bodies (Sallarès et al., 2003; Sallarès et al., 2005; Grevemeyer et al., 2001; Watts and Brink, 1989). Hot

mantle is therefore either unnecessary for the formation of high velocity lower crust under hotspot trails, or alternatively it is not a diagnostic component of the hotspot concept.

An alternative interpretation for the source of high lower crustal velocities is related to the lithospheric thickness and age at the time of its interaction with the hotspot (Richards et al., 2013). Thick and old lithosphere promotes crystallization and fractionation at depth, leading to the formation of thick, high velocity, ultramafic underplatings (7.4 to 8.0 km/s), whereas thin and young lithosphere may allow melt ascent to depths at which gabbroic rocks with velocities of 6.8 to 7.5 km/s can crystallize.

The Walvis Ridge in general seems not to be characterized by exceptionally high seismic velocities (this study, P100 west, Kessling, 2008). Areas with high velocities have only been found in association with the South Atlantic volcanic margin (P100, P3, Fromm et al., in review). The ages of the Walvis Ridge and oceanic lithosphere east of 6°E are not well constrained, but plate kinematic reconstructions and age dating of dredge samples suggests that the ridge may have been emplaced on ∼6-12 Ma old lithosphere (Pérez-Díaz and Eagles, 2014; Bolli et al., 1978; Hay and Sibuet, 1984). The absence of an ultramafic body with velocities higher than 7.5 km/s is consistent with this suggested relation to lithosphere age.

Geodynamic framework Unfortunately, the timing and geometry of the South Atlantic opening from M0 to C34 (83.0 to 120.6, Gee and Kent, 2007) is not as tightly constrained as for later times because of the lack of magnetic reversal isochrons during the Cretatecous quiet period. Reconstructions for this period vary considerably, reflecting the differing weights given to the remaining plate kinematic constraints e.g. Seton et al., 2012; Heine et al., 2013; Pérez-Díaz and Eagles, 2014.

During initial opening, the Sao Paolo Plateau (SPP) was still attached to South Africa and seafloor spreading north of Walvis Ridge was focussed at a mid-ocean ridge lying west of it (Mohriak et al., 2010). Remnants of abandoned ridges in this location have been interpreted from gravity anomalies at the 'Abimael Ridge' (Mohriak et al., 2010; Sandwell et al., 2014) and from bathymetric and gravity features at the Rio Grande Rise (Pérez-Díaz and Eagles, 2014). Successive jumps transferred the spreading centre to locations nearer to the African coast, eventually detaching the SPP from the African plate (Fig. 3.4.16). The following sea floor spreading shifted the SPP along the transform fault of the FFZ, leaving the steep northern escarpment at Walvis Ridge and normal oceanic crust devoid of any abnormal volcanism to the north of the fracture zone (P3, Fromm et al., in review). The exact timing for this event varies according to the different authors from 95 Ma (Seton et al., 2012) to 85 Ma (Fig. 3.4.16, Pérez-Díaz and Eagles, 2014).

Surprisingly, in this study we do not find evidence for normal oceanic crust north of the FFZ in the Angola Basin. Solely judging by the morphology of Walvis Ridge, we expected to find normal oceanic crust as observed closer to the coast (Fig. 3.4.2, Profile 3, Fromm et al., in review). There, the thick crust of
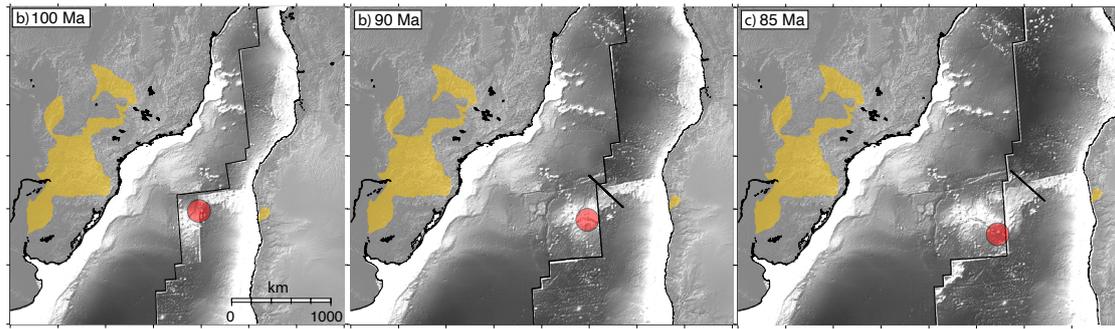
Figure 3.4.16:   Reconstruction of the South Atlantic opening (Pérez-Díaz and Eagles, 2014).   Flood basalt provinces are marked in orange, red circle denotes the predicted hotspot location (O'Connor and Duncan, 1990). Profile location is indicated in b) and c).

the Walvis Ridge abruptly thins to normal oceanic crust (nearly 30 km within 30 km). Instead, we observe traces of volcanic activity: an additional basement high (km 25) underlain by thickened oceanic crust and a thick layer of basaltic material on pre-existing oceanic crust (km 80-140).

The influence of the fracture zone is completely different between the two profiles. At P3, the fracture zone coincides with a zone of dramatic crustal thinning, whereas the fracture zone has only minor influence on the velocity structure and Moho topography at P150. A possible explanation for this contrast is the distance between the fracture zone and the axis of the Walvis Ridge, expressed as the zone with the maximum thickness. This distance is only 30 km at P3, but more than 100 km along P150. We suspect that the Walvis Ridge at P3 is incomplete, and that parts might have been sheared off to be preserved on the South American plate. At P150 the transform fault has not affected the crustal root of Walvis Ridge, but the adjacent oceanic basin.

The timing of events is crucial for the interpretation of this structure. The fracture zone is not recognizable in bathymetry or reflection data, only in a slight velocity decrease in the lower crust and as a local minimum in free air gravity data (Fig. 3.4.13, 3.4.14). From this, it seems that the upper basalt layers north of the FFZ were emplaced after the transform fault became inactive and the SPP was sheared off. Thus, we find a change in timing compared to the eastern Walvis Ridge at P3. There, transform faulting occurred after the emplacement of Walvis Ridge, possibly removing parts of the volcanic material, creating a steep escarpment and leaving undisturbed oceanic crust north of it. In contrast, at least some volcanic activity occurred after the transform faulting at P150 and volcanic rocks covered the fracture zone. Now, the question arises weather this occurred contemporaneous with emplacement of the main Walvis Ridge or during a later, second stage volcanism.

Reconstructions show that the hotspot was located near P150 around 100 Ma (O'Connor and Duncan, 1990). At that time the Angola Basin north of the ridge did not yet exist and the SPP lay adjacent to the north of Walvis Ridge

(Fig. 3.4.16 a). Contemporaneous emplacement of the northern edifice with the Walvis Ridge would require earlier opening of the Angola Basin. Alternatively, the northern edifice might have been emplaced in a second stage of volcanism. The most recent reconstruction of the South Atlantic opening predicts the creation of normal oceanic crust along P150 in the Angola Basin around 85 Ma (Fig. 3.4.16 c, Pérez-Díaz and Eagles, 2014). Therefore, the northern edifice would post date the main eruption by at least 15 million years. Even though the hotspot model requires an age progression, late stage volcanism is observed at another hotspot trail, the Ninetyeast Ridge (Grevemeyer et al., 2001). Both the Ninetyeast Ridge and the Walvis Ridge are aligned with major transform faults. Reactivation of these fracture zones might have triggered the late stage, non-age progressive, magmatism in each case.

We therefore interpret the northern edifice as a product of late stage volcanism, but additional age constraints for the seamounts are awaited and will clarify the situation (Hoernle et al., 2014).

The influence of the Florianopolis fracture zone   Intraplate stress release above local mantle fertility inhomogeneities has been suggested as an alternative origin for linear volcanic chains (Anderson, 2001; Anderson, 2005). In accordance with this model, previous studies have proposed the Walvis Ridge as the site of a failed rift arm or 'leaky' fracture zone (Fairhead and Wilson, 2005; Haxel and Dziak, 2005).

Our study revealed remnants of the FFZ covered beneath basalts and an undisturbed crustal root of the Walvis Ridge. Again the exact timing of events is crucial for its interpretation. The uppermost basaltic layer was emplaced after the active phase of the transform fault that built the FFZ in this part of the Walvis Ridge. Fracture zones are commonly interpreted as weak zones within the crust, which preferentially become reactivated or focus magmatism. It has been previously stated that plumes might play a more passive role and merely utilize existing weak zones as migration paths to the surface, even if this requires lateral flow over a longer distance towards the weak zone (Sleep, 2006).

If the FFZ predates emplacement of Walvis Ridge (eliminating the necessity for late stage volcanism), then it seems it did not act as a pre-existing weak zone to focus magmatism and crustal growth. The velocity structure of leaky transform faults is not well determined. Funck et al., 2007 observed increased velocities across a leaky transform fault in the Davis Strait, whereas Uenzelmann-Neben and Gohl, 2004 detected normal oceanic velocities with increased crustal thickness at the Aghulas Ridge, which is a candidate for a 'leaky' transform fault influenced by the Discovery hotspot. Here, the crustal thickening is achieved in the upper crust. In contrast, Hagen, 2008 observed thickened crust with indications for locally increased velocities marking dykes. The decreased seismic velocities and densities at the FFZ oppose the interpretation of the fracture zone as a migration path for volcanic material. Melt from the mantle would cause increased and not decreased velocities and densities. Furthermore, the crustal root of the Walvis

Ridge lies 100 km distant from the fracture zone and both events seem to have been localized independently of each other.

Assuming a different timing of events, the Walvis Ridge might have been emplaced before the active transform fault, to be followed by secondary volcanism that obscured the FFZ. In this case, the action of the transform fault might have triggered the late stage volcanism north of Walvis Ridge. Even if the volcanism completely post-dates the transform, it is surprising that the FFZ did not channel any melt to the surface leading to thickened oceanic crust at the location of the fracture zone. We might interpret this to mean that the oceanic crust was young and weak enough for melt to migrate towards the surface at the hotspot location, rather than to accumulate and migrate towards thinner and weaker lithosphere. Although we do not know the exact timing of events, we can rule out the fracture zone as a migration path for the surface volcanism. Therefore, it is unlikely that the Walvis Ridge originated as a leaky transform fault.

3.4.8 Conclusion

We presented a model of the deep crustal structure of Walvis Ridge at 6°E. The model shows that the Walvis Ridge consists of thickened oceanic crust composed of basaltic layers, pillow basalts and sheeted dikes in the upper crust and gabbroic rocks in the lower crust. The maximum crustal thickness at Walvis Ridge is 18±2 km embedded in 7±1 km thick oceanic crust of the Angola and Cape Basins. Our results show additional volcanic structures north of Walvis Ridge: a basement high underlain by 12 km thick igneous crust and basaltic layers covering old oceanic crust and the Florianopolis Fracture Zone. The extent of the Walvis Ridge and the area affected by related magmatism is therefore larger than previously estimated. The crustal velocity structure suggests that this part of the ridge was emplaced in a deep marine environment. We do not find high seismic velocities in the lower crust, which would indicate high mantle temperatures. The absence of high velocities in the lower crust is consistent with emplacement of the Walvis Ridge on young oceanic crust. The magmatic material north of the ridge indicates that extensive volcanism occurred after the Sao Paolo Plateau sheared off the Walvis Ridge along the FFZ. The basaltic layers cover and obscure the FFZ. Therefore they have been emplaced after the active phase of the transform fault. But the oceanic crust north of the fracture zone, which is buried beneath this basalt layers, has formed at a time when the hotspot was already further away. Therefore, this volcanic activity likely occurred as second stage volcanism and not together with the formation of the main Walvis Ridge. The activation of the transform fault might have triggered this second stage volcanism, opening new pathways for hotspot melt trapped beneath the lithosphere. The large distance between the fracture zone and the centre of the Walvis Ridge suggest that both structures evolved independently from each other. Therefore, we support a hotspot origin of the the ridge and reject a major role of the fracture zone in the emplacement of the Walvis Ridge.

4   Conclusions

The aim of this thesis was to determine the crustal structure of the Walvis Ridge and to interpret the results within the geodynamic framework. I could address all of objectives raised in section 1.3.

The extent and volume of magmatic underplating
I found magmatic underplating in form of a high velocity lower crustal body (HVLCB) at the continental margin. Its western termination is at a similar distance from the shore as observed at other seismic profiles south of the Walvis Ridge. But unlike these profiles south of the Walvis Ridge, the eastern boundary of the HVLCB intrudes 100 km further into the continental crust. Yet, the thickness of this HVLCB is not greater than at the southern profiles. To summarize, the Walvis Ridge does not display a further/additional thickening of the HVLCB but an increased extent towards the continental crust.

Interaction of continental lithosphere and the proposed plume
The continental crust is affected by high seismic velocities indicating intruded plume material in prolongation of the Walvis Ridge. The intrusive body terminates at the Kaoko fold belt, which has an otherwise undisturbed crustal root. A complementary, orthogonal oriented, seismic profile confirms the existence of this intrusion and further constrains its width. It is narrower than observed offshore and as wide as the northern Etendeka flood basalts. Thus, the proposed mantle plume affected only a small area of continental crust.

Implications of pre-existing continental structures
The northern Etendeka flood basalts are oriented parallel or coincident with deep reaching faults, which likely acted as migration paths. However, these faults reach further than the surface basalts and the crustal underplating. I therefore conclude that the mantle anomaly at the time of breakup had only limited extent. A broad plume head should have affected the crust over a large area, especially in the presence of existing faults, and not only localized to the onset of the Walvis Ridge. I interpret the HVLCB to have been created by a small mantle anomaly, which we may call hotspot or plume tail.

A plume initiated breakup?
The localized crustal modification suggests that no plume head existed during the initial rift stage. Therefore it is unlikely that the South Atlantic opening was initiated by an arriving plume head.

The origin of the Walvis Ridge and the importance of fracture zones
The Walvis Ridge consists of thickened oceanic crust composed of pillow basalts, sheeted dikes and gabbros. Numerous seamounts are buried beneath a thick sediment cover at the massive eastern Walvis Ridge revealing a continuation of the

western guyot province. Further offshore a fracture zone is covered by basaltic material indicating active volcanism after the transform fault has become inactive. The centre of the Walvis Ridge is 100 km south of this fracture zone and both seem to have been formed independently from each other. I therefore conclude that the Walvis Ridge is not a leaky fracture zone, but instead is derived from a local mantle anomaly.

The evolution of the Walvis Ridge
The crustal thickness of the Walvis Ridge and the size of buried seamounts decreases with distance from shore, which confirms a previously suggested general decline of hotspot activity. Close to the continental margin I observed volcaniclastic material indicating phreatic eruptions in shallow waters. Further offshore large amounts of volcanic debris are absent indicating a change in the eruption style to deep submarine environment.

Although models are always ambiguous and their interpretation is a subjective matter depending on the current knowledge and zeitgeist, I contributed to the data base which is the foundation for the development of new hypotheses and ideas.

5   Outlook

Even though I could address many research objections, I also discovered new details, which rose new questions. I showed that at least some volcanism occurred at 6°E after the FFZ became inactive. But has the top basalt layer, covering the FFZ, been emplaced contemporaneously with the Walvis Ridge? If so, the reconstructed trail of the Tristan hotspot and the opening of the South Atlantic need to be revised. If not, what caused the late stage volcanism? Further age constraints are required to be able to analyse the sequence of events. Rock samples have already been collected in that region and new datings will clarify the situation (Hoernle et al., 2014).

I revealed distinct changes along the Walvis Ridge: from subaerial to submarine eruption style; a change in timing between the formation of the ridge and the activation of the FFZ; and finally, a slight decrease in volcanic activity observed in decreasing seamount sizes and crustal thickness. We know that the crustal thickness further decreases in the guyot province, but what about the massive N-S oriented portion of the ridge at 5° E? The bathymetric expression suggest a crustal thickening, but we've been fooled by bathymetry before. Is there another change in the eruption style? Back to phreatic eruptions? What happened at the conjugate Rio Grande Rise? Is it constructed with the same architecture as its counterpart? Have the Rio Grande Rise and the Walvis Ridge been emplaced as a single large plateau like Iceland today? Deep seismic profiles across both structures are needed to constrain this chapter in the history of the Walvis Ridge.

If the debate between plume- and plates-adherer will ever be solved is uncertain. We rely on indirect measurements, laboratory experiments and simulations to make an educated guess about the Earth's interior, which is out of our direct reach. The fracture zone seems to have had no influence on the formation of Walvis Ridge and I favour a mantle anomaly as a source of the Walvis Ridge. We may call it plume or a fertile patch of inhomogeneous mantle. The possibility of a deep mantle plume cannot be ruled out and crustal thickness is a key observable for testing simulations of mantle plumes. The crustal models can then be compared to numerical simulations of plume derived thickened crust. R. Gassmöller has already compared a plume simulation to the 'real world' crustal thickness derived from the seismic model at 6°E (Gassmöller et al., 2015). With this method we can test sets of mantle parameters (e.g. temperature or flow rate), which best account for the observed crustal thickness. This procedure could be applied to the whole Walvis Ridge using a regional 3D gravity model. The available seismic data can be used to constrain the gravity model and to extrapolate crustal thickness for the whole area.

The indications for a hotspot trace underneath the African continent contradict the reconstructions of the early hotspot path. Current models predict presence of the early Tristan hotspot at the South American plate. But this is the result of the presumption that the Tristan hotspot has been close to the large Paraná flood basalts. As a consequence, plates reveal an irregular movement during the

initial rifting and breakup of Gondwana. Furthermore, a rather large mobility of the hotspot itself is required and conflicts with the plume model prediction of the fixity of mantle plumes. New reconstructions without these assumptions should be evaluated for a possible hotspot trace beneath the African continent as initially proposed by Duncan, 1984.

References

Adam, C., V. Vidal, and J. Escartín (2007). "80-Myr history of buoyancy and volcanic fluxes along the trails of the Walvis and St. Helena hotspots (South Atlantic)". In: *Earth and Planetary Science Letters* 261.3, pp. 432–442.

Anderson, D. L. (2001). "Top-down tectonics?" In: *Science* 293.5537, pp. 2016–2018.

Anderson, D. L. (2005). "Scoring hotspots: The plume and plate paradigms". In: *Geological Society of America Special Papers* 388, pp. 31–54.

Anderson, D. L. and W. B. Hamilton (2008). "Zombie Science & Geoscience". http://www.mantleplumes.org/Zombie.html.

Anderson, D. L. and J. H. Natland (2007). "Evidence for mantle plumes?" In: *Nature* 450.7169, E15–E15.

Armitage, J. J., J. S. Collier, and T. A. Minshull (2010). "The importance of rift history for volcanic margin formation". In: *Nature* 465.7300, pp. 913–917.

Bailey, K. and G. Foulger (2003). "Tristan volcano complex: oceanic end-point of a major African lineament". In: Penrose Conference: Hveragerdi, Iceland.

Bauer, K., S. Neben, B. Schreckenberger, R. Emmermann, K. Hinz, N. Fechner, K. Gohl, A. Schulze, R. Trumbull, and K. Weber (2000). "Deep structure of the Namibia continental margin as derived from integrated geophysical studies". In: *Journal of Geophysical Research* 105.B11, pp. 25829–25.

Becker, K., D. Franke, R. B. Trumbull, M. Schnabel, I. Heyde, B. Schreckenberger, H. Koopmann, K. Bauer, W. Jokat, and C. M. Krawczyk (2014). "Asymmetry of high-velocity lower crust on the South Atlantic rifted margins and implications for the interplay of magmatism and tectonics in continental break-up". In: *Solid Earth Discussions* 6.1, pp. 1335–1370.

Behn, M. D., J. M. Sinton, and R. S. Detrick (2004). "Effect of the Galápagos hotspot on seafloor volcanism along the Galápagos Spreading Center (90.9–97.6°W)". In: *Earth and Planetary Science Letters* 217.3–4, pp. 331 –347.

Behrmann, J., L. Planert, A. Shulgin, H. Kraft, P. Schröder, and E. Labahn (2012). *Plumes, Large Igneous Province Rocks and associated deformation: a geophysical study of Walvis Ridge, offshore Namibia*. Tech. rep. Leitstelle Deutsche Forschungsschiffe Institut für Meereskunde der Universität Hamburg.

Bolli, H., W. Ryan, J. Foresman, W. Hottman, H Kagami, J. Longoria, B. McKnight, M Melguen, J Natland, F Proto Decima, et al. (1978). "Walvis Ridge – Sites 362 and 363". In: *Initial Rep. Deep Sea Drill. Proj* 40, pp. 183–356.

Braile, L. W. and R. B. Smith (1975). "Guide to the Interpretation of Crustal Refraction Profiles". In: *Geophysical Journal International* 40.2, pp. 145–176.

Brune, S., A. A. Popov, and S. V. Sobolev (2012). "Modeling suggests that oblique extension facilitates rifting and continental break-up". In: *Journal of Geophysical Research: Solid Earth (1978–2012)* 117.B8.

Brune, S., A. A. Popov, and S. V. Sobolev (2013). "Quantifying the thermomechanical impact of plume arrival on continental break-up". In: *Tectonophysics* 604, pp. 51–59.

Bryan, S. E. and L. Ferrari (2013). "Large igneous provinces and silicic large igneous provinces: Progress in our understanding over the last 25 years". In: *Geological Society of America Bulletin* 125.7-8, pp. 1053–1078.

Buiter, S. J. and T. H. Torsvik (2014). "A review of Wilson Cycle plate margins: A role for mantle plumes in continental break-up along sutures?" In: *Gondwana Research* 26.2, pp. 627–653.

Cande, S. C., J. L. Labrecque, R. L. Larson, W. Pittman III, and X. Golovchenko (1989). *Magnetic lineations of the world's ocean basins*. Tulsa, OK, United States (USA).

Cande, S. C. and D. R. Stegman (2011). "Indian and African plate motions driven by the push force of the Reunion plume head". In: *Nature* 475.7354, pp. 47–52.

Cappelletti, A., F. Tsikalas, Y. Nestola, C. Cavozzi, A. Argnani, M. Meda, and F. Salvi (2013). "Impact of lithospheric heterogeneities on continental rifting evolution: Constraints from analogue modelling on South Atlantic margins". In: *Tectonophysics* 608, pp. 30–50.

Christensen, N. and W. Mooney (1995). "Seismic velocity structure and composition of the continental crust: A global view". In: *Journal of Geophysical Research* 100.B7, pp. 9761–9788.

Christensen, N. I. (1982). "Seismic velocities". In: *Handbook of physical properties of rocks*. Vol. 2. CRC Press, Boca Raton, Florida, pp. 1–228.

Coffin, M. F., R. A. Duncan, O. Eldholm, J. G. Fitton, F. A. Frey, H. C. Larsen, J. J. Mahoney, A. D. Saunders, R. Schlich, and P. J. Wallace (2006). "Large igneous provinces and scientific ocean drilling: Status quo and a look ahead". In: *Oceanography* 19.4, pp. 150–160.

Collier, J., T. Minshull, J. Hammond, R. Whitmarsh, J. Kendall, V. Sansom, C. Lane, and G. Rumpker (2009). "Factors influencing magmatism during continental breakup: New insights from a wide-angle seismic experiment across the conjugate Seychelles-Indian margins". In: *Journal of Geophysical Research* 114.B3, B03101.

Comin-Chiaramonti, P, A De Min, V. Girardi, and E Ruberti (2011). "Post-Paleozoic magmatism in Angola and Namibia: a review". In: *Geological Society of America Special Papers* 478, pp. 223–247.

Contreras-Reyes, E., I. Grevemeyer, A. Watts, L. Planert, E. R. Flueh, and C Peirce (2010). "Crustal intrusion beneath the Louisville hotspot track". In: *Earth and Planetary Science Letters* 289.3, pp. 323–333.

Contrucci, I., L. Matias, M. Moulin, L. Géli, F. Klingelhofer, H. Nouzé, D. Aslanian, J. Olivet, J. Réhault, and J. Sibuet (2004). "Deep structure of the West African continental margin (Congo, Zaire, Angola), between 5 S and 8 S, from reflection/refraction seismics and gravity data". In: *Geophysical Journal International* 158.2, pp. 529–553.

Courtillot, V., C. Jaupart, I. Manighetti, P. Tapponnier, and J. Besse (1999). "On causal links between flood basalts and continental breakup". In: *Earth and Planetary Science Letters* 166, pp. 177–195.

Courtillot, V., A. Davaille, J. Besse, and J. Stock (2003). "Three distinct types of hotspots in the Earth's mantle". In: *Earth and Planetary Science Letters* 205.3–4, pp. 295 –308.

Crough, S. T., W. J. Morgan, and R. B. Hargraves (1980). "Kimberlites: their relation to mantle hotspots". In: *Earth and Planetary Science Letters* 50.1, pp. 260–274.

Davis, A. S., L. B. Gray, D. A. Clague, and J. R. Hein (2002). "The Line Islands revisited: New 40Ar/39Ar geochronologic evidence for episodes of volcanism due to lithospheric extension". In: *Geochemistry, Geophysics, Geosystems* 3.3, pp. 1–28.

Duncan, R. A. (1984). "Age progressive volcanism in the New England seamounts and the opening of the central Atlantic Ocean". In: *Journal of Geophysical Research: Solid Earth (1978–2012)* 89.B12, pp. 9980–9990.

Eagles, G. (2007). "New angles on South Atlantic opening". In: *Geophysical Journal International* 168.1, pp. 353–361.

Elliott, G., C. Berndt, and L. Parson (2009). "The SW African volcanic rifted margin and the initiation of the Walvis Ridge, South Atlantic". In: *Marine Geophysical Research* 30.3, pp. 207–214.

Ernesto, M., L. Marques, E. Piccirillo, E. Molina, N. Ussami, P. Comin-Chiaramonti, and G. Bellieni (2002). "Paraná Magmatic Province–Tristan da Cunha plume system: fixed versus mobile plume, petrogenetic considerations and alternative heat sources". In: *Journal of Volcanology and Geothermal Research* 118.1, pp. 15–36.

Fairhead, J. D. and M. Wilson (2005). "Plate tectonic processes in the South Atlantic Ocean: Do we need deep mantle plumes?" In: *Geological Society of America Special Papers* 388, pp. 537–553.

Farnetani, C. G., M. A. Richards, and M. S. Ghiorso (1996). "Petrological models of magma evolution and deep crustal structure beneath hotspots and flood basalt provinces". In: *Earth and Planetary Science Letters* 143.1, pp. 81–94.

Flueh, E. R. and J. Bialas (1996). "A digital, high data capacity ocean bottom recorder for seismic investigations". In: *Int. Underwater Systems Design* 18, pp. 18–20.

Foster, D. A., B. D. Goscombe, and D. R. Gray (2009). "Rapid exhumation of deep crust in an obliquely convergent orogen: The Kaoko Belt of the Damara Orogen". In: *Tectonics* 28.4, TC4002.

Foulger, G. R. (2011). *Plates vs plumes: A geological controversy*. John Wiley & Sons.

Fromm, T. (in review). "PRay - A graphical user interface for interactive visualization and modification of rayinvr models". submitted to Journal of Applied Geophysics.

Fromm, T., W. Jokat, and J. H. Behrmann. "Interaction between hotspot and fracture zone: The crustal structure of Walvis Ridge at 6°E". to be submitted.

Fromm, T., W. Jokat, J. H. Behrmann, T. Ryberg, and M. Weber. "The onset of Walvis Ridge: plume influence at the continental margin". to be submitted.

Fromm, T., L. Planert, W. Jokat, T. Ryberg, M. Weber, and J. H. Behrmann (in review). "South Atlantic opening - A plume induced breakup?" submitted to Geology.

Funck, T., H. R. Jackson, K. E. Louden, and F. Klingelhöfer (2007). "Seismic study of the transform-rifted margin in Davis Strait between Baffin Island (Canada) and Greenland: What happens when a plume meets a transform". In: *Journal of Geophysical Research: Solid Earth (1978–2012)* 112.B4.

Gallagher, K. and C. Hawkesworth (1994). "Mantle plumes, continental magmatism and asymmetry in the South Atlantic". In: *Earth and Planetary Science Letters* 123.1, pp. 105–117.

Gassmöller, R., B. Steinberger, J. Dannberg, E. Bredow, and T. Torsvik (2015). "Models and observations of plume-ridge interaction in the South Atlantic and their implications for crustal thickness variations". In: *EGU General Assembly Conference Abstracts.*

Gee, J. S. and D. V. Kent (2007). "Source of oceanic magnetic anomalies and the geomagnetic polarity time scale". In: *Treatise on Geophysics, vol. 5: Geomagnetism*, pp. 455–507.

Gladczenko, T., J. Skogseid, and O. Eldhom (1998). "Namibia volcanic margin". In: *Marine Geophysical Research* 20.4, pp. 313–341.

Götze, H.-J. and B. Lahmeyer (1988). "Application of three-dimensional interactive modeling in gravity and magnetics". In: *Geophysics* 53.8, pp. 1096–1108.

Grevemeyer, I., E. Flueh, C. Reichert, J. Bialas, D. Kläschen, and C. Kopp (2001). "Crustal architecture and deep structure of the Ninetyeast Ridge hotspot trail from active-source ocean bottom seismology". In: *Geophysical Journal International* 144.2, pp. 414–431.

Grevemeyer, I. and E. R. Flueh (2000). "Crustal underplating and its implications for subsidence and state of isostasy along the Ninetyeast Ridge hotspot trail". In: *Geophysical Journal International* 142.2, pp. 643–649.

Griffin, W., G. Begg, and S. Y. O'Reilly (2013). "Continental-root control on the genesis of magmatic ore deposits". In: *Nature Geoscience* 6.11, pp. 905–910.

Griffiths, R. W. and I. H. Campbell (1990). "Stirring and structure in mantle starting plumes". In: *Earth and Planetary Science Letters* 99.1–2, pp. 66 –78.

Griffiths, R. and I. Campbell (1991). "Interaction of mantle plume heads with the Earth's surface and onset of small-scale convection". In: *Journal of Geophysical Research: Solid Earth (1978–2012)* 96.B11, pp. 18295–18310.

Gurnis, M. (1988). "Large-scale mantle convection and the aggregation and dispersal of supercontinents". In: *Nature* 332.6166, pp. 695–699.

Hagen, C. (2008). "Krustenstruktur des Agulhas-Rückens und der Cape Rise Seamounts zwischen 38 °-42 ° S und 12 °-16 ° E". Diplomarbeit. Christian-Albrechts-Universitaet zu Kiel.

Haxel, J. and R. Dziak (2005). "Evidence of explosive seafloor volcanic activity from the Walvis Ridge, South Atlantic Ocean". In: *Geophysical research letters* 32.13.

Hay, W. and J. Sibuet (1984). *Initial Reports of the Deep Sea Drilling Project.* Vol. 75. Washington D.C., U.S. Government Printing Office, pp. 295–445.

Heine, C., J. Zoethout, and R. D. Müller (2013). "Kinematics of the South Atlantic rift". In: *arXiv preprint arXiv:1301.2096*.

Heit, B., X. Yuan, W. Geissler, B. Lushetile, M. Weber, and W. Jokat (2013). "Crustal Thickness and Lithospheric Structure in Northwestern Namibia from the WALPASS experiment". In: *EGU General Assembly Conference Abstracts*. Vol. 15, p. 1233.

Heit, B., X. Yuan, M. Weber, W. Geissler, W. Jokat, B. Lushetile, and K.-H. Hoffmann (2015). "Crustal thickness and Vp/Vs ratio in NW Namibia from receiver functions: evidence for magmatic underplating due to mantle-plume – crust interaction." In: *Geophysical Research Letters*.

Hill, D. P. and J. J. Zucca (1987). "Geophysical constraints on the structure of Kilauea and Mauna Loa volcanoes and some implications for seismomagmatic processes". In: *US Geol. Surv. Prof. Pap* 1350.2, pp. 903–917.

Hirano, N., E. Takahashi, J. Yamamoto, N. Abe, S. P. Ingle, I. Kaneoka, T. Hirata, J.-I. Kimura, T. Ishii, Y. Ogawa, et al. (2006). "Volcanism in response to plate flexure". In: *Science* 313.5792, pp. 1426–1428.

Hirsch, K., K. Bauer, and M. Scheck-Wenderoth (2009). "Deep structure of the western South African passive margin—Results of a combined approach of seismic, gravity and isostatic investigations". In: *Tectonophysics* 470.1, pp. 57–70.

Hoernle, K., R. Werner, and C. Lüter (2014). *RV SONNE Fahrtbericht/Cruise Report SO233 WALVIS II, 14.05-21.06. 2014, Cape Town, South Africa-Walvis Bay, Namibia*. Tech. rep. GEOMAR Helmholtz-Zentrum für Ozeanforschung Kiel.

Hofmann, A. W. and S. R. Hart (2007). "Another nail in which coffin?" In: *Science* 315.5808, pp. 39–40.

Holbrook, W., H. Larsen, J. Korenaga, T. Dahl-Jensen, I. Reid, P. Kelemen, J. Hopper, G. Kent, D. Lizarralde, S. Bernstein, et al. (2001). "Mantle thermal structure and active upwelling during continental breakup in the North Atlantic". In: *Earth and Planetary Science Letters* 190.3, pp. 251–266.

Holden, J. C. and P. Vogt (1977). "Graphic solutions to problems of plumacy". In: *Eos, Transactions American Geophysical Union* 58.7, pp. 573–580.

Inoue, H., M. F. Coffin, Y. Nakamura, K. Mochizuki, and L. W. Kroenke (2008). "Intrabasement reflections of the Ontong Java Plateau: Implications for plateau construction". In: *Geochemistry, Geophysics, Geosystems* 9.4.

Ito, G., J. Lin, and C. W. Gable (1996). "Dynamics of mantle flow and melting at a ridge-centered hotspot: Iceland and the Mid-Atlantic Ridge". In: *Earth and Planetary Science Letters* 144, pp. 53 –74.

Jokat, W., T. Boebel, M. König, and U. Meyer (2003). "Timing and geometry of early Gondwana breakup". In: *Journal of Geophysical Research* 108.B9.

Kessling, S. (2008). "Die Tiefenstruktur der Kruste des Discovery Seamounts und des südlichen Walfischrückens im Südatlantik". Diplomarbeit. Universitaet Jena.

King, S. D. and D. L. Anderson (1995). "An alternative mechanism of flood basalt formation". In: *Earth and Planetary Science Letters* 136.3, pp. 269–279.

King, S. D. and J. Ritsema (2000). "African Hot Spot Volcanism: Small-Scale Convection in the Upper Mantle Beneath Cratons". In: *Science* 290.5494, pp. 1137–1140.

Korenaga, J., W. Holbrook, G. Kent, P. Kelemen, R. Detrick, H. Larsen, J. Hopper, and T. Dahl-Jensen (2000). "Crustal structure of the southeast Greenland margin from joint refraction and reflection seismic tomography". In: *Journal of Geophysical Research* 105.B9, pp. 21591–21.

Le Pichon, X. and P. J. Fox (1971). "Marginal offsets, fracture zones, and the early opening of the North Atlantic". In: *Journal of Geophysical Research* 76.26, pp. 6294–6308.

Ludwig, W. J., J. E. Nafe, and C. L. Drake (1970). "Seismic refraction". In: *The sea*. Ed. by A.E.Maxwell. Vol. 4. Part 1. Wiley-Intersci., Hoboken,N. J., pp. 53–84.

Lundin, E. and A. Doré (2005). "NE Atlantic break-up: a re-examination of the Iceland mantle plume model and the Atlantic–Arctic linkage". In: *Geological Society, London, Petroleum Geology Conference series*. Vol. 6. Geological Society of London, pp. 739–754.

Lundin, E. R. and A. G. Doré (2011). "Hyperextension, serpentinization, and weakening: A new paradigm for rifted margin compressional deformation". In: *Geology* 39.4, pp. 347–350.

Lutter, W., R. Nowack, and L. Braile (1990). "Seismic imaging of upper crustal structure using travel times from the PASSCAL Ouachita experiment". In: *Journal of Geophysical Research: Solid Earth (1978–2012)* 95.B4, pp. 4621–4631.

Maystrenko, Y. P., M. Scheck-Wenderoth, A. Hartwig, Z. Anka, A. B. Watts, K. K. Hirsch, and S. Fishwick (2013). "Structural features of the Southwest African continental margin according to results of lithosphere-scale 3D gravity and thermal modelling". In: *Tectonophysics* 604, pp. 104–121.

McNutt, M. K., D. W. Caress, J. Reynolds, K. A. Jordahl, and R. A. Duncan (1997). "Failure of plume theory to explain midplate volcanism in the southern Austral islands". In: *Nature* 389.6650, pp. 479–482.

McNutt, M. K. (2006). "Another nail in the plume coffin?" In: *Science* 313.5792, p. 1394.

Mohriak, W., M Nóbrega, M. Odegard, B. Gomes, and W. Dickson (2010). "Geological and geophysical interpretation of the Rio Grande Rise, south-eastern Brazilian margin: extensional tectonics and rifting of continental and oceanic crusts". In: *Petroleum Geoscience* 16.3, pp. 231–245.

Moore, A., T. Blenkinsop, and F. W. Cotterill (2008). "Controls on post-Gondwana alkaline volcanism in Southern Africa". In: *Earth and Planetary Science Letters* 268.1, pp. 151–164.

Morgan, W. J. (1971). "Convection plumes in the lower mantle". In: *Nature* 230.

Morgan, W. (1981). *Hotspot tracks and the opening of the Atlantic and Indian oceans*. Vol. 7. The Sea. Wiley Interscience, pp. 443–487.

Moulin, M., D. Aslanian, and P. Unternehr (2010). "A new starting point for the South and Equatorial Atlantic Ocean". In: *Earth-Science Reviews* 98.1–2, pp. 1 –37.

Nürnberg, D. and R. D. Müller (1991). "The tectonic evolution of the South Atlantic from Late Jurassic to present". In: *Tectonophysics* 191.1, pp. 27–53.

O'Connor, J. and R. Duncan (1990). "Evolution of the Walvis Ridge-Rio Grande rise hot spot systen: implications for African and South American plate motions over plumes". In: *Journal of Geophysical Research* 95.B11, pp. 17475–17502.

O'Connor, J. and W. Jokat (in prep). "Evidence for a buried plume track in the Walvis Ridge Tristan-Gough plume trail discovered buried in the Walvis Ridge Newly discovered seamount chains reveal a buried plume trail in the Walvis Ridge". In:

O'Connor, J., W. Jokat, A. le Roex, C. Class, J. Wijbrans, S. Keßling, K. Kuiper, and O. Nebel (2012). "Hotspot trails in the South Atlantic controlled by plume and plate tectonic processes". In: *Nature Geoscience.*

Pavlis, N. K., S. A. Holmes, S. C. Kenyon, and J. K. Factor (2008). "An earth gravitational model to degree 2160: EGM2008". In: *EGU General Assembly*, pp. 13–18.

Peate, D. W. (1997). "The Paraná-Etendeka Province". In: *Large igneous provinces: Continental, oceanic, and planetary flood volcanism*, pp. 217–245.

Pérez-Díaz, L. and G. Eagles (2014). "Constraining South Atlantic growth with seafloor spreading data". In: *Tectonics* 33.9, pp. 1848–1873.

Planert, L., J. Behrmann, B. Heincke, A. Marti, A. Neska, M. Jegen, W. Jokat, and T. Ryberg (2013). "Geophysical constraints on the structure of the SW African passive continental margin around Walvis Ridge". In: *Sample Colloquium.*

Rabinowitz, P. D. and J. LaBrecque (1979). "The Mesozoic South Atlantic Ocean and evolution of its continental margins". In: *Journal of Geophysical Research: Solid Earth (1978–2012)* 84.B11, pp. 5973–6002.

Raddick, M. J., E. Parmentier, and D. S. Scheirer (2002). "Buoyant decompression melting: A possible mechanism for intraplate volcanism". In: *Journal of Geophysical Research: Solid Earth (1978–2012)* 107.B10, ECV–7.

Renne, P. R., J. M. Glen, S. C. Milner, and A. R. Duncan (1996). "Age of Etendeka flood volcanism and associated intrusions in southwestern Africa". In: *Geology* 24.7, pp. 659–662.

Richards, M., E. Contreras-Reyes, C. Lithgow-Bertelloni, M. Ghiorso, and L. Stixrude (2013). "Petrological interpretation of deep crustal intrusive bodies beneath oceanic hotspot provinces". In: *Geochemistry, Geophysics, Geosystems* 14.3, pp. 604–619.

Richards, M. A., R. A. Duncan, and V. E. Courtillot (1989). "Flood basalts and hot-spot tracks: plume heads and tails". In: *Science* 246.4926, pp. 103–107.

Richards, M. A., D. L. Jones, R. A. Duncan, and D. J. DePaolo (1991). "A mantle plume initiation model for the Wrangellia flood basalt and other oceanic plateaus". In: *Science* 254.5029, pp. 263–267.

Richardson, K., J. Smallwood, R. White, D. Snyder, and P. Maguire (1998). "Crustal structure beneath the Faroe Islands and the Faroe–Iceland ridge". In: *Tectonophysics* 300.1, pp. 159–180.

Ridley, V. A. and M. A. Richards (2010). "Deep crustal structure beneath large igneous provinces and the petrologic evolution of flood basalts". In: *Geochemistry Geophysics Geosystems* 11.9, Q09006.

Rohde, J. K., P. van den Bogaard, K. Hoernle, F. Hauff, and R. Werner (2012). "Evidence for an age progression along the Tristan-Gough volcanic track from new 40Ar/39Ar ages on phenocryst phases". In: *Tectonophysics* 604, pp. 60–71.

Ryberg, T., C. Haberland, M. Weber, W. Jokat, J. H. Behrmann, and A. Gassner (2014). *LISPWAL : Lithospheric structure of the Namibian Continental passive margin at the intersection with the Walvis Ridge from amphibious seismic investigations ; November 2010 - January 2011 Namibia.* Tech. rep. Deutsches GeoForschungsZentrum GFZ.

Ryberg, T., C. Haberland, T. Haberlau, M. H. Weber, K. Bauer, J. H. Behrmann, and W. Jokat (2015). "Crustal structure of northwest Namibia: Evidence for plume-rift-continent interaction". In: *Geology* 43.8, pp. 739–742.

Sallarès, V., P. Charvis, E. R. Flueh, and J. Bialas (2003). "Seismic structure of Cocos and Malpelo Volcanic Ridges and implications for hot spot-ridge interaction". In: *Journal of geophysical research* 108.B12, p. 2564.

Sallarès, V., P. Charvis, E. R. Flueh, and J. Bialas (2005). "Seismic structure of the Carnegie ridge and the nature of the Galapagos hotspot". In: *Geophysical Journal International* 161.3, pp. 763–788.

Sandwell, D. T. and W. H. Smith (2009). "Global marine gravity from retracked Geosat and ERS-1 altimetry: Ridge segmentation versus spreading rate". In: *Journal of Geophysical Research: Solid Earth (1978–2012)* 114.B1.

Sandwell, D. T., R. D. Müller, W. H. F. Smith, E. Garcia, and R. Francis (2014). "New global marine gravity model from CryoSat-2 and Jason-1 reveals buried tectonic structure". In: *Science* 346.6205, pp. 65–67.

Schinkel, J. (2006). "Tiefenstruktur der Kontinent-Ozean-Grenze vor dem Orange Fluss, Namibia". Diplomarbeit. Friedrich-Schiller-Universitaet Jena.

Seton, M, R. Müller, S Zahirovic, C Gaina, T Torsvik, G Shephard, A Talsma, M Gurnis, M Turner, and M Chandler (2012). "Global continental and ocean basin reconstructions since 200 Ma". In: *Earth-Science Reviews* 113.3-4, pp. 212–270.

Sheth, H. (1999). "Flood basalts and large igneous provinces from deep mantle plumes: fact, fiction, and fallacy". In: *Tectonophysics* 311.1, pp. 1–29.

Sibuet, J.-C., W. Hay, A. Prunier, L. Montadert, K. Hinz, and J. Fritsch (1984). "The Eastern Walvis Ridge and Adjacent Basins (South Atlantic): Morphology, Stratigraphy, and Structural Evolution in Light of the Results of Legs 40 and 75". In: *Initial Reports of the Deep Sea Drilling Project.* Integrated Ocean Drilling Program (IODP).

Sleep, N. H. (2006). "Mantle plumes from top to bottom". In: *Earth-Science Reviews* 77.4, pp. 231–271.

Sobolev, S. V., A. V. Sobolev, D. V. Kuzmin, N. A. Krivolutskaya, A. G. Petrunin, N. T. Arndt, V. A. Radko, and Y. R. Vasiliev (2011). "Linking mantle plumes,

large igneous provinces and environmental catastrophes". In: *Nature* 477.7364, pp. 312–316.

Song, J. and ten Brink (2004). "RayGUI 2.0 - A Graphical User Interface for Interactive Forward and Inversion Ray-Tracing". In: *U.S. Geological Survey Open-File Report 2004-1426.*

Storey, B. C. (1995). "The role of mantle plumes in continental breakup: case histories from Gondwanaland". In: *Nature* 377.6547, pp. 301–308.

Tan, K.-K., R. B. Thorpe, and Z. Zhao (2011). "On predicting mantle mushroom plumes". In: *Geoscience Frontiers* 2.2, pp. 223–235.

Torsvik, T. H., S. Rousse, C. Labails, and M. A. Smethurst (2009). "A new scheme for the opening of the South Atlantic Ocean and the dissection of an Aptian salt basin". In: *Geophysical Journal International* 177.3, pp. 1315–1333.

Torsvik, T. H., K. Burke, B. Steinberger, S. J. Webb, and L. D. Ashwal (2010). "Diamonds sampled by plumes from the core-mantle boundary". In: *Nature* 466.7304, pp. 352–355.

Turner, S., M. Regelous, S. Kelley, C. Hawkesworth, and M. Mantovani (1994). "Magmatism and continental break-up in the South Atlantic: high precision ^{40}Ar-^{39}Ar geochronology". In: *Earth and Planetary Science Letters* 121.3, pp. 333–348.

Uenzelmann-Neben, G. and K. Gohl (2004). "The Agulhas Ridge, South Atlantic: the peculiar structure of a fracture zone". In: *Marine Geophysical Researches* 25.3-4, pp. 305–319.

Ussami, N., C. A. M. Chaves, L. S. Marques, and M. Ernesto (2012). "Origin of the Rio Grande Rise–Walvis Ridge reviewed integrating palaeogeographic reconstruction, isotope geochemistry and flexural modelling". In: *Geological Society, London, Special Publications* 369.

VanDecar, J., D. James, and M. Assumpção (1995). "Seismic evidence for a fossil mantle plume beneath South America and implications for plate driving forces". In: *Nature* 378.6552, pp. 25–31.

Watts, A. B. and U. S. ten Brink (1989). "Crustal structure, flexure, and subsidence history of the Hawaiian Islands". In: *Journal of Geophysical Research: Solid Earth* 94.B8, pp. 10473–10500.

Watts, A., D. Sandwell, W. Smith, and P. Wessel (2006). "Global gravity, bathymetry, and the distribution of submarine volcanism through space and time". In: *Journal of geophysical research* 111.B8, B08408.

Wessel, P. and W. H. Smith (2000). "GMT-The Generic Mapping Tools". In: *Web site: http://gmt. soest. hawaii. edu.*

White, R. and D. McKenzie (1989). "Magmatism at rift zones: the generation of volcanic continental margins and flood basalts". In: *Journal of Geophysical Research: Solid Earth (1978–2012)* 94.B6, pp. 7685–7729.

White, R., G. Spence, S. Fowler, D. McKenzie, G. Westbrook, and A. Bowen (1987). "Magmatism at rifted continental margins". In: *Nature* 330, pp. 439–444.

White, R., D. McKenzie, and R. O'Nions (1992). "Oceanic crustal thickness from seismic measurements and rare earth element inversions". In: *J. geophys. Res* 97.19, pp. 683–19.

White, R., L. Smith, A. Roberts, P. Christie, N. Kusznir, A. Roberts, D Healy, R Spitzer, A Chappell, J. Eccles, et al. (2008). "Lower-crustal intrusion on the North Atlantic continental margin". In: *Nature* 452.7186, pp. 460–464.

Wilson, J. T. (1965). "Evidence from ocean islands suggesting movement in the earth". In: *Philosophical Transactions of the Royal Society of London. Series A, Mathematical and Physical Sciences* 258.1088, pp. 145–167.

Wolfe, C. J., M. K. McNutt, and R. S. Detrick (1994). "The Marquesas archipelagic apron: Seismic stratigraphy and implications for volcano growth, mass wasting, and crustal underplating". In: *Journal of Geophysical Research: Solid Earth (1978–2012)* 99.B7, pp. 13591–13608.

Zelt, B. (2004a). "vmed - Analysis tool and interactive editor for rayinvr velocity models". In: *Web site: http://www.soest.hawaii.edu/users/bzelt/vmed/vmed.html*.

Zelt, B. (2004b). "ZP - Software for plotting and picking seismic refraction data in SEGY format". In: *http://www.soest.hawaii.edu/users/bzelt/zp/zp.html*.

Zelt, C. A. and R. B. Smith (1992). "Seismic traveltime inversion for 2-D crustal velocity structure". In: *Geophysical Journal International* 108.1, pp. 16–34.

Zelt, C. (1999). "Modelling strategies and model assessment for wide-angle seismic traveltime data". In: *Geophysical Journal International* 139.1, pp. 183–204.

Ziegler, P. A. and S. Cloetingh (2004). "Dynamic processes controlling evolution of rifted basins". In: *Earth-Science Reviews* 64.1-2, pp. 1 –50.

A   Appendix

A.1   Ray tracing results for profile 100
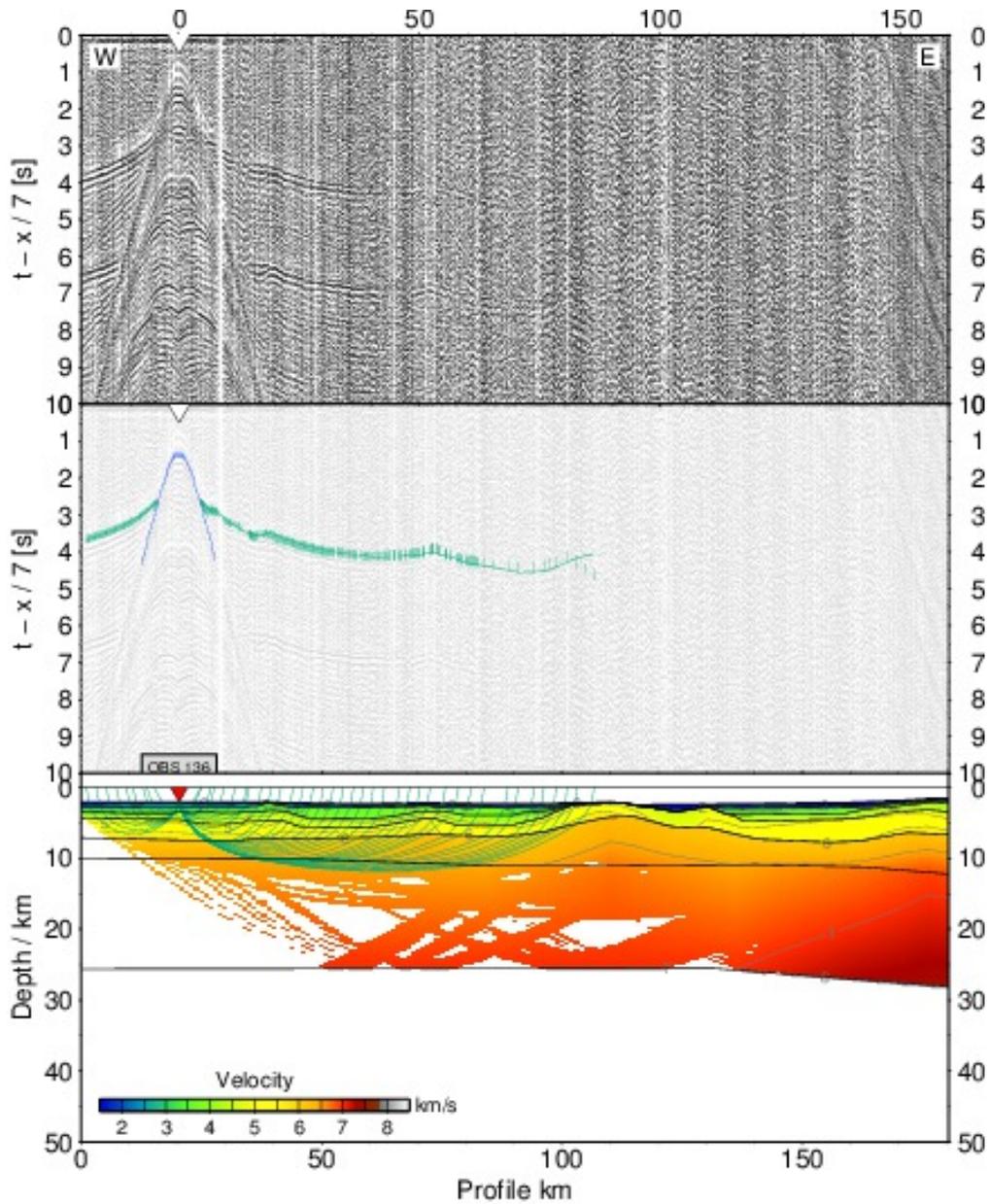
Figure A.1.1: Ray tracing results for station 136, profile 100. top) seismogram, center) seismogram overlain by picked phases (vertical bars) and calculated travel times (lines), bottom) ray path within the model. The uncertainty of the picked phases is resembled by the line length of the vertical bar. Line colors denote the ray type: blue - reflected phase, green - refracted phase
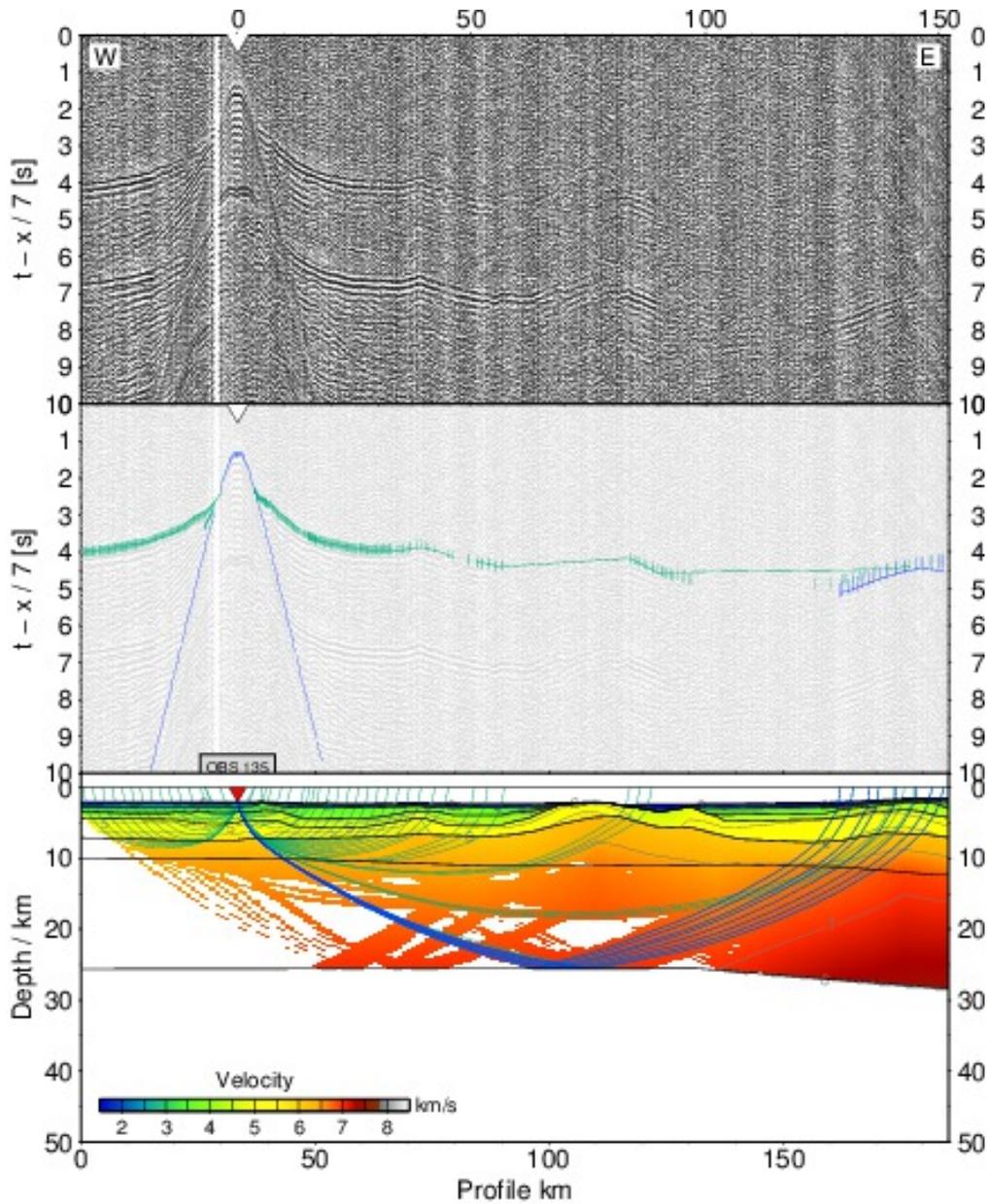
Figure A.1.2: Ray tracing results for station 135, profile 100. top) seismogram, center) seismogram overlain by picked phases (vertical bars) and calculated travel times (lines), bottom) ray path within the model. The uncertainty of the picked phases is resembled by the line length of the vertical bar. Line colors denote the ray type: blue - reflected phase, green - refracted phase
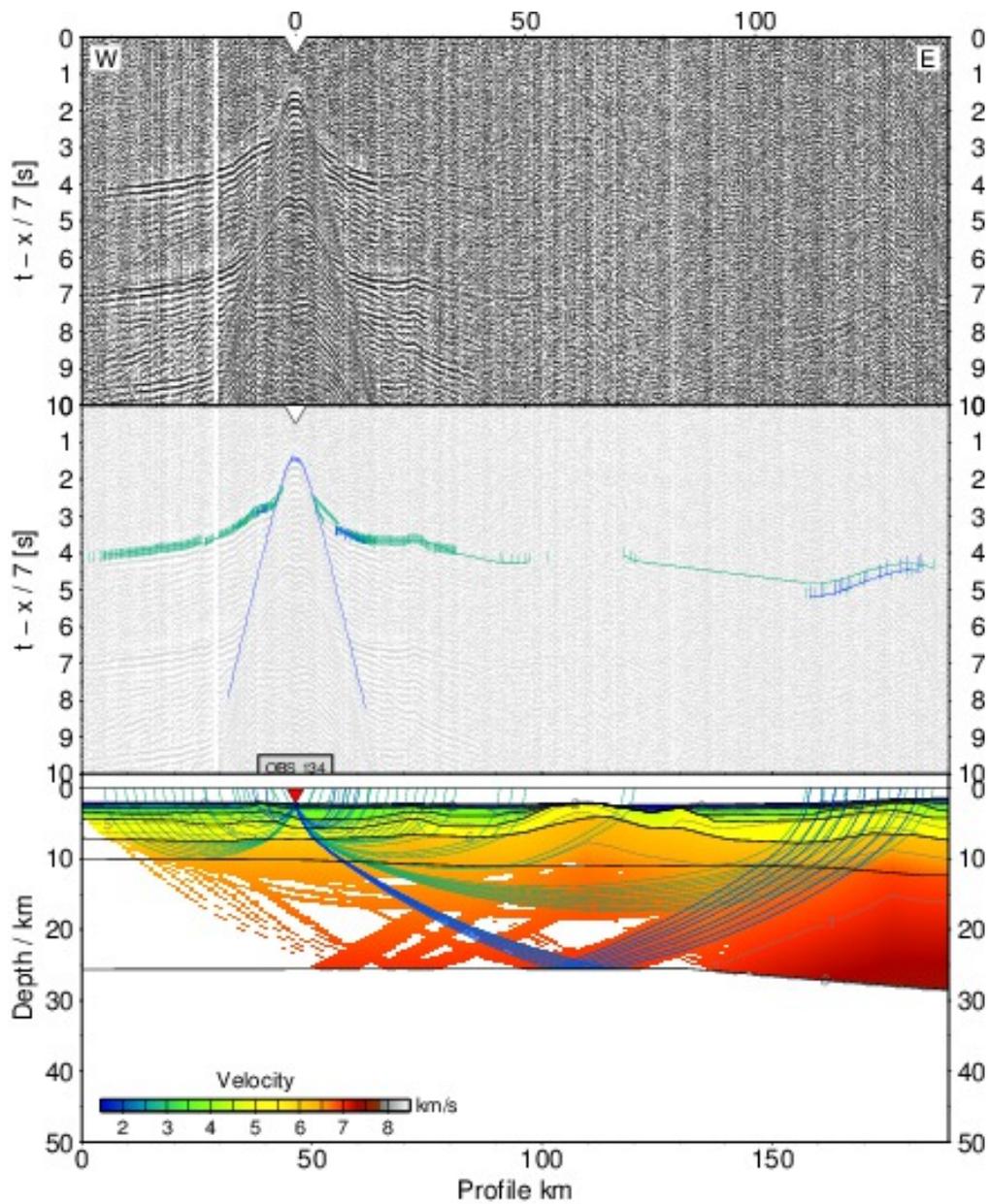
Figure A.1.3: Ray tracing results for station 134, profile 100. top) seismogram, center) seismogram overlain by picked phases (vertical bars) and calculated travel times (lines), bottom) ray path within the model. The uncertainty of the picked phases is resembled by the line length of the vertical bar. Line colors denote the ray type: blue - reflected phase, green - refracted phase
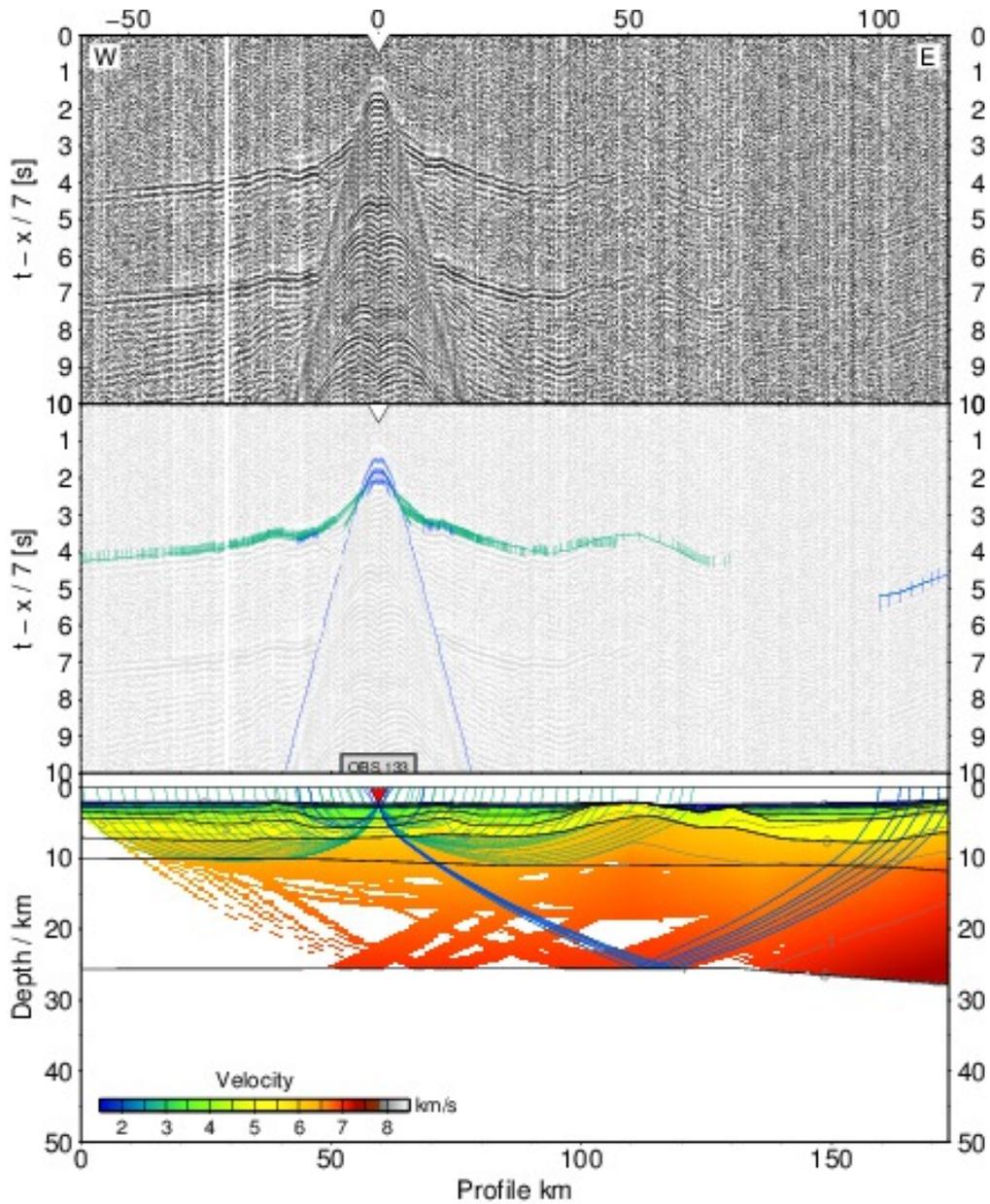
Figure A.1.4:   Ray tracing results for station 133, profile 100. top) seismogram, center) seismogram overlain by picked phases (vertical bars) and calculated travel times (lines), bottom) ray path within the model. The uncertainty of the picked phases is resembled by the line length of the vertical bar. Line colors denote the ray type: blue - reflected phase, green - refracted phase
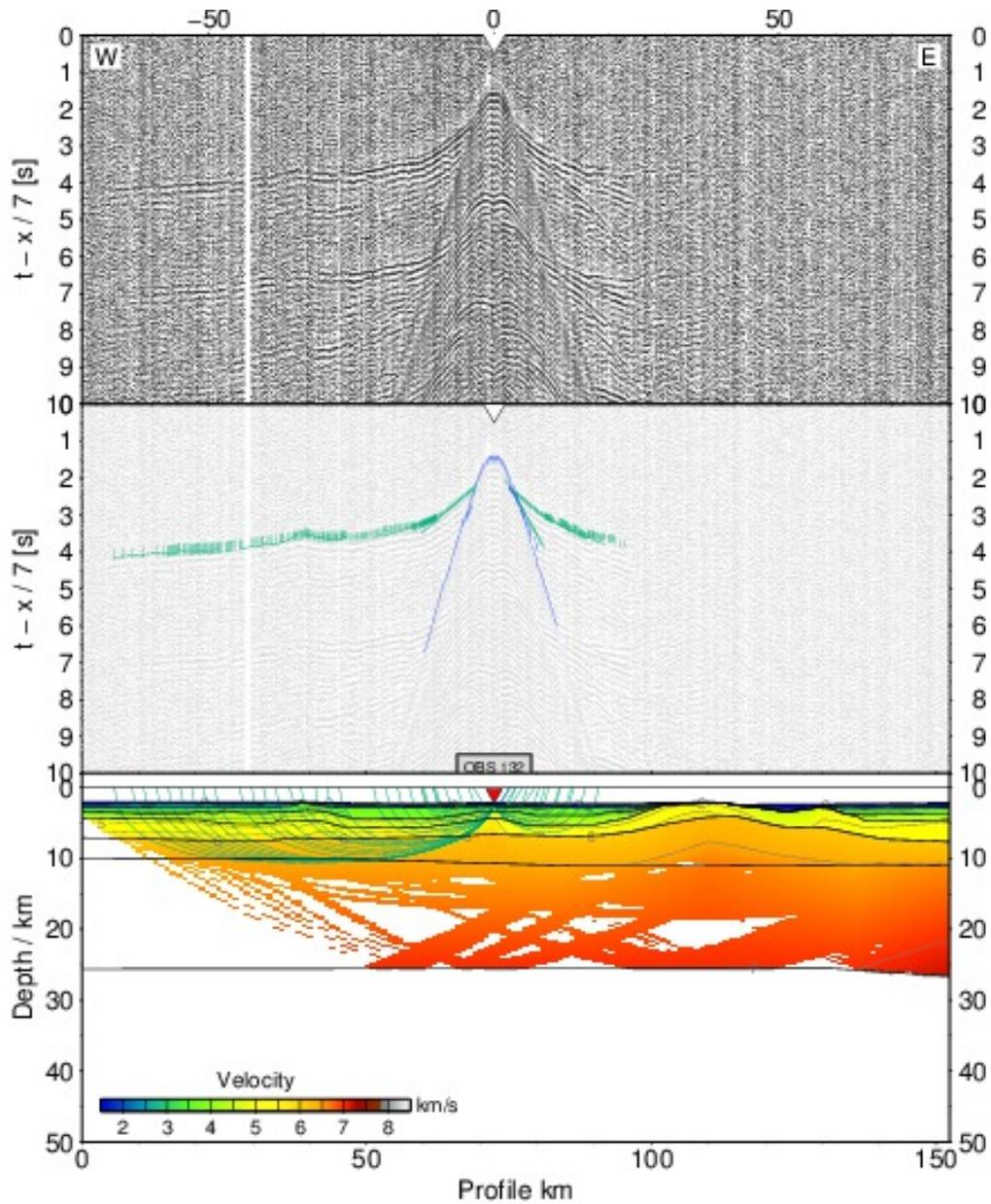
Figure A.1.5: Ray tracing results for station 132, profile 100. top) seismogram, center) seismogram overlain by picked phases (vertical bars) and calculated travel times (lines), bottom) ray path within the model. The uncertainty of the picked phases is resembled by the line length of the vertical bar. Line colors denote the ray type: blue - reflected phase, green - refracted phase
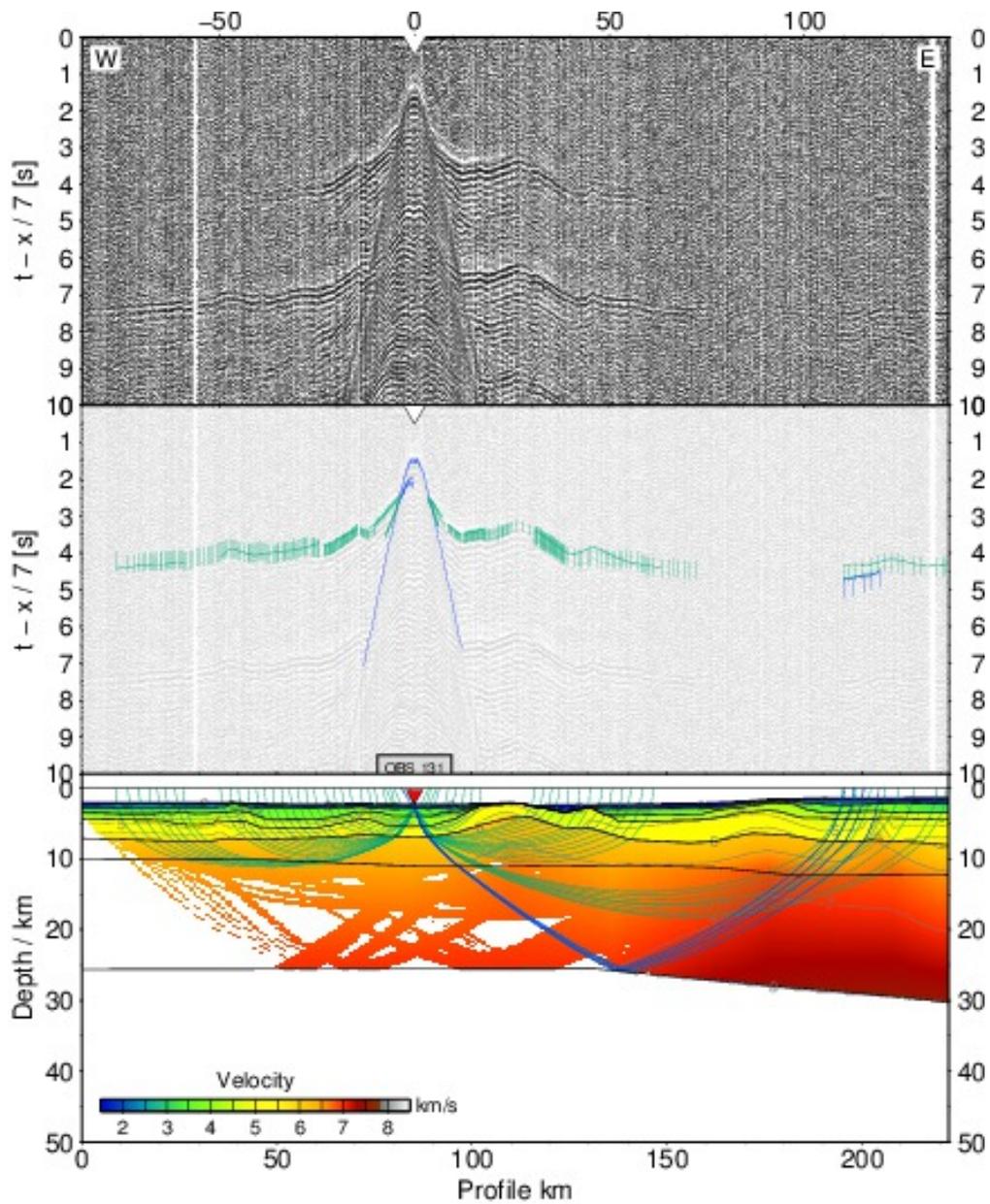
Figure A.1.6: Ray tracing results for station 131, profile 100. top) seismogram, center) seismogram overlain by picked phases (vertical bars) and calculated travel times (lines), bottom) ray path within the model. The uncertainty of the picked phases is resembled by the line length of the vertical bar. Line colors denote the ray type: blue - reflected phase, green - refracted phase
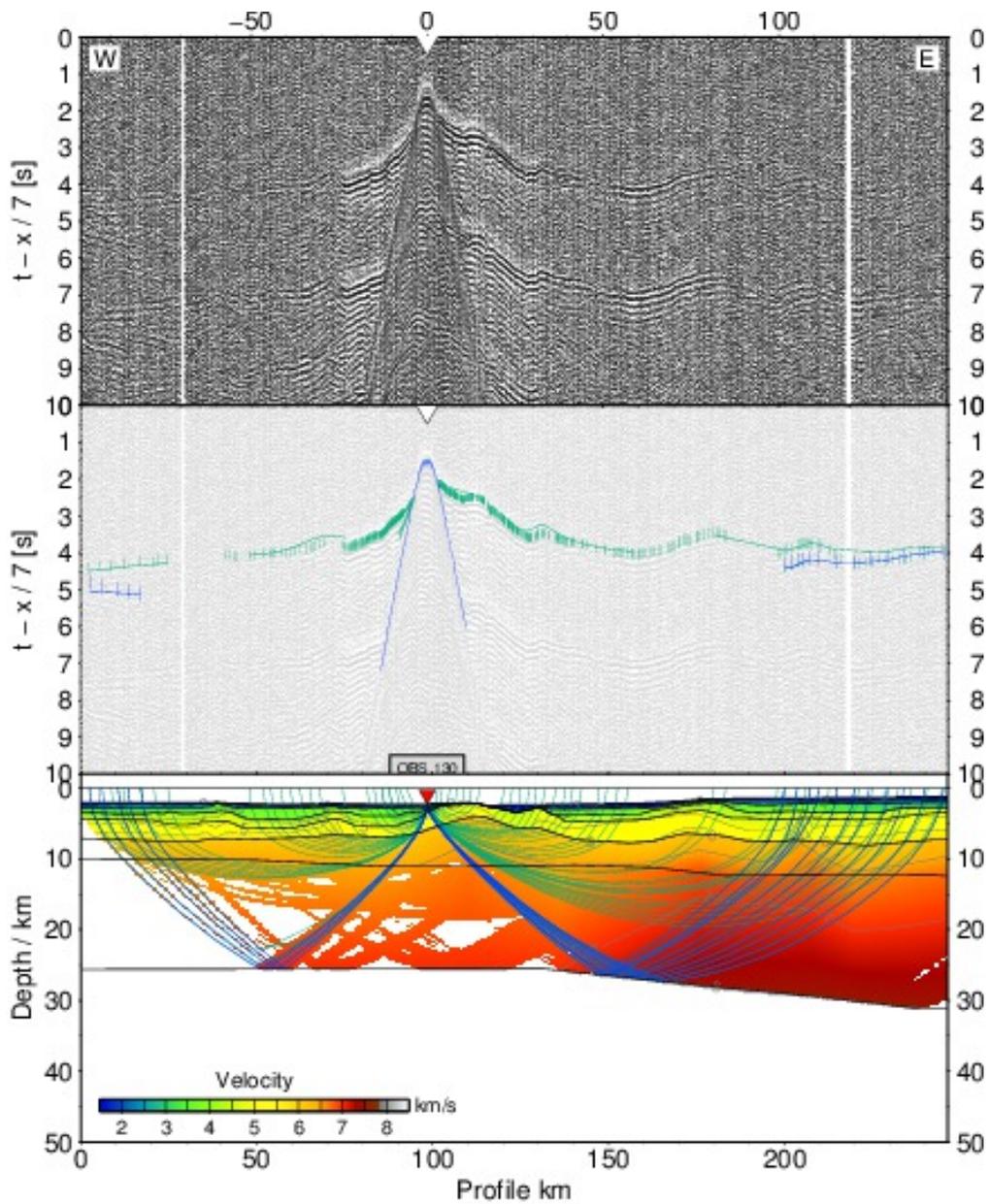
Figure A.1.7: Ray tracing results for station 130, profile 100. top) seismogram, center) seismogram overlain by picked phases (vertical bars) and calculated travel times (lines), bottom) ray path within the model. The uncertainty of the picked phases is resembled by the line length of the vertical bar. Line colors denote the ray type: blue - reflected phase, green - refracted phase
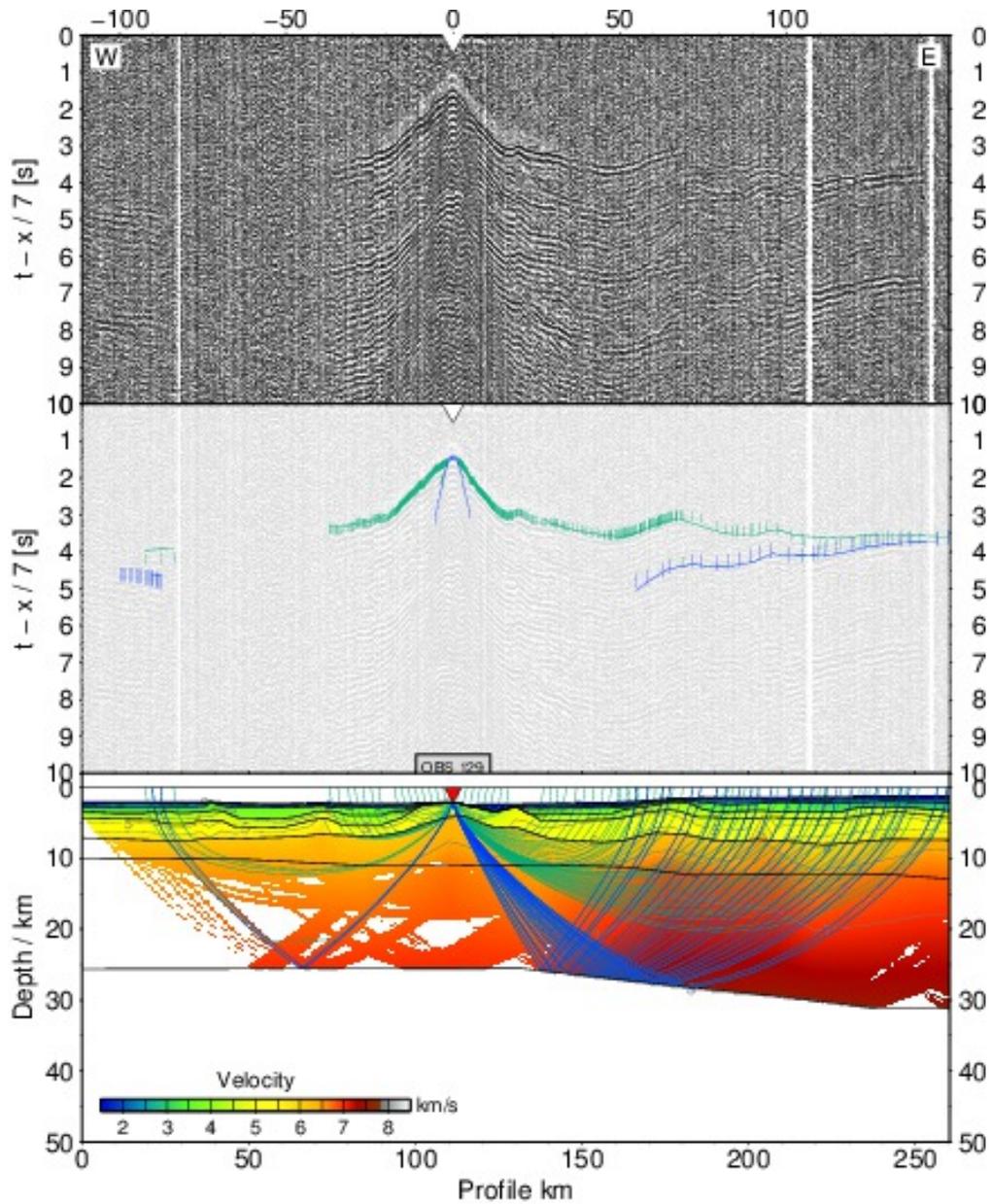
Figure A.1.8: Ray tracing results for station 129, profile 100. top) seismogram, center) seismogram overlain by picked phases (vertical bars) and calculated travel times (lines), bottom) ray path within the model. The uncertainty of the picked phases is resembled by the line length of the vertical bar. Line colors denote the ray type: blue - reflected phase, green - refracted phase
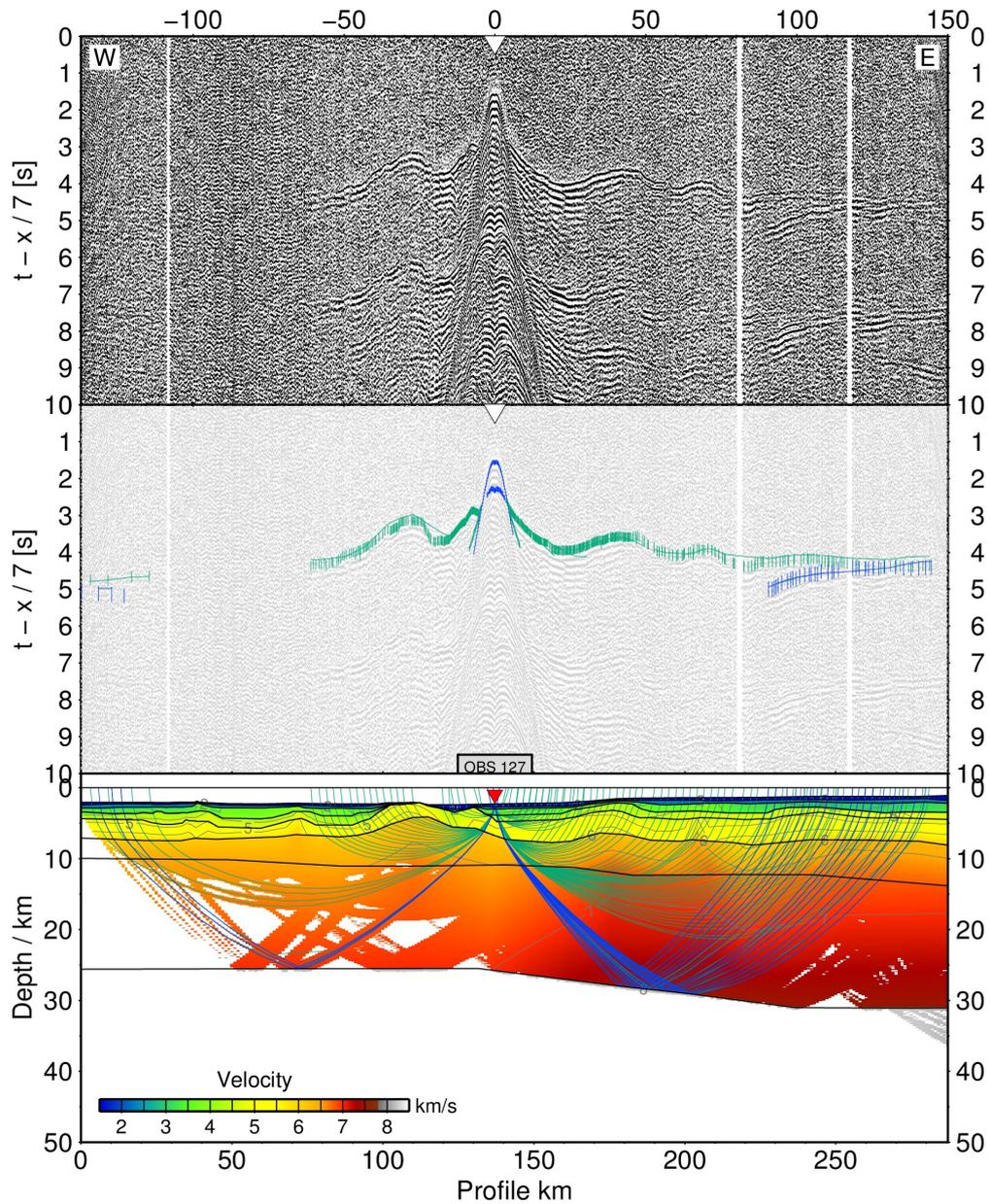
Figure A.1.9: Ray tracing results for station 127, profile 100. top) seismogram, center) seismogram overlain by picked phases (vertical bars) and calculated travel times (lines), bottom) ray path within the model. The uncertainty of the picked phases is resembled by the line length of the vertical bar. Line colors denote the ray type: blue - reflected phase, green - refracted phase
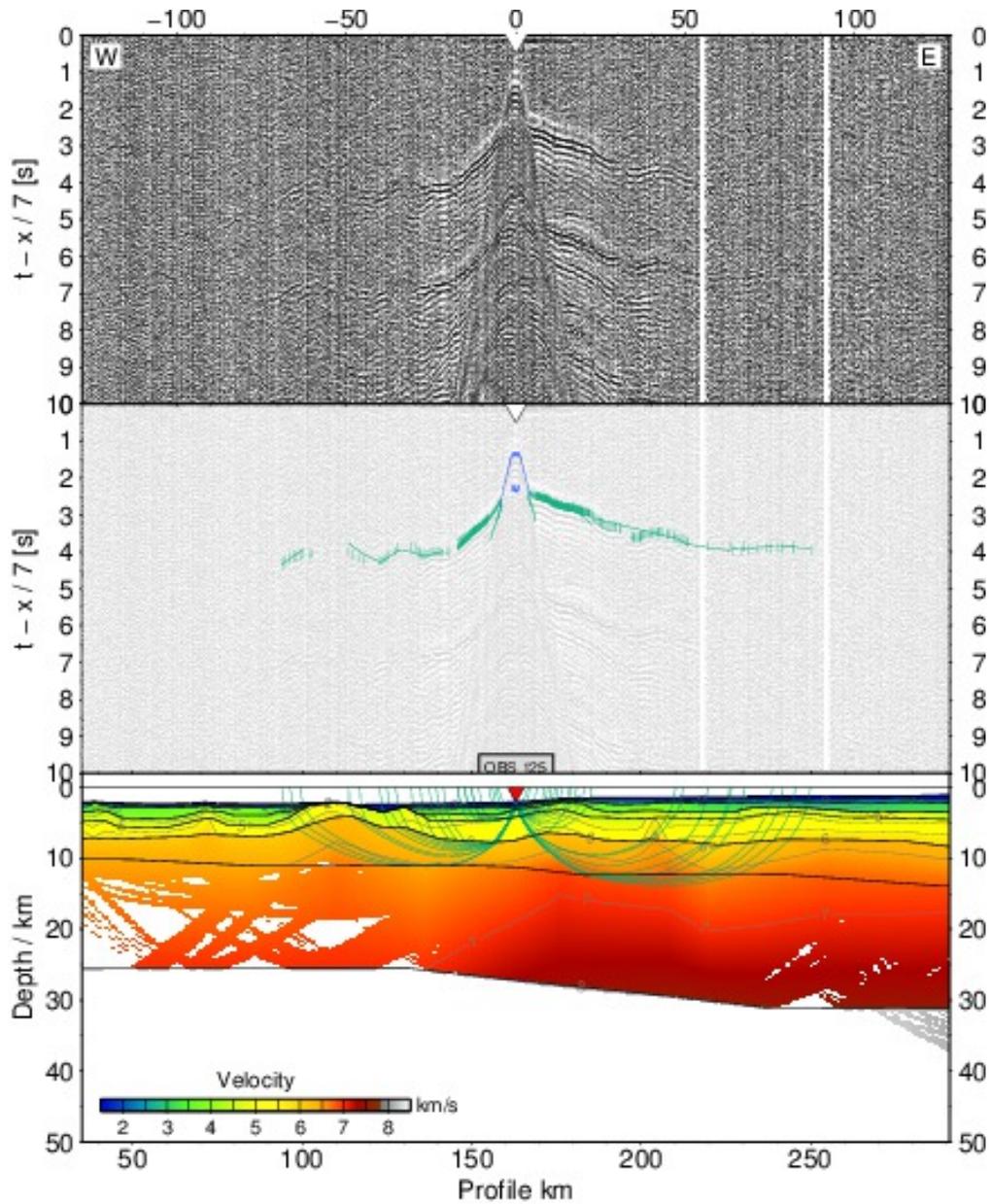
Figure A.1.10: Ray tracing results for station 125, profile 100. top) seismogram, center) seismogram overlain by picked phases (vertical bars) and calculated travel times (lines), bottom) ray path within the model. The uncertainty of the picked phases is resembled by the line length of the vertical bar. Line colors denote the ray type: blue - reflected phase, green - refracted phase
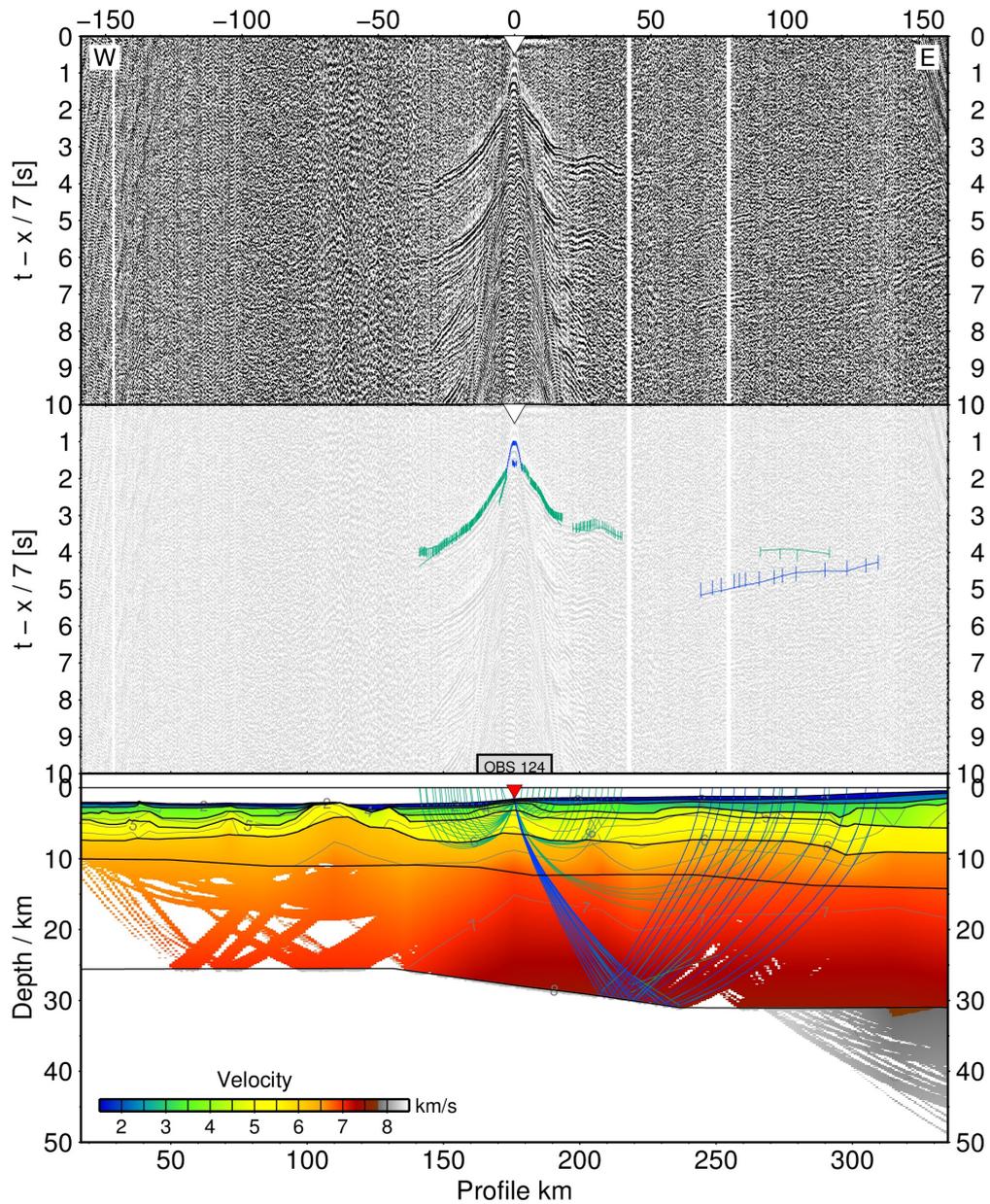
Figure A.1.11: Ray tracing results for station 124, profile 100. top) seismogram, center) seismogram overlain by picked phases (vertical bars) and calculated travel times (lines), bottom) ray path within the model. The uncertainty of the picked phases is resembled by the line length of the vertical bar. Line colors denote the ray type: blue - reflected phase, green - refracted phase
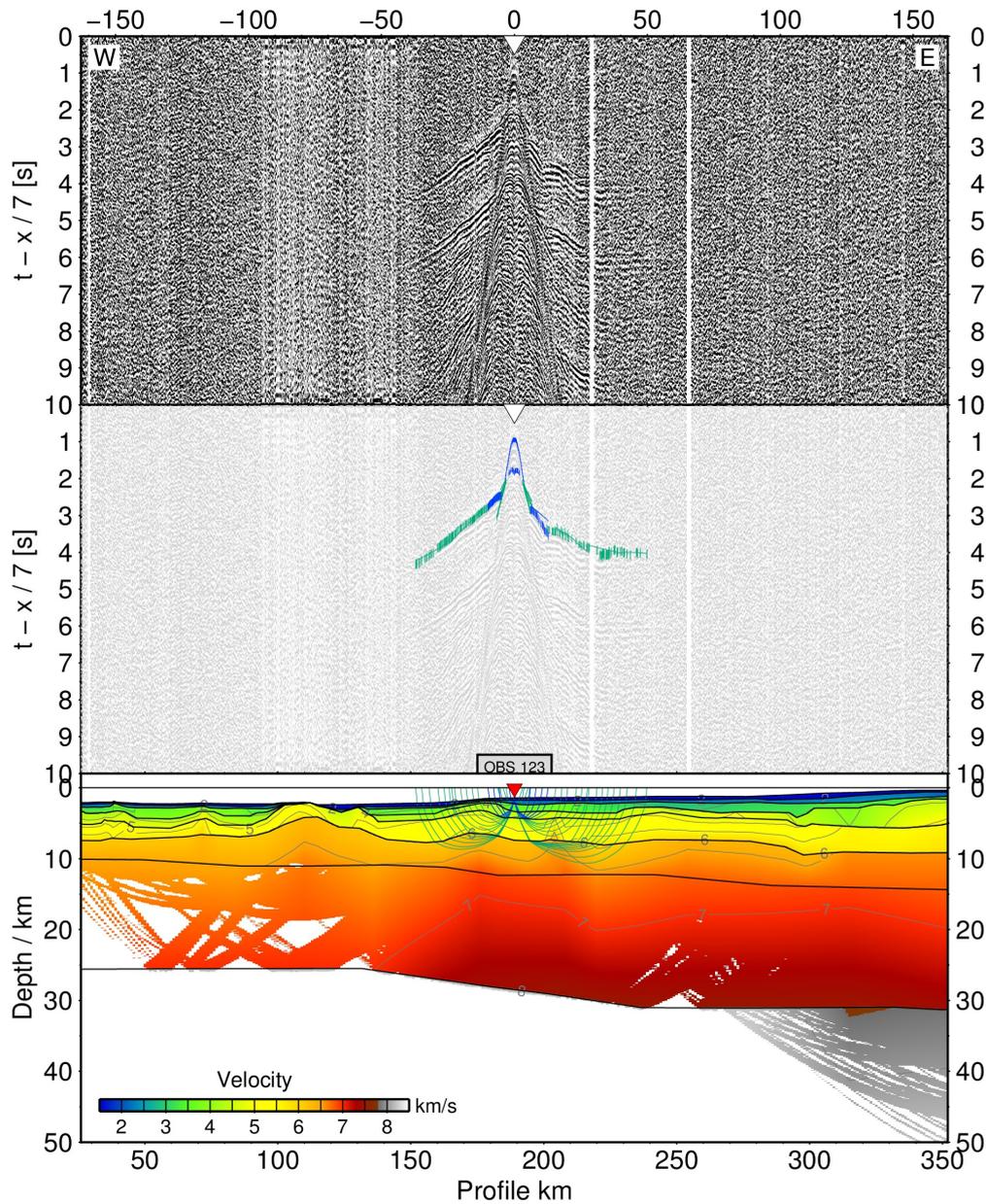
Figure A.1.12: Ray tracing results for station 123, profile 100. top) seismogram, center) seismogram overlain by picked phases (vertical bars) and calculated travel times (lines), bottom) ray path within the model. The uncertainty of the picked phases is resembled by the line length of the vertical bar. Line colors denote the ray type: blue - reflected phase, green - refracted phase
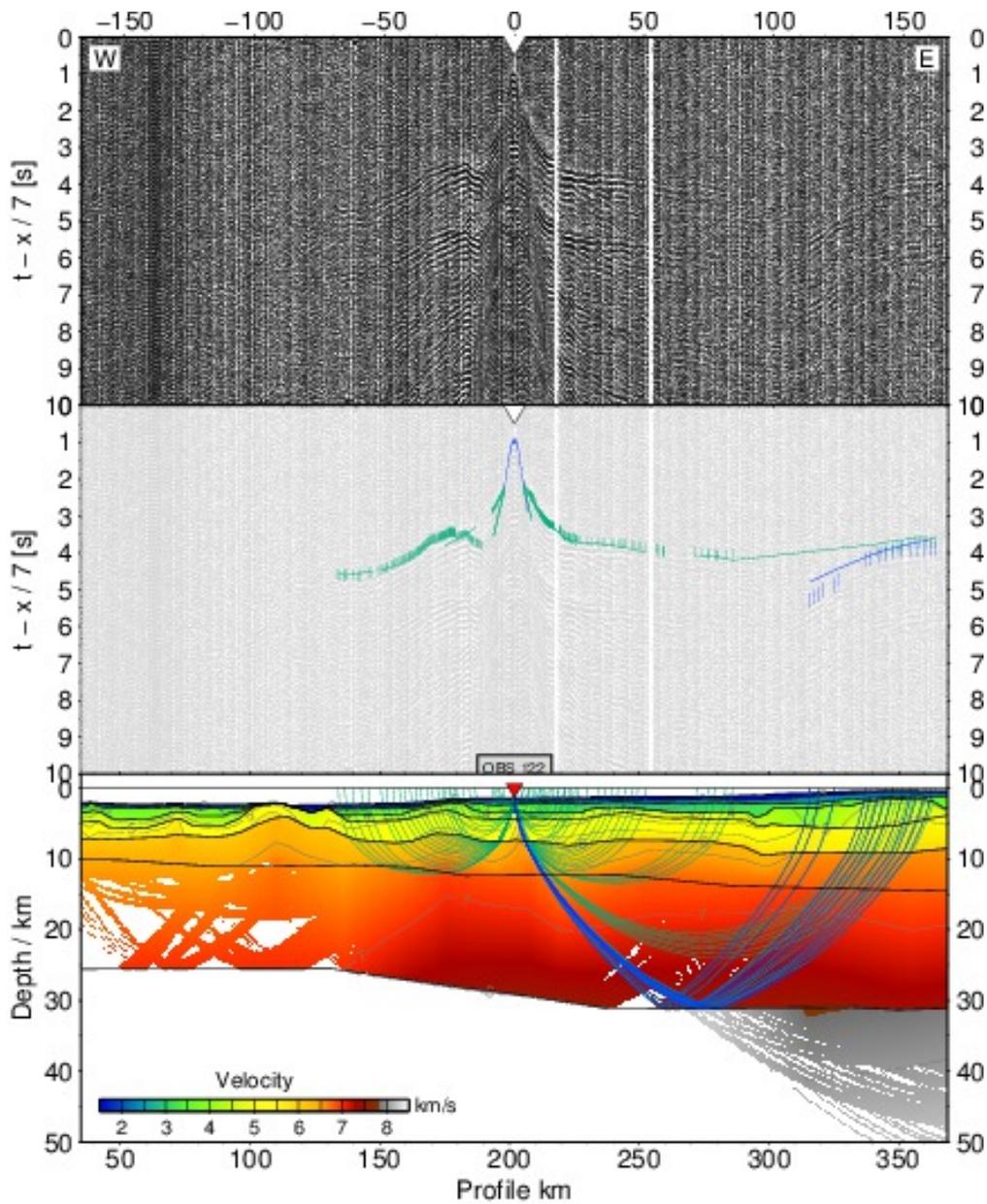
Figure A.1.13: Ray tracing results for station 122, profile 100. top) seismogram, center) seismogram overlain by picked phases (vertical bars) and calculated travel times (lines), bottom) ray path within the model. The uncertainty of the picked phases is resembled by the line length of the vertical bar. Line colors denote the ray type: blue - reflected phase, green - refracted phase
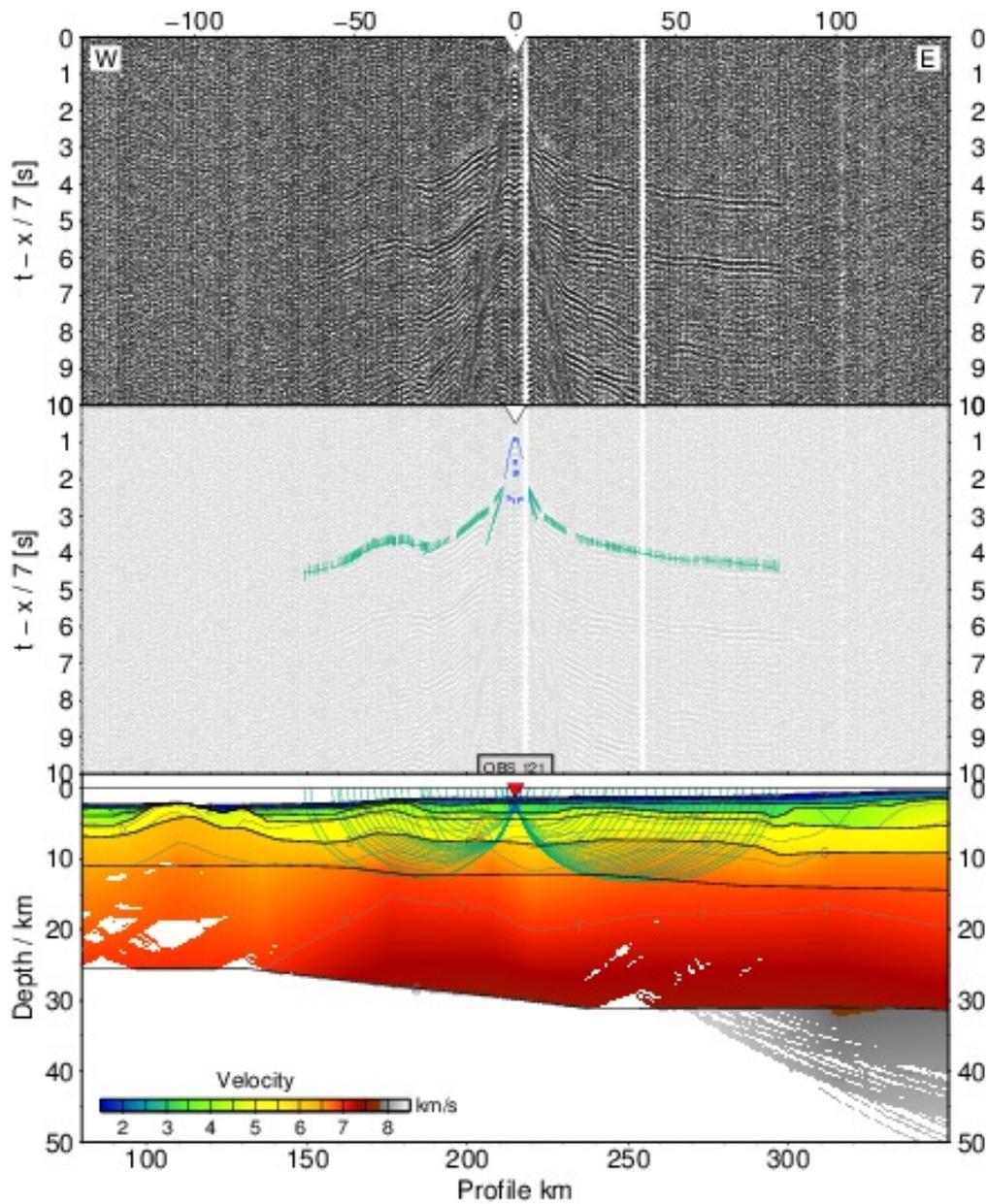
Figure A.1.14: Ray tracing results for station 121, profile 100. top) seismogram, center) seismogram overlain by picked phases (vertical bars) and calculated travel times (lines), bottom) ray path within the model. The uncertainty of the picked phases is resembled by the line length of the vertical bar. Line colors denote the ray type: blue - reflected phase, green - refracted phase
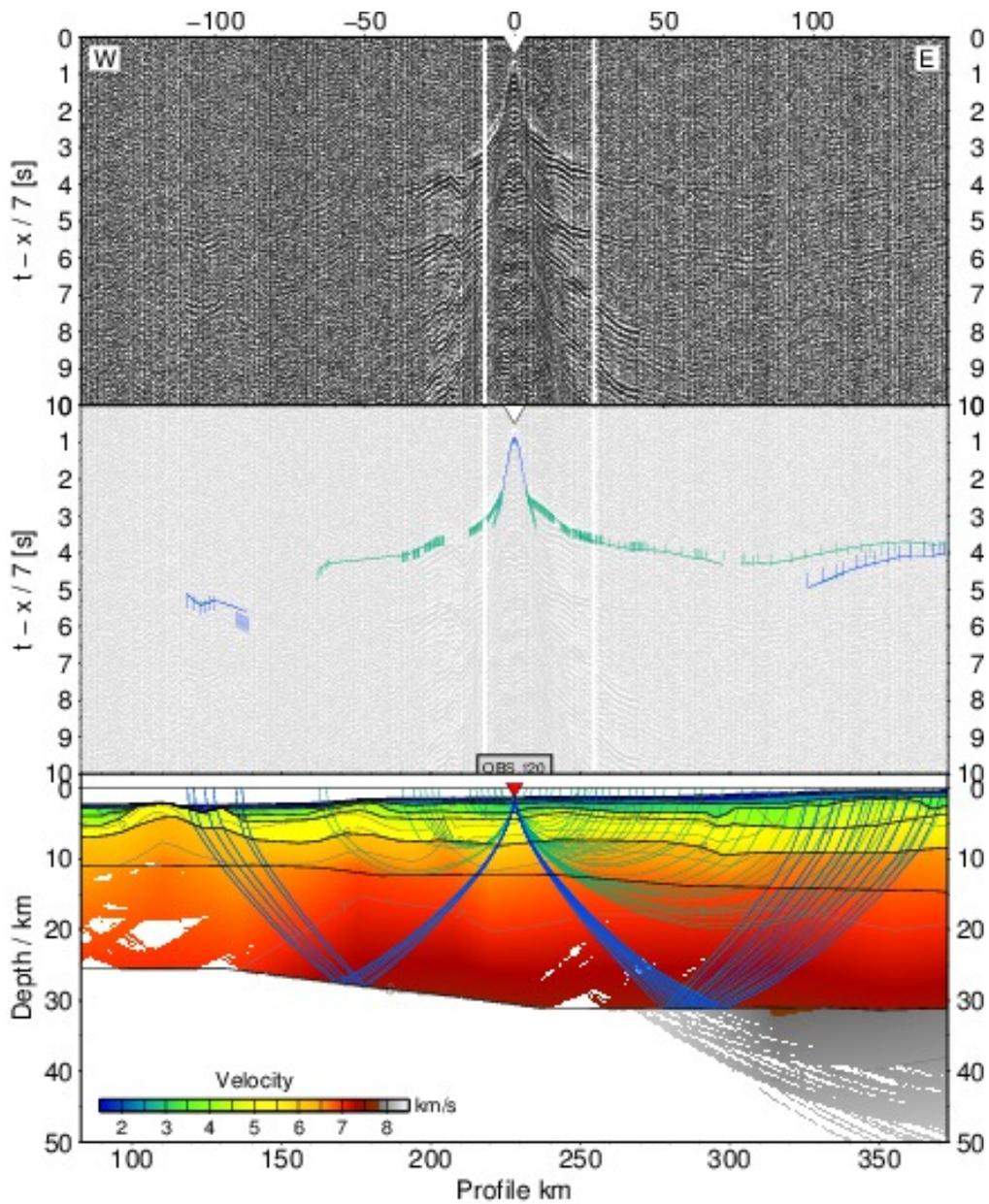
Figure A.1.15: Ray tracing results for station 120, profile 100. top) seismogram, center) seismogram overlain by picked phases (vertical bars) and calculated travel times (lines), bottom) ray path within the model. The uncertainty of the picked phases is resembled by the line length of the vertical bar. Line colors denote the ray type: blue - reflected phase, green - refracted phase
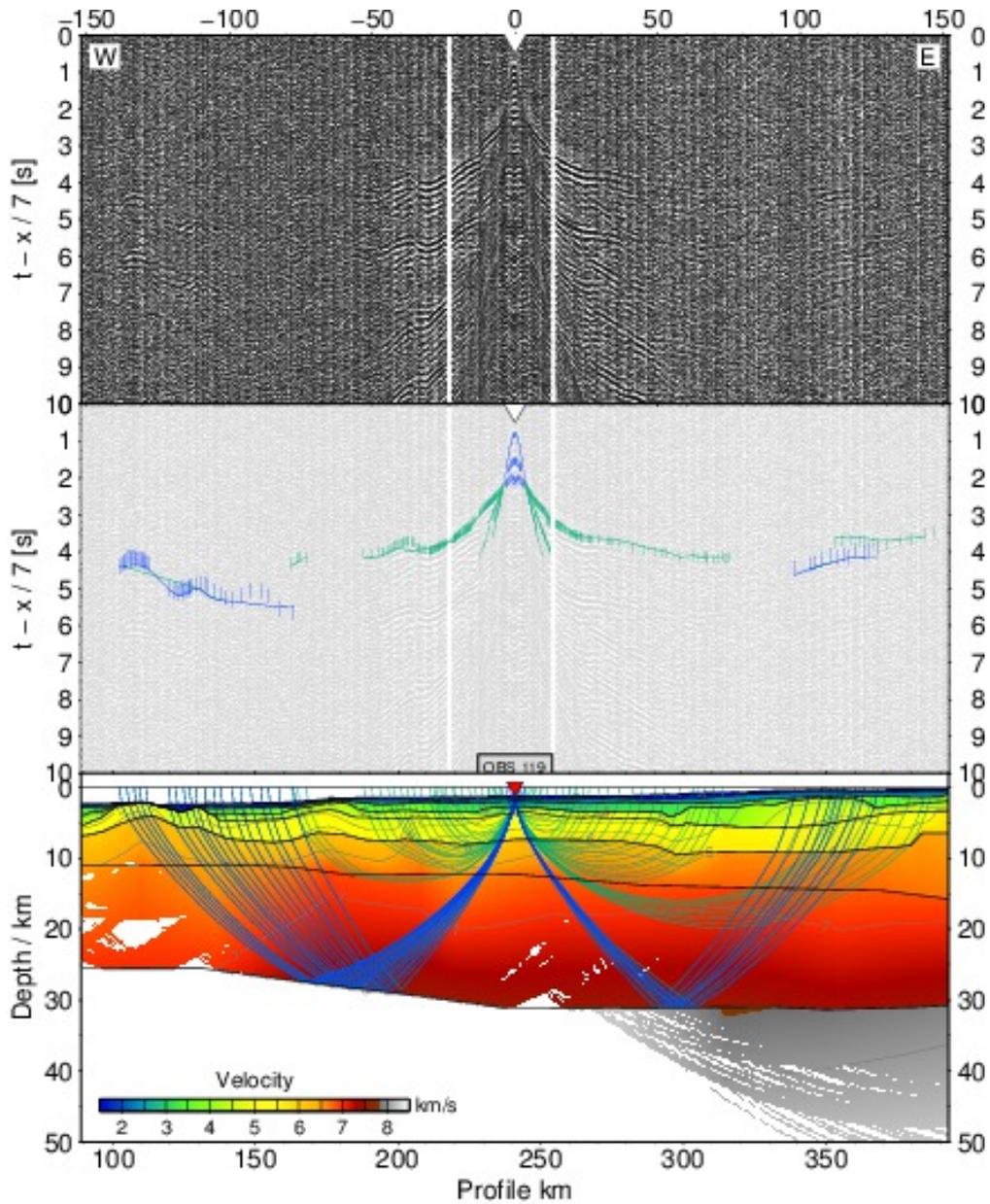
Figure A.1.16: Ray tracing results for station 119, profile 100. top) seismogram, center) seismogram overlain by picked phases (vertical bars) and calculated travel times (lines), bottom) ray path within the model. The uncertainty of the picked phases is resembled by the line length of the vertical bar. Line colors denote the ray type: blue - reflected phase, green - refracted phase
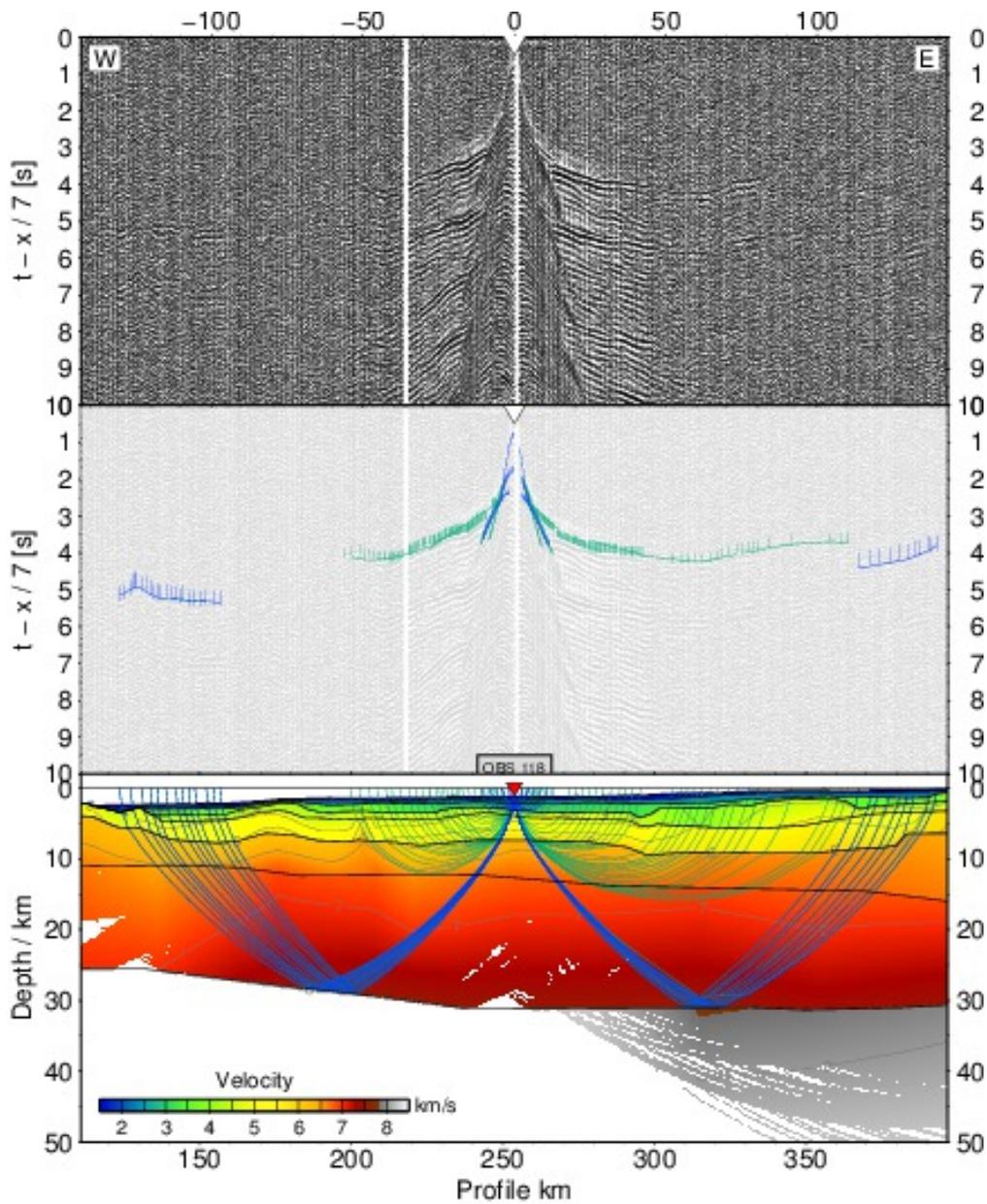
Figure A.1.17: Ray tracing results for station 118, profile 100. top) seismogram, center) seismogram overlain by picked phases (vertical bars) and calculated travel times (lines), bottom) ray path within the model. The uncertainty of the picked phases is resembled by the line length of the vertical bar. Line colors denote the ray type: blue - reflected phase, green - refracted phase
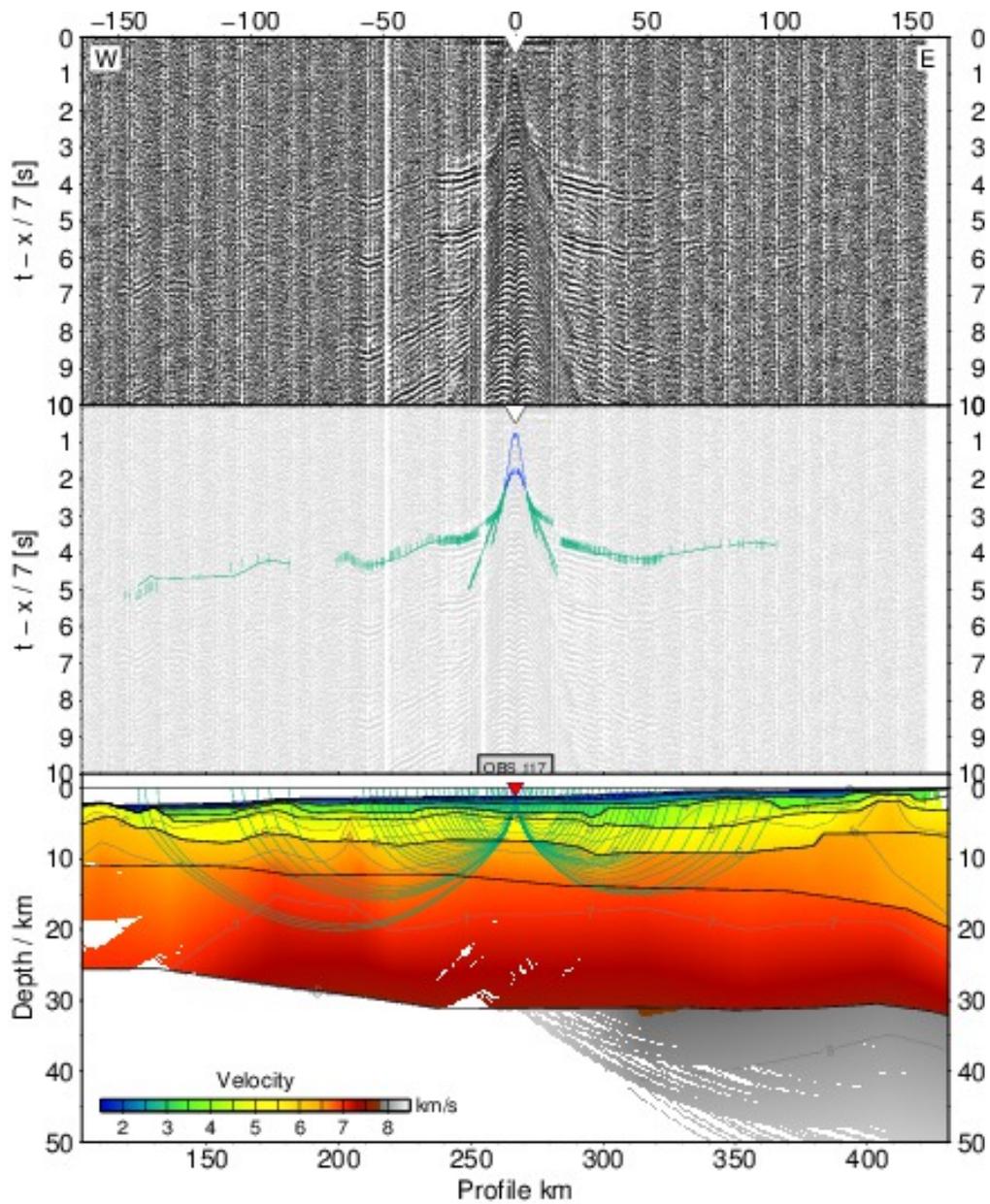
Figure A.1.18: Ray tracing results for station 117, profile 100. top) seismogram, center) seismogram overlain by picked phases (vertical bars) and calculated travel times (lines), bottom) ray path within the model. The uncertainty of the picked phases is resembled by the line length of the vertical bar. Line colors denote the ray type: blue - reflected phase, green - refracted phase
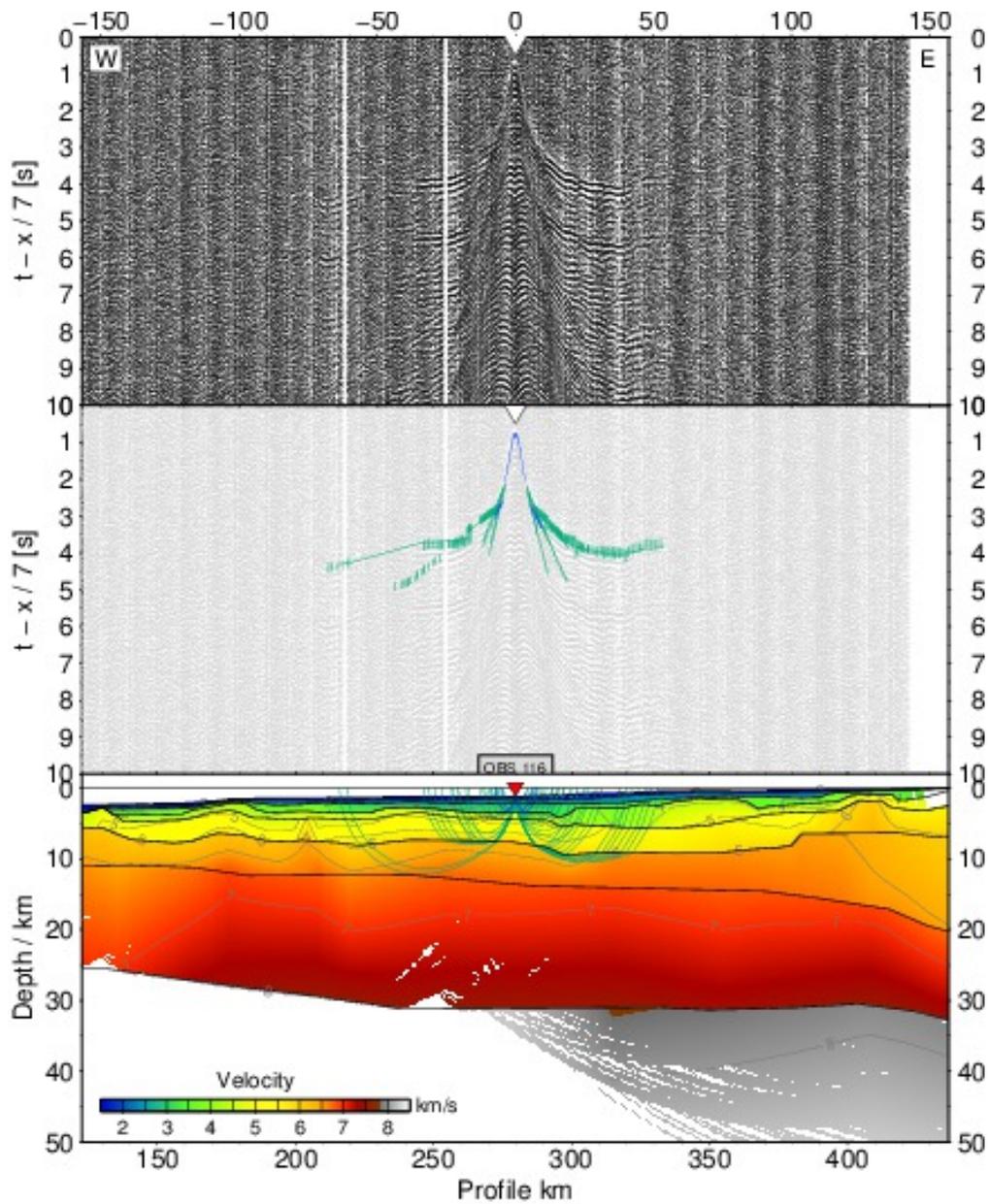
Figure A.1.19: Ray tracing results for station 116, profile 100. top) seismogram, center) seismogram overlain by picked phases (vertical bars) and calculated travel times (lines), bottom) ray path within the model. The uncertainty of the picked phases is resembled by the line length of the vertical bar. Line colors denote the ray type: blue - reflected phase, green - refracted phase
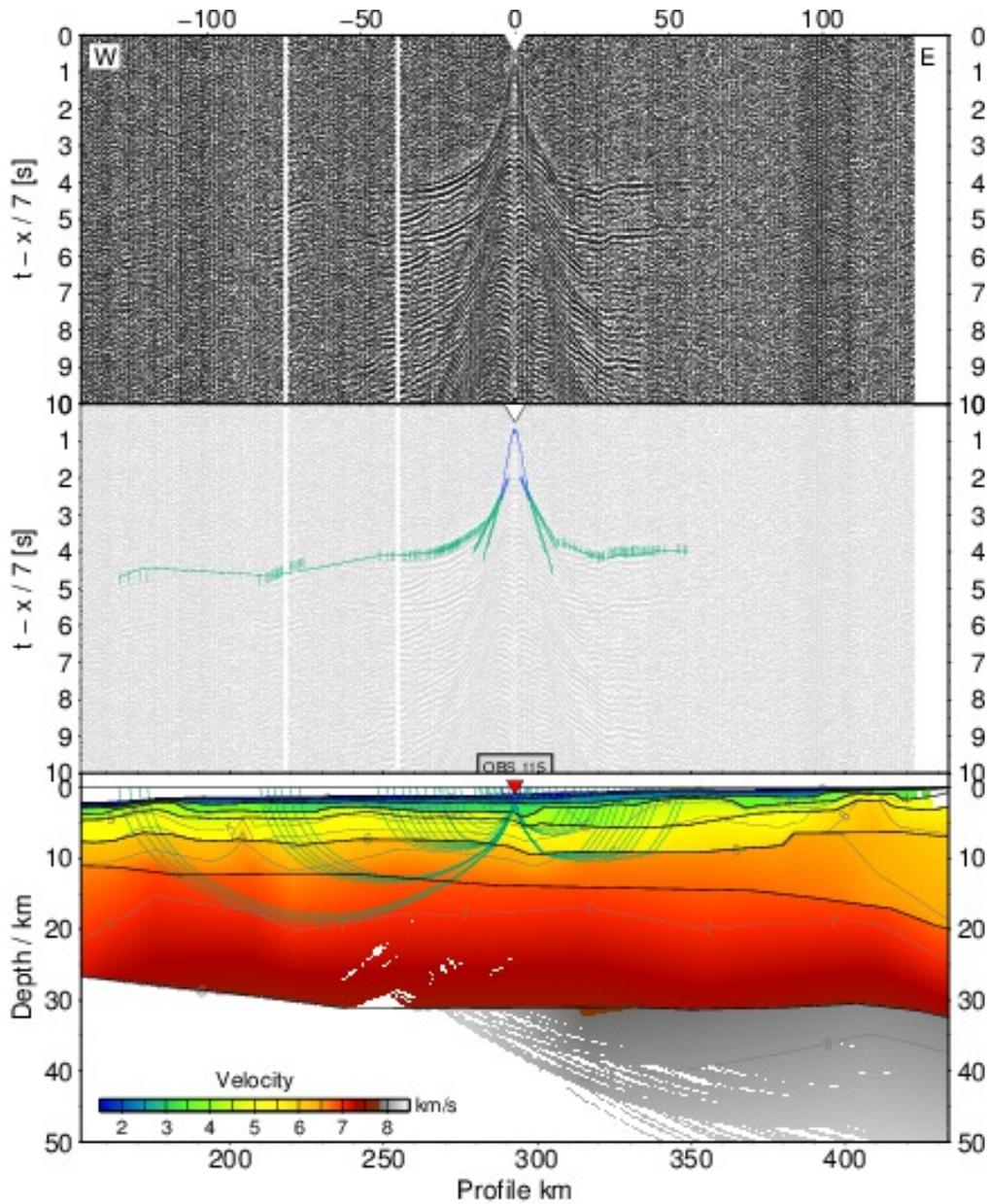
Figure A.1.20: Ray tracing results for station 115, profile 100. top) seismogram, center) seismogram overlain by picked phases (vertical bars) and calculated travel times (lines), bottom) ray path within the model. The uncertainty of the picked phases is resembled by the line length of the vertical bar. Line colors denote the ray type: blue - reflected phase, green - refracted phase
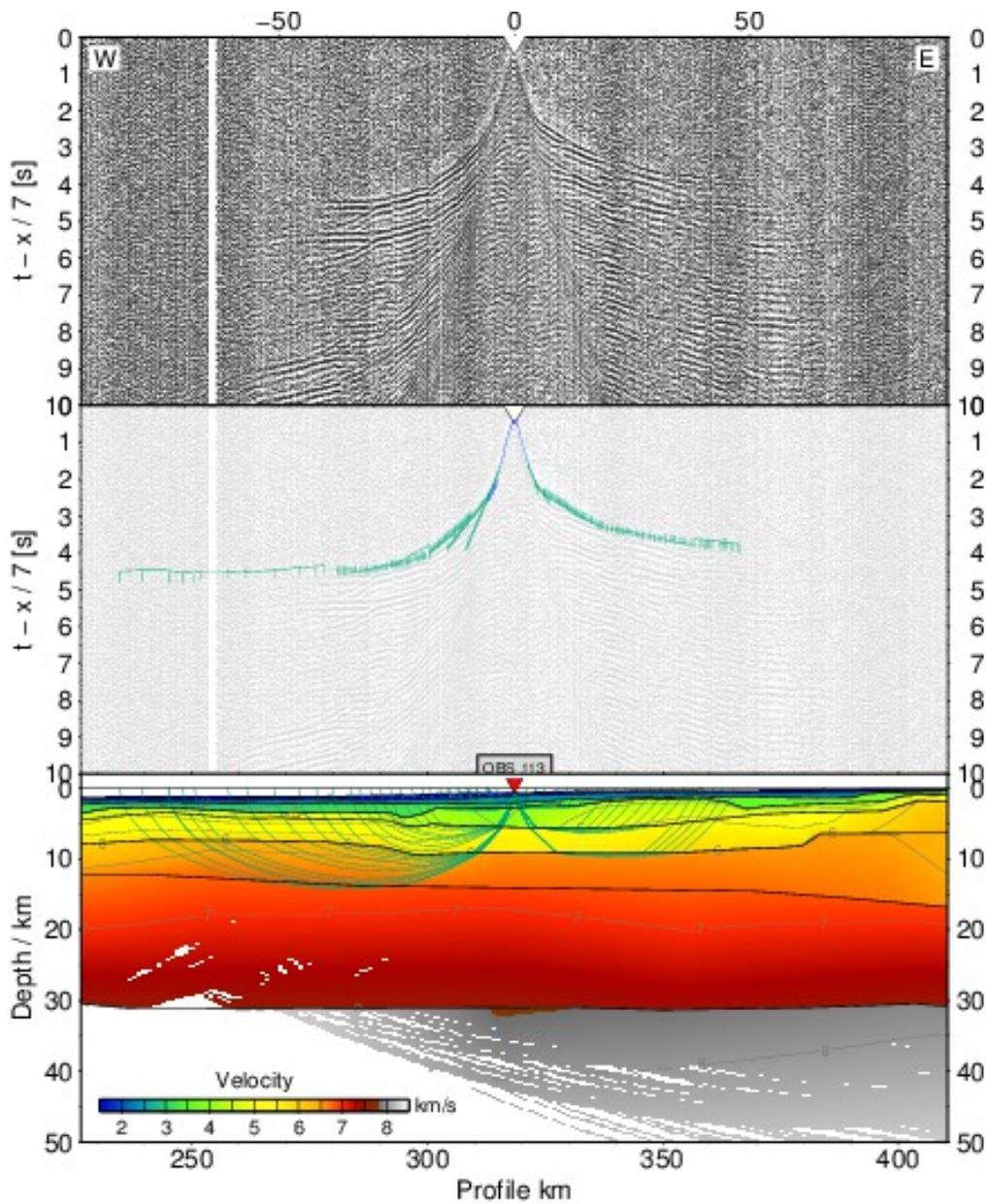
Figure A.1.21: Ray tracing results for station 113, profile 100. top) seismogram, center) seismogram overlain by picked phases (vertical bars) and calculated travel times (lines), bottom) ray path within the model. The uncertainty of the picked phases is resembled by the line length of the vertical bar. Line colors denote the ray type: blue - reflected phase, green - refracted phase
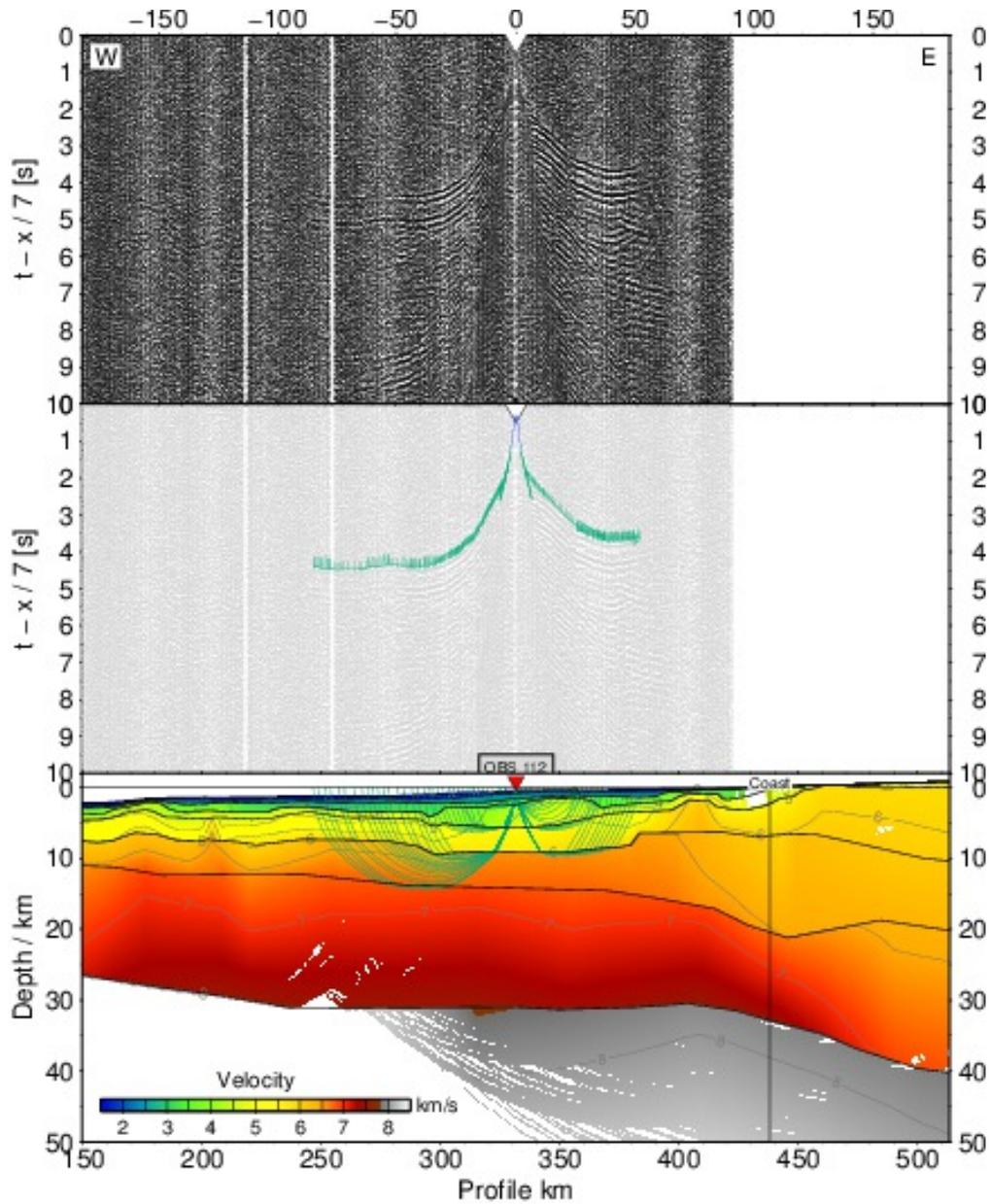
Figure A.1.22: Ray tracing results for station 112, profile 100. top) seismogram, center) seismogram overlain by picked phases (vertical bars) and calculated travel times (lines), bottom) ray path within the model. The uncertainty of the picked phases is resembled by the line length of the vertical bar. Line colors denote the ray type: blue - reflected phase, green - refracted phase
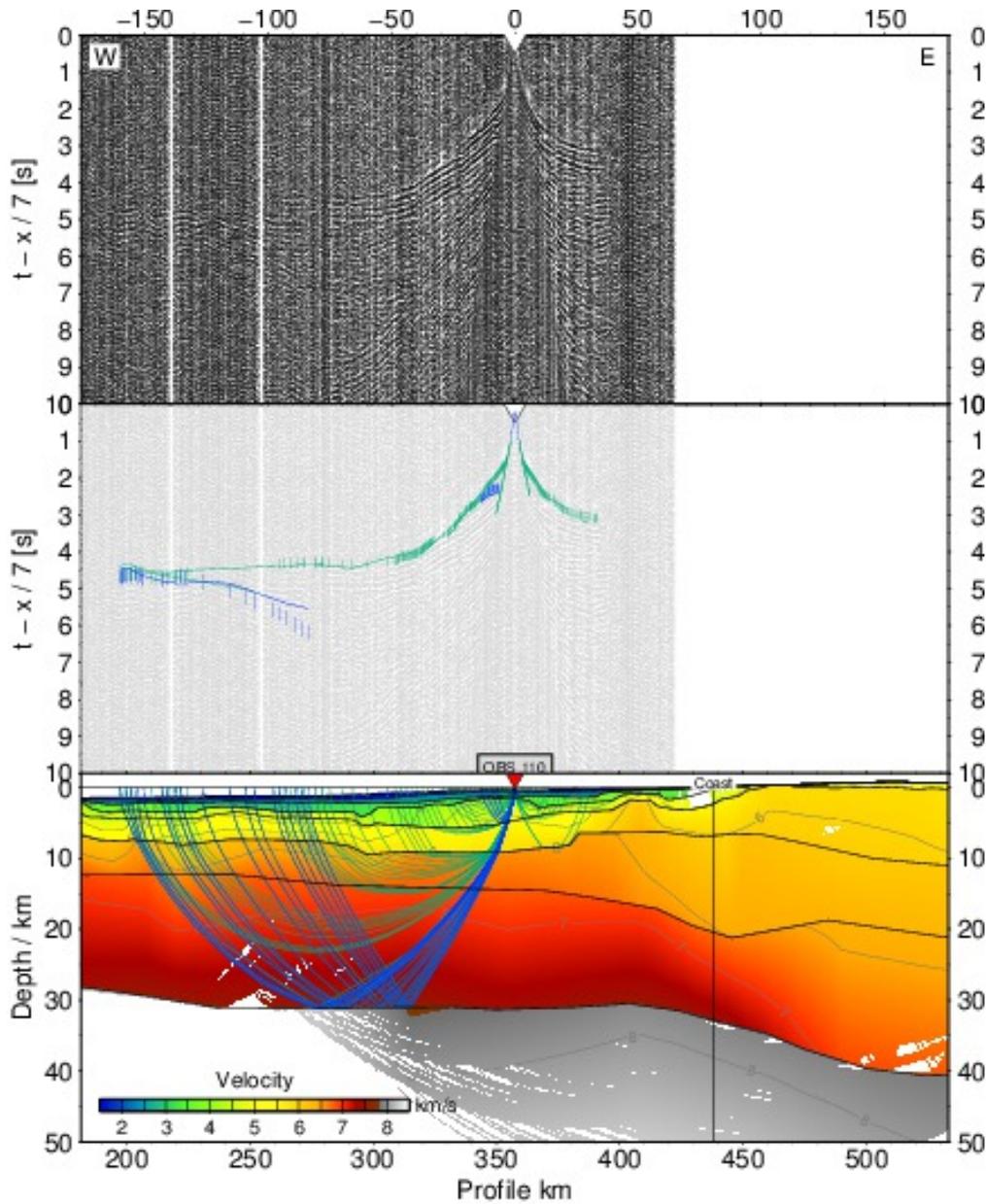
Figure A.1.23: Ray tracing results for station 110, profile 100. top) seismogram, center) seismogram overlain by picked phases (vertical bars) and calculated travel times (lines), bottom) ray path within the model. The uncertainty of the picked phases is resembled by the line length of the vertical bar. Line colors denote the ray type: blue - reflected phase, green - refracted phase
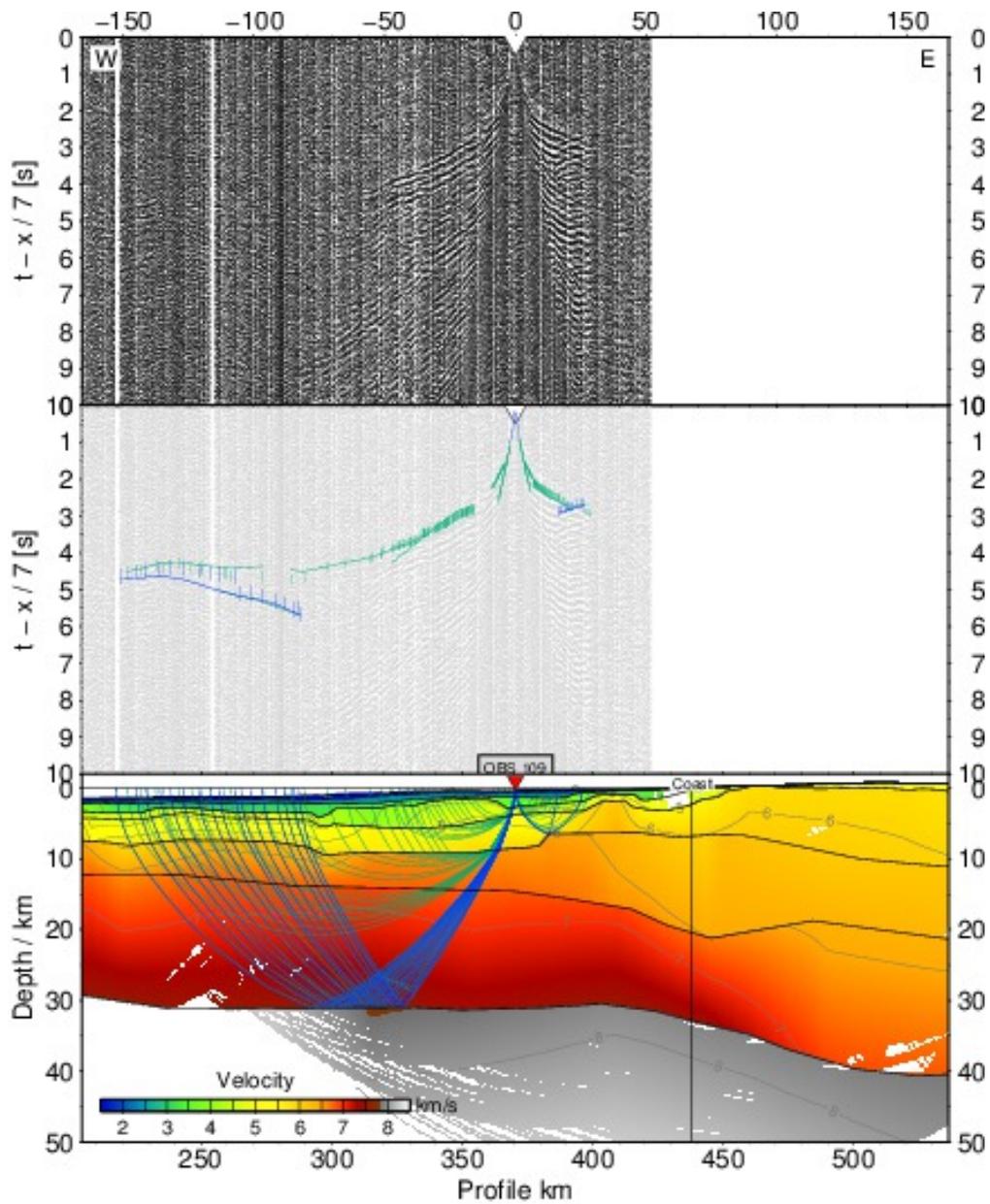
Figure A.1.24: Ray tracing results for station 109, profile 100. top) seismogram, center) seismogram overlain by picked phases (vertical bars) and calculated travel times (lines), bottom) ray path within the model. The uncertainty of the picked phases is resembled by the line length of the vertical bar. Line colors denote the ray type: blue - reflected phase, green - refracted phase
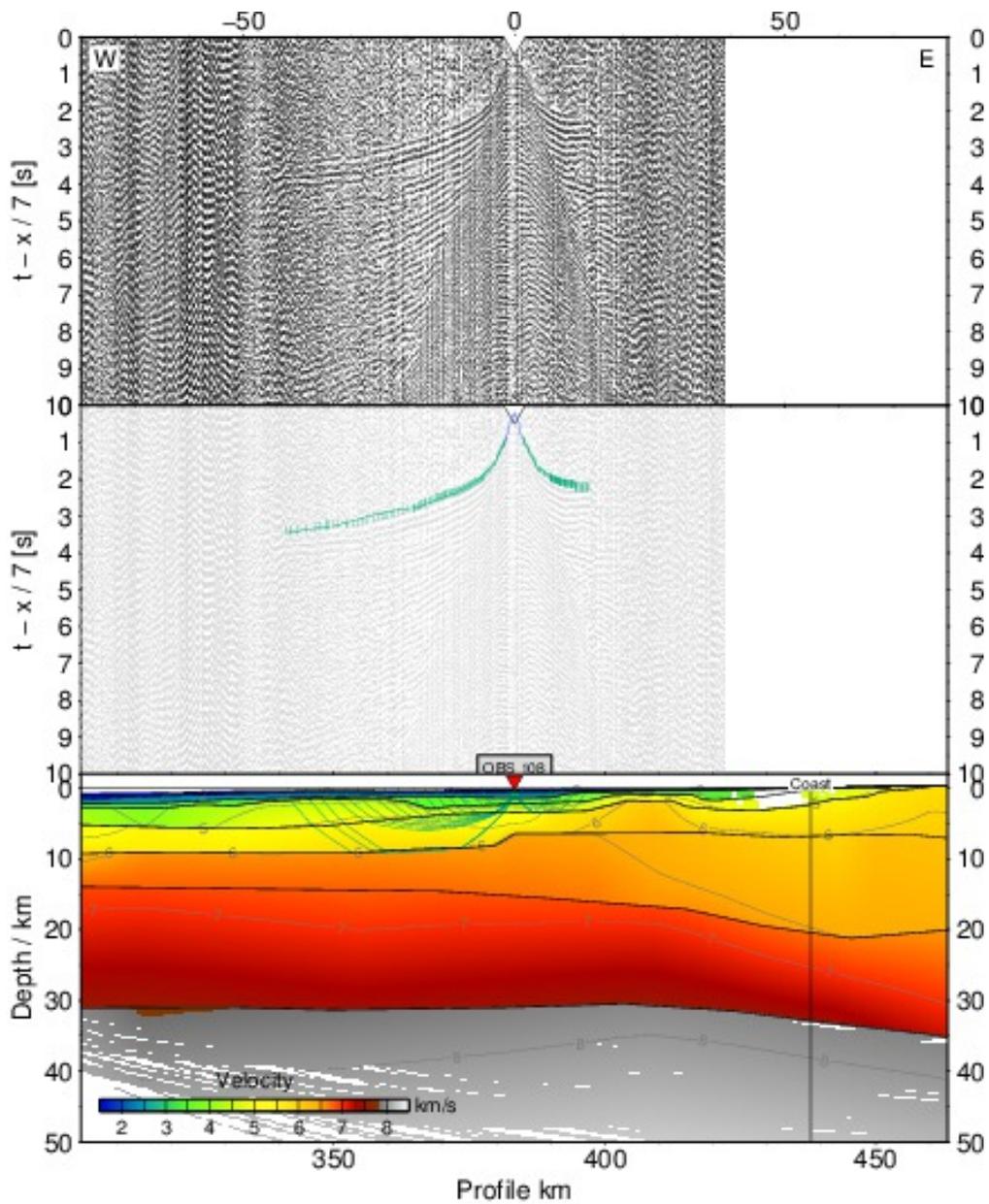
Figure A.1.25: Ray tracing results for station 108, profile 100. top) seismogram, center) seismogram overlain by picked phases (vertical bars) and calculated travel times (lines), bottom) ray path within the model. The uncertainty of the picked phases is resembled by the line length of the vertical bar. Line colors denote the ray type: blue - reflected phase, green - refracted phase
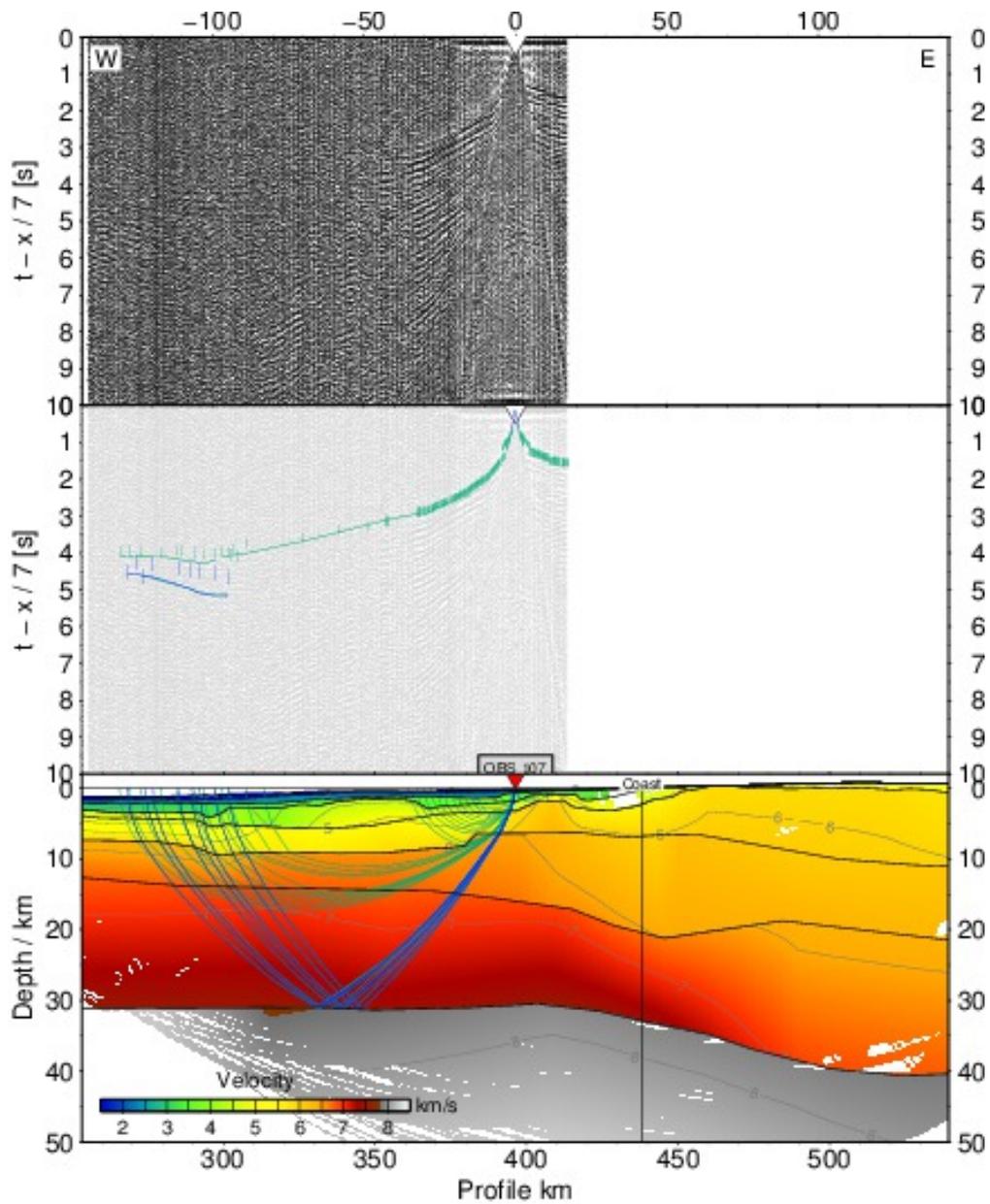
Figure A.1.26: Ray tracing results for station 107, profile 100. top) seismogram, center) seismogram overlain by picked phases (vertical bars) and calculated travel times (lines), bottom) ray path within the model. The uncertainty of the picked phases is resembled by the line length of the vertical bar. Line colors denote the ray type: blue - reflected phase, green - refracted phase
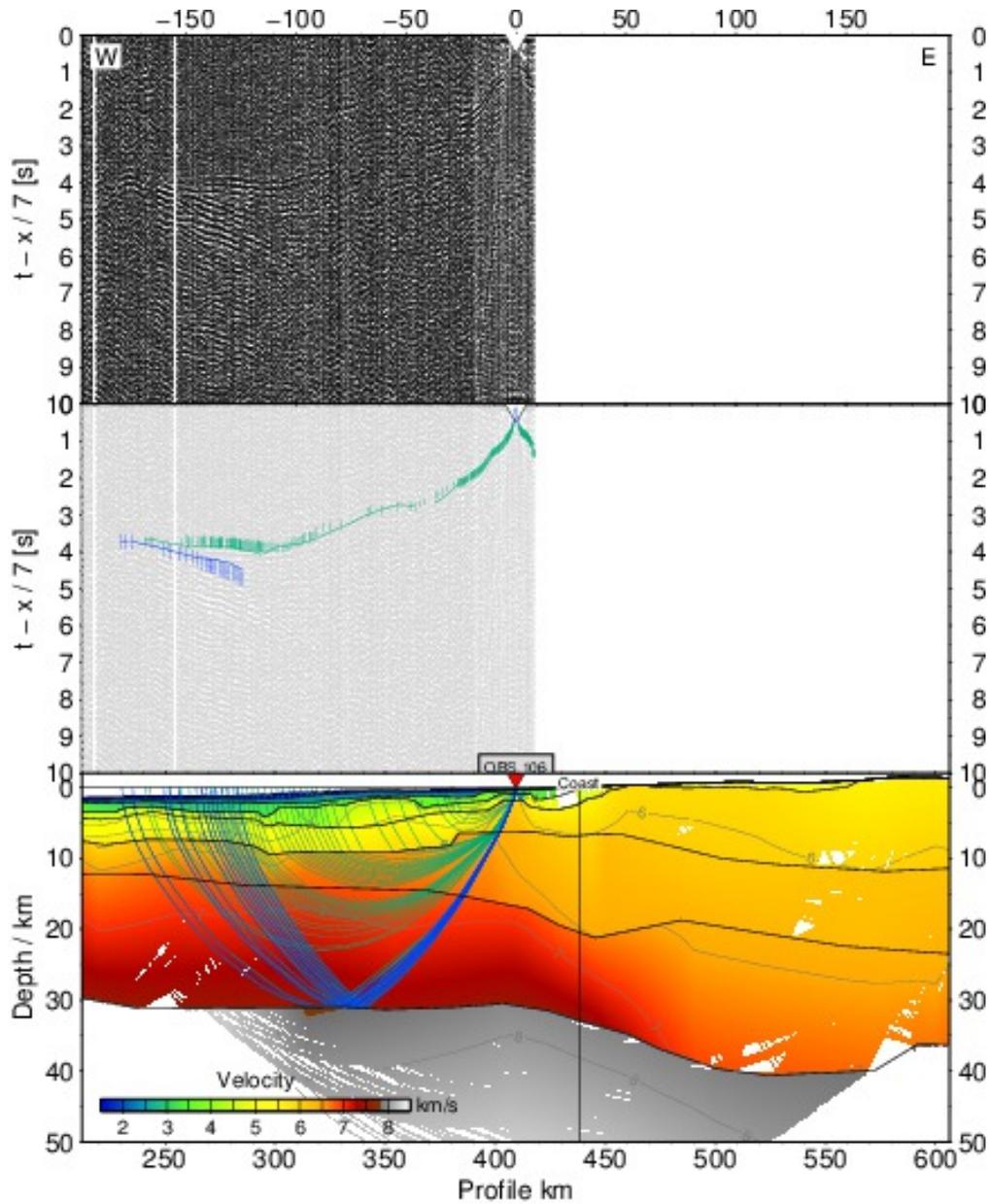
Figure A.1.27: Ray tracing results for station 106, profile 100. top) seismogram, center) seismogram overlain by picked phases (vertical bars) and calculated travel times (lines), bottom) ray path within the model. The uncertainty of the picked phases is resembled by the line length of the vertical bar. Line colors denote the ray type: blue - reflected phase, green - refracted phase
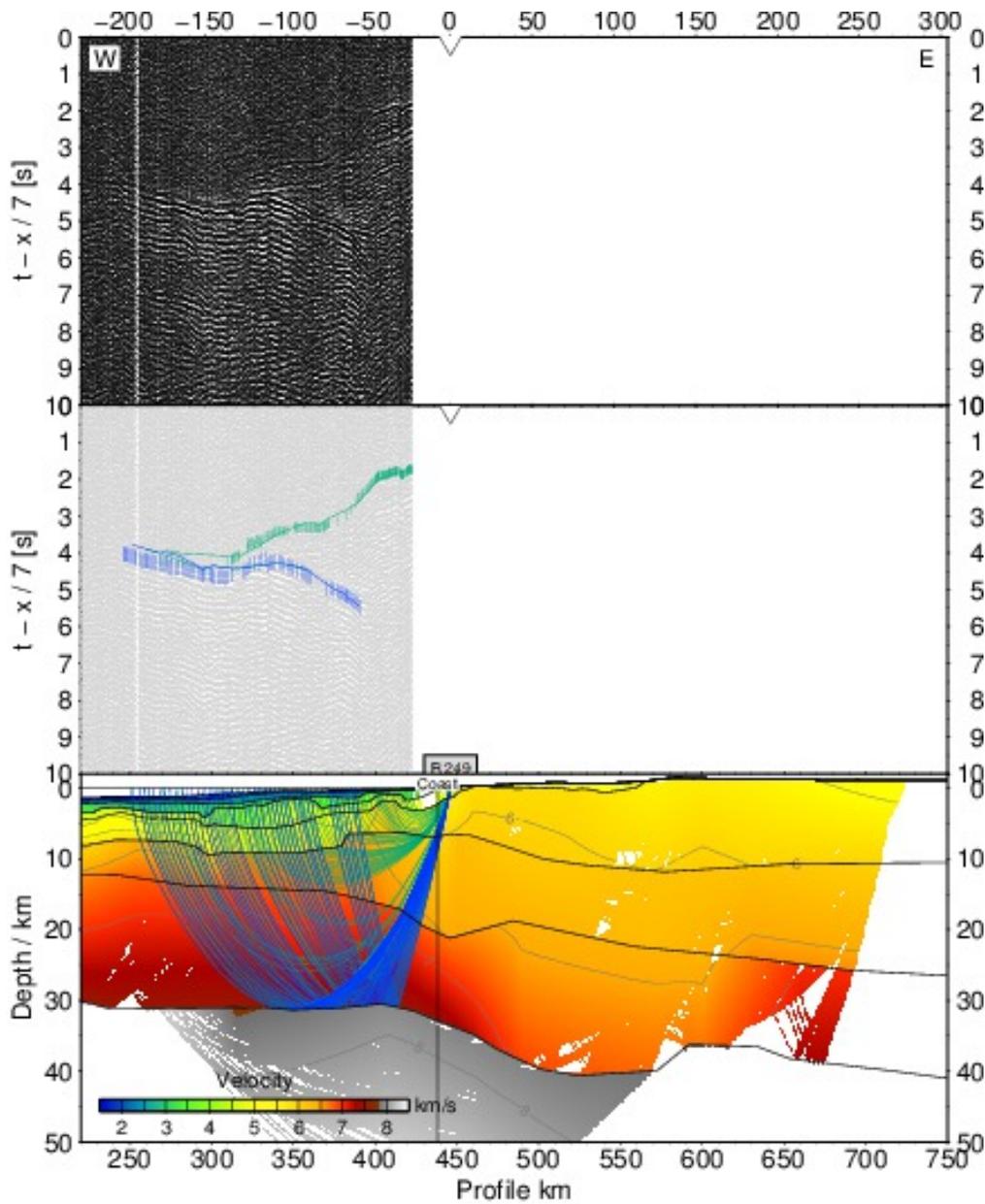
Figure A.1.28: Ray tracing results for station 249, profile 100. top) seismogram, center) seismogram overlain by picked phases (vertical bars) and calculated travel times (lines), bottom) ray path within the model. The uncertainty of the picked phases is resembled by the line length of the vertical bar. Line colors denote the ray type: blue - reflected phase, green - refracted phase
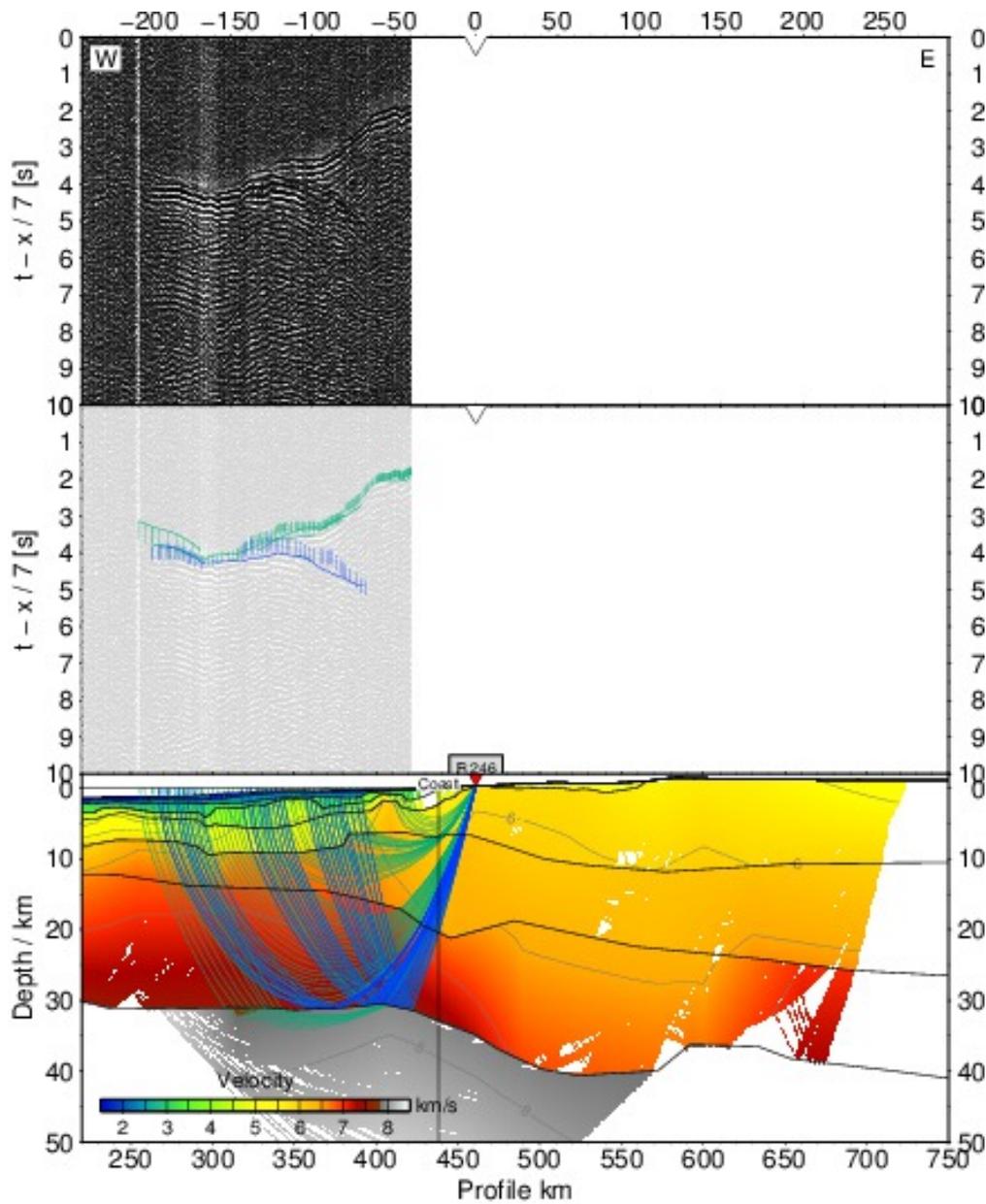
Figure A.1.29: Ray tracing results for station 246, profile 100. top) seismogram, center) seismogram overlain by picked phases (vertical bars) and calculated travel times (lines), bottom) ray path within the model. The uncertainty of the picked phases is resembled by the line length of the vertical bar. Line colors denote the ray type: blue - reflected phase, green - refracted phase
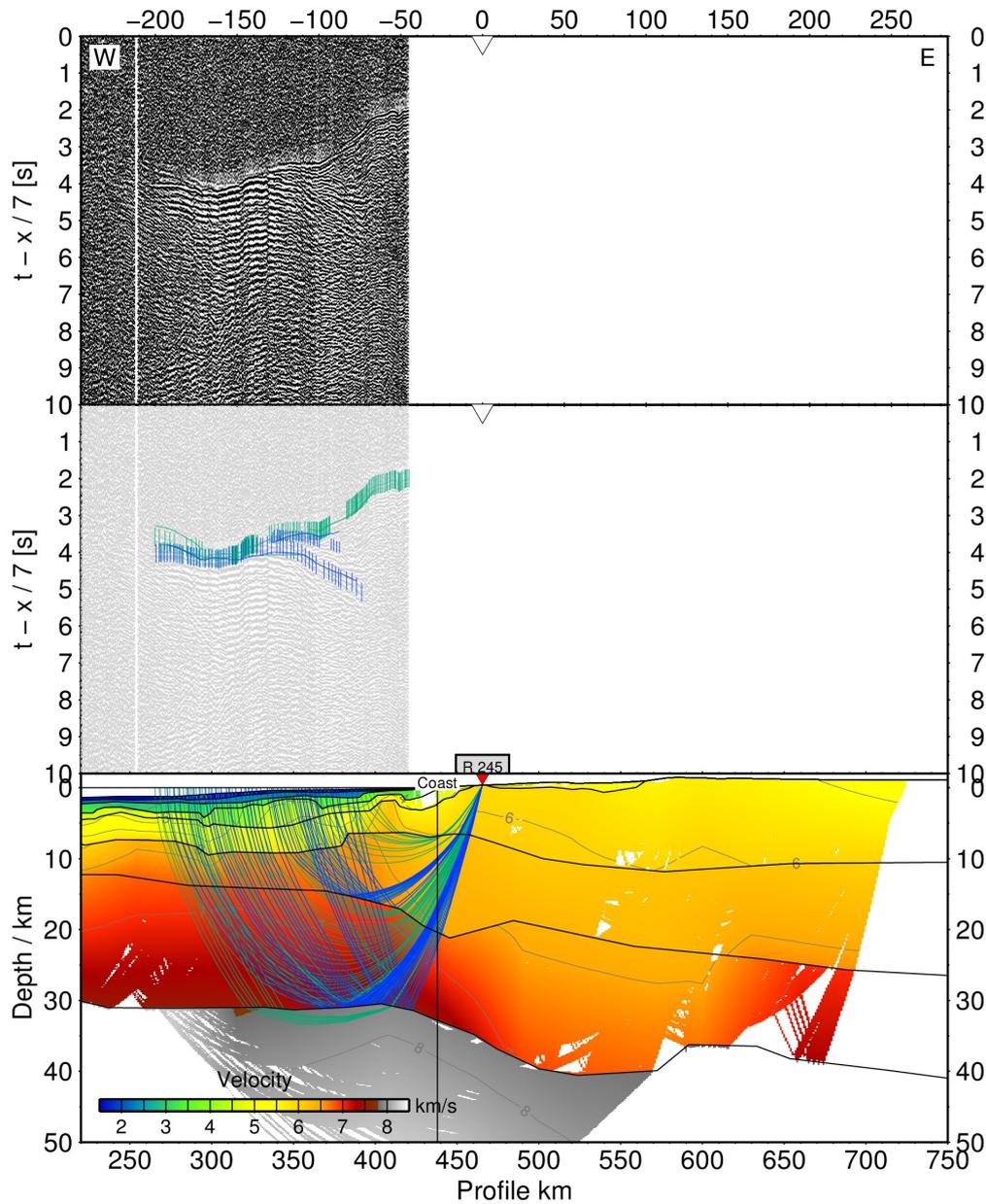
Figure A.1.30: Ray tracing results for station 245, profile 100. top) seismogram, center) seismogram overlain by picked phases (vertical bars) and calculated travel times (lines), bottom) ray path within the model. The uncertainty of the picked phases is resembled by the line length of the vertical bar. Line colors denote the ray type: blue - reflected phase, green - refracted phase
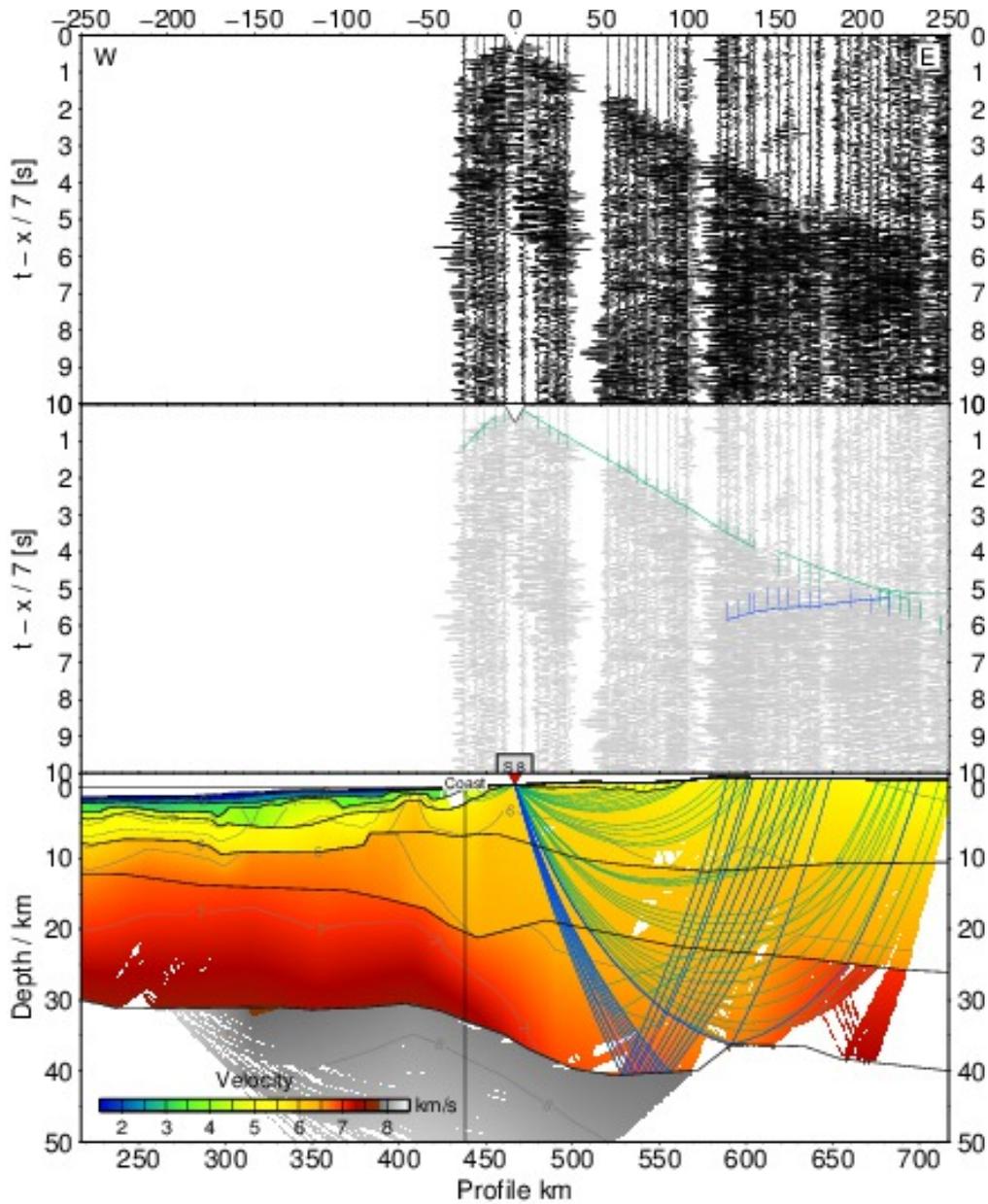
Figure A.1.31: Ray tracing results for station 8, profile 100. top) seismogram, center) seismogram overlain by picked phases (vertical bars) and calculated travel times (lines), bottom) ray path within the model. The uncertainty of the picked phases is resembled by the line length of the vertical bar. Line colors denote the ray type: blue - reflected phase, green - refracted phase
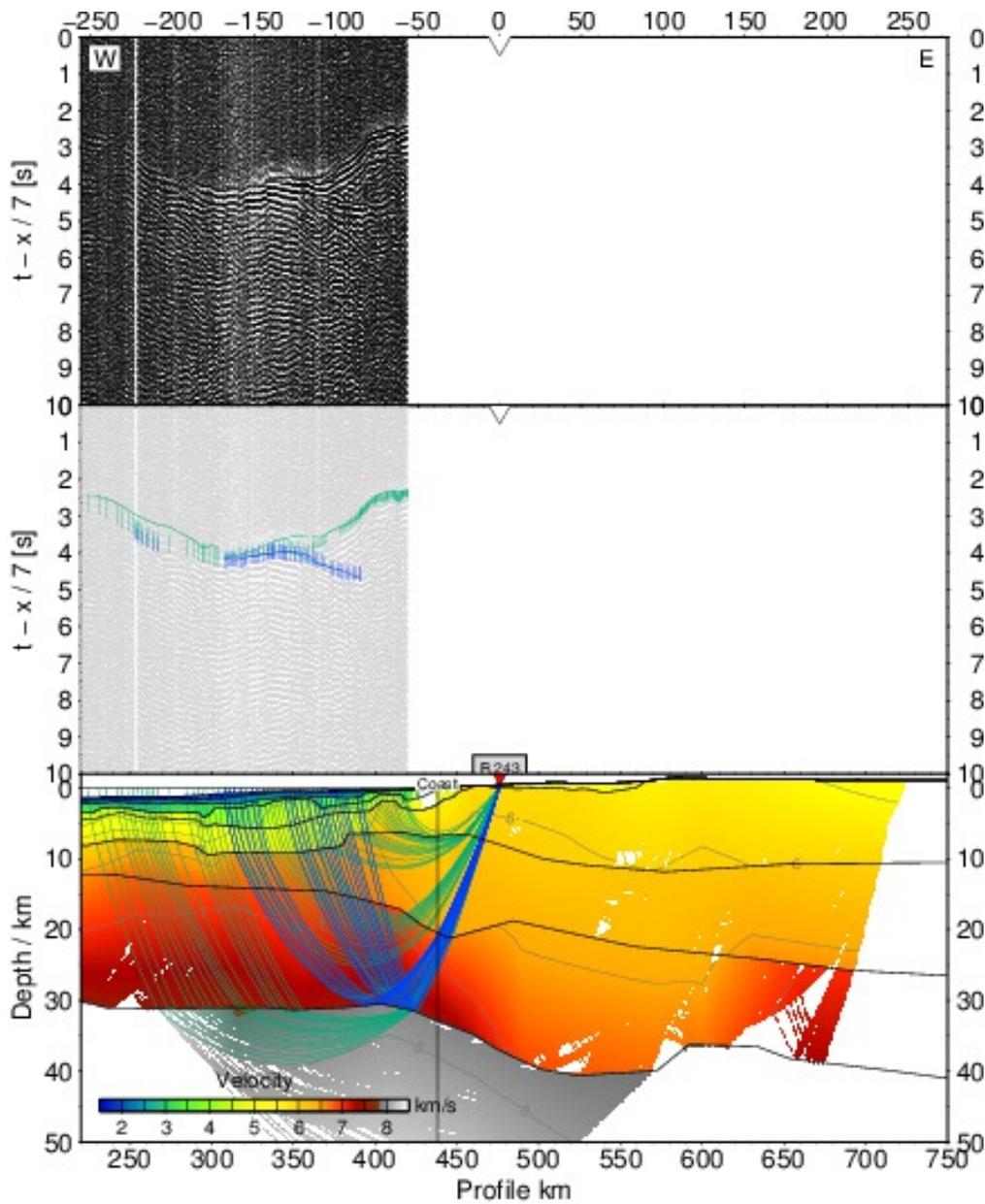
Figure A.1.32: Ray tracing results for station 243, profile 100. top) seismogram, center) seismogram overlain by picked phases (vertical bars) and calculated travel times (lines), bottom) ray path within the model. The uncertainty of the picked phases is resembled by the line length of the vertical bar. Line colors denote the ray type: blue - reflected phase, green - refracted phase
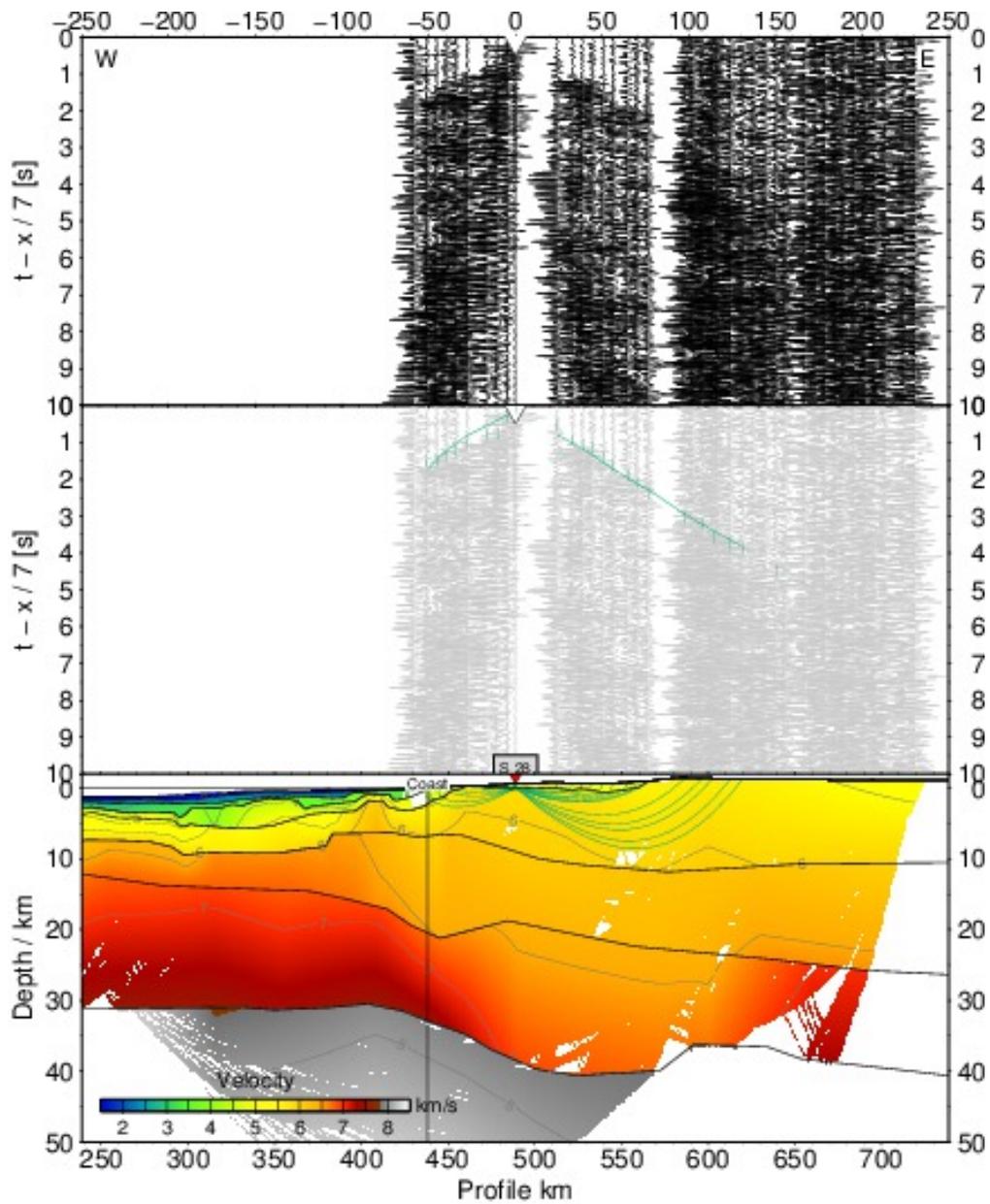
Figure A.1.33:   Ray tracing results for station 28, profile 100. top) seismogram, center) seismogram overlain by picked phases (vertical bars) and calculated travel times (lines), bottom) ray path within the model. The uncertainty of the picked phases is resembled by the line length of the vertical bar. Line colors denote the ray type: blue - reflected phase, green - refracted phase
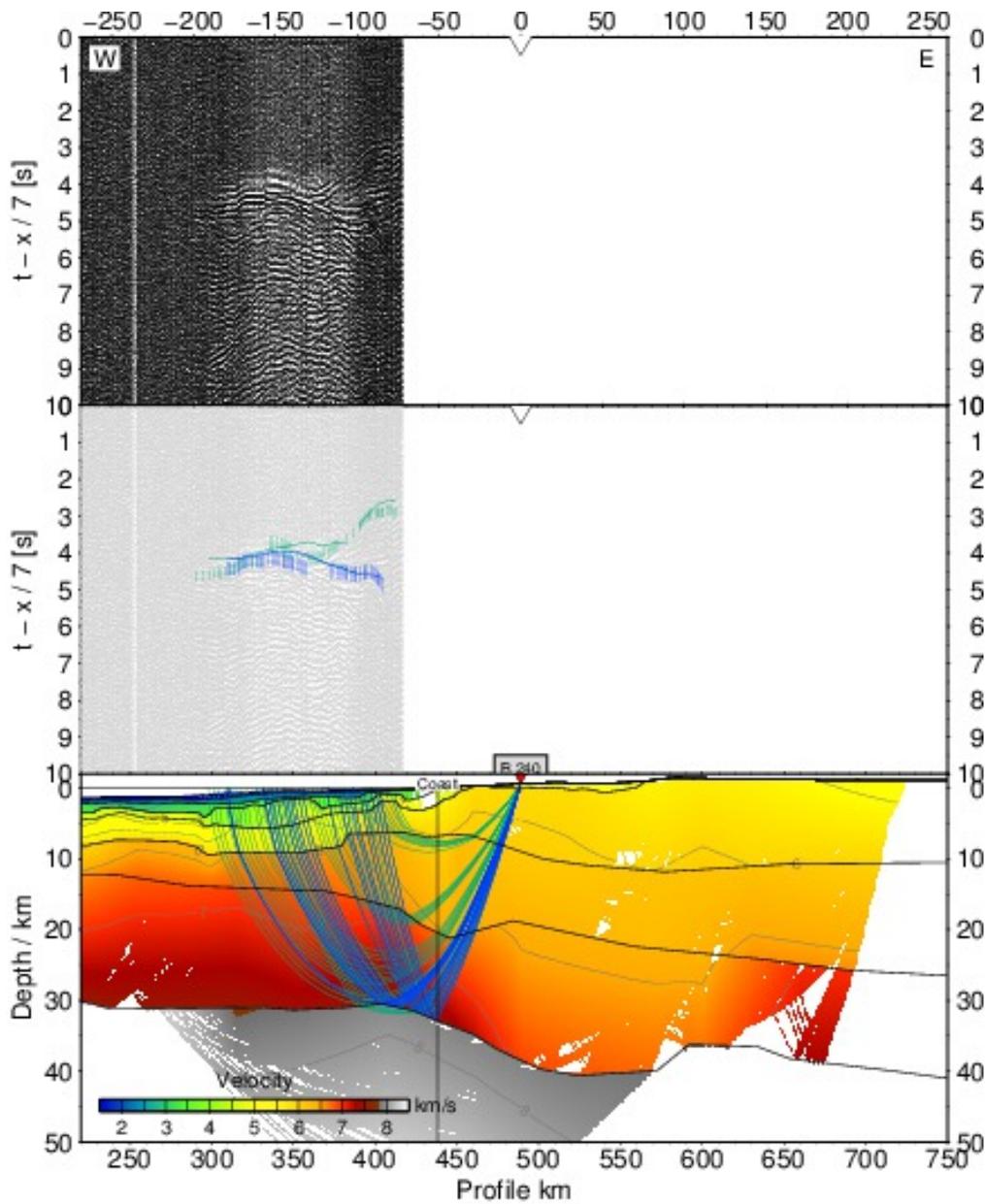
Figure A.1.34: Ray tracing results for station 240, profile 100. top) seismogram, center) seismogram overlain by picked phases (vertical bars) and calculated travel times (lines), bottom) ray path within the model. The uncertainty of the picked phases is resembled by the line length of the vertical bar. Line colors denote the ray type: blue - reflected phase, green - refracted phase
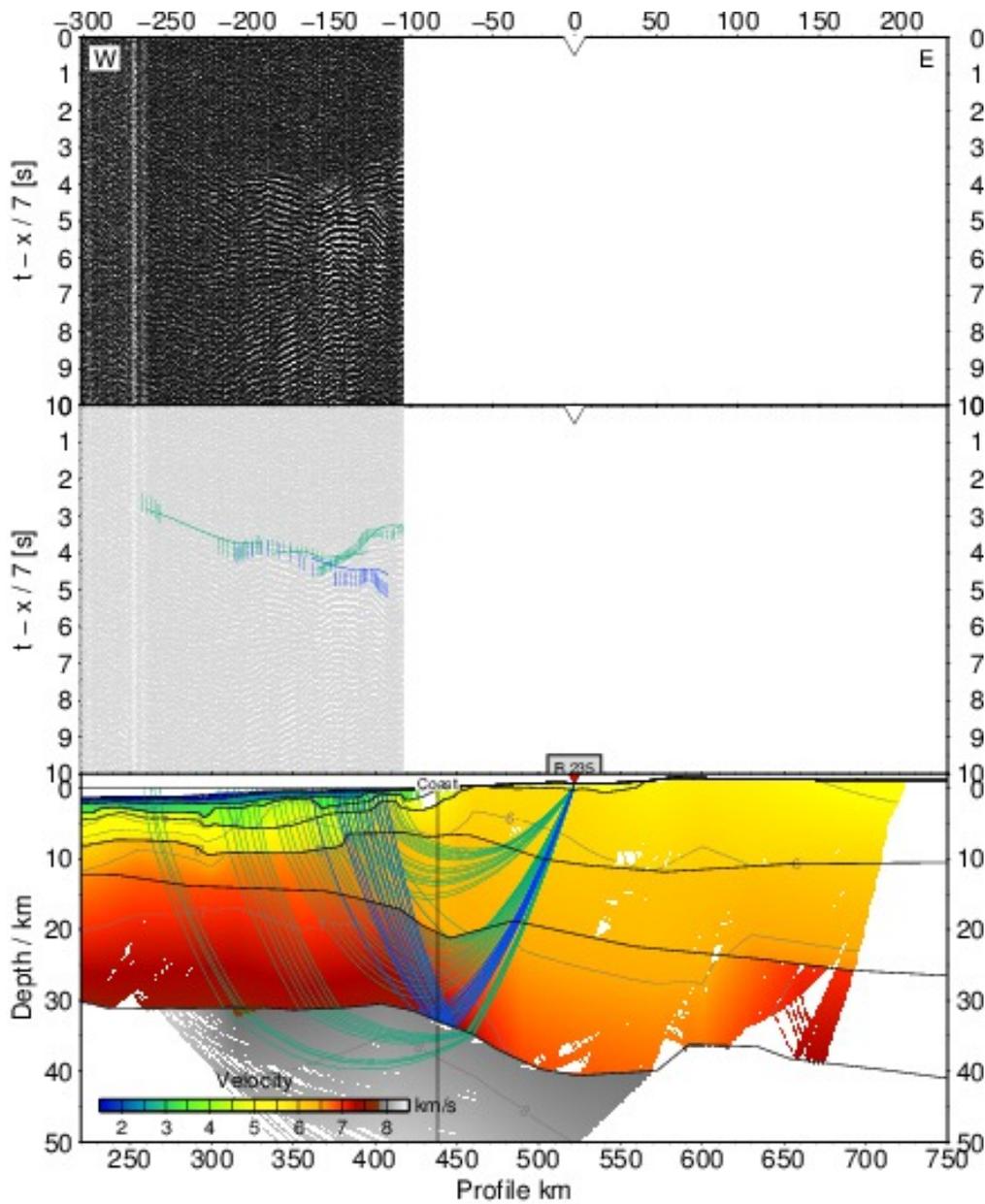
Figure A.1.35: Ray tracing results for station 235, profile 100. top) seismogram, center) seismogram overlain by picked phases (vertical bars) and calculated travel times (lines), bottom) ray path within the model. The uncertainty of the picked phases is resembled by the line length of the vertical bar. Line colors denote the ray type: blue - reflected phase, green - refracted phase
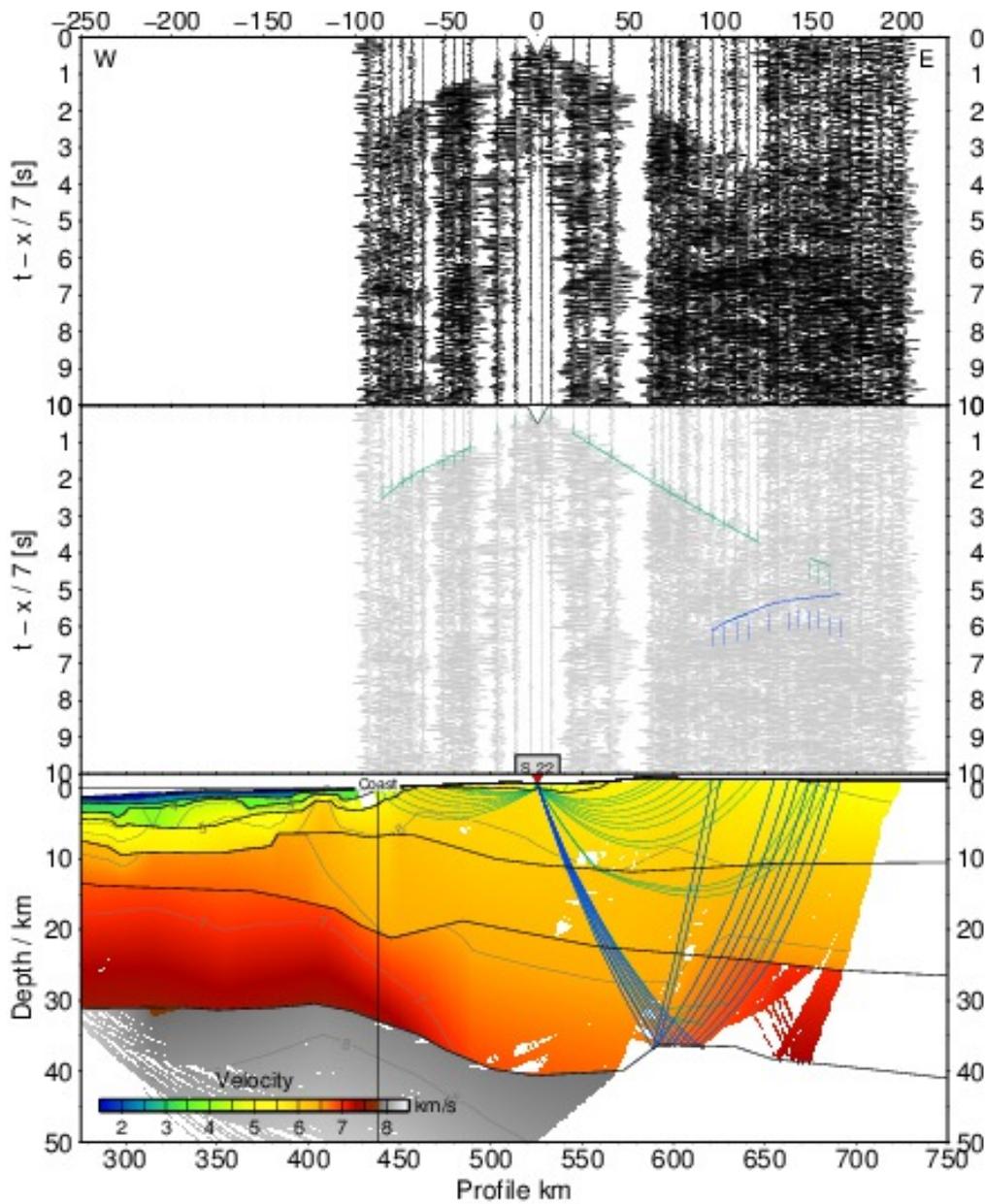
Figure A.1.36: Ray tracing results for station 22, profile 100. top) seismogram, center) seismogram overlain by picked phases (vertical bars) and calculated travel times (lines), bottom) ray path within the model. The uncertainty of the picked phases is resembled by the line length of the vertical bar. Line colors denote the ray type: blue - reflected phase, green - refracted phase
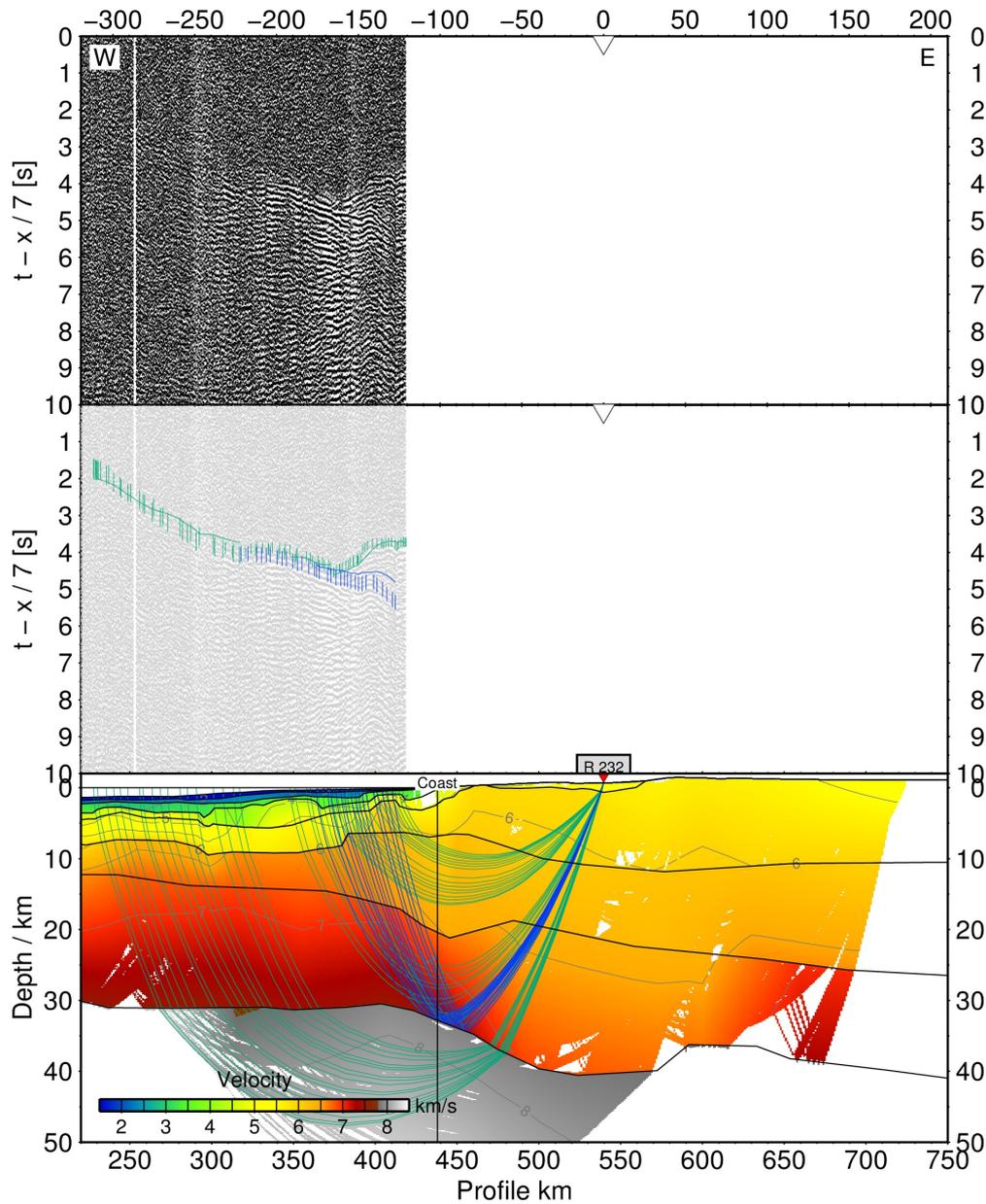
Figure A.1.37: Ray tracing results for station 232, profile 100. top) seismogram, center) seismogram overlain by picked phases (vertical bars) and calculated travel times (lines), bottom) ray path within the model. The uncertainty of the picked phases is resembled by the line length of the vertical bar. Line colors denote the ray type: blue - reflected phase, green - refracted phase
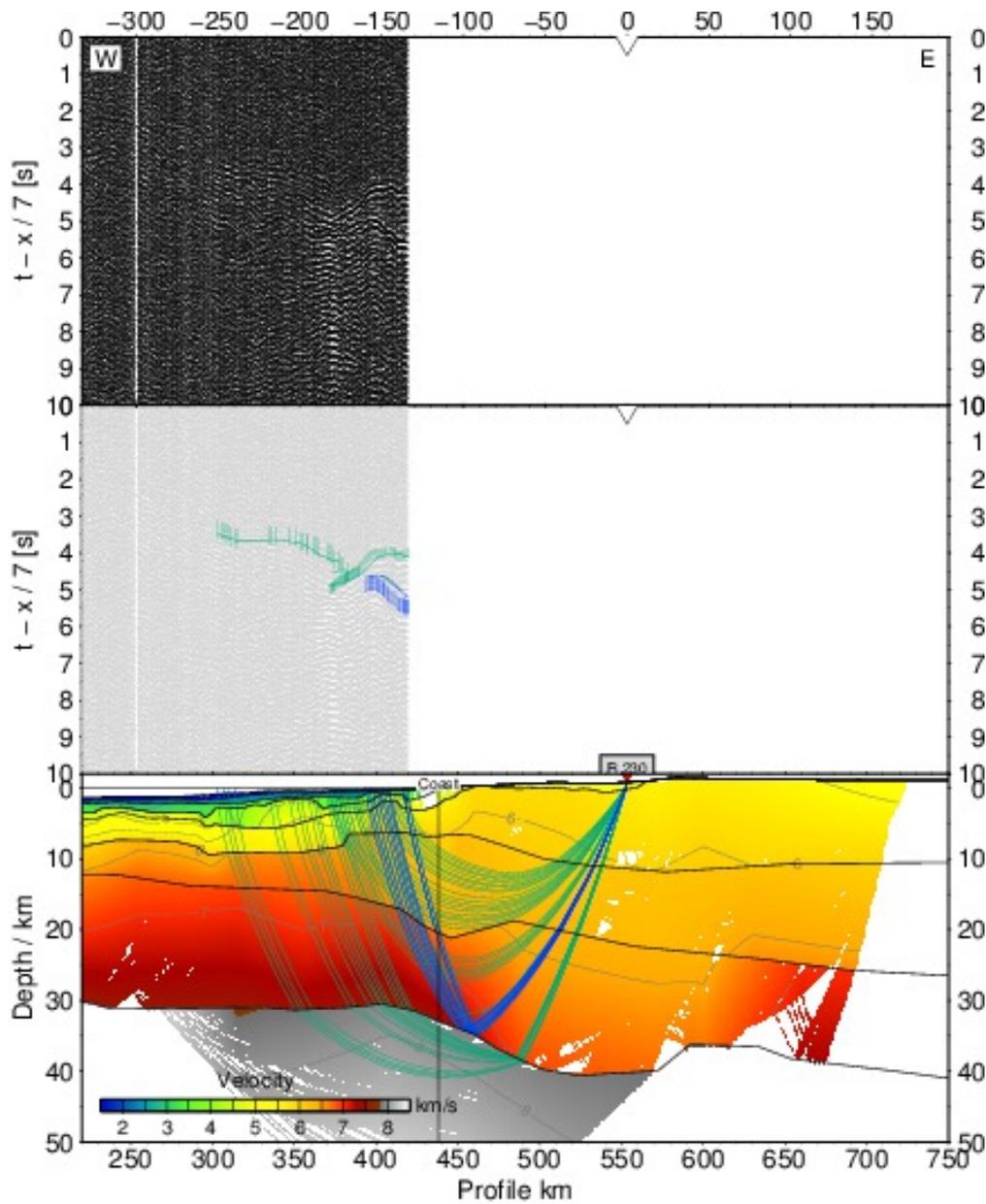
Figure A.1.38: Ray tracing results for station 230, profile 100. top) seismogram, center) seismogram overlain by picked phases (vertical bars) and calculated travel times (lines), bottom) ray path within the model. The uncertainty of the picked phases is resembled by the line length of the vertical bar. Line colors denote the ray type: blue - reflected phase, green - refracted phase
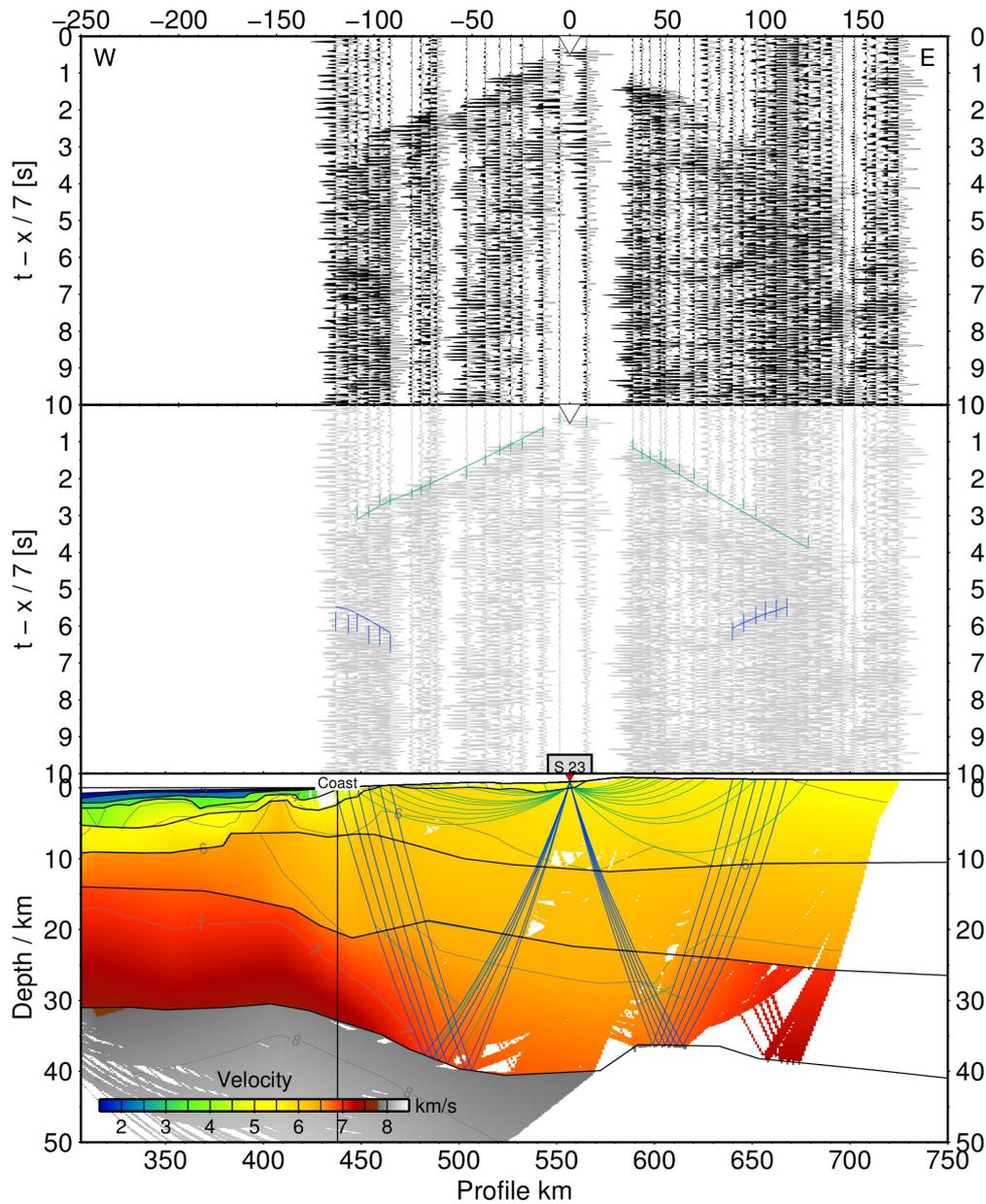
Figure A.1.39: Ray tracing results for station 23, profile 100. top) seismogram, center) seismogram overlain by picked phases (vertical bars) and calculated travel times (lines), bottom) ray path within the model. The uncertainty of the picked phases is resembled by the line length of the vertical bar. Line colors denote the ray type: blue - reflected phase, green - refracted phase
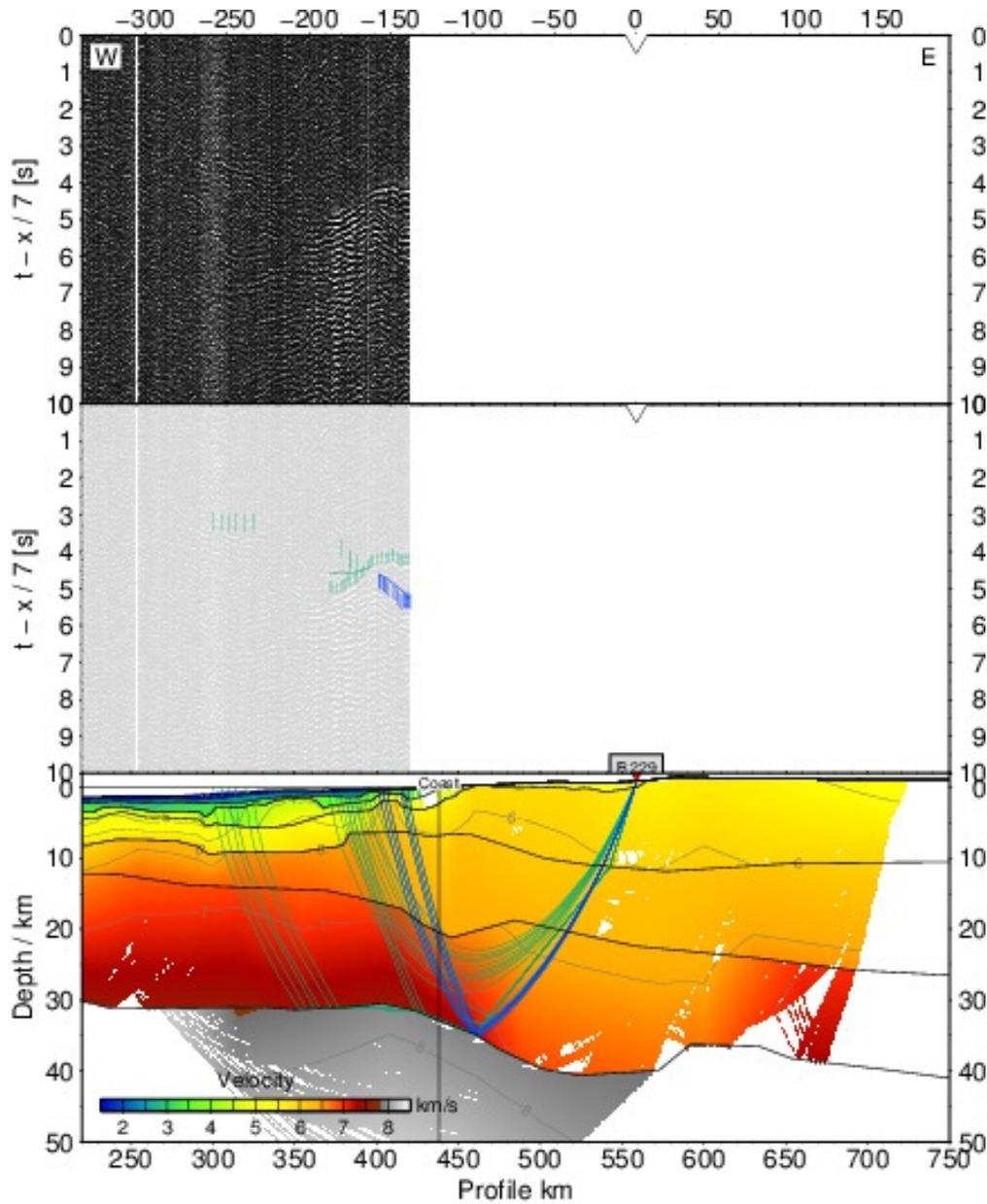
Figure A.1.40: Ray tracing results for station 229, profile 100. top) seismogram, center) seismogram overlain by picked phases (vertical bars) and calculated travel times (lines), bottom) ray path within the model. The uncertainty of the picked phases is resembled by the line length of the vertical bar. Line colors denote the ray type: blue - reflected phase, green - refracted phase
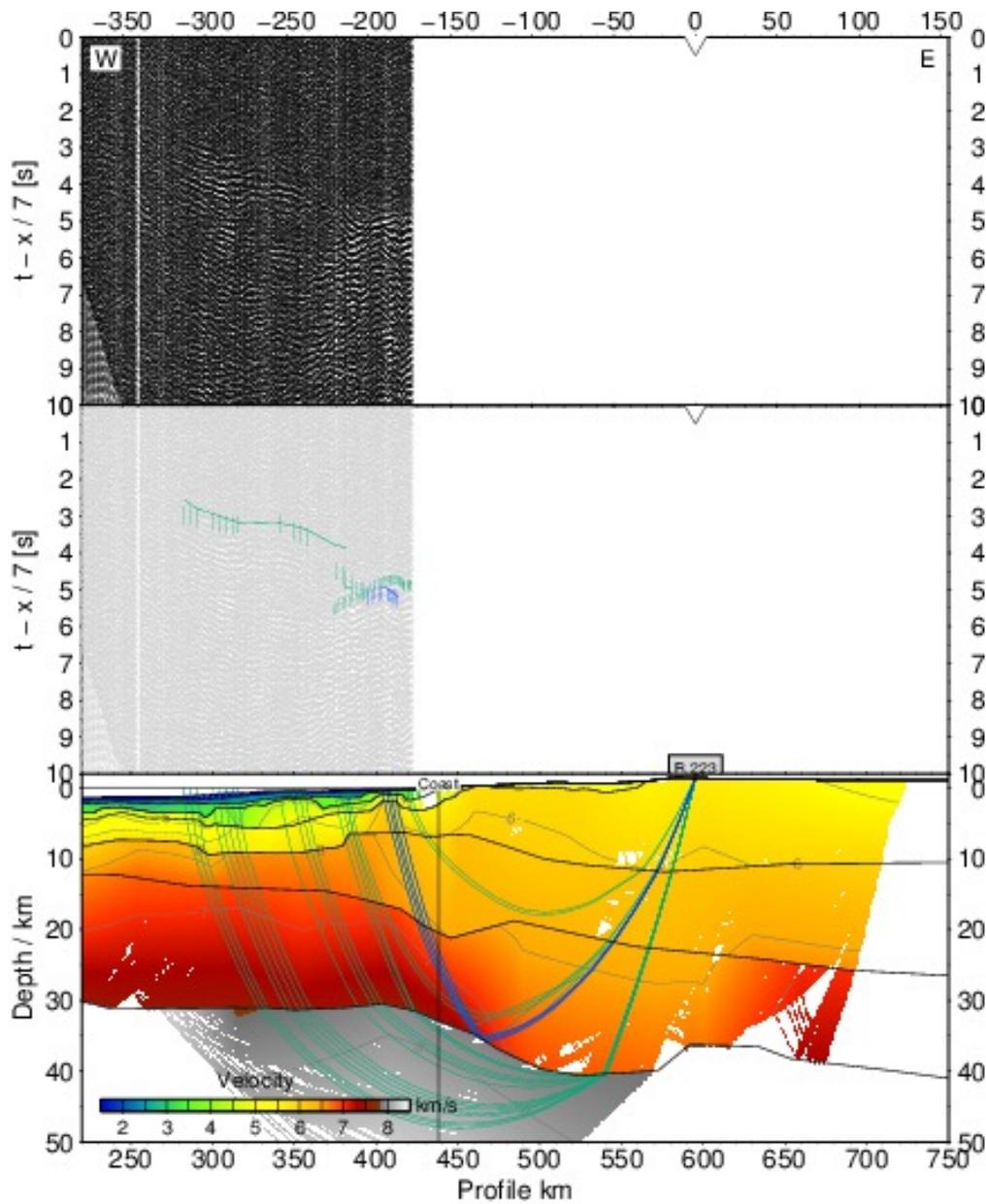
Figure A.1.41: Ray tracing results for station 223, profile 100. top) seismogram, center) seismogram overlain by picked phases (vertical bars) and calculated travel times (lines), bottom) ray path within the model. The uncertainty of the picked phases is resembled by the line length of the vertical bar. Line colors denote the ray type: blue - reflected phase, green - refracted phase
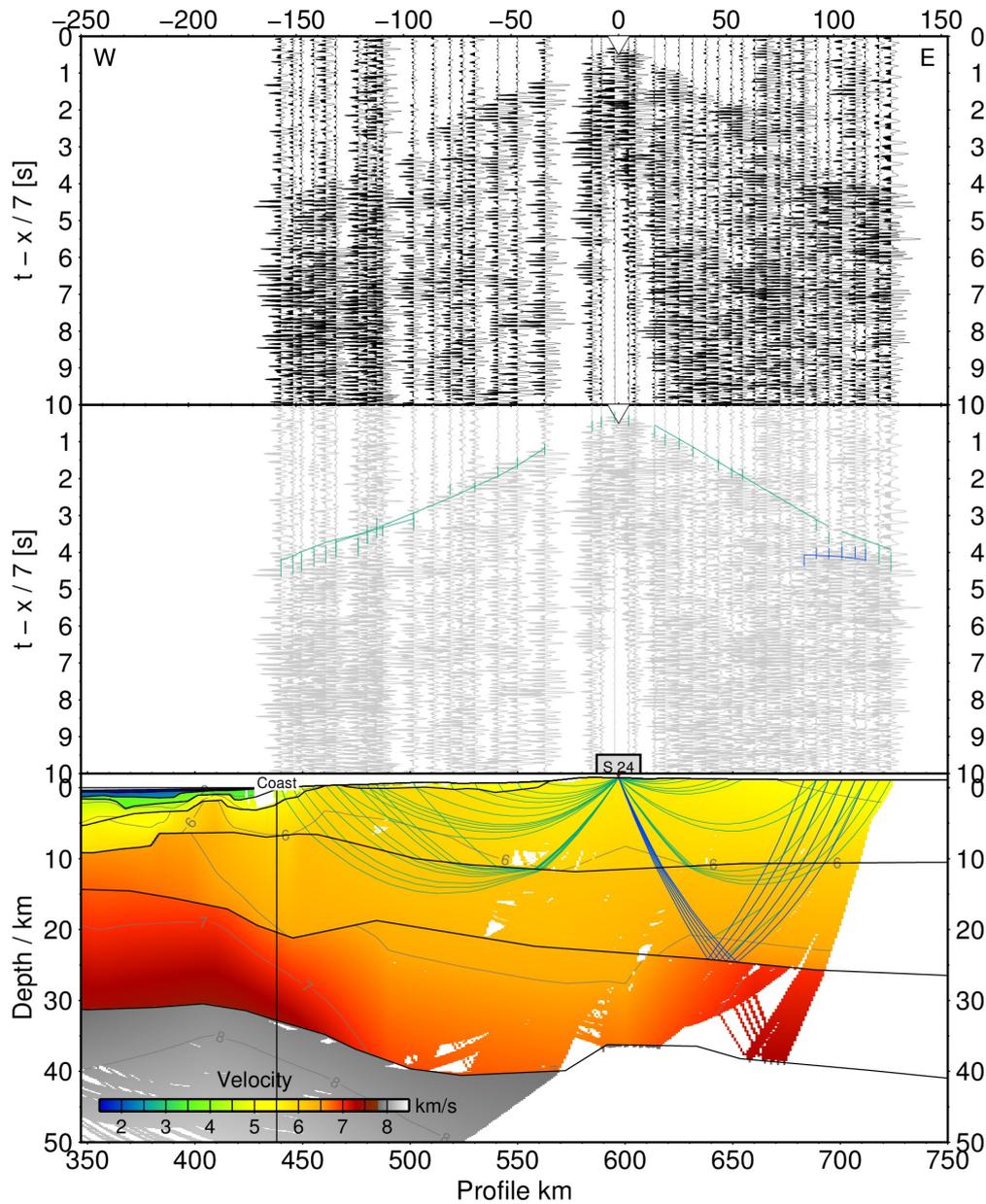
Figure A.1.42: Ray tracing results for station 24, profile 100. top) seismogram, center) seismogram overlain by picked phases (vertical bars) and calculated travel times (lines), bottom) ray path within the model. The uncertainty of the picked phases is resembled by the line length of the vertical bar. Line colors denote the ray type: blue - reflected phase, green - refracted phase
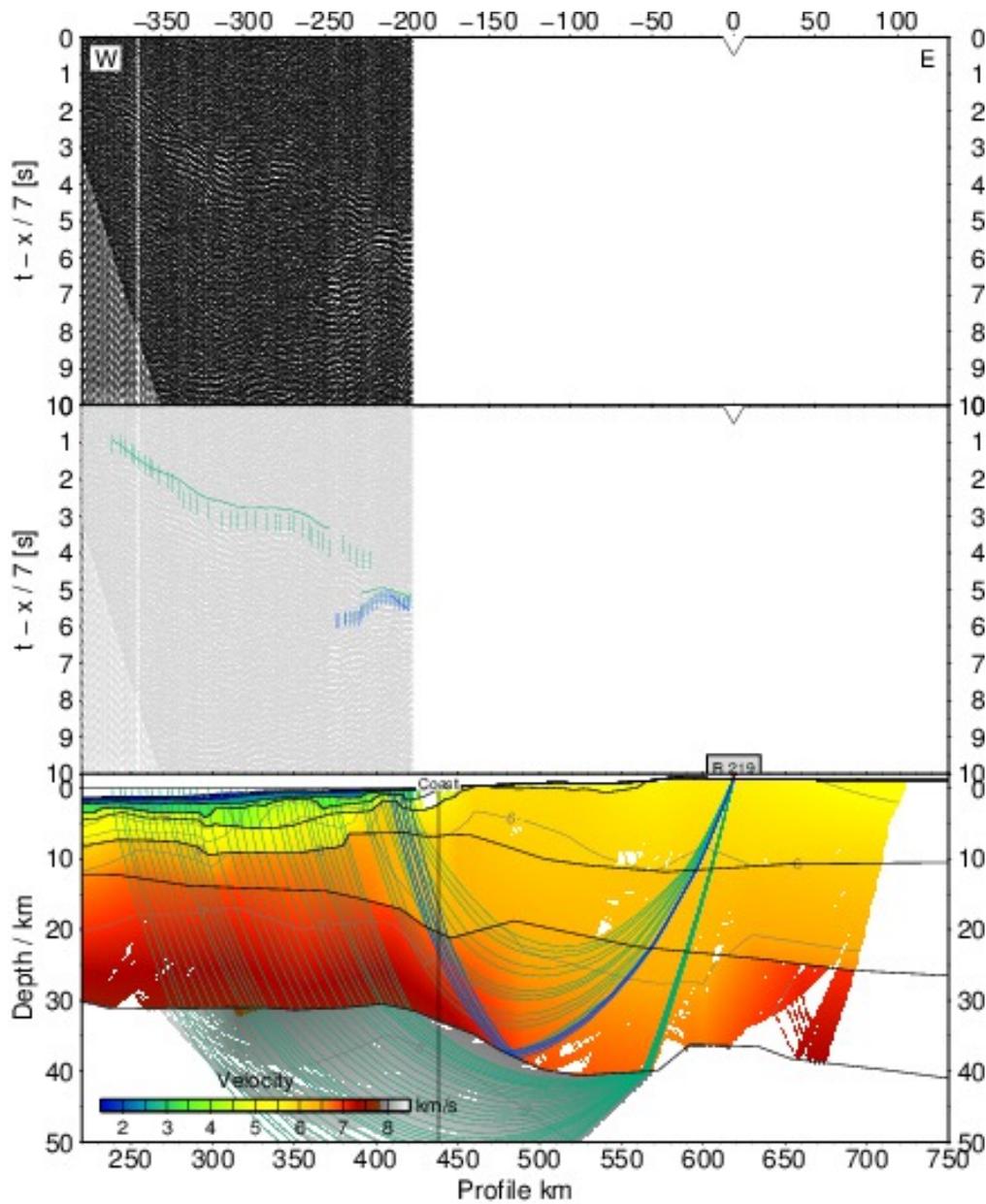
Figure A.1.43: Ray tracing results for station 219, profile 100. top) seismogram, center) seismogram overlain by picked phases (vertical bars) and calculated travel times (lines), bottom) ray path within the model. The uncertainty of the picked phases is resembled by the line length of the vertical bar. Line colors denote the ray type: blue - reflected phase, green - refracted phase
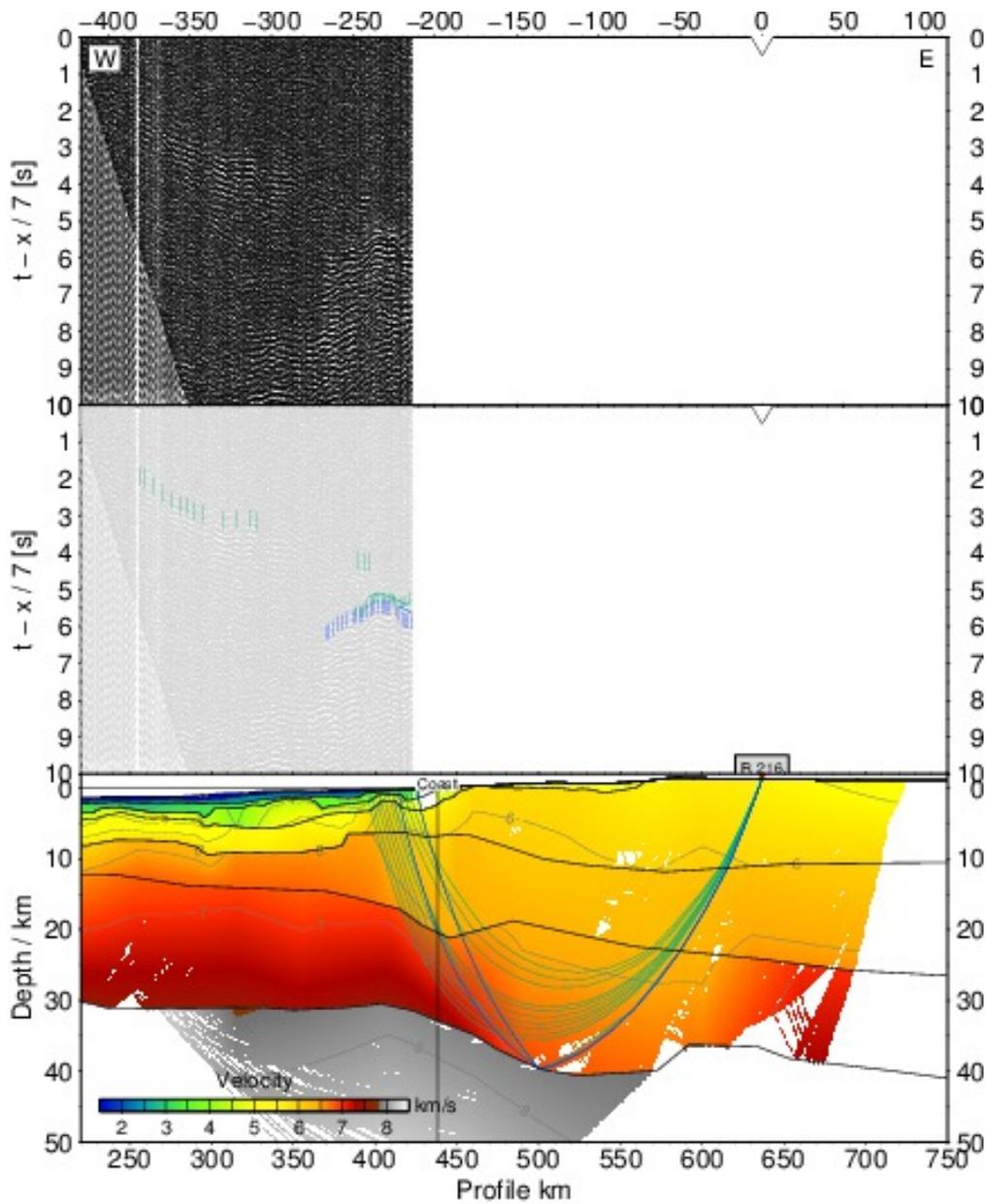
Figure A.1.44: Ray tracing results for station 216, profile 100. top) seismogram, center) seismogram overlain by picked phases (vertical bars) and calculated travel times (lines), bottom) ray path within the model. The uncertainty of the picked phases is resembled by the line length of the vertical bar. Line colors denote the ray type: blue - reflected phase, green - refracted phase
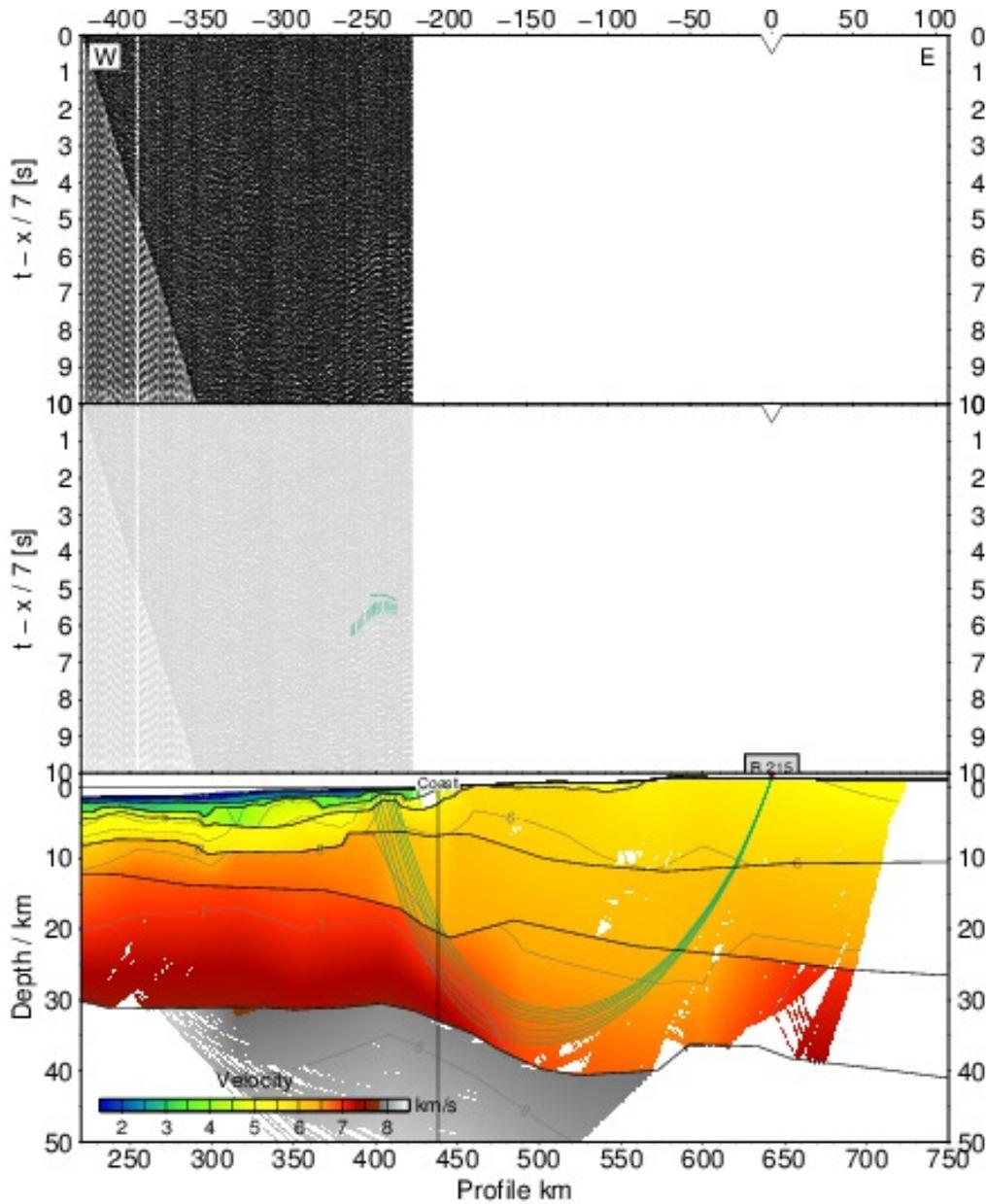
Figure A.1.45: Ray tracing results for station 215, profile 100. top) seismogram, center) seismogram overlain by picked phases (vertical bars) and calculated travel times (lines), bottom) ray path within the model. The uncertainty of the picked phases is resembled by the line length of the vertical bar. Line colors denote the ray type: blue - reflected phase, green - refracted phase
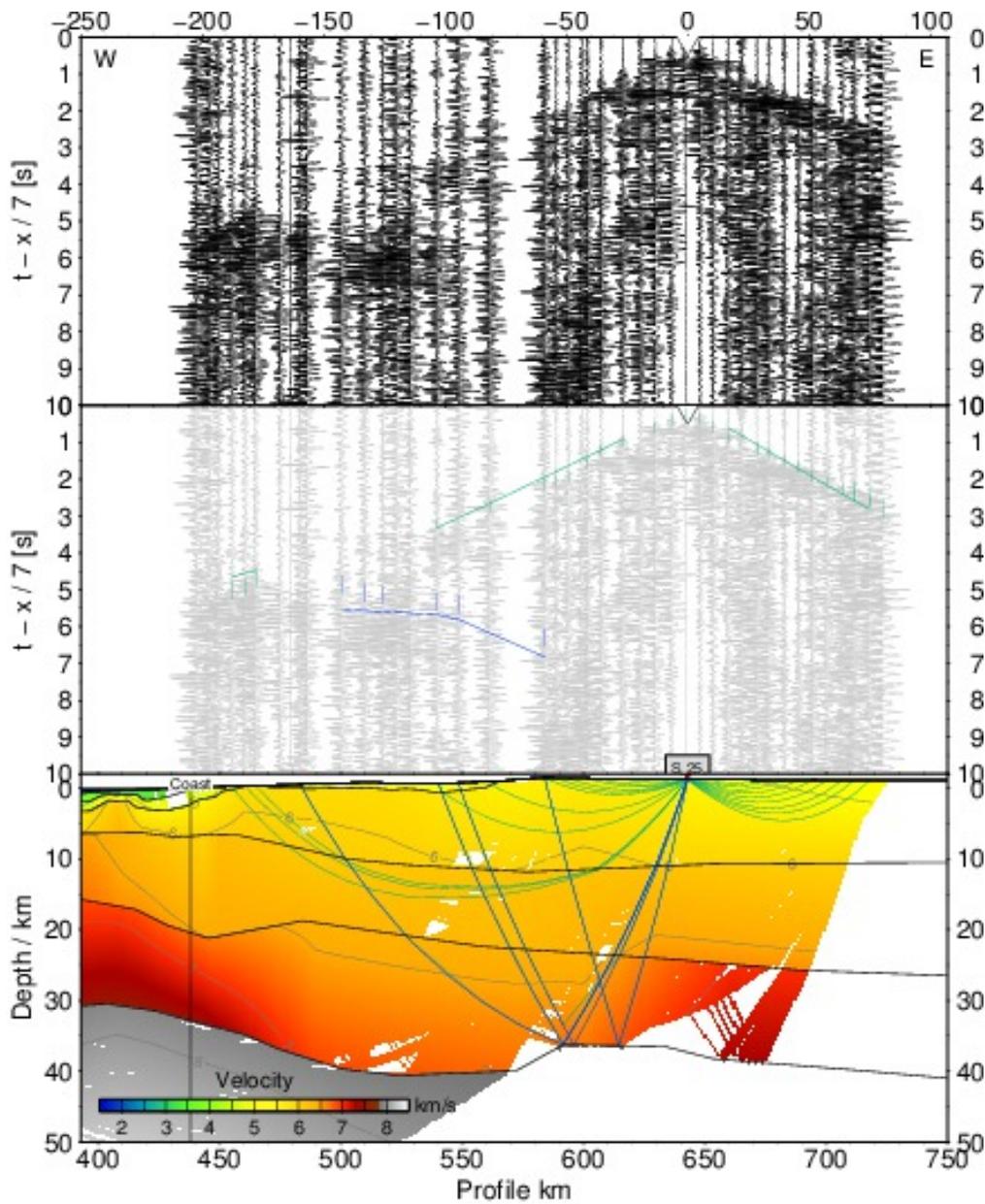
Figure A.1.46: Ray tracing results for station 25, profile 100. top) seismogram, center) seismogram overlain by picked phases (vertical bars) and calculated travel times (lines), bottom) ray path within the model. The uncertainty of the picked phases is resembled by the line length of the vertical bar. Line colors denote the ray type: blue - reflected phase, green - refracted phase
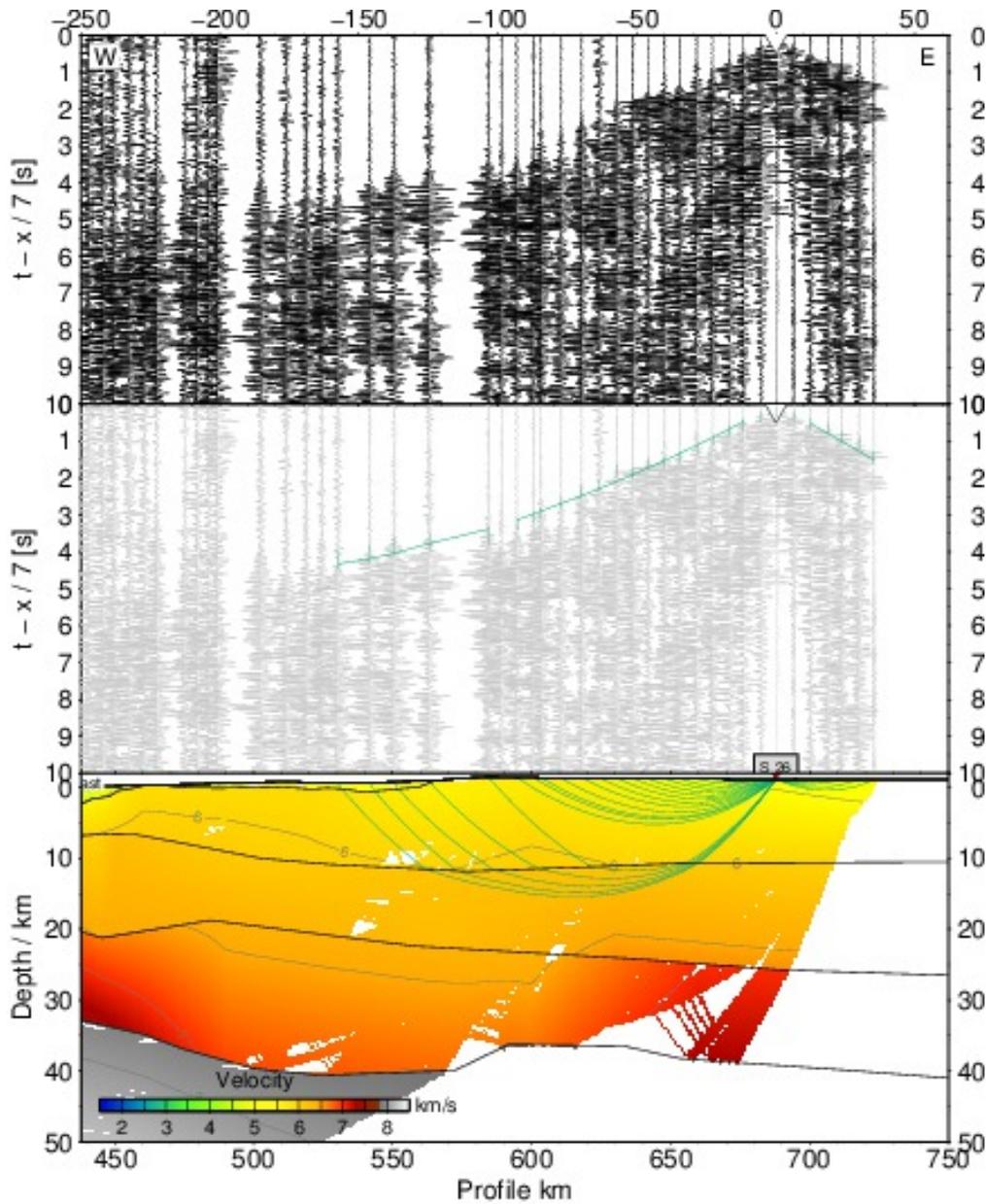
Figure A.1.47:   Ray tracing results for station 26, profile 100. top) seismogram, center) seismogram overlain by picked phases (vertical bars) and calculated travel times (lines), bottom) ray path within the model. The uncertainty of the picked phases is resembled by the line length of the vertical bar. Line colors denote the ray type: blue - reflected phase, green - refracted phase
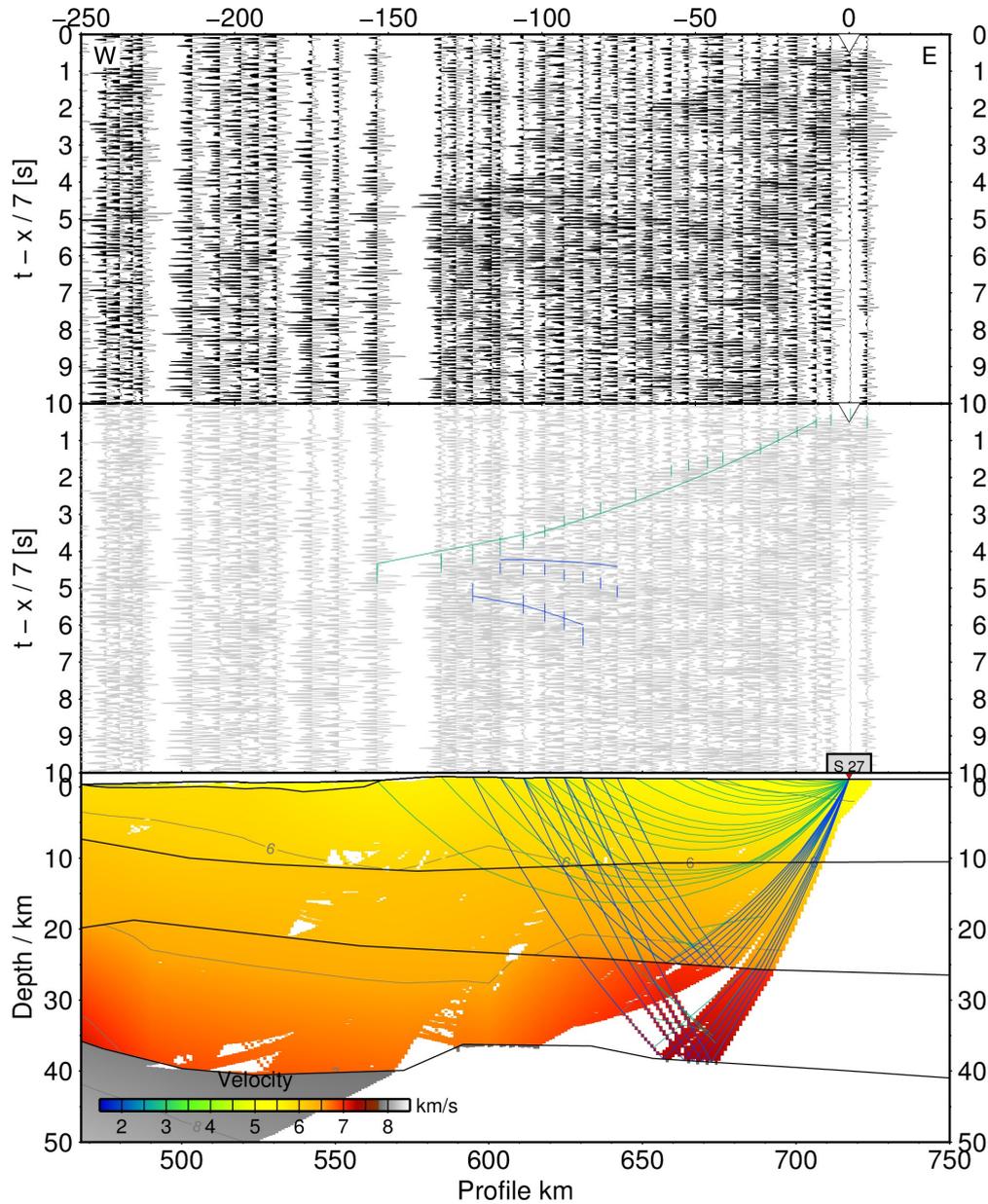
Figure A.1.48: Ray tracing results for station 27, profile 100. top) seismogram,
center) seismogram overlain by picked phases (vertical bars) and calculated travel
times (lines), bottom) ray path within the model. The uncertainty of the picked
phases is resembled by the line length of the vertical bar. Line colors denote the
ray type: blue - reflected phase, green - refracted phase

A.2   Ray tracing results for profile 150
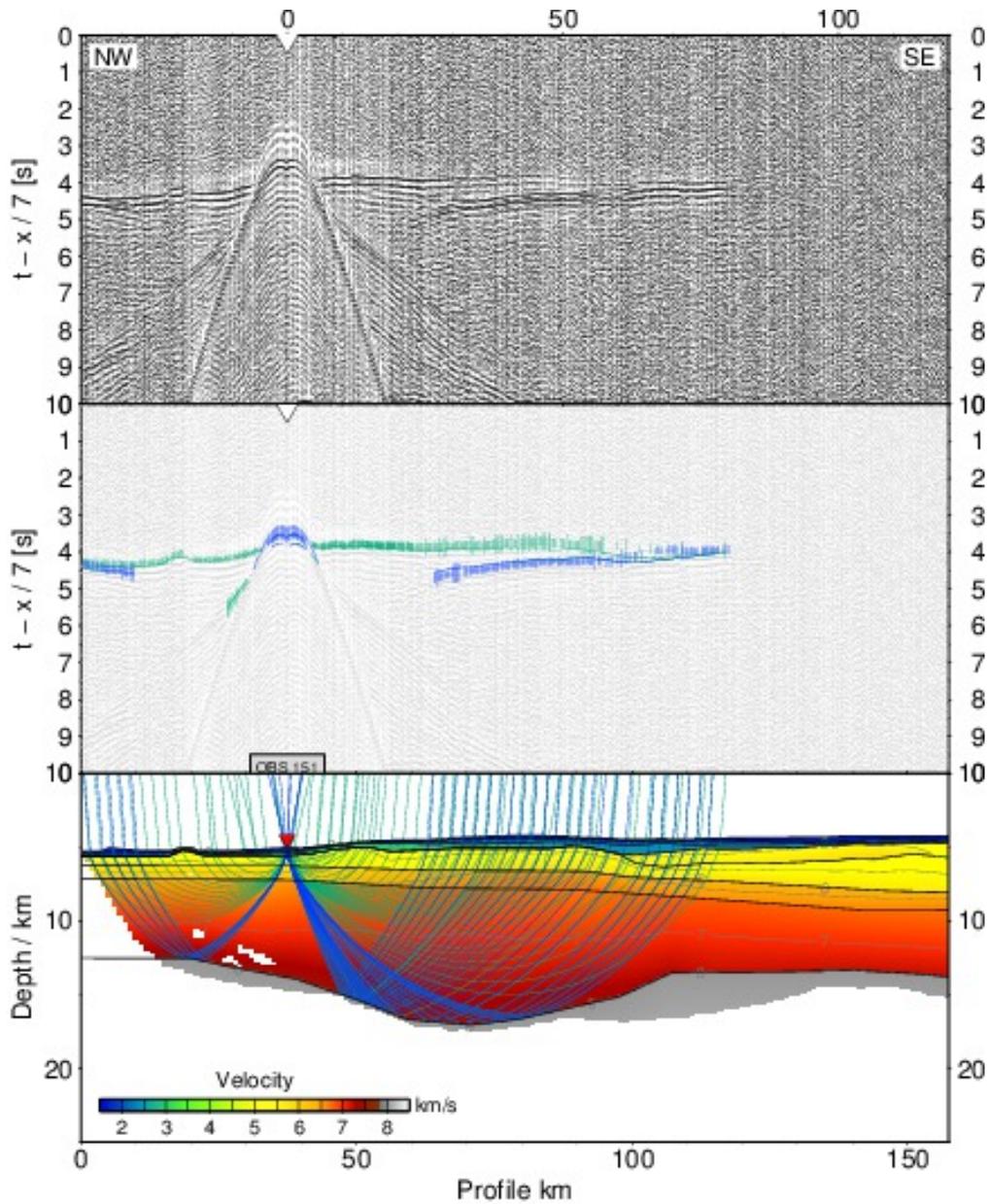
Figure A.2.1: Ray tracing results for station 151, profile 150. top) seismogram, center) seismogram overlain by picked phases (vertical bars) and calculated travel times (lines), bottom) ray path within the model. The uncertainty of the picked phases is resembled by the line length of the vertical bar. Line colors denote the ray type: blue - reflected phase, green - refracted phase
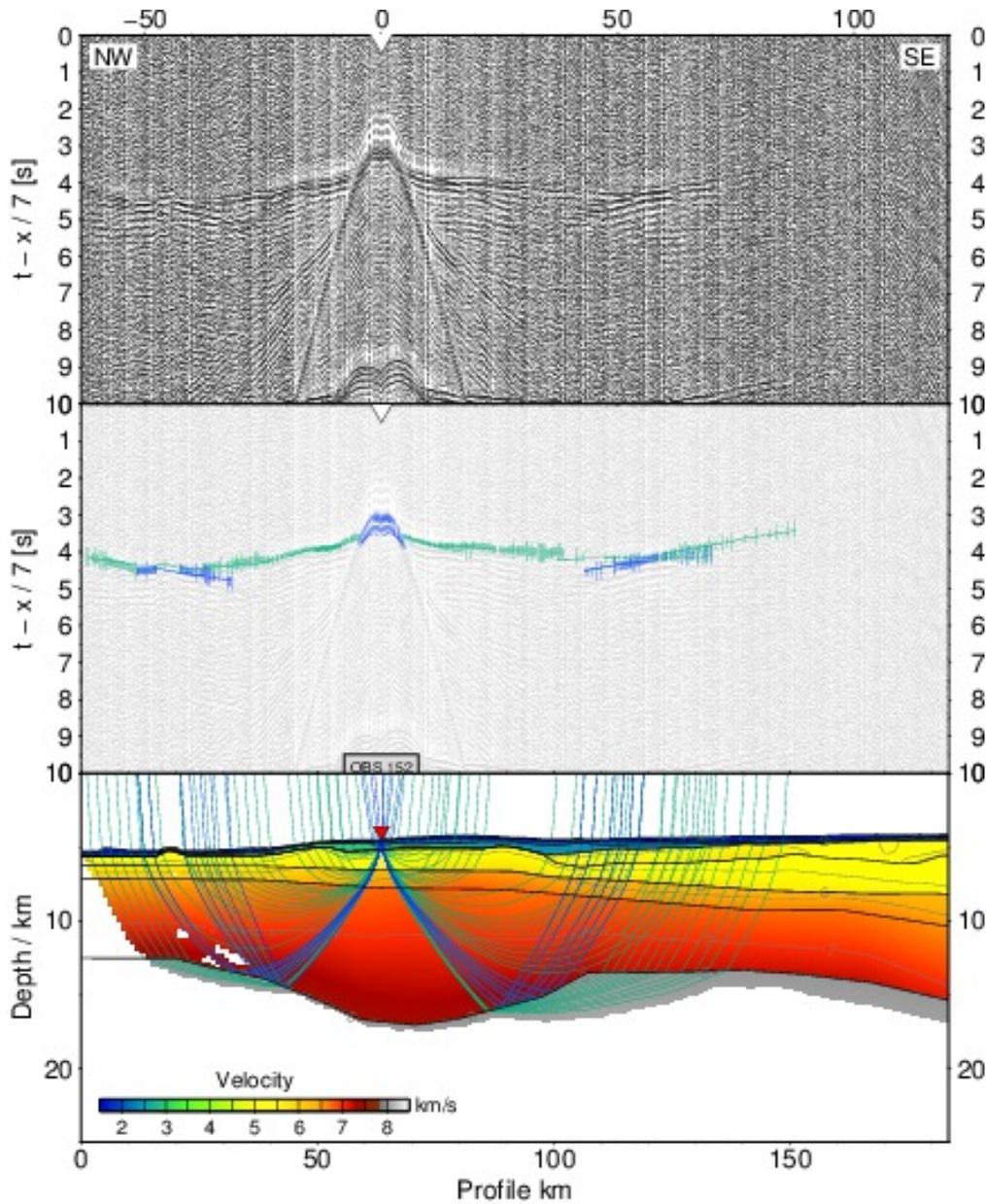
Figure A.2.2: Ray tracing results for station 152, profile 150. top) seismogram, center) seismogram overlain by picked phases (vertical bars) and calculated travel times (lines), bottom) ray path within the model. The uncertainty of the picked phases is resembled by the line length of the vertical bar. Line colors denote the ray type: blue - reflected phase, green - refracted phase
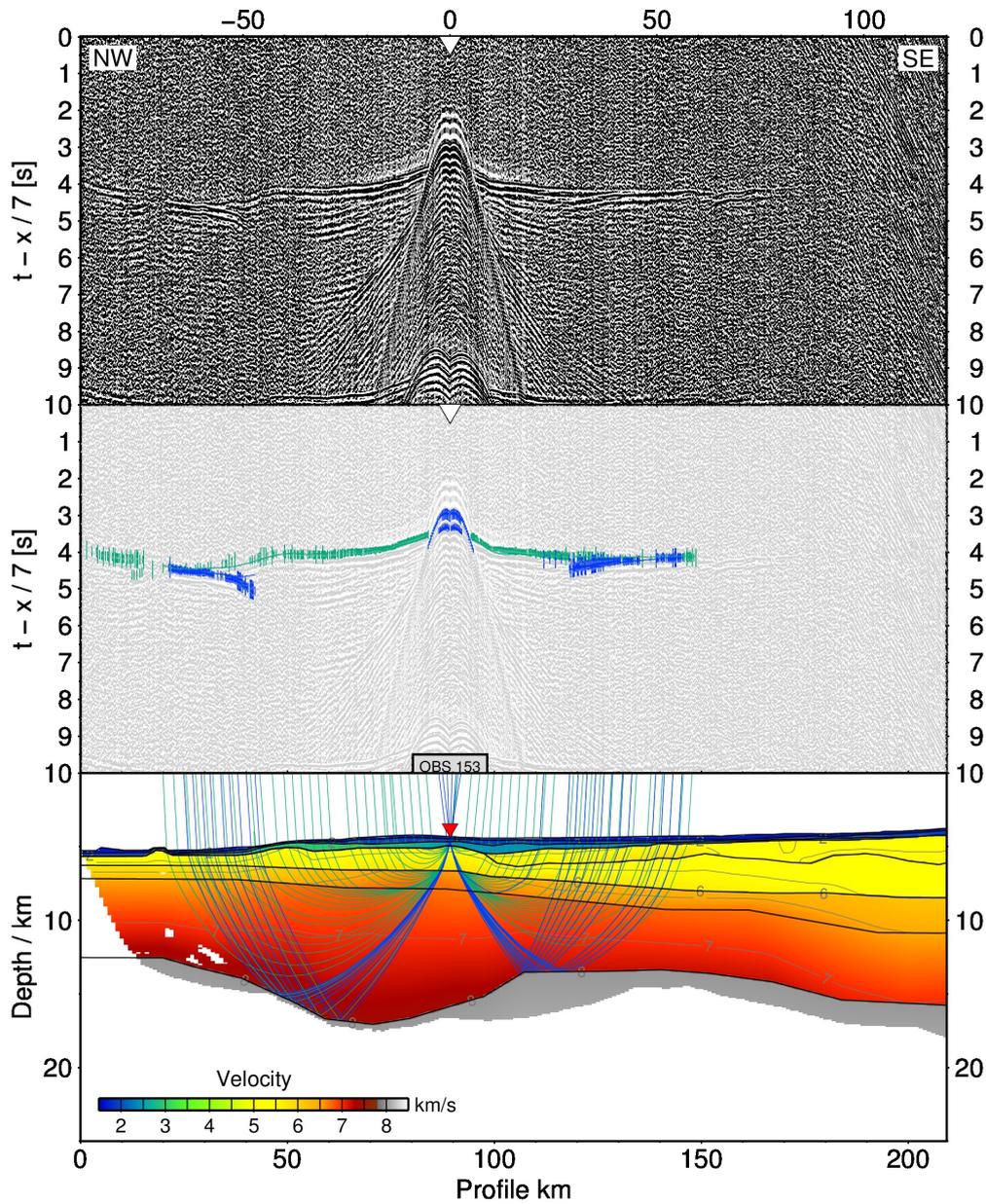
Figure A.2.3: Ray tracing results for station 153, profile 150. top) seismogram, center) seismogram overlain by picked phases (vertical bars) and calculated travel times (lines), bottom) ray path within the model. The uncertainty of the picked phases is resembled by the line length of the vertical bar. Line colors denote the ray type: blue - reflected phase, green - refracted phase
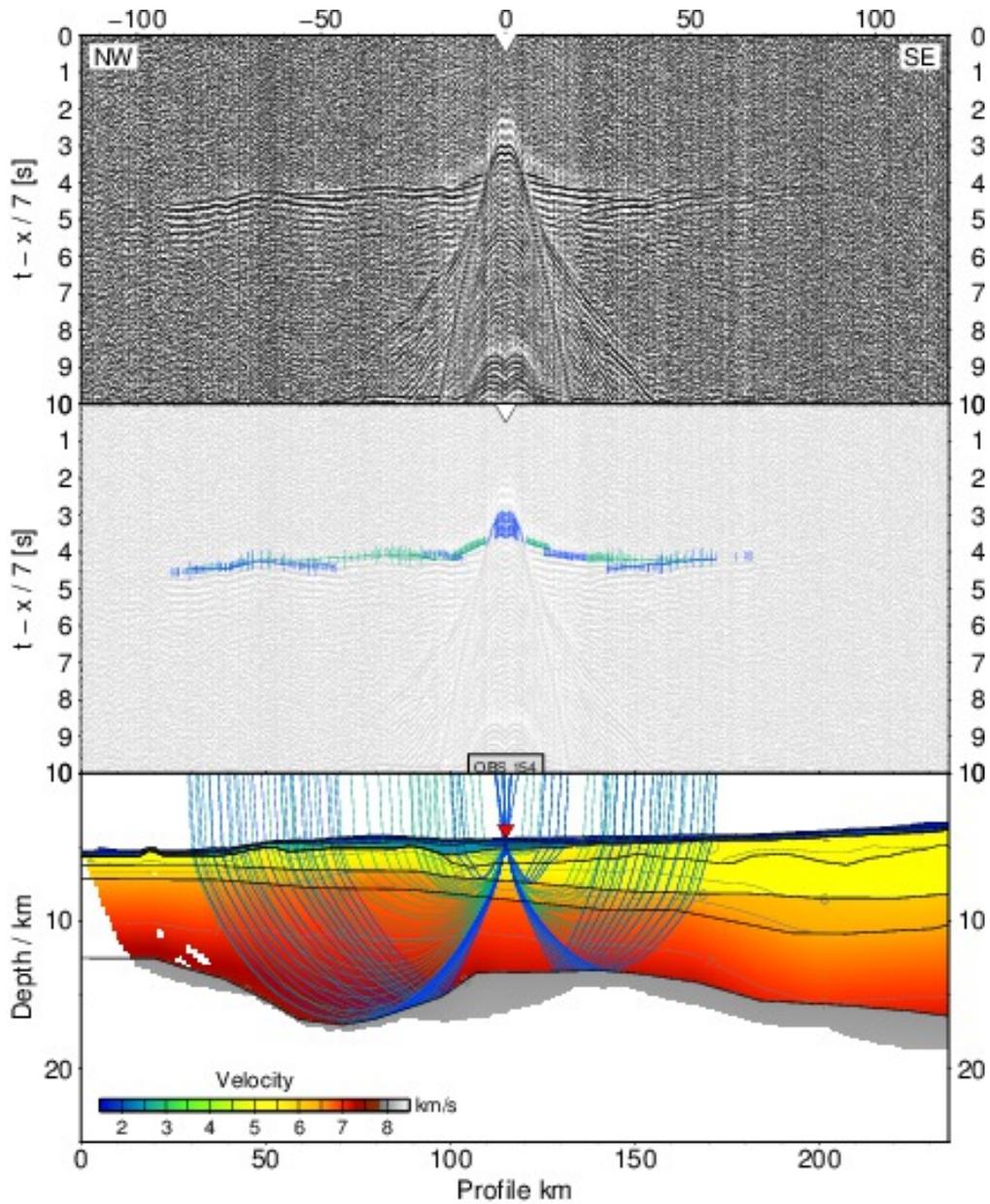
Figure A.2.4: Ray tracing results for station 154, profile 150. top) seismogram, center) seismogram overlain by picked phases (vertical bars) and calculated travel times (lines), bottom) ray path within the model. The uncertainty of the picked phases is resembled by the line length of the vertical bar. Line colors denote the ray type: blue - reflected phase, green - refracted phase
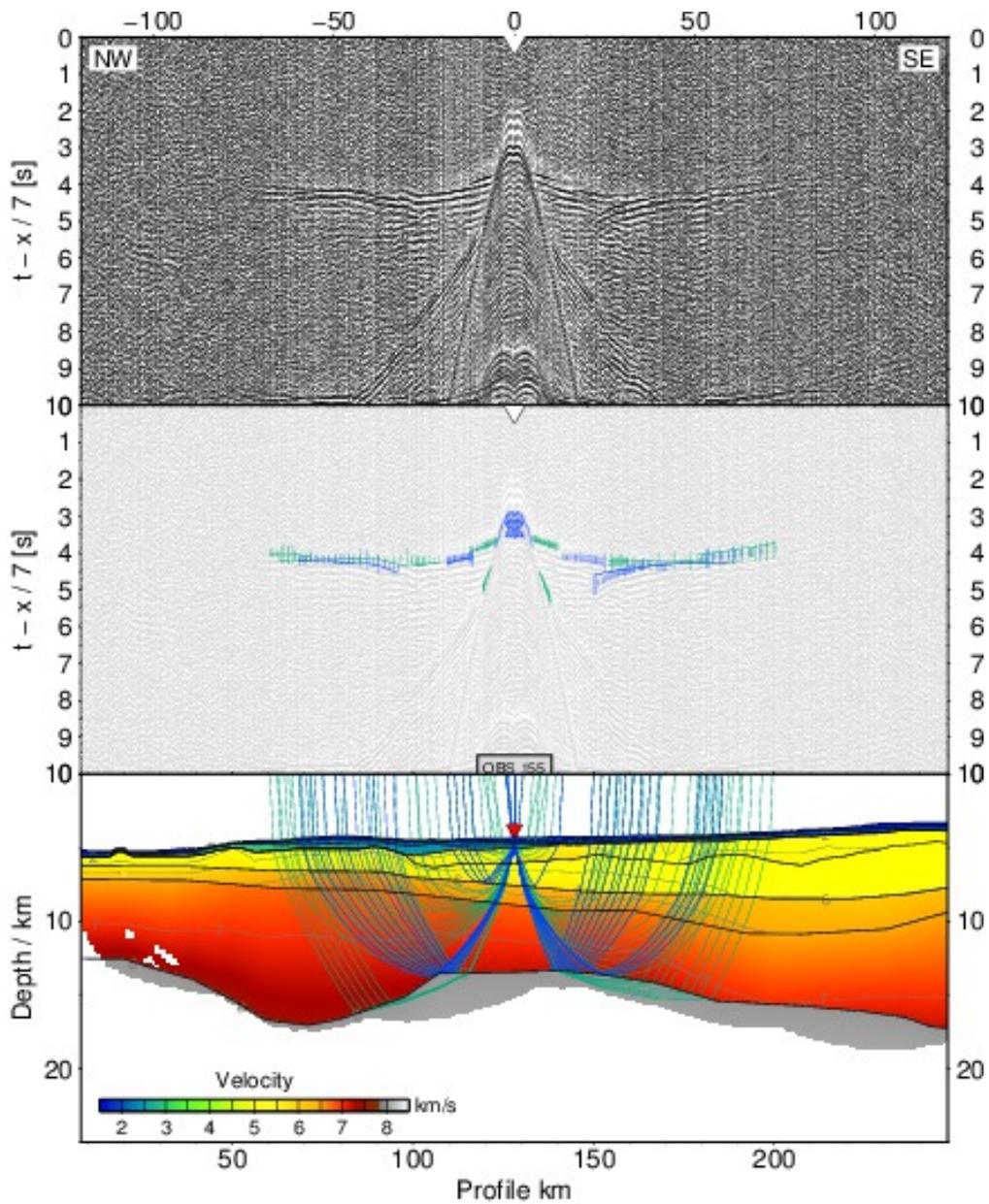
Figure A.2.5: Ray tracing results for station 155, profile 150. top) seismogram, center) seismogram overlain by picked phases (vertical bars) and calculated travel times (lines), bottom) ray path within the model. The uncertainty of the picked phases is resembled by the line length of the vertical bar. Line colors denote the ray type: blue - reflected phase, green - refracted phase
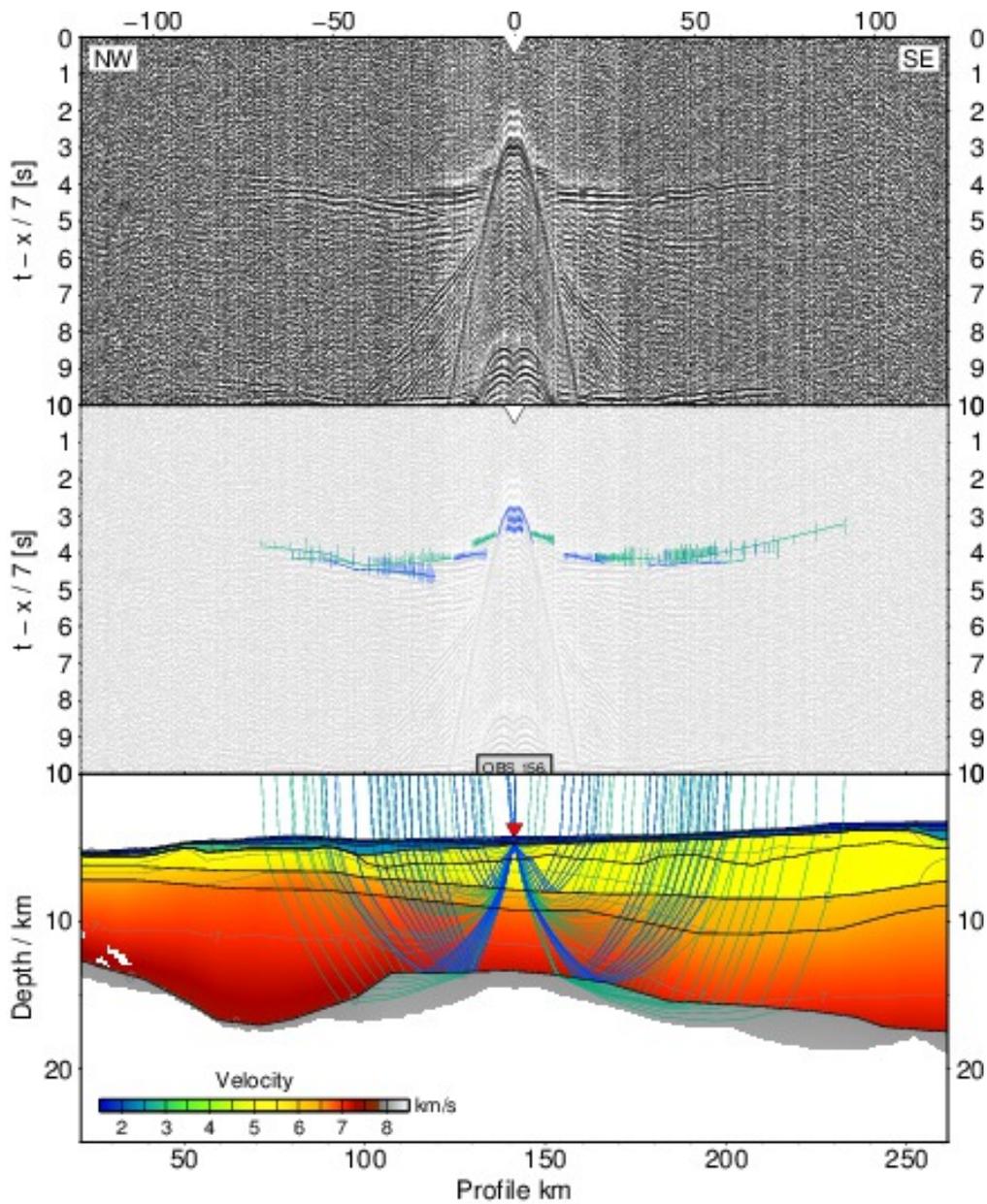
Figure A.2.6: Ray tracing results for station 156, profile 150. top) seismogram, center) seismogram overlain by picked phases (vertical bars) and calculated travel times (lines), bottom) ray path within the model. The uncertainty of the picked phases is resembled by the line length of the vertical bar. Line colors denote the ray type: blue - reflected phase, green - refracted phase
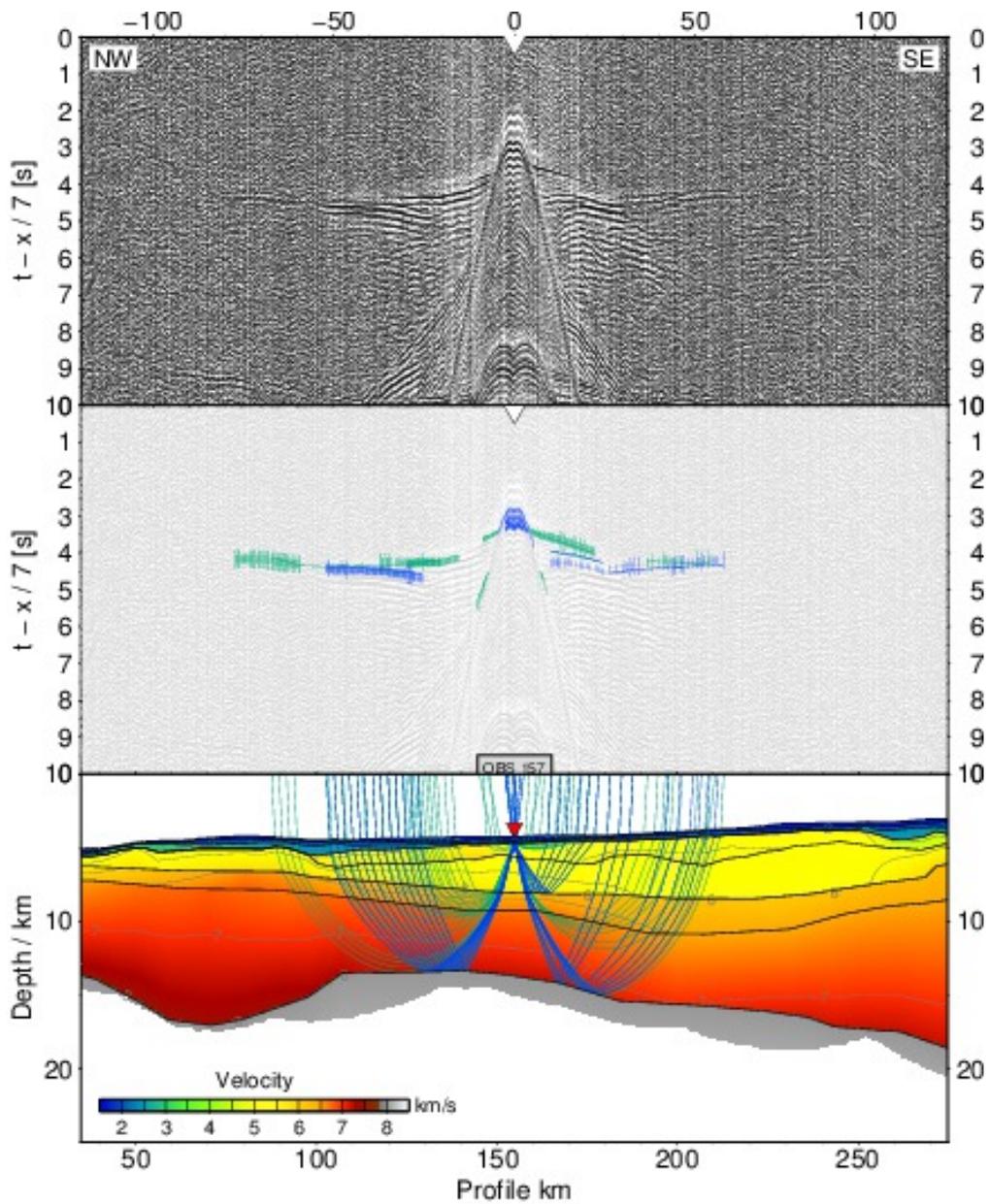
Figure A.2.7: Ray tracing results for station 157, profile 150. top) seismogram, center) seismogram overlain by picked phases (vertical bars) and calculated travel times (lines), bottom) ray path within the model. The uncertainty of the picked phases is resembled by the line length of the vertical bar. Line colors denote the ray type: blue - reflected phase, green - refracted phase
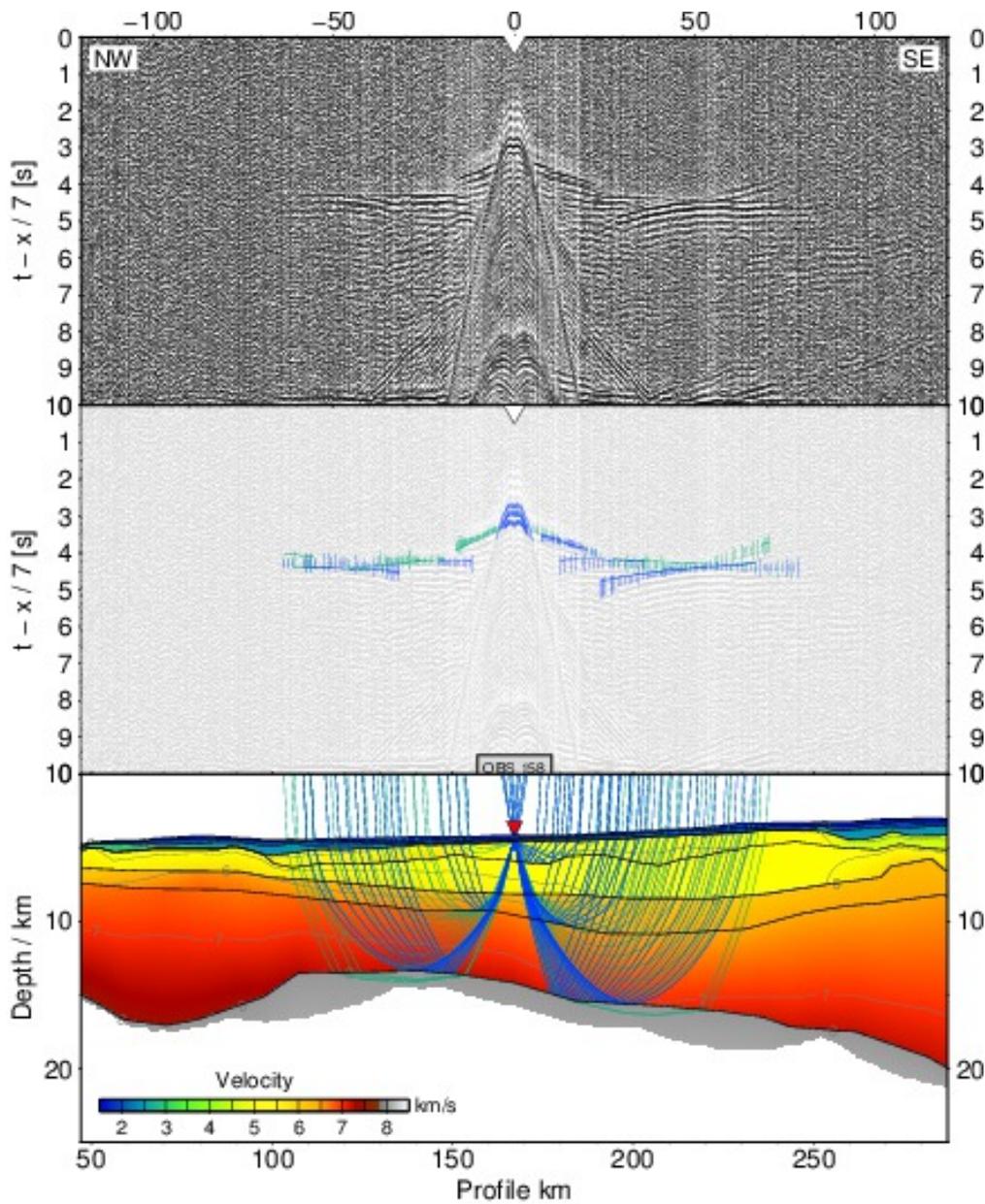
Figure A.2.8: Ray tracing results for station 158, profile 150. top) seismogram, center) seismogram overlain by picked phases (vertical bars) and calculated travel times (lines), bottom) ray path within the model. The uncertainty of the picked phases is resembled by the line length of the vertical bar. Line colors denote the ray type: blue - reflected phase, green - refracted phase
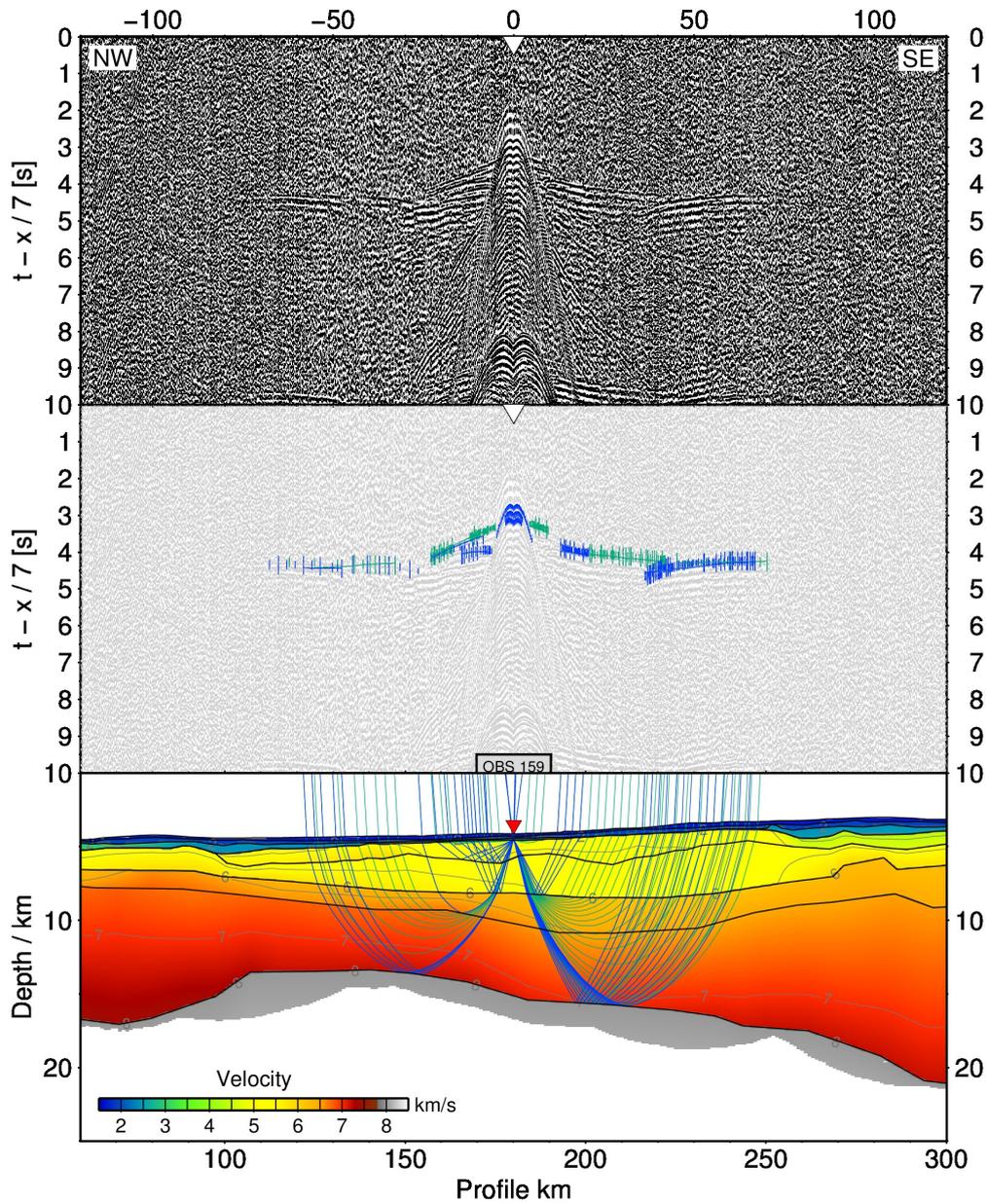
Figure A.2.9: Ray tracing results for station 159, profile 150. top) seismogram, center) seismogram overlain by picked phases (vertical bars) and calculated travel times (lines), bottom) ray path within the model. The uncertainty of the picked phases is resembled by the line length of the vertical bar. Line colors denote the ray type: blue - reflected phase, green - refracted phase
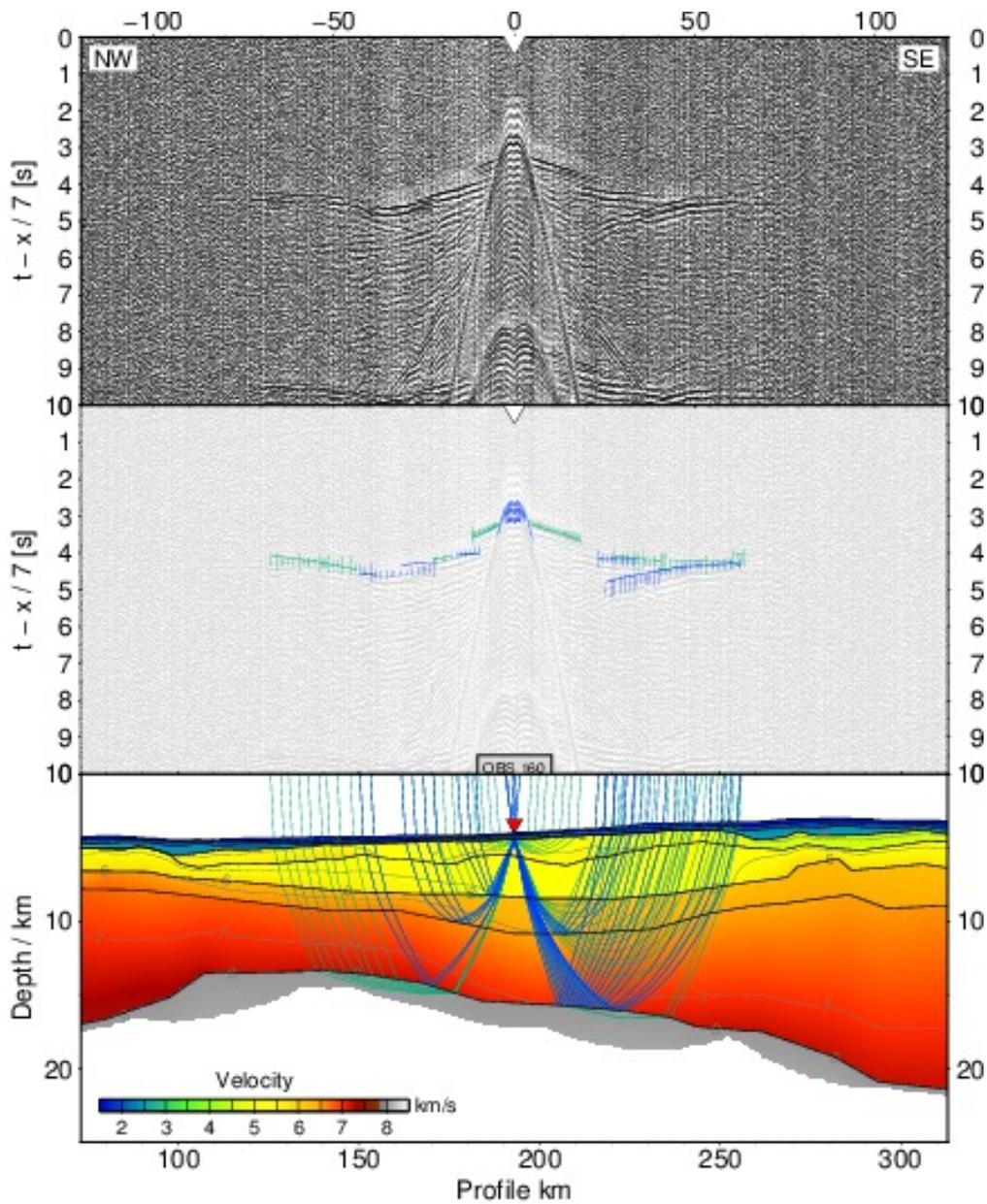
Figure A.2.10: Ray tracing results for station 160, profile 150. top) seismogram, center) seismogram overlain by picked phases (vertical bars) and calculated travel times (lines), bottom) ray path within the model. The uncertainty of the picked phases is resembled by the line length of the vertical bar. Line colors denote the ray type: blue - reflected phase, green - refracted phase
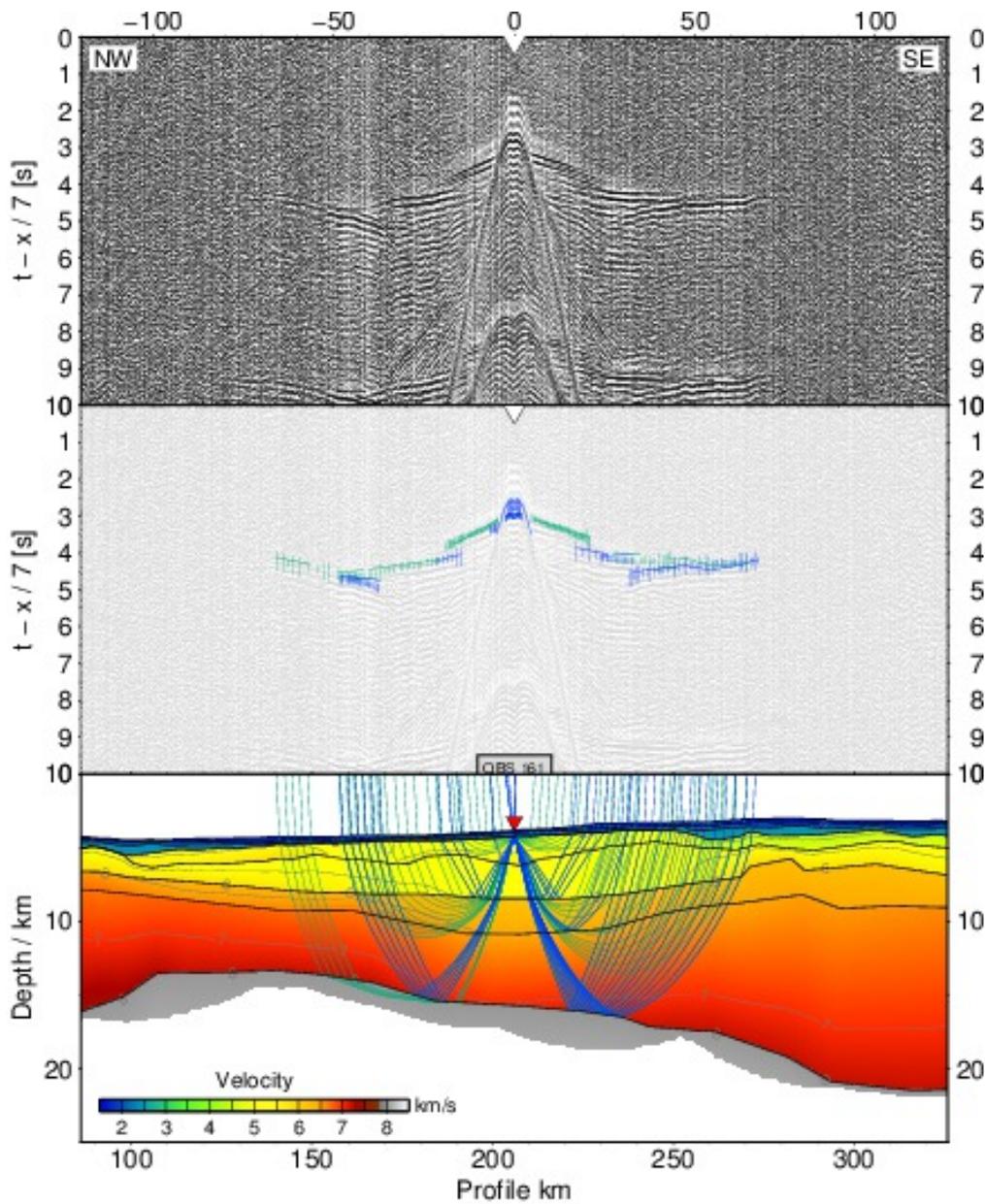
Figure A.2.11: Ray tracing results for station 161, profile 150. top) seismogram, center) seismogram overlain by picked phases (vertical bars) and calculated travel times (lines), bottom) ray path within the model. The uncertainty of the picked phases is resembled by the line length of the vertical bar. Line colors denote the ray type: blue - reflected phase, green - refracted phase
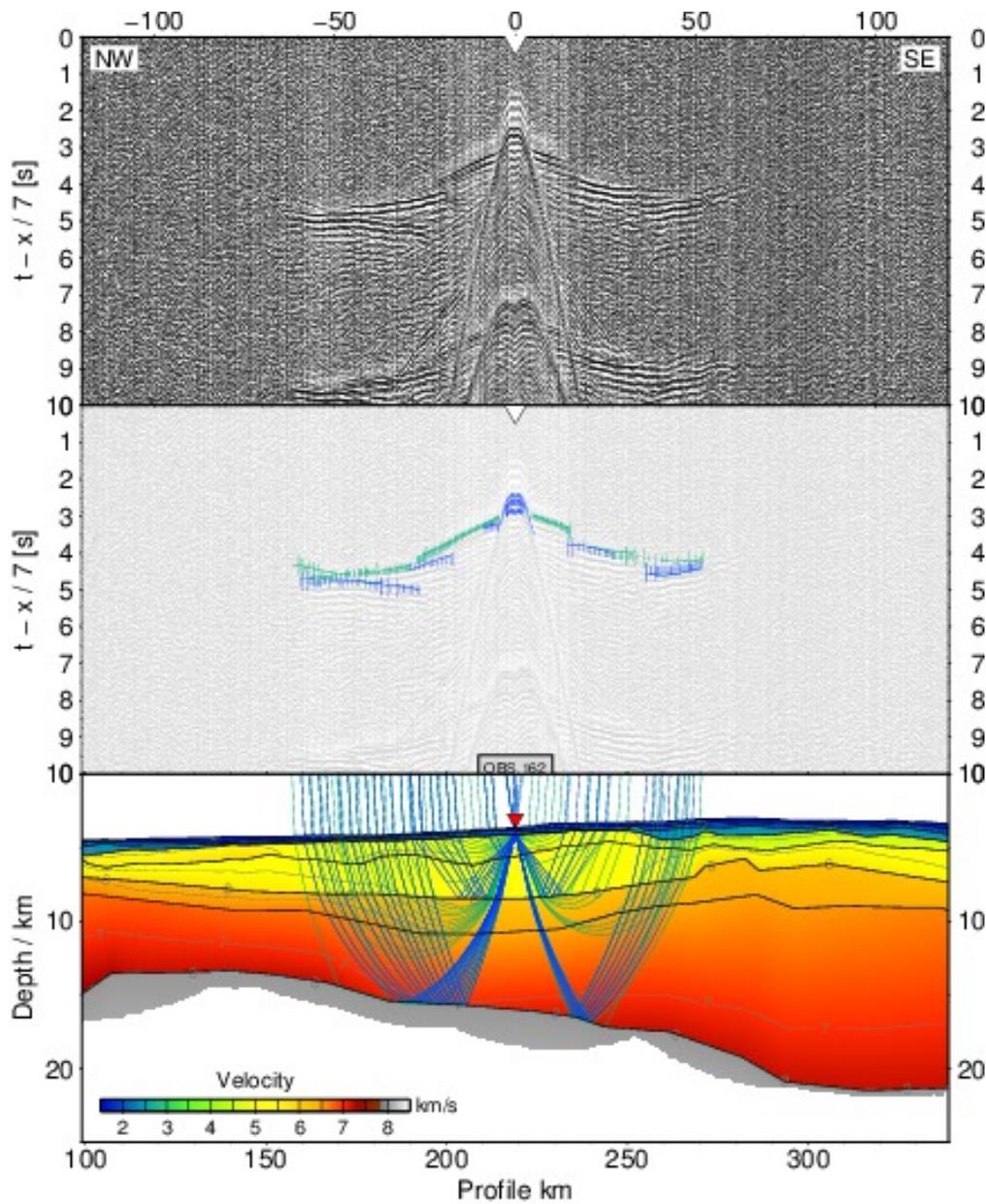
Figure A.2.12: Ray tracing results for station 162, profile 150. top) seismogram, center) seismogram overlain by picked phases (vertical bars) and calculated travel times (lines), bottom) ray path within the model. The uncertainty of the picked phases is resembled by the line length of the vertical bar. Line colors denote the ray type: blue - reflected phase, green - refracted phase
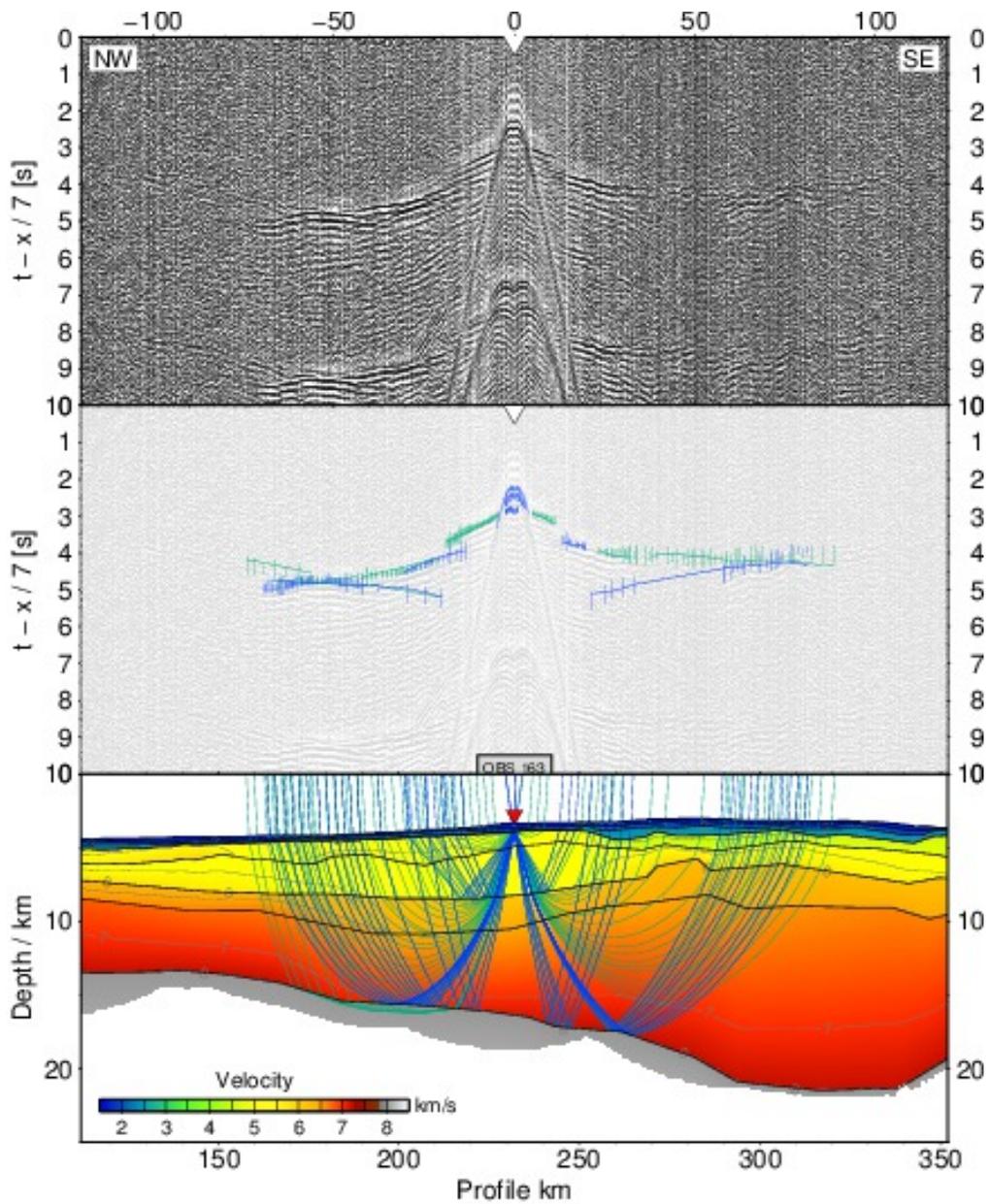
Figure A.2.13: Ray tracing results for station 163, profile 150. top) seismogram, center) seismogram overlain by picked phases (vertical bars) and calculated travel times (lines), bottom) ray path within the model. The uncertainty of the picked phases is resembled by the line length of the vertical bar. Line colors denote the ray type: blue - reflected phase, green - refracted phase
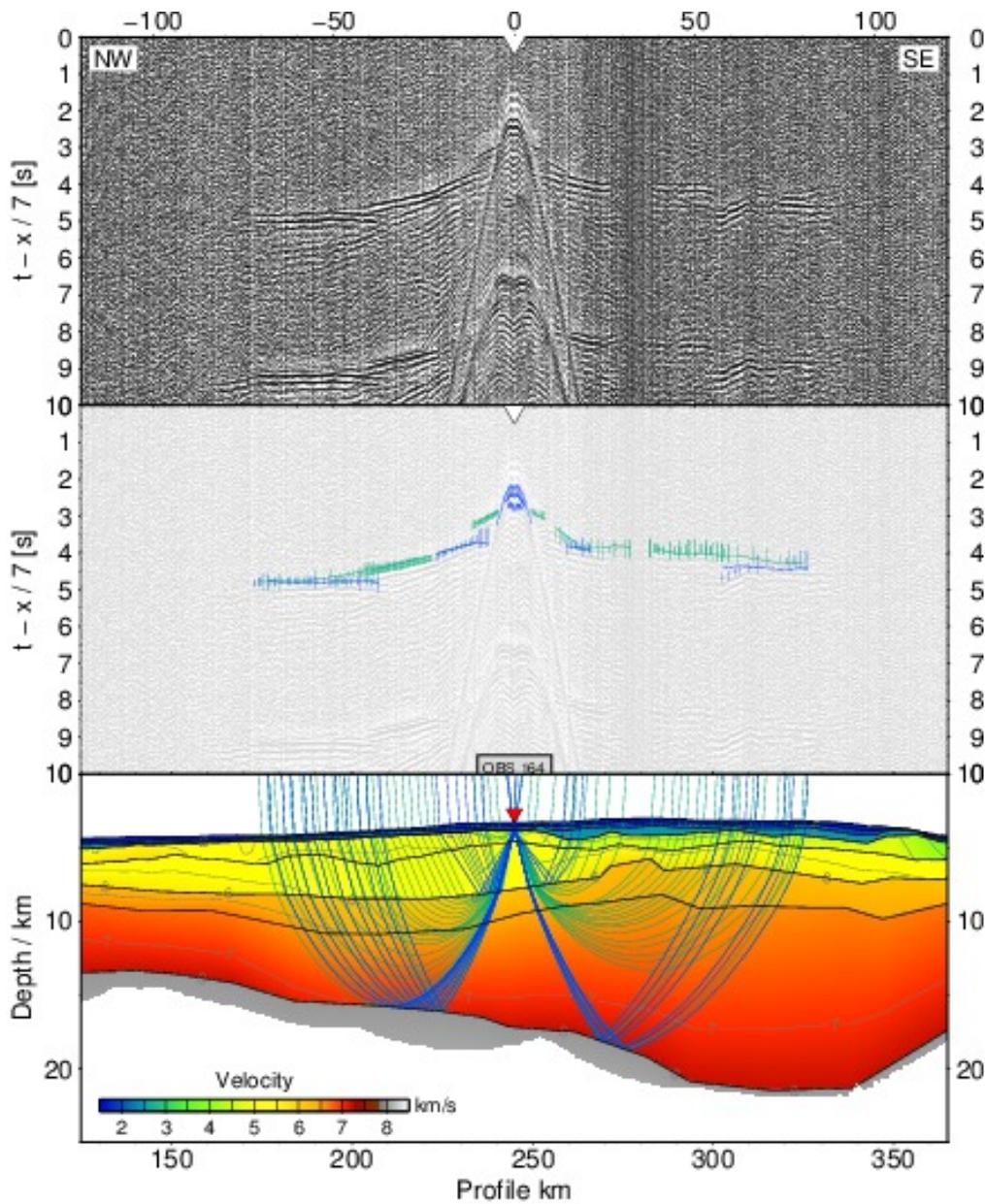
Figure A.2.14: Ray tracing results for station 164, profile 150. top) seismogram, center) seismogram overlain by picked phases (vertical bars) and calculated travel times (lines), bottom) ray path within the model. The uncertainty of the picked phases is resembled by the line length of the vertical bar. Line colors denote the ray type: blue - reflected phase, green - refracted phase
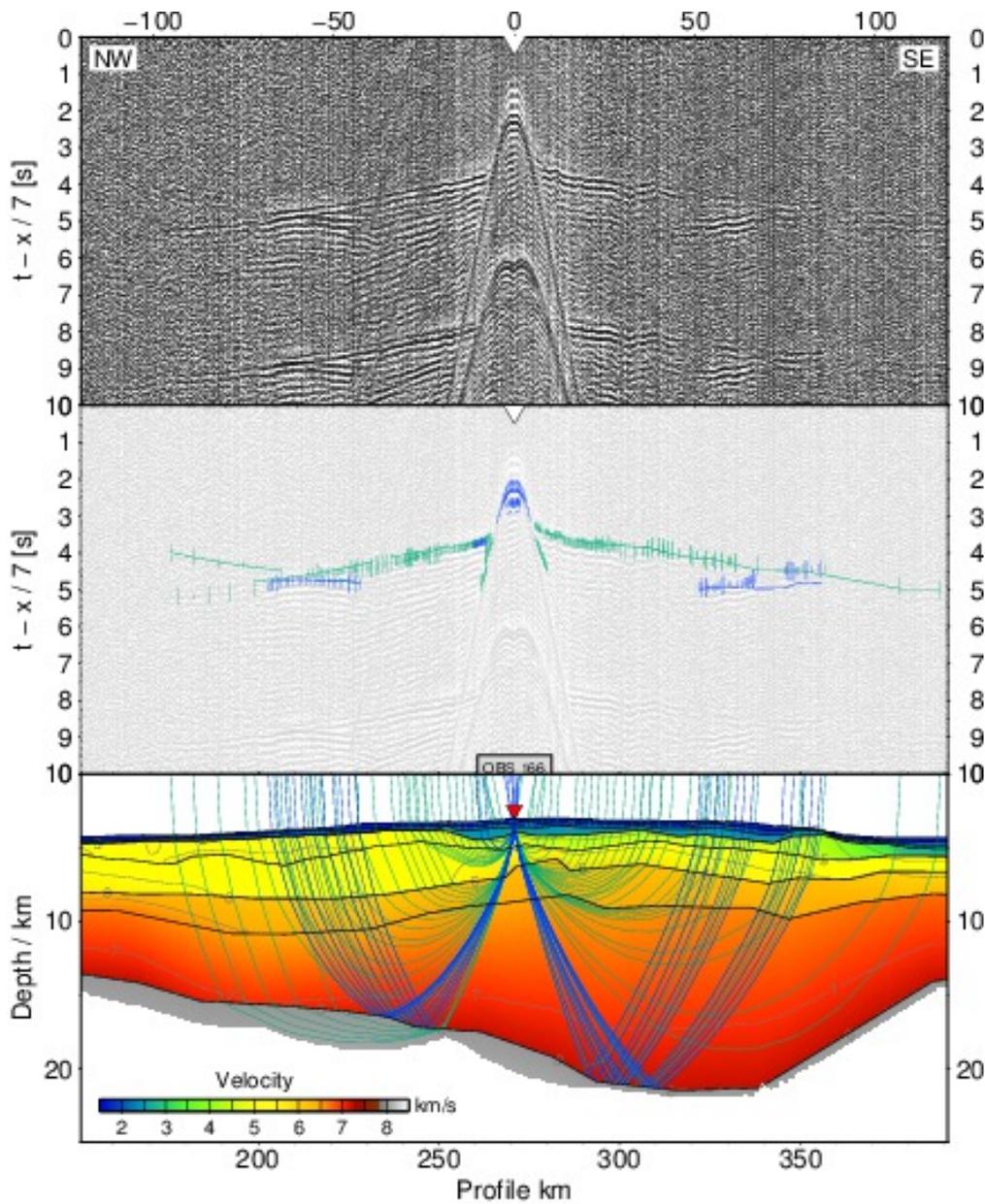
Figure A.2.15: Ray tracing results for station 166, profile 150. top) seismogram, center) seismogram overlain by picked phases (vertical bars) and calculated travel times (lines), bottom) ray path within the model. The uncertainty of the picked phases is resembled by the line length of the vertical bar. Line colors denote the ray type: blue - reflected phase, green - refracted phase
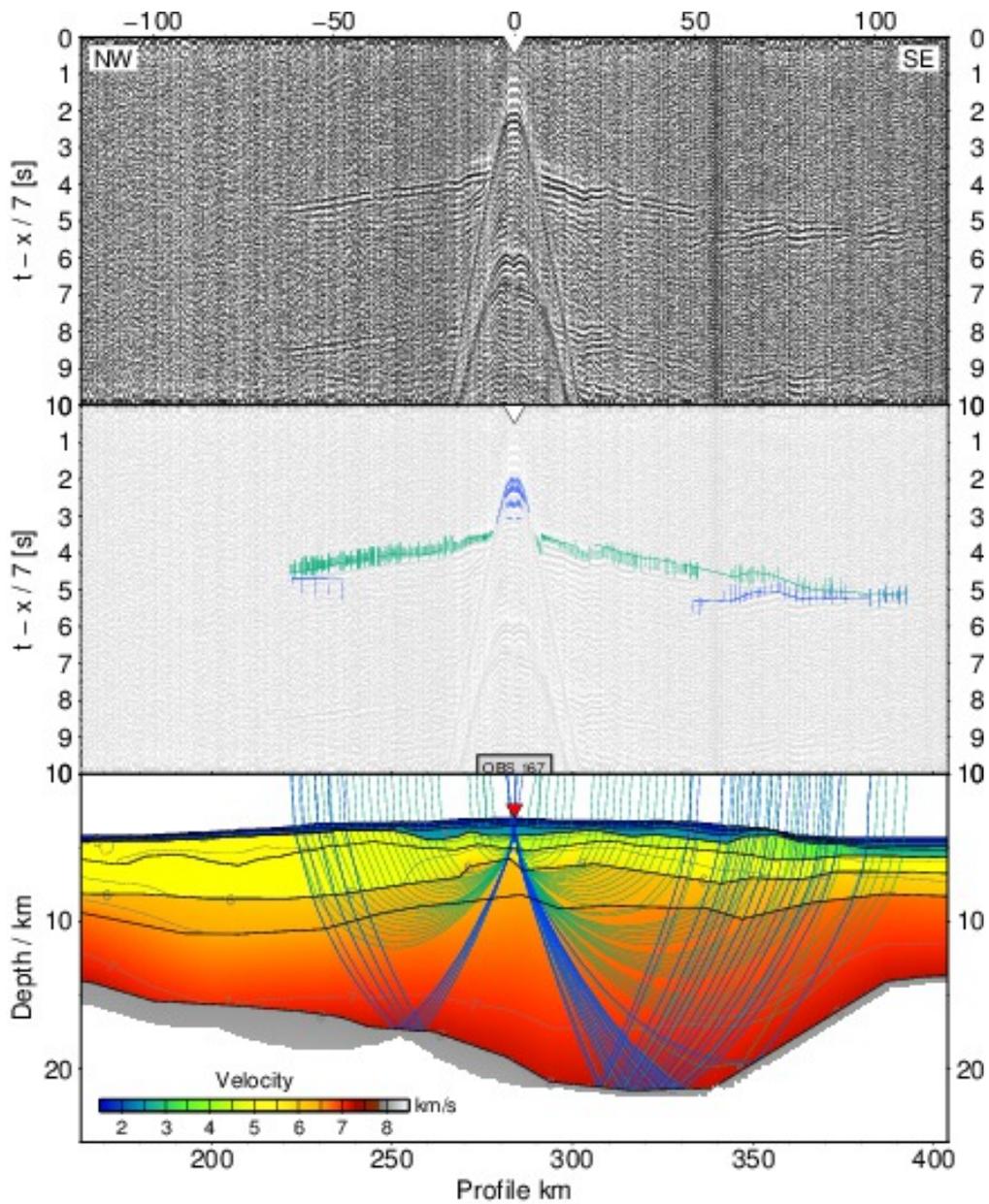
Figure A.2.16: Ray tracing results for station 167, profile 150. top) seismogram, center) seismogram overlain by picked phases (vertical bars) and calculated travel times (lines), bottom) ray path within the model. The uncertainty of the picked phases is resembled by the line length of the vertical bar. Line colors denote the ray type: blue - reflected phase, green - refracted phase
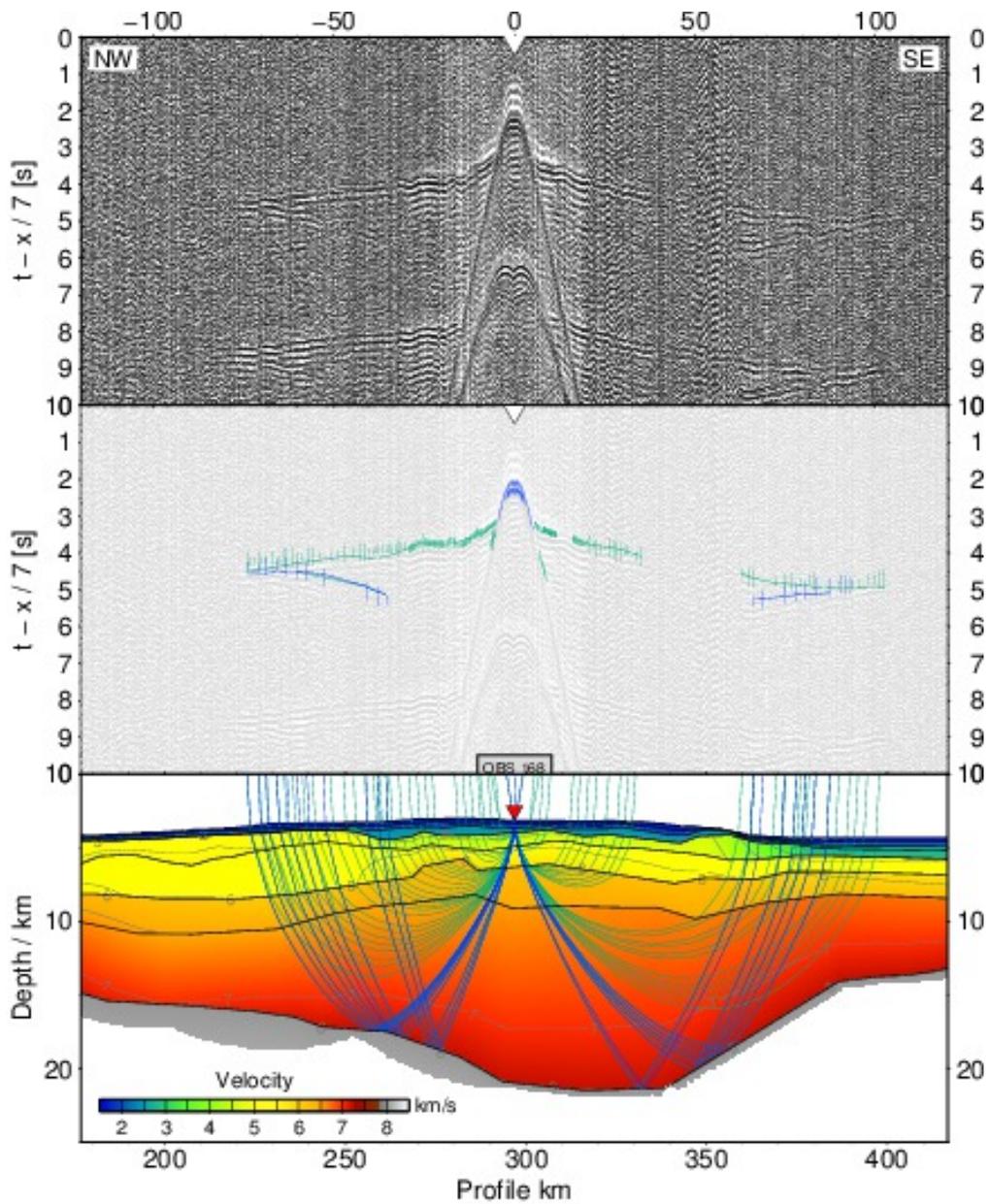
Figure A.2.17: Ray tracing results for station 168, profile 150. top) seismogram, center) seismogram overlain by picked phases (vertical bars) and calculated travel times (lines), bottom) ray path within the model. The uncertainty of the picked phases is resembled by the line length of the vertical bar. Line colors denote the ray type: blue - reflected phase, green - refracted phase
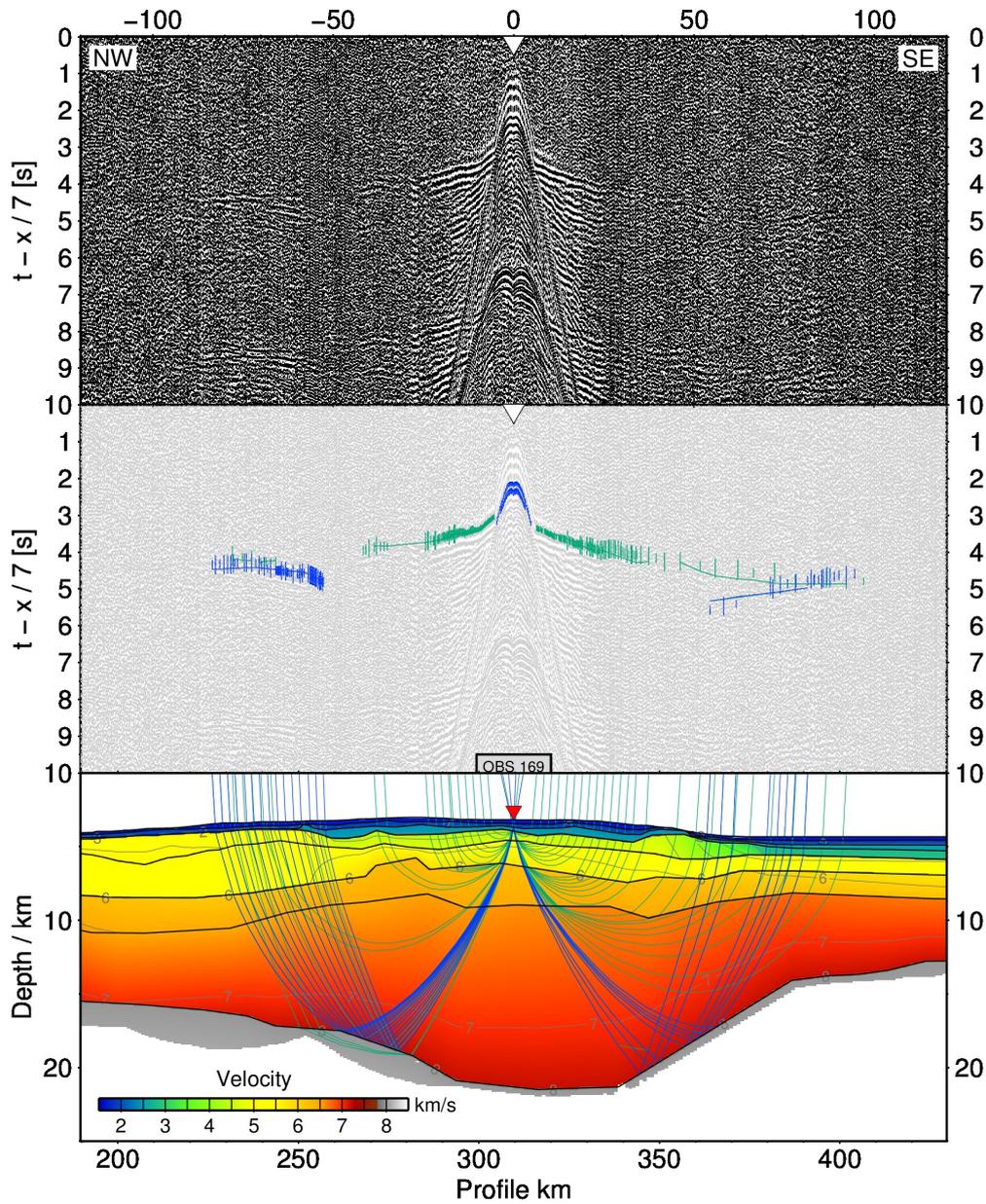
Figure A.2.18: Ray tracing results for station 169, profile 150. top) seismogram, center) seismogram overlain by picked phases (vertical bars) and calculated travel times (lines), bottom) ray path within the model. The uncertainty of the picked phases is resembled by the line length of the vertical bar. Line colors denote the ray type: blue - reflected phase, green - refracted phase
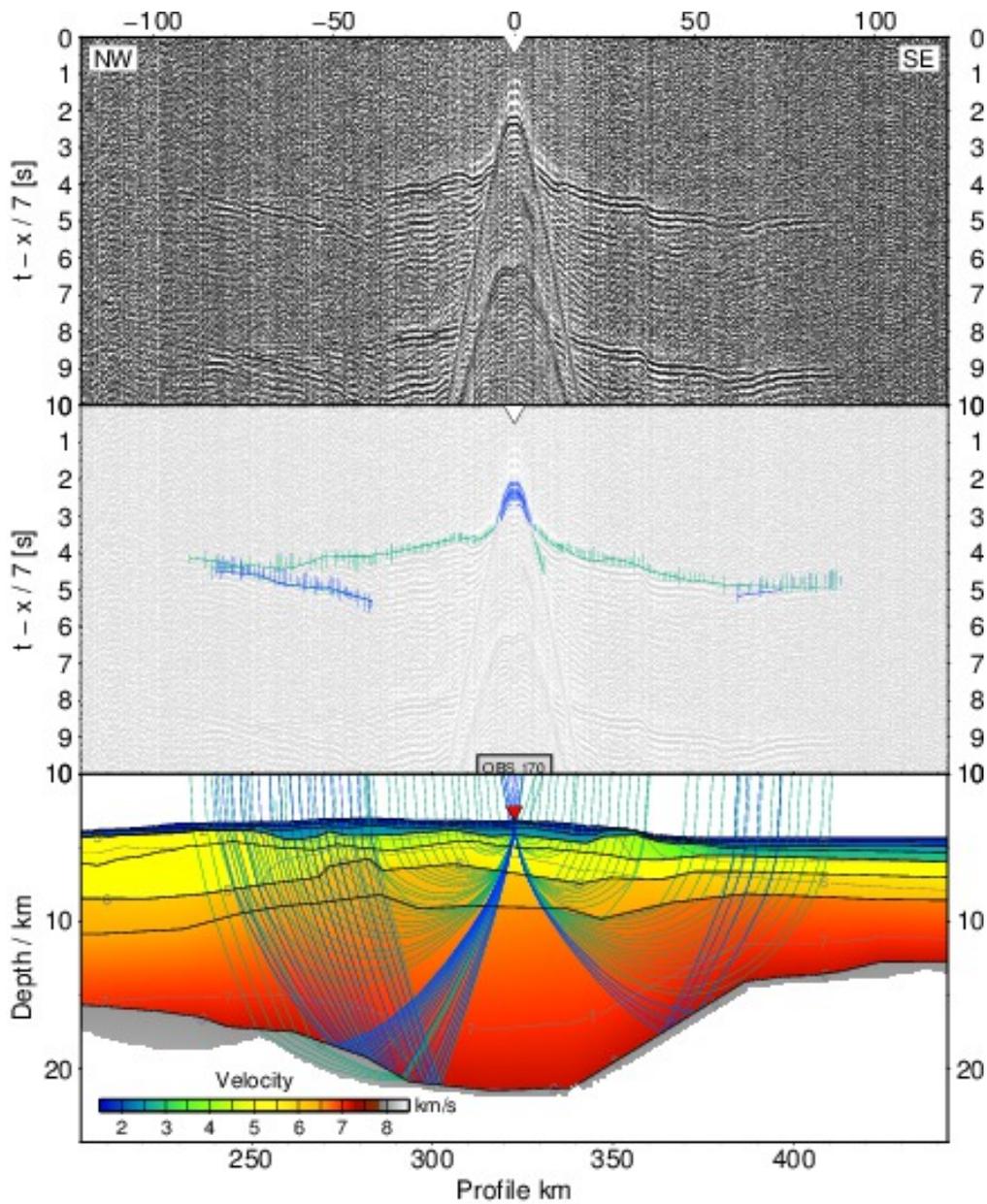
Figure A.2.19: Ray tracing results for station 170, profile 150. top) seismogram, center) seismogram overlain by picked phases (vertical bars) and calculated travel times (lines), bottom) ray path within the model. The uncertainty of the picked phases is resembled by the line length of the vertical bar. Line colors denote the ray type: blue - reflected phase, green - refracted phase
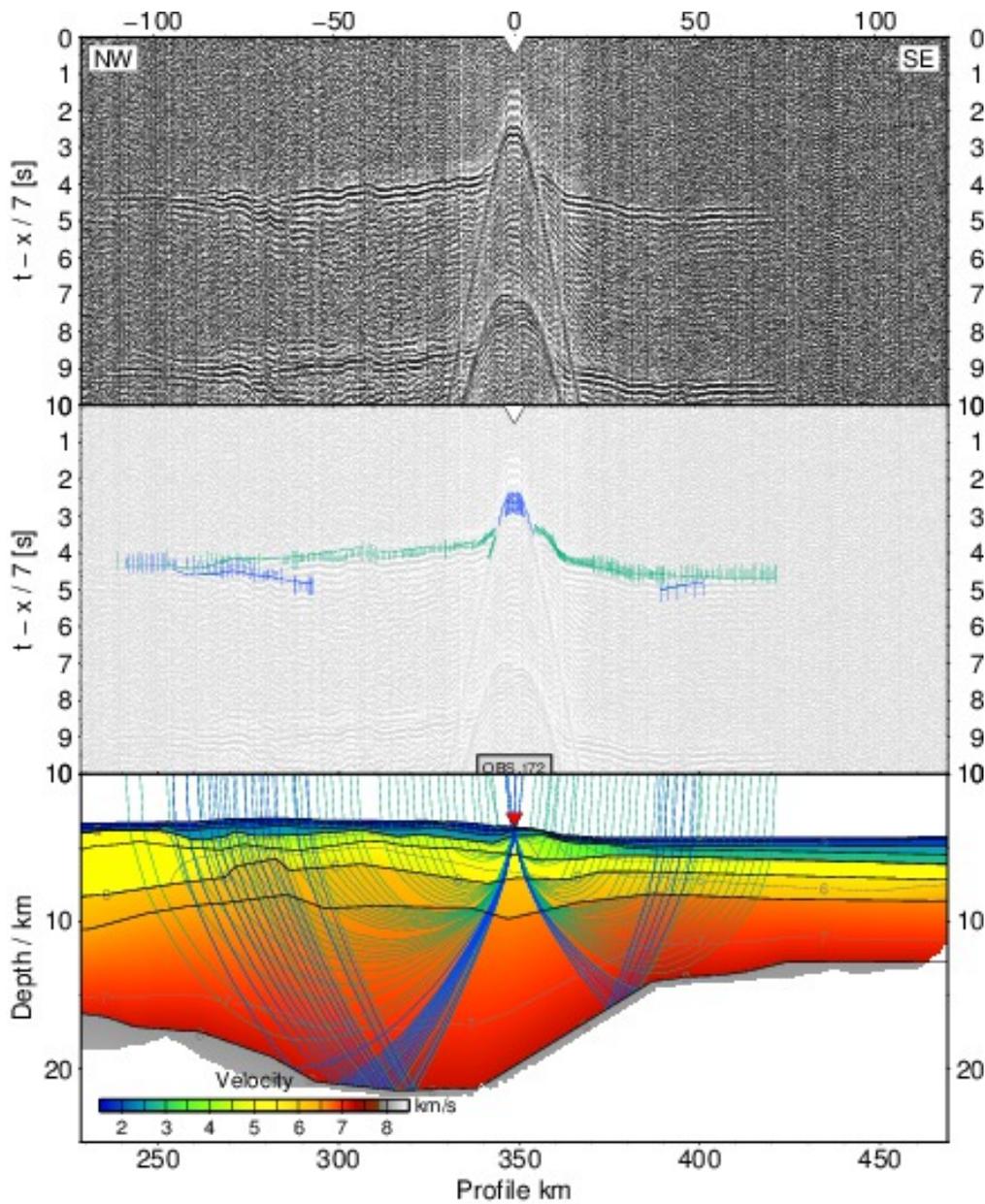
Figure A.2.20: Ray tracing results for station 172, profile 150. top) seismogram, center) seismogram overlain by picked phases (vertical bars) and calculated travel times (lines), bottom) ray path within the model. The uncertainty of the picked phases is resembled by the line length of the vertical bar. Line colors denote the ray type: blue - reflected phase, green - refracted phase
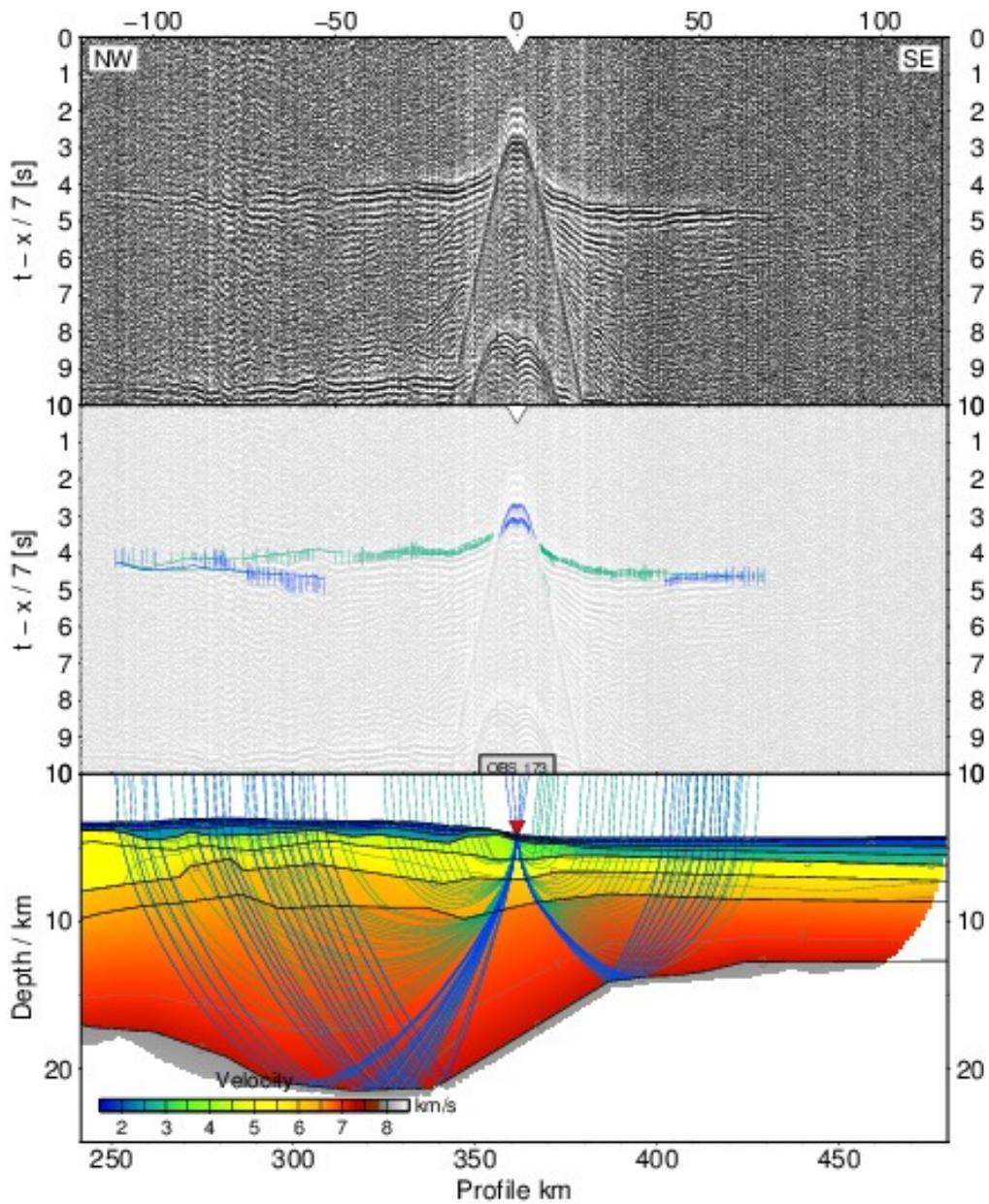
Figure A.2.21: Ray tracing results for station 173, profile 150. top) seismogram, center) seismogram overlain by picked phases (vertical bars) and calculated travel times (lines), bottom) ray path within the model. The uncertainty of the picked phases is resembled by the line length of the vertical bar. Line colors denote the ray type: blue - reflected phase, green - refracted phase
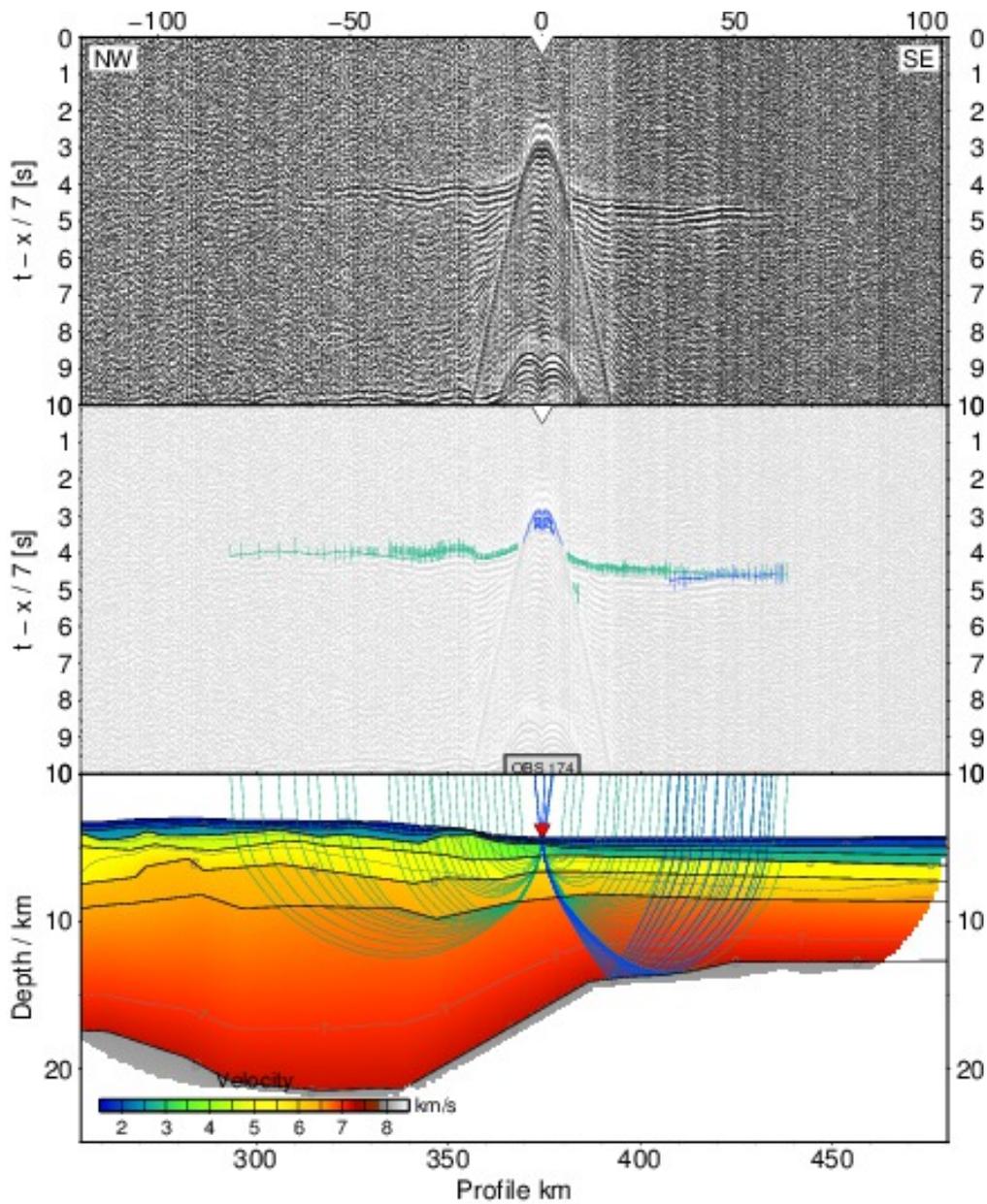
Figure A.2.22: Ray tracing results for station 174, profile 150. top) seismogram, center) seismogram overlain by picked phases (vertical bars) and calculated travel times (lines), bottom) ray path within the model. The uncertainty of the picked phases is resembled by the line length of the vertical bar. Line colors denote the ray type: blue - reflected phase, green - refracted phase
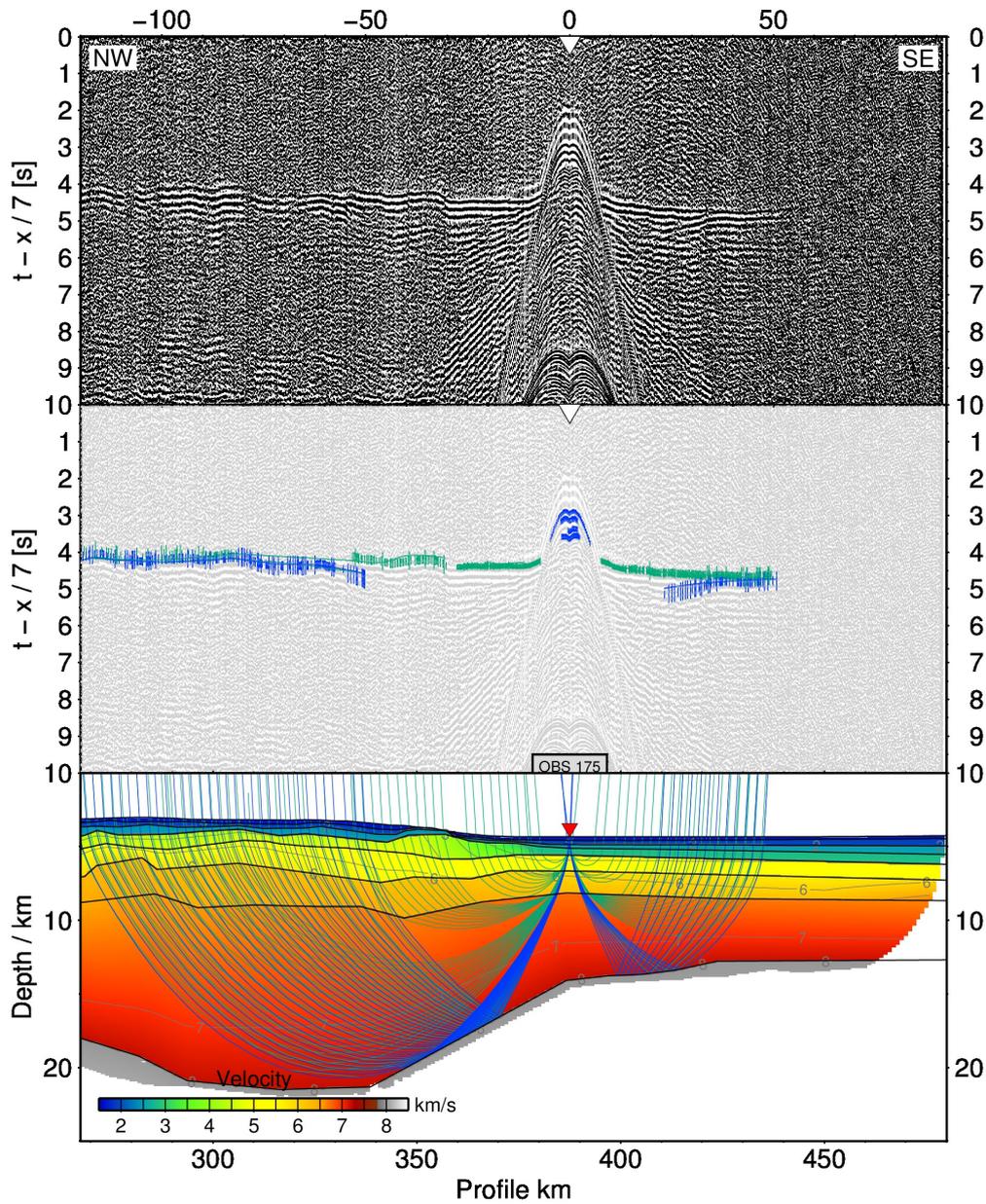
Figure A.2.23: Ray tracing results for station 175, profile 150. top) seismogram, center) seismogram overlain by picked phases (vertical bars) and calculated travel times (lines), bottom) ray path within the model. The uncertainty of the picked phases is resembled by the line length of the vertical bar. Line colors denote the ray type: blue - reflected phase, green - refracted phase
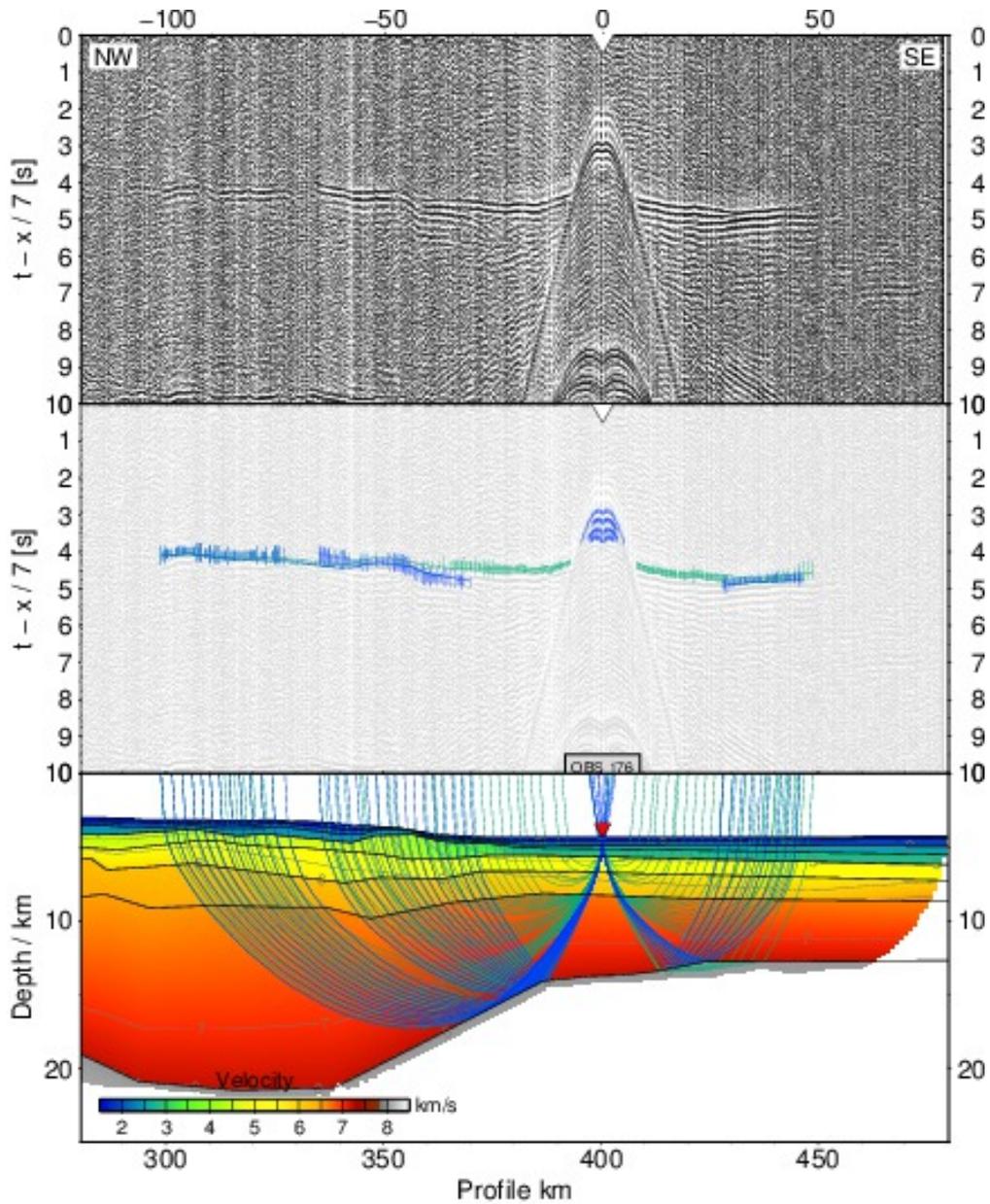
Figure A.2.24: Ray tracing results for station 176, profile 150. top) seismogram, center) seismogram overlain by picked phases (vertical bars) and calculated travel times (lines), bottom) ray path within the model. The uncertainty of the picked phases is resembled by the line length of the vertical bar. Line colors denote the ray type: blue - reflected phase, green - refracted phase
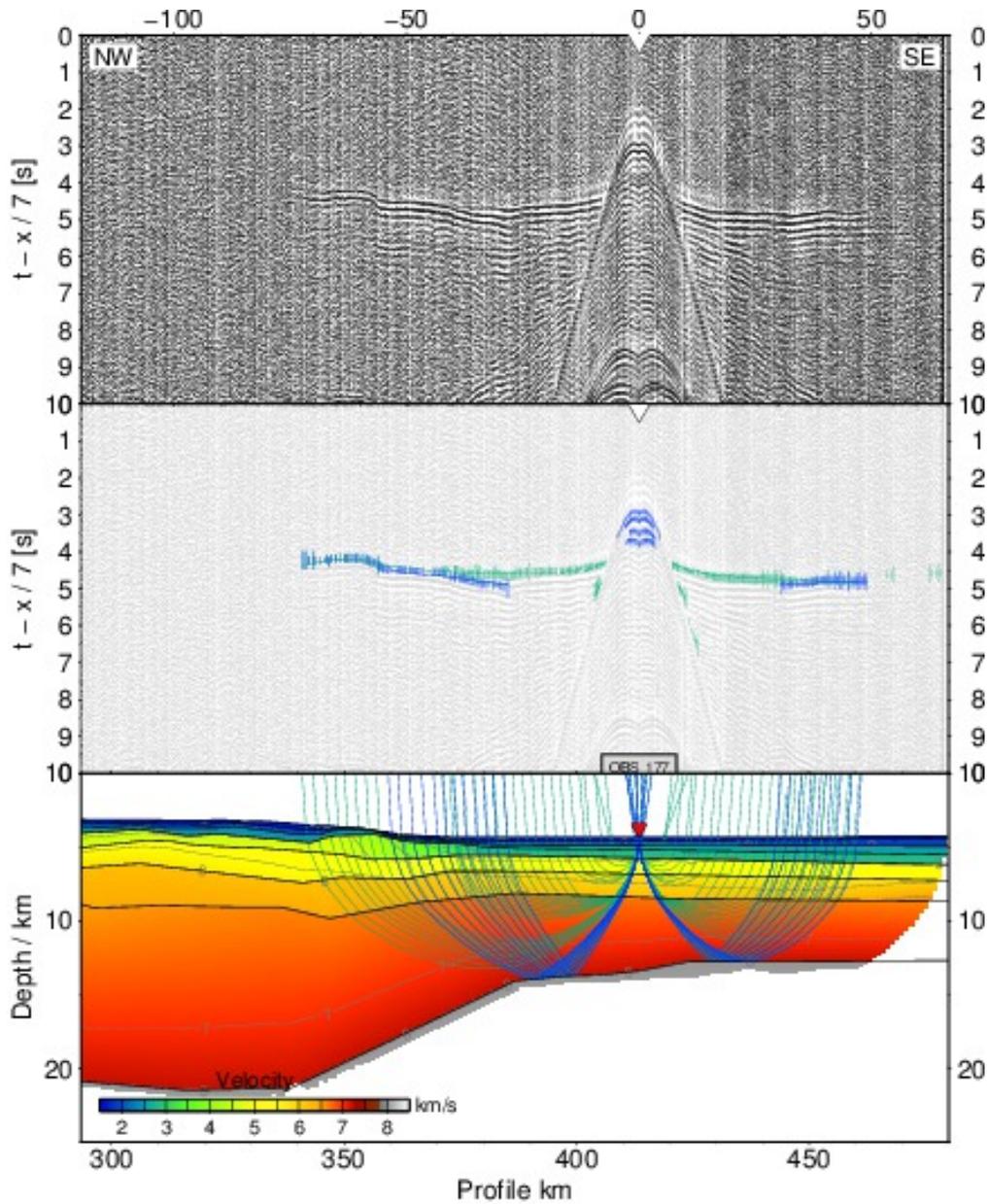
Figure A.2.25: Ray tracing results for station 177, profile 150. top) seismogram, center) seismogram overlain by picked phases (vertical bars) and calculated travel times (lines), bottom) ray path within the model. The uncertainty of the picked phases is resembled by the line length of the vertical bar. Line colors denote the ray type: blue - reflected phase, green - refracted phase
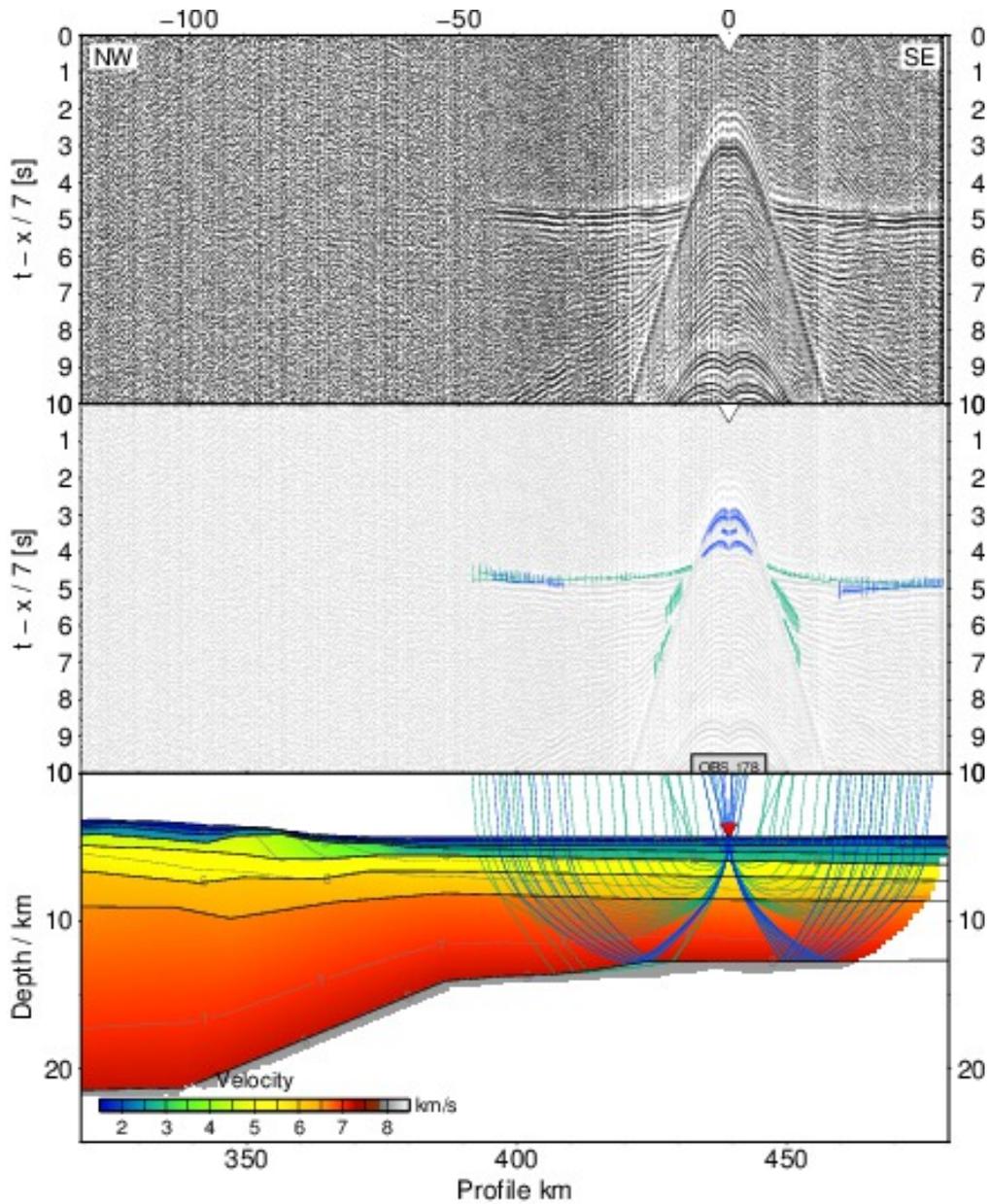
Figure A.2.26: Ray tracing results for station 178, profile 150. top) seismogram, center) seismogram overlain by picked phases (vertical bars) and calculated travel times (lines), bottom) ray path within the model. The uncertainty of the picked phases is resembled by the line length of the vertical bar. Line colors denote the ray type: blue - reflected phase, green - refracted phase
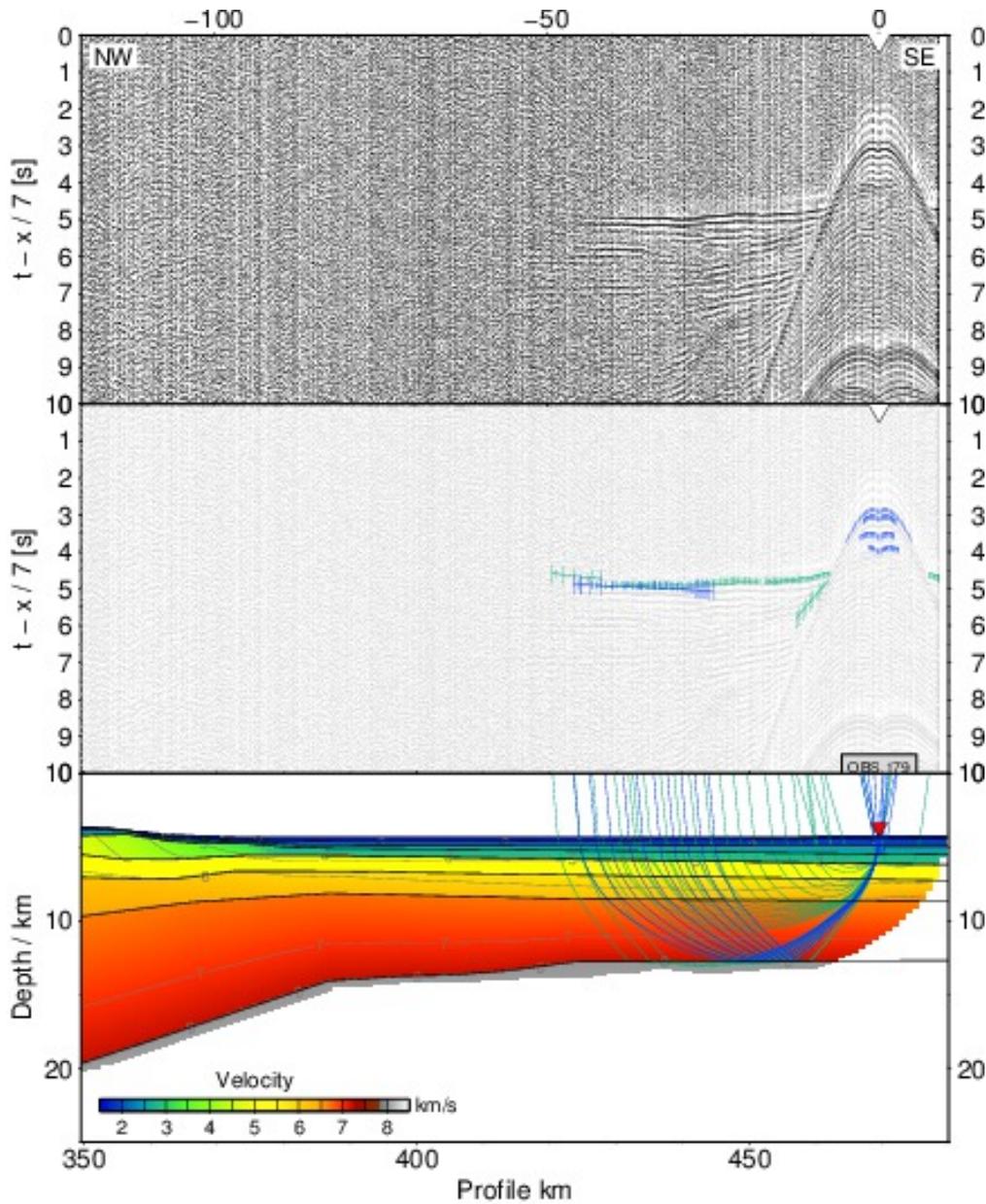
Figure A.2.27: Ray tracing results for station 179, profile 150. top) seismogram, center) seismogram overlain by picked phases (vertical bars) and calculated travel times (lines), bottom) ray path within the model. The uncertainty of the picked phases is resembled by the line length of the vertical bar. Line colors denote the ray type: blue - reflected phase, green - refracted phase

Acknowledgement - Danksagung